

For Reference

NOT TO BE TAKEN FROM THIS ROOM

Ex libris
UNIVERSITATIS
ALBERTAENSIS





Digitized by the Internet Archive
in 2020 with funding from
University of Alberta Libraries

<https://archive.org/details/Olson1981>

THE UNIVERSITY OF ALBERTA

RELEASE FORM

NAME OF AUTHOR . . . Maynard Roy Olson

TITLE OF THESIS . . . An Optical Fiber Transmission System for a
Low-Frequency Radio Telescope Array
.

DEGREE FOR WHICH THESIS WAS PRESENTED . . . Master of Science

YEAR THIS DEGREE GRANTED . . . Spring 1981

Permission is hereby granted to THE UNIVERSITY OF ALBERTA
LIBRARY to reproduce single copies of this thesis and to lend
or sell such copies for private, scholarly or scientific
research purposes only.

The author reserves other publication rights, and neither
the thesis nor extensive extracts from it may be printed or
otherwise reproduced without the author's written permission.

THE UNIVERSITY OF ALBERTA

AN OPTICAL FIBER TRANSMISSION SYSTEM FOR A
LOW-FREQUENCY RADIO TELESCOPE ARRAY

by



MAYNARD ROY OLSON

A THESIS

SUBMITTED TO THE FACULTY OF GRADUATE STUDIES AND RESEARCH
IN PARTIAL FULFILMENT OF THE REQUIREMENTS FOR THE DEGREE
OF MASTER OF SCIENCE

IN

ELECTRICAL ENGINEERING

DEPARTMENT OF ELECTRICAL ENGINEERING

EDMONTON, ALBERTA

SPRING, 1981

THE UNIVERSITY OF ALBERTA
FACULTY OF GRADUATE STUDIES AND RESEARCH

The undersigned certify that they have read, and recommend to the Faculty of Graduate Studies and Research, for acceptance, a thesis entitled "An Optical Fiber Transmission System for a Low-Frequency Radio Telescope Array" submitted by Maynard Roy Olson in partial fulfilment of the requirements for the degree of Master of Science in Electrical Engineering.

DEDICATION

To My Parents

ABSTRACT

An optical fiber transmission feeder system is presented for the proposed radio telescope array in southwestern Alberta. The advantages of optical fibers over coaxial cables are outlined. Principles of light transmission in fibers are discussed as are dispersion, attenuation and other properties. Various optical sources and detectors are examined and their merits and demerits are considered. A number of methods are examined for coupling light signals among the optical components such as sources, thin-film waveguides, fibers and detectors. Loss mechanisms in fiber splices and connections are also discussed. Various antenna groupings in the array are considered from the standpoint of signal multiplexing. It is determined that 48 antennas is a practical maximum for r.f. multiplexing while keeping the total length of transmission line to a minimum. The different modulation schemes are appraised for their usefulness in the proposed transmission system. An analog FDM, intensity-modulated system is determined to be the most practical at this time. A transmission system design is finally presented and its performance is appraised. It is concluded that an optical fiber transmission feeder system can meet or exceed the performance specified provided that the estimated performance of the r.f. components, as outlined, can be met.

ACKNOWLEDGEMENTS

The author wishes to thank Dr. D. Routledge and Dr. J. F. Vaneldik, thesis supervisors, for their encouragement and guidance during the course of this work. The financial support provided by the Department of Electrical Engineering and the National Research Council of Canada is gratefully acknowledged. The author also wishes to thank his wife, Henda, for her continued encouragement and for typing this tome in her scarce spare time.

TABLE OF CONTENTS

CHAPTER	PAGE
1. INTRODUCTION	1
1.1 General Array Specifications	1
1.2 Coaxial Cable Limitations	3
1.3 Use of Optical Fibers	6
1.3.1 Transmission Losses	6
1.3.2 Electromagnetic Interference	7
1.3.3 Size, Weight and Flexibility	8
1.4 Optical Fiber Transmission System	8
1.5 Summary	13
2. OPTICAL FIBERS	14
2.1 General	14
2.2 Transmission in Fibers	14
2.3 Dispersion	22
2.3.1 Material and Waveguide Dispersion	23
2.3.2 Multimode Dispersion	30
2.3.2.1 Step-Index Profile	30
2.3.2.2 Graded-Index Profile	36
2.3.3 Dispersion-Limiting Techniques	38
2.3.4 Summary	40
2.4 Attenuation	46
2.4.1 Material Absorption	46
2.4.2 Material Scattering	48
2.4.3 Waveguide Scattering	50
2.4.4 Physical Bends	51

2.4.5	Cladding Design Effects	53
2.4.6	Summary	54
2.5	Crosstalk	56
2.6	Polarization	58
2.7	Physical Properties	61
(a)	Tensile Strength	61
(b)	Impact Resistance	61
(c)	Flexing & Twisting	62
(d)	Environmental Properties	62
2.8	Summary	63
3.	OPTICAL SOURCES	64
3.1	Laser Diodes	65
3.1.1	General	65
3.1.2	Laser Diode Performance	70
(a)	Threshold Current Density	70
(b)	Efficiency and Power	70
(c)	Beamwidth	74
(d)	Modulation	75
(e)	Noise	76
(f)	Reliability	76
3.2	Light-Emitting Diodes	78
3.2.1	General	78
(a)	Surface-Emitters	80
(b)	Edge-Emitters	80

3.2.2	LED Performance	81
(a)	Radiance and Current Density	81
(b)	Efficiency and Power	83
(c)	Modulation	86
(d)	Linearity	89
(e)	Noise	90
(f)	Reliability	90
3.3	Summary	91
4.	PHOTODETECTORS	92
4.1	General	92
4.2	Photodiodes	93
(a)	Materials	93
(b)	Non-avalanche Photodiodes	94
(c)	Avalanche Photodiodes	94
(d)	Responsivity & Efficiency	96
(e)	Risetime & Bandwidth	96
(f)	Temperature Stability	99
(g)	Noise Performance	99
(h)	Linearity	108
4.3	Summary	108
5.	COUPLING	109
5.1	Direct Coupler	110
5.2	Prism-Film Coupler	115
5.3	Birefringent Coupler	132
5.4	Grating Coupler	134
5.5	Tapered-Film Coupler	136

5.6	Splicing & Connecting	139
5.7	Summary	148
6.	MODULATION AND MULTIPLEXING	150
6.1	Feeder System Configuration	150
6.2	Modulation	160
6.2.1	Digital Modulation	161
6.2.2	Pulse Modulation	165
6.2.3	Analog Modulation & Frequency Division Multiplexing	169
6.2.3.1	Frequency & Phase Modulation	170
6.2.3.2	Amplitude Modulation	174
6.3	Optical Multiplexing	186
6.3.1	Antenna Signal Distribution	186
6.3.2	Local Oscillator Distribution	189
6.4	Summary	190
7.	TRANSMISSION SYSTEM DESIGN	192
7.1	System Configuration	192
7.1.1	General	192
7.1.2	Transmitting Section	196
7.1.2.1	Central Transmitting Location (CTL)	196
7.1.2.2	Optical Multiplexing Location (OML)	200
7.1.3	Receiving Section	204
7.1.3.1	Optical Demultiplexing	204
7.1.3.2	R. F. Demultiplexing	206
7.1.3.3	Local Oscillator	209

7.2	Optical Link Design	211
7.2.1	Antenna Signal Link	211
7.2.2	Local Oscillator Link	221
7.3	System Noise Temperature	224
7.3.1	Antenna Signal Link	224
7.3.2	Local Oscillator Link	237
7.4	Excitation Errors	242
8.	SUMMARY AND CONCLUSIONS	251
	REFERENCES	255
	APPENDICES	
	A - Multimode Dispersion as a Function of Refractive Index Profile	266
	B - Experimental Dispersion Results	269
	C - Experimental Attenuation Results	275
	D - Optical Fiber State-of-the-Art	277
	E - Crosstalk in Multimode Fibers	279
	F - Linearity Measurements on LED's	284
	G - Photodetector Noise Performance	287
	H - Linearity Measurements on Photodiodes	290
	I - Direct Coupling of LED's to Step-Index Fibers	293
	J - Direct Coupling of LED's to Parabolic-Index Fibers	305
	K - Grating Couplers -- Theory and Practice	310
	L - Transmission Line Lengths for a 24 Channel System	316
	M - Wavelength-Division Multiplexer Design	323

LIST OF TABLES

TABLE	TITLE	PAGE
2.1	Contribution of Impurities in Glass to Absorption	47
2.2	Polarization Effects and Losses	60
3.1	Effect of Area on Radiance	82
3.2	Comparison of Absolute Radiance Values For Three Types of Diodes	82
5.1	Summary of Results of Analyses for Disc and Stripe Geometries With and Without a Lens	111
5.2	Fibers Used to Measure Coupling Efficiency	114
5.3	Laser-to-Fiber Coupling Efficiency in Percent	114
5.4	Coupling Efficiency as a Function of Spectral Width	131
5.5	Coupling Efficiency as a Function of Beam Divergence	131
6.1	Primary Feeder Quantities (km)	157
6.2	Branch Feeder Quantities (km)	158
6.3	Bandwidth vs. Attenuation Discrimination for 3 dB Bandwidth Separation of 200 KHz	179
6.4	Channel Spacing vs. Filter Types	180
7.1	Summary of Excitation Error Estimates	250
C.1	Spectral Attenuation of 3 Multimode Fibers	276

LIST OF FIGURES

FIGURE	TITLE	PAGE
1.1	Tee-array configuration	2
1.2	General optical fiber transmission system configuration	9
1.3	Physical system configuration	12
2.1	Optical fiber cross-section	15
2.2	Optical fiber refractive index profiles (a) step-index (b) graded-index	15
2.3	Ray transmission in an optical fiber	17
2.4	Normalized propagation constant b as a function of normalized frequency v for a number of linearly polarized modes	20
2.5	Waveguide dispersion curve: (a) without considering material dispersion (b) including material dispersion effects	25
2.6	Dispersion characteristics of several lower-order modes in an optical fiber	25
2.7	Dispersion coefficient $kd^2\beta/dk^2$ as a function of frequency for fused silica SiO_2	28
2.8	Calculated wavenumber dispersion β'' as a function of λ for several optical fibers of varying core-cladding index difference and core diameters	31
2.9	Dispersion as a function of source spectral width and center wavelength	31
2.10	Wavelength dependence of fused silica glass (a) dependence of index n (b) dependence of $dn/d\lambda$ (c) dependence of $d^2n/d\lambda^2$	37
2.11	Ray propagation in a graded-index fiber	37
2.12	Multimode dispersion	41
2.13	Material dispersion, $\tau = \delta\lambda \frac{\lambda_0}{c} \frac{d^2n}{d\lambda^2}$	42
2.14	Waveguide dispersion, $\tau = \frac{2n_1}{c} \frac{\delta\lambda}{\lambda_0} \Delta$	42
2.15	Attenuation due to bends for two waveguides	52

FIGURE	TITLE	PAGE
2.16	Spectral attenuation of various optical fibers	55
2.17	Typical optical fiber transmission system	61
3.1	Cross-section of a typical stripe-contact laser diode	68
3.2	Buried heterostructure (BH) injection laser diode	68
3.3	Development of GaAs lasers since 1963, showing progressive reduction of reported threshold current densities at room temperature	71
3.4	Threshold current density as a function of temperature for homojunction, single-heterojunction (SH), double-heterojunction and large optical cavity lasers with cavity length L	71
3.5	Power emitted from one facet of a typical stripe-geometry aluminum gallium arsenide laser diode in CW operation at various temperatures	72
3.6	Cross-section of surface-emitting LED	85
3.7	Output characteristic for Burrus-type surface-emitting LED	85
3.8	Power emitted as a function of drive current for a normal and a restricted edge-emitting LED	88
3.9	Modulation characteristics of highly-doped GaAs and InGaAs high-radiance diodes	88
4.1	Construction of non-avalanching p-i-n photodiodes	95
4.2	Construction of avalanche photodiodes	95
4.3	Spectral response of p-i-n silicon and germanium photodetectors	98
4.4	Equivalent circuit of a photodiode	98
4.5	Signal-to-component noise ratio vs. incident power for a photodetector with unity gain	104
4.6	Signal-to-component noise ratio vs. incident power for a photodetector with a gain of 10	105
5.1	Prism-film coupler	116
5.2	Thin-film optical waveguide showing the three cases of optical propagation	117

FIGURE	TITLE	PAGE
5.3	Waveguide mode characteristics as a function of film thickness and angle of refraction for (a) $0.532\ \mu\text{m}$ (b) $1.06\ \mu\text{m}$	121
5.4	Propagation angle as a function of wavelength for TE_0 and TM_0 modes in film waveguides of different thickness	122
5.5	Angle of incidence for TE_0 modes in prisms of various angles φ and indices of refraction n_p	125
5.6	Angle of incidence for TE_0 modes as a function of prism index of refraction for prisms of different angles	127
5.7	Refractive-index ellipsoid for birefringent material with a waveguide superimposed at an angle to the optic axis	133
5.8	Schematic of a birefringent coupler	133
5.9	Angle of incidence as a function of wavelength for a grating coupler with periodicity $g = 0.5\ \mu\text{m}$ and $c/v_p = 1.55$	137
5.10	Tapered-film coupler	137
5.11	Loss caused by mismatches in fiber core diameters or numerical aperture	141
5.12	Loss caused by mismatch in refractive-index profiles	141
5.13	Loss caused by lateral misalignment of centers of identical step-index fibers	142
5.14	Loss caused by angular misalignment of axes of identical step-index fibers	142
5.15	Loss caused by separation of the ends of perfectly aligned identical step-index fibers	142
5.16	Loss in dB vs. normalized offset d/a , separation L/a , and angular misalignment $\varphi/\sin^{-1}(\text{N.A.})$ for graded-index fibers	144
6.1	Tee array configuration	152
6.2	Possible antenna groupings within the array	152

FIGURE	TITLE	PAGE
6.3	Dimensions used to determine transmission line lengths	156
6.4	Transmission line requirements as a function of the number of channels multiplexed	159
6.5	Basic PCM transmitter	166
6.6	Basic DPCM transmitter	166
6.7	Frequency modulation bandwidth for noise modulation	173
6.8	Amplitude modulation waveforms	175
6.9	Typical "passband" SSB-FDM modulation spectrum for an n-channel transmission system	183
6.10	Typical spectra of two passband, SSB-FDM systems	183
7.1	Transmission system configuration	193
7.2	Central transmitting location configuration	197
7.3	Optical multiplexing location configuration	201
7.4	Optical demultiplexing configuration	205
7.5	R.F. demultiplexing configuration	207
7.6	Local oscillator distribution	210
7.7	Optical antenna signal link and power budget	212
7.8	Signal-to-component noise ratio versus incident power for a photodetector with unity gain	218
7.9	Signal-to-component noise ratio versus incident power for a photodetector with a gain of 10	219
7.10	Optical local oscillator link and power budget	222
7.11	Transmission system model for noise temperature calculations	230
7.12	Transmitter model for noise temperature calculations	230
7.13	Receiver model for noise temperature calculations	230
7.14	Optical antenna signal link model for noise temperature calculations	238
7.15	Local oscillator model for noise temperature calculations	238

FIGURE	TITLE	PAGE
E.1	Input angular power distribution	280
E.2	Far-end crosstalk vs. core/cladding ratio	280
E.3	Far-end crosstalk vs. numerical aperture	281
E.4	Far-end crosstalk vs. fiber length	281
E.5	Far-end crosstalk vs. kappa	282
E.6	Far-end crosstalk vs. wavelength	282
F.1	Variation of nonlinear distortion (a) with direct bias and (b) with modulation depth	285
F.2	Total harmonic distortion in a typical DH high-radiance LED	285
F.3	Total harmonic distortion as a function of ambient temperature in typical Ge-doped, DH LED's	286
H.1	Nonlinear distortion as a function of incident power	292
I.1	LED/fiber coupling configuration	295
I.2	Percent coupling efficiency as a function of fiber numerical aperture	295
I.3	Percent coupling efficiency as a function of the ratio of the LED/fiber separation to LED radius for fibers of numerical aperture N.A. = 0.1, 0.2 and 0.3	297
I.4	Percent coupling efficiency as a function of the ratio of the LED/fiber separation to LED radius for different ratios of LED to fiber core radii	297
I.5	LED/fiber coupling configuration using a lens	301
I.6	Coupling configuration using a stripe-geometry LED butted against an optical fiber	301
I.7	Coupling configuration using a stripe-geometry LED and a lens	303
J.1	Geometry of a source exciting a fiber core	308
J.2	Normalized total power P_f injected into a parabolic-index fiber as a function of the distance L between source and fiber	308

FIGURE	TITLE	PAGE
J.3	Normalized total power P_f injected into a parabolic-index fiber as a function of the transverse source displacement d for several values of the distance L of the source from the fiber and for $\Delta = 0.01$	308
J.4	Total power injected into the fiber with a high-brightness, Burrus-type LED as a function of normalized source radius r	309
J.5	Normalized ratio of total power P_f injected into the fiber relative to the electrical drive power of the diode as a function of the normalized source radius	309
K.1	Grating coupler cross-sections (a) normal grating coupler (b) reverse coupler	311

GLOSSARY OF SYMBOLS

SYMBOL	MEANING	TYPICAL PAGE REFERENCE
a	radius of fiber core	14
b	radius of fiber cladding	14
c	velocity of light in vacuum	23
d	axial offset mismatch of fibers/source	142
e	electron charge	70
f	frequency	70
f_c	carrier frequency	182
f_{cu}, f_{cl}	upper, lower carrier frequencies	184
f_h	highest frequency of interest	163
f_{if}	intermediate frequency	4
f_m	modulating frequency	184
g	periodicity of grating	310
h	Planck's constant	287
i	electric current	70
i_d	primary photodetector dark current	288
i_L	photodetector leakage current	289
i_{ph}	primary photodetector photocurrent	287
$\langle i_B^2 \rangle$	mean-square photodetector beat noise current	289
$\langle i_D^2 \rangle$	mean-square photodetector dark current	288
$\langle i_L^2 \rangle$	mean-square photodetector leakage current	289
$\langle i_Q^2 \rangle$	mean-square photodetector quantum noise current	288

SYMBOL	MEANING	TYPICAL PAGE REFERENCE
$\langle i_s^2 \rangle$	mean-square photodetector signal current	287
$\langle i_T^2 \rangle$	mean-square thermal noise current	288
j	current density	110
j_{th}	laser diode threshold current density	70
k	Boltzmann's constant	288
k_a	wavenumber in grating superstrate	313
k_e	equivalent wave vector	313
k_o	wavenumber in free space	18
k_s	wavenumber in grating substrate	313
k_w	propagation constant of grating guided wave	313
l_{c_i}	optical link coupler losses	213
l_f	transmission loss in fiber	49
l_{opt}	optical link loss	234
l_r	radiation attenuation in fiber due to bends	51
l_{PTF}	loss in primary transmission feeder	213
l_{STF}	loss in secondary transmission feeder	213
m	modulation index	170
n_1	refractive index of fiber core	14
n_2	refractive index of fiber cladding	14
n_a	refractive index of air	115
n_e	effective refractive index	27
n_f	refractive index of thin-film waveguide	115
n_i	refractive index for incident ray	133
n_o	refractive index of external medium	16
n_p	refractive index of prism	123

SYMBOL	MEANING	TYPICAL PAGE REFERENCE
n_r	refractive index for reflected ray	133
n_s	refractive index of thin-film substrate	115
n_{ex}	extraordinary refractive index	132
n_{or}	ordinary refractive index	132
p_b	power of background light on photodetector	288
p_o	average received optical power	287
p_1, p_2	thin-film waveguide width factors	126
q	normalized optical propagation constant	19
r	radius	14
r_s	radius of source	293
s	optical source	293
t	time	163
t_1	propagation time of axial ray in fiber	32
t_2	propagation time of reflected ray in fiber	32
t_r	pulse risetime in photodetector	97
u	optical propagation parameter	18
v_s	voltage across optical source	70
w	optical propagation parameter	18
x, y, z	Cartesian co-ordinate axes	300
A	area of emission of LED	79
B	bandwidth	40
C	capacitance	106
C_i	amplifier input capacitance	97

SYMBOL	MEANING	TYPICAL PAGE REFERENCE
C_j	photodiode junction capacitance	97
C_{stray}	photodiode stray capacitance	97
D	distortion due to FM band limiting	172
F	equipment noise figure	225
F_a	baseband amplifier noise figure	100
F_d	photodetector excess noise factor	288
G	gain of device or equipment	100
$G_{a,b,c,d}$	gains of local oscillator link stages	239
G_{bf}	branch feeder gain	225
G_o	gain of optical link	225
G_r	gain of receiver section	232
G_t	gain of transmitter section	229
$G_{1,2,3,4}$	gains of transmitter subsections	226
$G_{6,7,8}$	gains of receiver subsections	229
H	fiber input angular power distribution	279
I_c	optical power coupled into fiber	79
I_t	total radiated power from source	83
K	optical coupling parameter	279
L	length, distance	27
L_c	fiber coupling length	39
L_j	length of active junction in LED	300
L_l	distance between leading and trailing edges	126
M	mode number	118
N.A.	numerical aperture of fiber	17
O	virtual point of convergence in prism	326

SYMBOL	MEANING	TYPICAL PAGE REFERENCE
P_f	normalized total optical power in fiber	308
P_{\max}	maximum useable power in fiber	49
P_{FM}	power in unmodulated FM carrier	172
Q	number of propagating modes in fiber	21
R	resistance	97
R_b	bit rate	27
R_i	amplifier input resistance	97
R_s	photodiode series resistance	97
S	prism-film coupling parameter	126
T	absolute temperature	288
T_e	noise temperature of equipment subsequent to antenna	224
T_o	absolute ambient temperature	225
T_{ant}	noise temperature of the antenna	224
T_{sys}	noise temperature of a receiving system	224
$T_{e_{\text{bf}}}$	noise temperature of branch feeder	225
T_{e_1}	noise temperature of local oscillator system	239
T_{e_o}	noise temperature of optical link	225
T_{e_r}	noise temperature of receiver section	229
T_{e_t}	noise temperature of transmitter section	226
$T_{e_{a,b,c,d,e}}$	noise temperature of local oscillator subsections	239
$T_{e_{1,2,3,4,5}}$	noise temperature of transmitter subsections	226
$T_{e_{6,7,8,9}}$	noise temperature of receiver subsections	229
U	fiber/LED coupling transmission coefficient	293
V_g, V_p	group, phase velocities	24
W_f	film waveguide thickness	118

SYMBOL	MEANING	TYPICAL PAGE REFERENCE
W_g	prism-film air gap spacing	128
W_{eff}	effective film waveguide thickness	126
X	crosstalk coupling factor	57
Y	number of spatial modes in fiber output	289
α	graded-index profile exponent	266
β	propagation constant	18
$\delta\lambda$	source spectral width (meters)	26
δf	source spectral width (Hertz)	289
δf_c	multiplexed carrier frequency separation	176
δA	amplitude overlap of adjacent pulses	27
δK_p	coaxial cable phase temperature coefficient	243
δT	ambient temperature range	4
$\epsilon_{\text{r.m.s.}}$	r.m.s. phase error due to temperature	243
η	photodiode quantum efficiency	96
η_c	optical coupling efficiency	126
η_q	optical source quantum efficiency	70
θ	external acceptance angle of fiber	16
θ_c	maximum acceptance angle of fiber	16
θ_p	prism angle	124
θ_L	angle between axis and ray through lens	298
λ	wavelength of optical signal	18
λ_a	wavelength in grating superstrate (air)	313
λ_g	wavelength of guided wave in film	312
λ_s	wavelength in grating substrate	313
λ_t	wavelength of telescope signal	150

SYMBOL	MEANING	TYPICAL PAGE REFERENCE
ν	normalized frequency of optical signal	19
ρ	photodiode spectral responsivity	96
σ	FWHM power density in fiber	49
τ	dispersion, pulse spread	26
τ_c	absolute delay in branch feeders	243
τ_g	group (envelope) delay	26
τ_i, τ_o	input, output pulse width	29
τ_D	material dispersion	40
τ_M	multimode dispersion	40
τ_W	waveguide dispersion	40
τ_T	total dispersion	40
ϕ	angle between light ray and normal to fiber axis	16
ϕ_a	angle between light ray and normal in air	115
ϕ_c	critical angle between light ray and normal to axis	16
ϕ_f	angle between light ray and normal in film	115
ϕ_i	angle between incident ray and normal	123
ϕ_p	angle between light ray and normal in prism	123
ϕ_r	angle of refraction in prism	123
ϕ_s	angle between light ray and normal in substrate	115
φ_c	absolute phase shift in branch feeders	243
χ_1, χ_2	fiber propagation constants	51
ψ	angle between light ray and axis in fiber	16
ψ_c	critical angle between ray and axis in fiber	33
ψ_i	angle between optic axis and incident beam	133
ψ_r	angle between optic axis and refracted beam	133

SYMBOL	MEANING	TYPICAL PAGE REFERENCE
ω	angular frequency	24
Γ	focal length of lens	298
Δ	relative index difference	33
Λ	optical source radiance	79
Ξ	spatial phase modulation amplitude	310
γ	incident polarization angle in fiber	60
Φ_{fa}, Φ_{fs}	arguments of Goos-Haenchen phase shifts	118
Ψ	output polarization angle in fiber	60
Ω_a	fiber acceptance solid angle	79
Ω_r	LED radiating solid angle	83
Ω_L	solid angle subtended by lens	298

CHAPTER 1

INTRODUCTION

1.1 General Array Specifications

A large, decametric radio telescope has been proposed [1,2,3] for a site in southwestern Alberta. This telescope, as envisaged, would operate in the band 12.330 - 13.200 MHz, with possible potential capability extended to the following frequency bands:

2.065 - 2.107 MHz

4.063 - 4.438 MHz

6.200 - 6.525 MHz

8.195 - 8.815 MHz

16.460 - 17.360 MHz

These bands are all allocated to maritime mobile communications [4] and are expected to be relatively quiet at the chosen site. It is anticipated that the system bandwidth will be in the order of 100 KHz, with possible extension to 200 KHz [3]. This thesis will be concerned with operation only in the 12.330 - 13.200 MHz band and with a system bandwidth of 200 KHz.

Current planning is for an array of some 2800 dipole antennas in a tee-shaped array with dimensions 5 km by 2.5 km as shown in Fig. 1.1. (This will be discussed in more detail in section 6.1.) The half-power beamwidth is expected to be better than 30 arcmin at the zenith. This instrument would be capable of mapping the radio sky with a contour resolution of better than 10,000 K as compared with 35,000 K for present maps at 10 MHz [1,2].

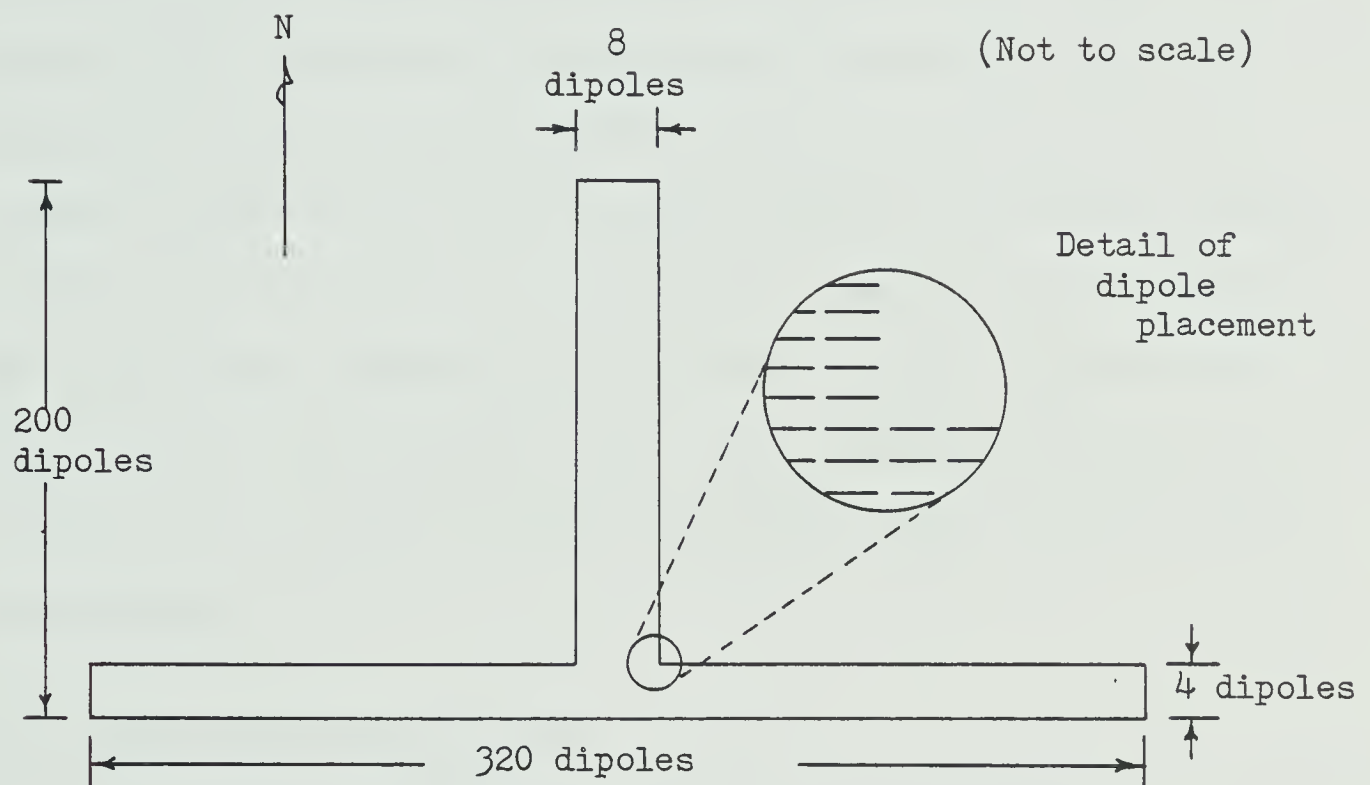


Fig. 1.1 Tee array configuration (After McLarnon [3]).

It has been estimated [3] that the proposed array will require sidelobe levels in the order of -60 dB or lower. This will probably require r.m.s. excitation levels to be accurate to approximately 1° in phase and 2% in amplitude [3]. While McLarnon [3] has determined that adequate sensitivity to point sources can be obtained with r.m.s. sidelobe levels in the order of -38 dB, he has indicated that observations of extended sources, such as galactic background radiation, would require lower sidelobe levels. For example, to provide 3000 K contours of the background brightness temperature distribution would require sidelobe levels in the order of -47 dB. A recent computer study [5] indicates that r.m.s. excitation errors of 4% in amplitude and 3° in phase yield sidelobe levels of ≤ 50 dB and a half-power beamwidth of 0.47° for a Gaussian tapered array. In this thesis it will be assumed that r.m.s. excitation errors will be limited to 1° in phase and 2% in amplitude. Array tapering will not be considered.

1.2 Coaxial Cable Limitations

Contemporary radio telescope arrays generally utilize coaxial cables for conveying the antenna signals to the observatory. McLarnon [3] has examined the feasibility of using a frequency-division-multiplexed (FDM) coaxial cable distribution system for the proposed array. This would allow a number of individual antenna signals to be transmitted to the observatory while minimizing the quantity of transmission line required. It is possible to pre-correlate a number of antenna signals out in the array and then transmit the single correlated signal back to the observatory. While this also will

conserve transmission line it greatly reduces the flexibility of the array as an instrument. McLarnon [3] outlined a number of limitations with coaxial cable, the more important of which are presented below.

Phase and Amplitude Effects

Frequency- and temperature-dependent effects in coaxial cables appear to necessitate the use of phase and amplitude compensation systems. For a system with no frequency conversion, studies of available coaxial cables indicate r.m.s. phase errors in the order of 18° for solid dielectric cables and 7° for foam at the working temperature extremes of -50°C to $+30^\circ\text{C}$. While the tolerances used for calculating these estimates were highly pessimistic, an order of magnitude improvement would be required to bring the phase errors within acceptable limits.

With frequency down-conversion, r.m.s. phase errors would be in the order of

$$0.018 f_{if} |\delta T|^\circ \quad (\text{assuming RG-62A/U cable}) \quad (1.1a)$$

or,
$$0.72 f_{if}^\circ \quad (1.1b)$$

at the temperature extremes where f_{if} (MHz) is the intermediate frequency of the mixing process and δT is the working temperature range. While this could result in acceptable phase errors, there is still the problem of distributing the local oscillator signal to the various mixers at the antennas with known phase error.

Cable attenuation is relatively linear with temperature change, so differential effects from one feeder to another would not be a serious problem.

Phase delay and amplitude equalization would require automatic control to keep errors minimal. The phase delay of RG-213/U, for example, may vary about 1% between 1 MHz and 3 MHz and will also vary with temperature. The amplitude variation over each channel will vary with that channel's location in the band, since attenuation is a function of frequency. Even with equalization, r.m.s. amplitude errors would probably be in the order of 0.1 dB. While this error is tolerable, if it were randomly distributed among the various channels, it could lead to serious sidelobe distortion.

Crosstalk

Inter-cable crosstalk must be no greater than -60 dB to contribute minimum r.m.s. excitation errors. Although crosstalk can have a detrimental effect on the sensitivity of the array by causing spurious fluctuations in the system noise temperature as the beam is scanned, this level is sufficiently low to effect negligible degradation. Crosstalk can also cause sidelobe deterioration by acting as premature cross-correlation of antenna signals.

Cable Deterioration

Standard coaxial cables are susceptible to deterioration by moisture and aging, which results in variations with time in transmission parameters. Although calibration can not be eliminated, this would require a continual recalibration of feedlines.

Further Study

A number of areas requiring further study were also outlined by McLarnon [3]. These include: cable spacing for adequately low inter-cable crosstalk, intermodulation crosstalk levels and sufficient protection from lightning.

1.3 Use of Optical Fibers

In view of the problems with coaxial cables, this thesis proposes a design using optical fibers in the feeder transmission system. Optical fibers offer significant advantages over coaxial cables. A number of these advantages will be briefly examined.

1.3.1 Transmission Losses

Typical attenuation in coaxial cables varies from about 23 dB/km at 10 MHz for RG-8/U to about 43 dB/km at 10 MHz for RG-58A/U [6]. These attenuations increase with frequency to about 65 dB/km and 161 dB/km, respectively, at 100 MHz. Better performance can be obtained by using typical 0.75 in. diameter CATV trunk cable. Such cable exhibits losses of about 6 dB/km at 10 MHz to about 18 dB/km at 100 MHz [6]. Other coaxial cables with air and foam dielectrics, such as HELIAXTM [7] are available with much lower losses but prohibitively higher prices.

Commercial optical fibers have attenuations less than 10 dB/km and laboratory fibers have exhibited attenuations in the 1 dB/km range and lower. This will be discussed in detail in section 2.4.

Spectral attenuation in fibers is essentially flat over a wide modulation band (thousands of GHz) [8]. This eliminates the

necessity of \sqrt{f} loss equalizers needed for coaxial cable systems.

Attenuation is essentially independent of temperature.

Experiments on fibers at Bell Telephone Laboratories [9] revealed a change in effective attenuation constant of -0.19% over the range $+25^{\circ}\text{C}$ to -200°C and $+1.05\%$ over the range $+25^{\circ}\text{C}$ to -196°C . This is equivalent to $-0.001\%/^{\circ}\text{C}$ above $+25^{\circ}\text{C}$ and $+0.006\%/^{\circ}\text{C}$ below $+25^{\circ}\text{C}$. For the ambient range expected (-50°C to $+30^{\circ}\text{C}$) this would correspond to a variation of -0.08% to $+0.03\%$ (-0.003 to $+0.001$ dB).

Dispersion in optical fibers is also essentially independent of temperature. Experiments on fibers at Bell Telephone Laboratories [10] have revealed that no significant changes in dispersion characteristics were observed over a temperature range of -40°C to $+67^{\circ}\text{C}$ through multikilometer fiber lengths.

Excitation errors in optical fibers due to temperature should be negligible.

1.3.2 Electromagnetic Interference

The field structure of a guided wave in an optical fiber is such that essentially complete isolation is assured [11]. Thus, the fiber does not contribute to interference in other systems and is essentially immune to interference by other sources.

Lightning Protection

Being non-conductive, fibers do not require protection against lightning and do not pose a hazard to personnel or equipment during lightning conditions. This is important for a large antenna array.

Electrical Isolation

Fibers provide complete isolation of source from receiver, so receiver and transmitter do not require a common ground. This eliminates the possibility of ground-loop currents which could contribute additional noise and crosstalk to the system. Also, fibers can be repaired without danger to equipment or personnel even while terminal equipment is energized.

1.3.3 Size, Weight and Flexibility

Optical fiber cables offer substantial size, weight and flexibility advantages over coaxial cables of equivalent communications capability. For example, Corning's CORGUIDE [12] optical fiber cable contains 6 fibers, has an outer cable diameter of only 5 mm, has a minimum recommended flexing radius of 2.5 cm and weighs only 25 kg/km. This implies reduced installation time and cost.

1.4 Optical Fiber Transmission System

The optical fiber transmission system can be configured in general as shown in Fig. 1.2. Both transmitter and receiver are comprised of an electrical and an optical signal transmission section. Both of these sections are shown to have individual multiplexing capabilities -- n channels for the electrical and m channels for the optical section. In the transmitter, the electrical section is comprised of the antenna dipoles, preamplifiers, baseband filters, signal encoders (or modulators), channel filters, r.f. multiplexer, and optical source driver. The optical section is comprised of the optical source, optical multiplexer, and coupler to the optical fiber.

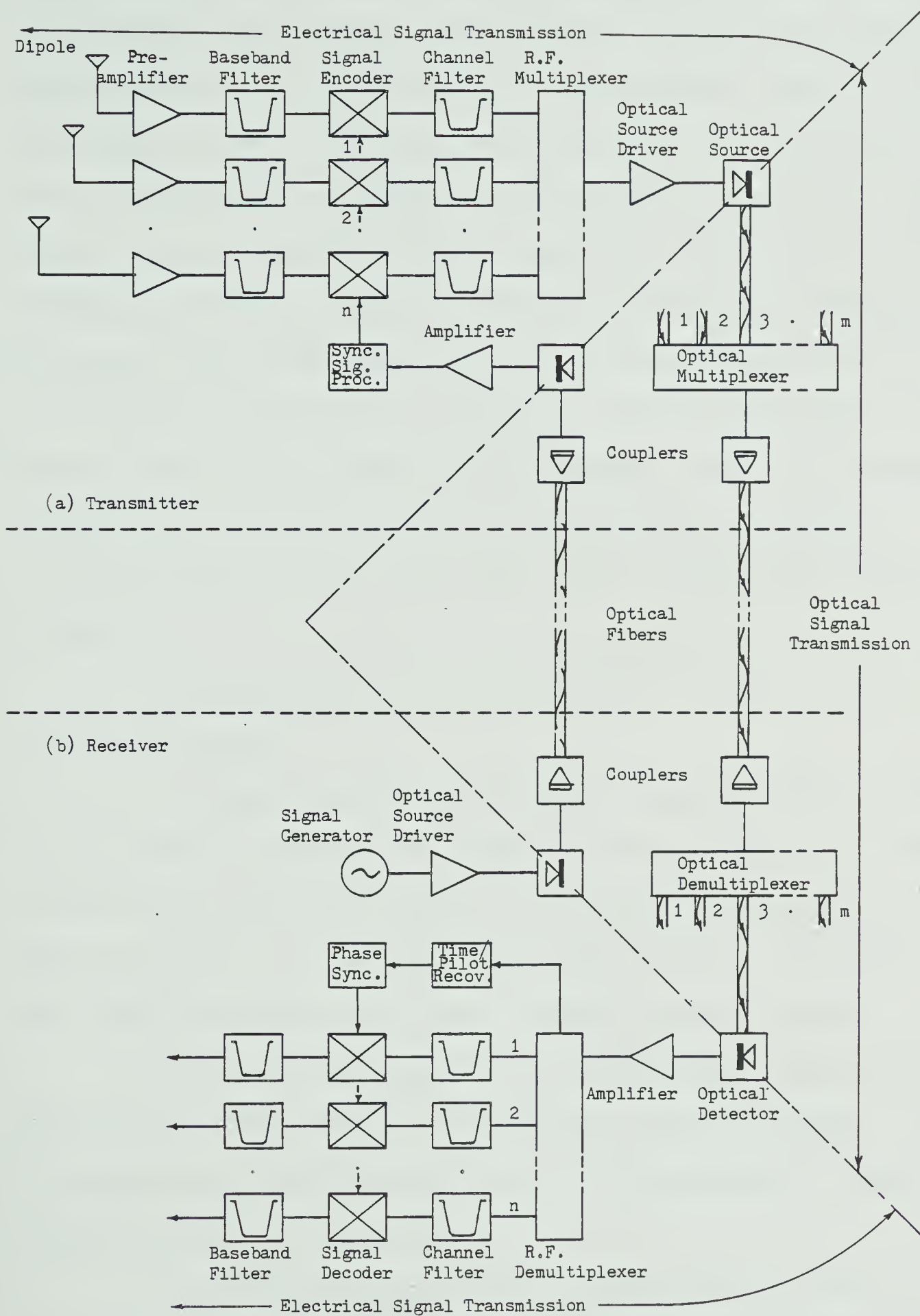


Fig. 1.2 General optical fiber transmission system configuration

In the receiver, the optical section consists of a coupler, optical demultiplexer, and detector. The electrical section has an amplifier (with equalization, if required), r.f. demultiplexer, channel filter and signal decoder. Associated with the encoding and decoding processes are synchronization or reference carrier signals, if required. These signals would be generated (in all likelihood) at the receiver (the observatory) and distributed over fibers to the central transmitting locations (CTL's) where they would receive necessary processing, such as filtering, amplification or frequency multiplication before being used in the encoding process. At the receiver, these synchronization signals must be used to decode the signals, after synchronization locking circuitry ensures the correct phase or timing with the incoming signal.

The proposed feeder system design will be based on the following criteria:

1. Signals from 48 antennas will be single-sideband, suppressed-carrier (SSB-SC) modulated and frequency-division-multiplexed (FDM) for transmission over optical fibers. It will be shown in chapter six that 48 channels is a reasonable upper limit for r.f. multiplexing and that SSB-SC modulation is the most practical for this system.

2. Four optical signals will be wavelength-division-multiplexed (WDM) onto a single fiber for transmission to the observatory. It will be determined in chapter six that four optical channels is a reasonable number for optical multiplexing.

3. A 200 MHz.km graded-index multimode optical fiber will be used throughout the array. Although wider bandwidth product fibers are available, this number will be seen to be consistent with the discussion

in chapters 2 and 6. Also, since we are considering a 48-channel system, there is no significant advantage in using a higher bandwidth-product fiber. In addition, lower bandwidth-product fibers are generally less expensive than their higher bandwidth-product counterparts.

4. It is expected that LED optical sources in conjunction with p-i-n photodiodes will provide satisfactory system performance. This appears to be reasonable as will be seen from the development in chapters 3, 4 and 7.

5. An equal-length feeder system will be used throughout the array. While this is more expensive than a minimum-length system in terms of extra transmission line, it will provide maximum versatility of the radio telescope as well as simplifying feeder calibration. In any event, it represents an upper limit to the amount of transmission line required.

6. The physical system configuration of the array will use dipole groupings in the north-south and east-west subarrays as shown in Fig. 1.3. This will be discussed in more detail in section 6.1.

7. The branch feeders, from the dipoles to the central transmitting locations (CTL's) will be coaxial cable. While McLarnon [3] has identified sources of errors associated with coaxial cables, the short lengths involved will introduce very little error, as will be shown in chapter 7. In addition, this will save converting the antenna signals into an optical signal for transmission to the CTL since, at that point, the signal is required to be in electrical form for frequency-division multiplexing.

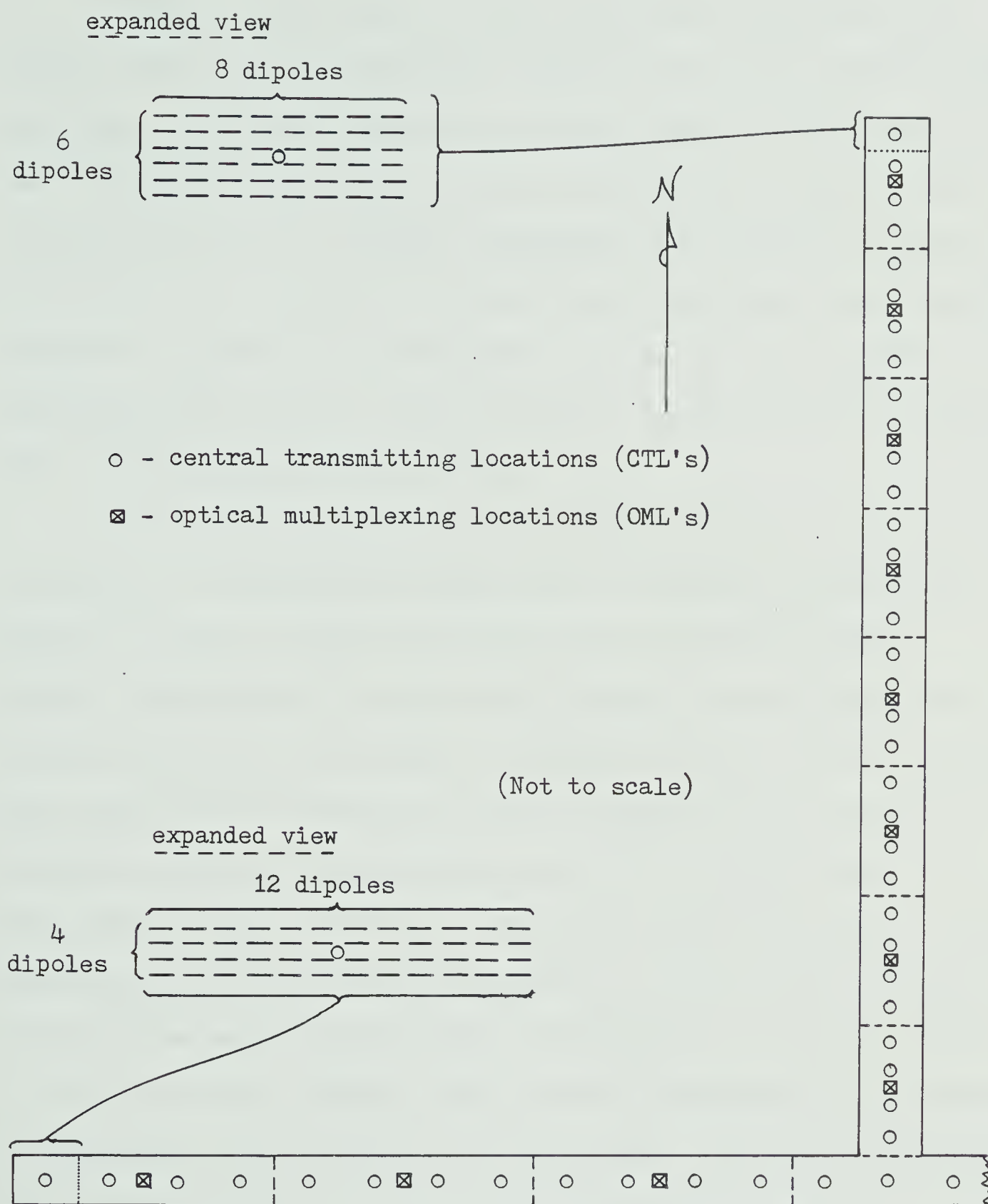


Fig. 1.3 Physical system configuration

1.5 Summary

Optical fibers appear to offer substantial advantages over coaxial cables for the transmission feeder system in the proposed radio telescope. The crucial parameters of r.m.s. phase and amplitude errors as a function of temperature that can be attributed to optical fiber transmission lines are virtually negligible as are crosstalk effects. It remains to be seen that an optical fiber transmission system can be designed to operate in the environment outlined and with adequate performance such that the array performance specifications can be met. This is the intention of this thesis.

In the following chapters, the characteristics of the various components of optical fiber systems will be examined in sufficient detail to establish their applicability in a transmission feeder system. The problems of coupling light energy from one component to another, and various techniques for accomplishing this, will be discussed. The physical array configuration will be examined with a viewpoint of grouping antennas for signal multiplexing onto a common feeder for transmission to the observatory. Modulation and multiplexing at radio frequency (r.f.) and optical wavelengths will be discussed in order to determine the most practical means of transmitting the antenna signals to the observatory. Finally, based upon the development to that point, a transmission system design will be presented. The system performance will then be appraised from the noise temperature and excitation error viewpoints.

CHAPTER 2

OPTICAL FIBERS

2.1 General

A typical optical fiber suitable for communication purposes is composed of a core with refractive index n_1 and radius a , and a cladding with refractive index n_2 and radius b . This can be represented schematically as shown in Fig. 2.1.

If the fiber is unclad, the second medium will be air (usually) and $n_2 = 1$. While this structure is a waveguide in its own right, it is "open", ie: the electromagnetic fields within the fiber extend into the second medium as evanescent fields. Since the fiber must be physically supported along its length, reflections and radiation will occur at these points, resulting in prohibitive losses [11,13]. For this reason, fibers are enclosed in a "cladding" and n_2 will be a variable depending on the material. The cladding radius b is chosen large enough to ensure that the exponentially decaying evanescent fields are essentially zero at $r = b$.

Studies have been performed by various researchers to determine the dispersion characteristics of fibers with various refractive index profiles. The two most common profiles to date are the step-index and graded-index profiles as shown in Fig. 2.2. The characteristics of each will be discussed in the following sections.

2.2 Transmission in Fibers

Optical fiber transmission is most easily described by an

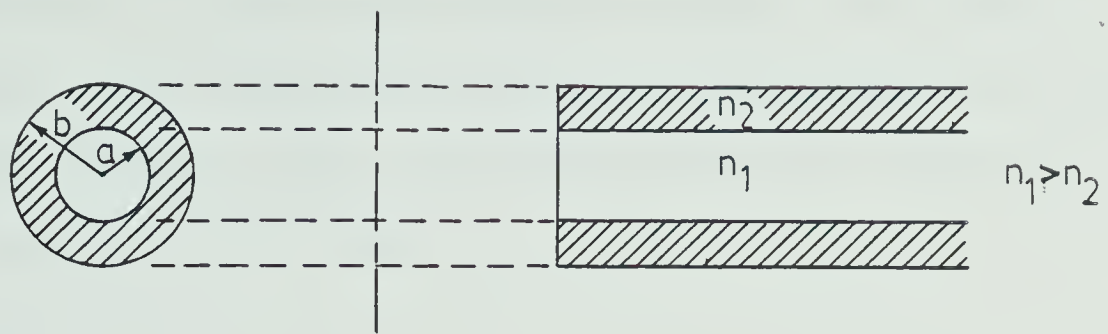


Fig. 2.1 Optical fiber cross-section

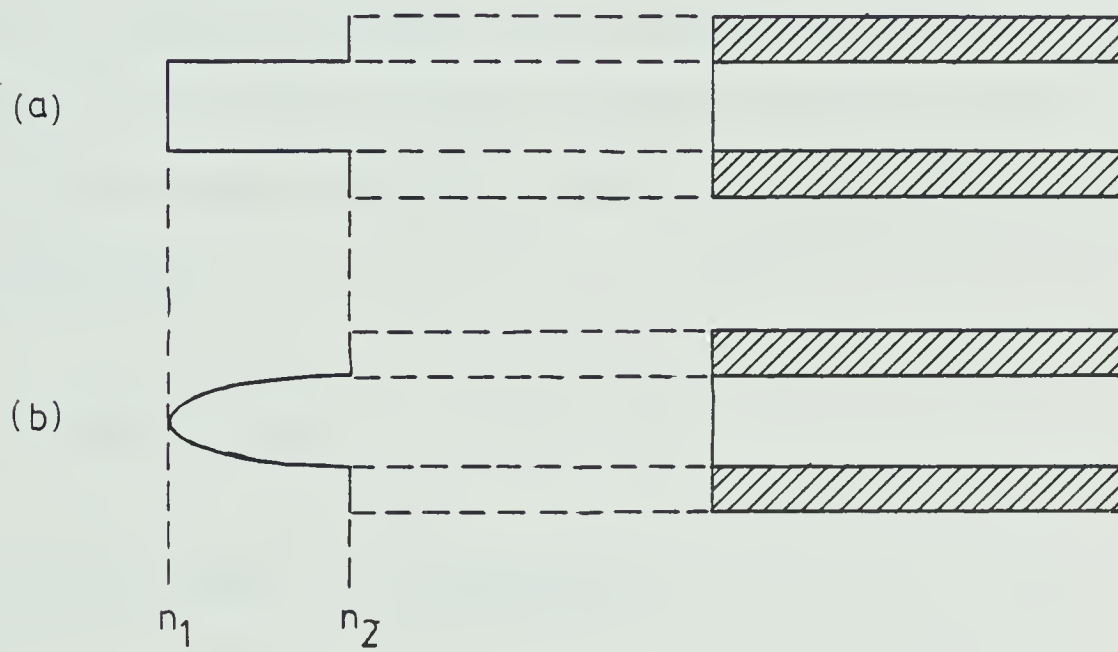


Fig. 2.2 Optical fiber refractive index profiles
(a) step-index (b) graded-index

investigation of meridional rays along a straight fiber with end faces normal to the fiber axis [14]. A meridional ray is one whose path is confined to a single plane through the axis of the fiber. Fig. 2.3 shows such a system with a light ray entering the core from a medium with refractive index n_0 and being reflected at the core-cladding interface. In this case, $n_0 < n_1$.

From Snell's law,

$$n_0 \sin \theta = n_1 \sin \psi = n_1 \cos \phi \quad (2.1)$$

where θ is the angle between the light ray and the axis in the external medium, ψ is the angle between the light ray and the axis in the fiber and ϕ is the angle between the light ray and the normal to the axis. For reflection,

$$\sin \phi > n_2/n_1, \quad (n_1 > n_2) \quad (2.2)$$

The critical angle ϕ_c is defined as

$$\sin \phi_c = n_2/n_1 \quad (2.3)$$

or,

$$\cos \phi_c = [1 - (n_2^2/n_1^2)]^{1/2} \quad (2.4)$$

From (2.1) and (2.4) then, we have

$$\cos \phi_c = (n_0/n_1) \sin \theta_c = [1 - (n_2^2/n_1^2)]^{1/2} \quad (2.5)$$

and,

$$\sin \theta_c = (n_1^2 - n_2^2)^{1/2}/n_0 \quad (2.6)$$

The term, $(n_1^2 - n_2^2)^{1/2}$, is defined as the numerical aperture (N.A.) and is a measure of the light-gathering ability of the fiber. For air, $n_0 = 1$ and the numerical aperture is equal to $\sin \theta_c$. Light rays entering at angles greater than θ_c will not be reflected at the core-cladding interface but will pass through into the cladding where they will be dissipated.

Matsumura [15] has examined the propagation of both meridional and skew rays (ie: those that do not pass through the axis) in fibers and derived expressions for the numerical aperture to account for such skew rays (see Appendix A).

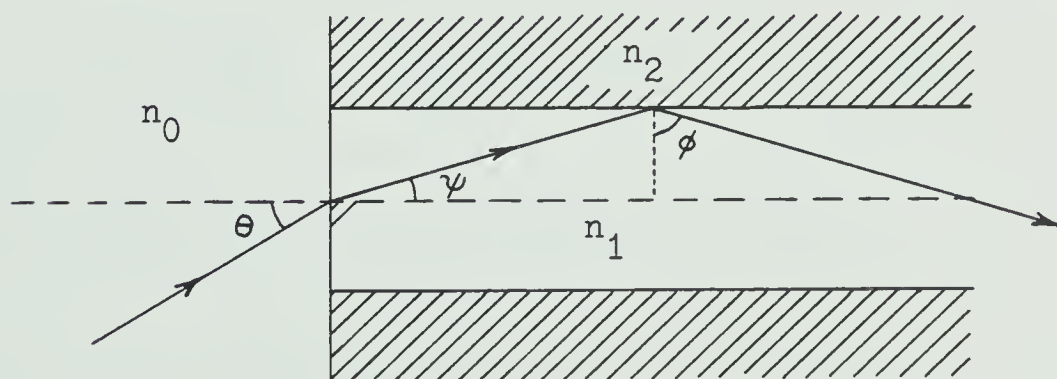


Fig. 2.3 Ray transmission in a step-index optical fiber

The numerical aperture for skew rays has been found [15] to be greater than that for meridional rays in step-index fibers, with the conclusion that step-index fibers can accept (and transmit) more light than graded-index fibers. Gloge and Marcatili [16] have determined that the step-index profile accepts twice as many modes of propagation as the parabolic one, and three times more than a cone-shaped profile. The relationship between numerical aperture and the number of modes will be made apparent in the following discussion on propagation in optical fibers.

If we define parameters [17],

$$u = a(k_o^2 n_1^2 - \beta^2)^{1/2} \quad (2.7)$$

$$w = a(\beta^2 - k_o^2 n_2^2)^{1/2} \quad (2.8)$$

where a is the core radius,

$$k_o = 2\pi/\lambda \quad , \text{ the wavenumber in free space} \quad (2.9)$$

$$\beta = k_o n \quad , \text{ the propagation constant} \quad (2.10)$$

and $n_1 k \geq \beta \geq n_2 k$

the mode field can be expressed by Bessel functions $J(ur/a)$ inside

the core ($r < a$) and by modified Hankel functions $K(wr/a)$ outside the core ($r > a$), where r is radial distance. Matching these fields at the core-cladding interface ($r = a$) yields functions $u(w)$ which characterize the various modes [18]. These functions are universal functions of the weakly guiding fiber ($\Delta \ll 1$) independent of specific materials and dimensions.

If another universal parameter v is introduced, where

$$v = (u^2 + w^2)^{1/2} \quad (2.11)$$

and if we substitute for u and w from (2.7) and (2.8), we get

$$v = ak_0(n_1^2 - n_2^2)^{1/2} \quad (2.12a)$$

$$= \frac{2\pi a}{\lambda}(n_1^2 - n_2^2)^{1/2} \quad (2.12b)$$

or,
$$v = \frac{2\pi a}{\lambda} \cdot (\text{N.A.}) \quad (2.12c)$$

This term can be considered as a normalized frequency. Introducing a normalized propagation constant q where

$$q = 1 - u^2/v^2 \quad (2.13a)$$

$$\approx (\beta/k_0 - n_2)/(n_1 - n_2) \quad (2.13b)$$

a plot of q vs. v can be made. Such a plot is shown in Fig. 2.4.

These curves represent the various modes which can propagate in the

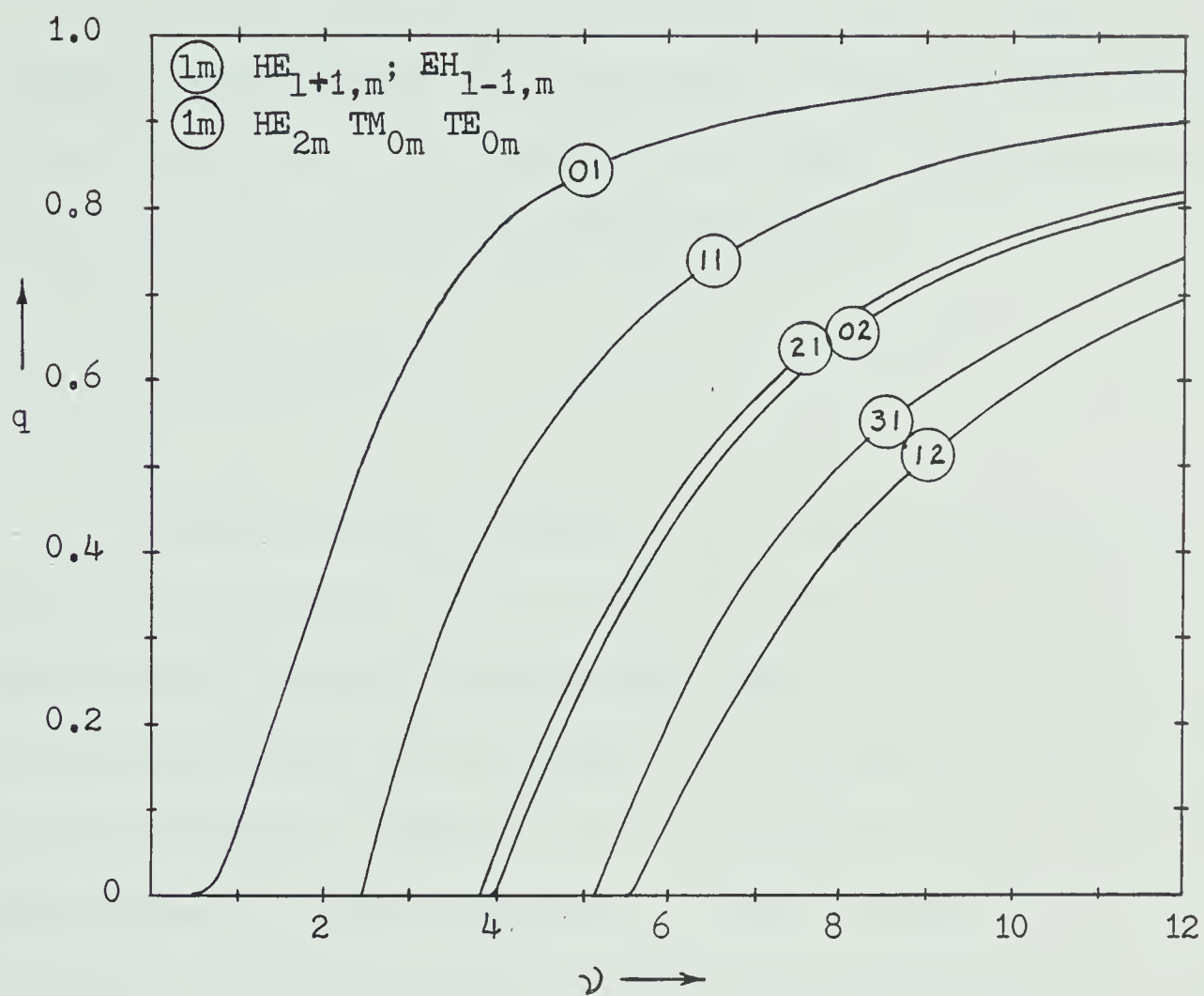


Fig. 2.4 Normalized propagation constant q as a function of normalized frequency ν for a number of linearly polarized modes (After Gloge [17]).

fiber. While the curves are plots of linearly polarized (LP) modes, as defined by Gloge [17], the more common HE, EH or TE, TM designation can be determined directly as shown in Fig. 2.4.

It can be seen that, for $\nu < 2.405$, only one mode will propagate in the fiber. This is the HE_{11} or dominant mode for which there is no cutoff. As ν increases, the number Q of propagating modes increases [17] and is given approximately by

$$Q \approx 1/2 \nu^2 \quad (2.14)$$

For communication purposes, it is desirable to limit the number of propagating modes to keep dispersion to a minimum [18]. This requires lowering the normalized frequency ν , which is accomplished by reducing either the core radius a or the numerical aperture for a given wavelength of operation, as per eq.(2.12). Since reducing the core radius introduces difficulties in manufacturing and coupling, the numerical aperture is usually made as low as practicable, ie: n_1/n_2 is kept small.

For optical sources having broad radiation patterns (e.g. LED's) the fiber numerical aperture must be as large as possible so as to collect a reasonable amount of emitted power. As the numerical aperture is increased, the normalized frequency ν increases proportionately. This implies multimode operation. On the other hand, a laser diode, having a narrow radiation beamwidth, can be used with a fiber having a small numerical aperture. If the normalized frequency ν is less than 2.405, this will result in single-mode operation.

A typical, contemporary, low-loss multimode (step-index) fiber

has the following parameters:

Numerical aperture	0.16 ($\theta_c = 9.2^\circ$)
Core diameter	$85\mu\text{m}$

If we consider a source with wavelength of $0.8\mu\text{m}$, the normalized frequency,

$$V = \frac{2\pi a}{\lambda} (\text{N.A.}) = \frac{2\pi(85 \times 10^{-6})}{0.8 \times 10^{-6}} (0.16) = 106.8$$

The number of possible propagating modes is then given by

$$Q \approx 1/2 V^2 = 5705$$

On the other hand, if we had a (step-index) fiber with a core diameter of only $5\mu\text{m}$ and a numerical aperture of 0.05 ($\theta = 2.9^\circ$), the normalized frequency,

$$V = \frac{2\pi(5 \times 10^{-6})}{0.8 \times 10^{-6}} (0.05) = 1.96$$

This is less than 2.405 and implies single-mode operation only.

2.3 Dispersion

The maximum information rate that may be carried by an optical fiber is determined by the group delay characteristics. Contributing factors to group-delay distortion are the following:

1. Material (Chromatic) Dispersion

- the variation in the index of refraction of the glass as a function of wavelength.

2. Waveguide Dispersion

- the variation in the waveguide dimensions (in wavelengths) with frequency change.

3. Multimode (Modal) Dispersion

- the variation in group delay among the various propagating modes if more than one mode is excited.

These three types of dispersion are considered in more detail in the following presentation.

2.3.1 Material and Waveguide Dispersion

The material and waveguide dispersion effects can be illustrated as shown in Fig. 2.5 in which the effective refractive index n_e is plotted as a function of normalized frequency ν [13,19]. Fig. 2.5(a) is a symbolic plot of the phase velocity for the dominant mode (HE_{11} , curve 1) and the next higher order modes (TE_{01} , TM_{01} combined, curve 2). This plot assumes that n_1 and n_2 do not change with frequency. It is again seen that for normalized frequencies less than 2.405 only the HE_{11} mode exists. Fig. 2.5(b) reflects (symbolically) the fact that the equivalent refractive index n_e goes monotonically from n_2 to n_1 as frequency increases, with n_1 and n_2 both a function of frequency.

The modal phase velocity V_p varies between the values appropriate to the bulk material of which the core and cladding are made. For conditions near cutoff (ν small), the field is only slightly bound to the core-cladding interface since a significant amount of the energy is distributed in the cladding. In this case, $V_p \rightarrow c/n_2$ where c

is the velocity of light in vacuum. For conditions far from cutoff (ν large), V_p is influenced most by the core since the decay in the cladding is quite rapid. In this case, $V_p \rightarrow c/n_1$. In general, then

$$c/n_1 \leq V_p \leq c/n_2 \quad (2.15)$$

Direct-detection of intensity modulated light suffers dispersion effects solely in the envelope of the light-signal [18]. This envelope propagates at the group velocity. Group velocity V_g is defined as

$$V_g = d\omega/d\beta \quad (2.16)$$

where ω is the angular frequency.

A typical ω - β diagram, showing the propagation characteristics of a number of lower order modes in an optical waveguide is shown in Fig. 2.6 [19,20]. The velocities of light in the core and cladding materials are shown as two straight lines with the mode lines for the optical waveguide lying between them. All guided propagating modes lie between $\beta = \omega n_1/c$ and $\beta = \omega n_2/c$.

We note that there exists a point of inflection for the dominant mode. In the vicinity of this point, the group velocity is almost independent of frequency. This means that pulses propagating in this mode keep their shape approximately undistorted if their carrier frequency is close to the inflection-point value.

The group velocity of a waveguide mode is given by the slope $d\omega/d\beta$ of the mode. The reciprocal of the group velocity has the

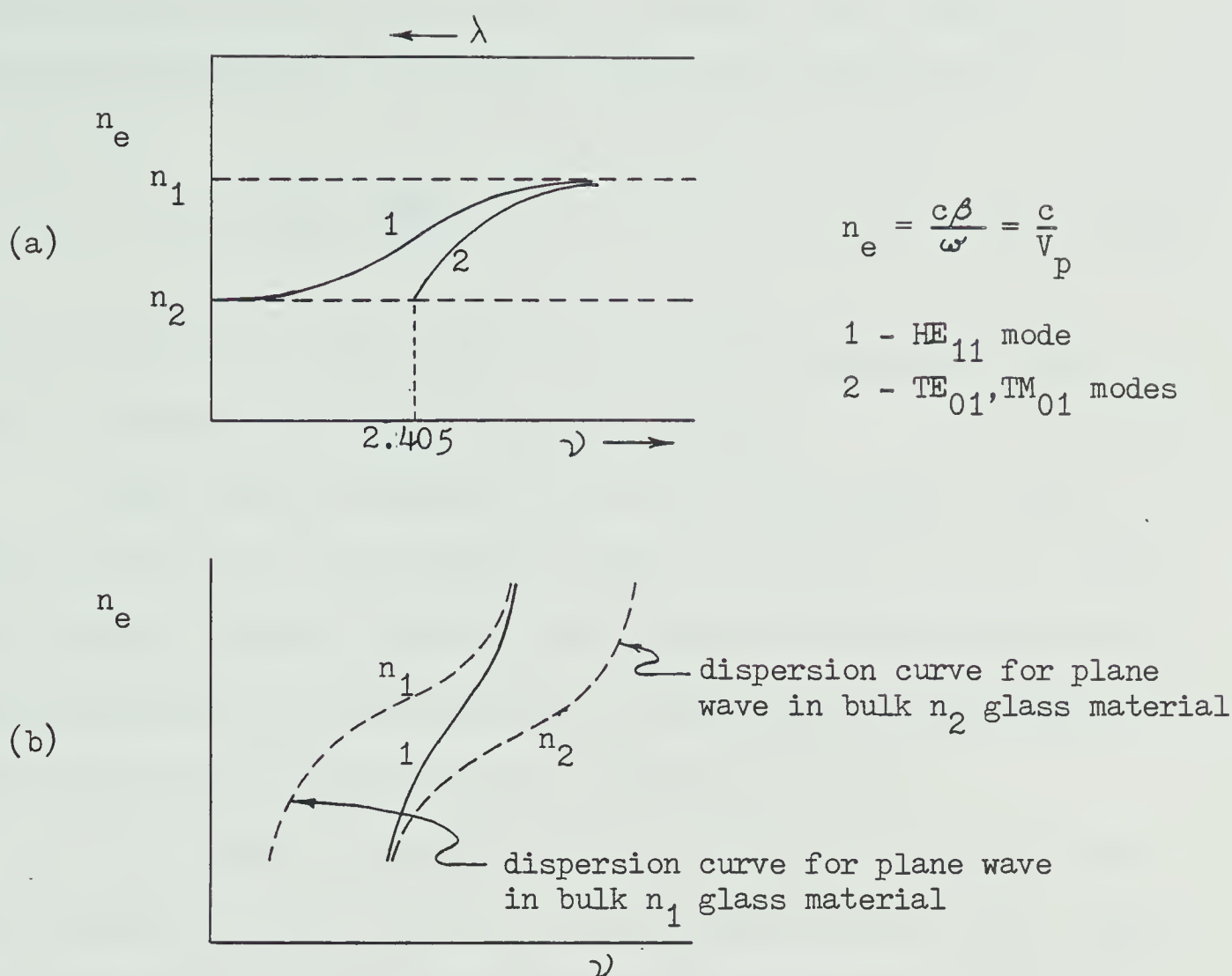


Fig. 2.5 Waveguide dispersion curve:
(a) without considering material dispersion
(b) including material dispersion effects
(After Gallawa [13] and Yeh [19]).

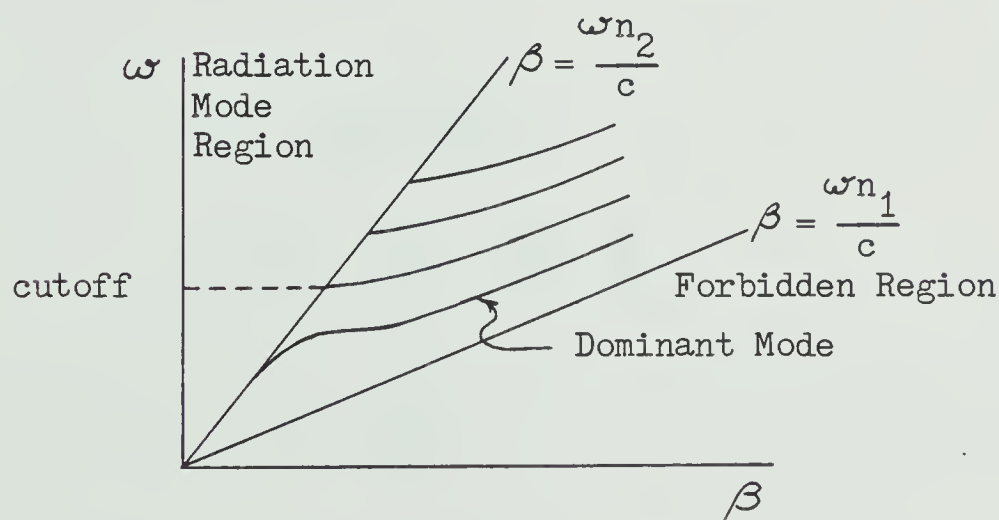


Fig. 2.6 Dispersion characteristics of several lower-order modes in an optical fiber (After Yeh [19]).

physical significance of delay per unit length. This quantity is termed the group delay (or envelope delay) and is defined as

$$\tau_g = \frac{d\beta}{d\omega} = \frac{1}{c} \frac{d\beta}{dk_o} \quad (2.17)$$

This is equivalent to the transit time per unit length of a light pulse of radiation at a given carrier frequency.

Light sources considered for optical communication cover a fairly wide frequency band ($\approx 4\%$ for LED's as opposed to 0.1% for GaAs laser diodes). Signals modulating the intensity of such carriers can suffer distortion in long fibers due to differences in group delay among the various optical frequency components present.

If the optical bandwidth is not too wide, the time delay per unit frequency and unit length of fiber is approximately $d\tau_g/df$ [18]. For a bandwidth B at optical frequency f the total delay caused by the frequency dependence of the group delay is given by

$$\begin{aligned} \tau &= \frac{B}{f} \cdot f \cdot \frac{d\tau_g}{df} \\ &= \frac{B}{f} \cdot f \cdot \frac{d}{df} \left[\frac{1}{c} \frac{d\beta}{dk_o} \right] \\ &= \frac{1}{c} \cdot \frac{B}{f} \cdot f \cdot \frac{d}{dk_o} \cdot \frac{dk_o}{df} \cdot \frac{d\beta}{dk_o} \end{aligned}$$

$$\begin{aligned} \text{or, } \tau &= \frac{1}{c} \cdot \frac{B}{f} \cdot k_o \frac{d^2\beta}{dk_o^2} \\ &= \frac{1}{c} \cdot \frac{\delta\lambda}{\lambda} \cdot k_o \frac{d^2\beta}{dk_o^2} \end{aligned} \quad (2.18)$$

where $\delta\lambda$ is the effective source spectral width and λ is the source

wavelength.

Gloge [18] has presented a graph of dispersion coefficient $(k_0 d^2 \beta / dk_0^2)$ as a function of frequency for fused silica and this is shown in Fig. 2.7. This indicates that an LED with $\delta \lambda = 40 \text{ nm}$, $\lambda = 0.8 \mu\text{m}$ suffers a material dispersion of

$$\tau = \frac{1}{3 \times 10^5} \cdot \frac{40 \times 10^{-9}}{0.8 \times 10^{-6}} \cdot (0.025) = 4.2 \text{ ns/km in fused silica (SiO}_2\text{)}$$

Kapron and Keck [21] considered both waveguide and material dispersion in their study of pulse repetition rates in optical fibers. They derived a maximum pulse rate R_b for a single mode fiber with Gaussian input pulses to be

$$R_b = [8\beta''L \ln \delta A]^{-1/2} \text{ bits/sec} \quad (2.19)$$

where $\beta'' = \frac{d^2 \beta}{d\omega^2} = \frac{\lambda^3}{2\pi c^3} \frac{d^2 n_e}{d\lambda^2}$, wavenumber dispersion (2.20)

$$n_e = \frac{\lambda \beta}{2\pi} \text{ and can be obtained from Fig. 2.5}$$

β is axial wavenumber

\ln is the natural logarithm

ω is radian frequency

L is propagation distance

δA is allowed amplitude overlap of adjacent pulses
(intersymbol interference)

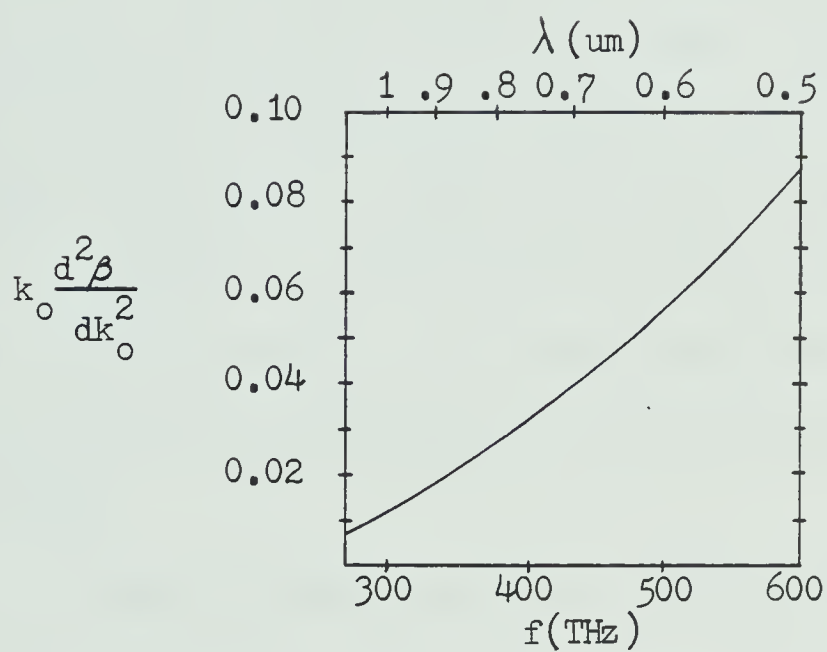


Fig. 2.7 Dispersion coefficient $k_o \frac{d^2 \beta}{dk_o^2}$ as a function of frequency for fused silica SiO_2 (After Gloge [18]).

This pulse rate assumes that the input pulse width has been optimized to take full advantage of the waveguide bandwidth, ie: a shorter pulse will exceed the guide bandwidth and a longer pulse will not utilize it fully.

A plot of wavenumber dispersion β'' as a function of wavelength is presented in Fig. 2.8 for a number of optical waveguides. Wavenumber dispersion is essentially the combined effect of material and waveguide dispersion. The point at which β'' passes through zero is the theoretical point at which waveguide and material dispersion have equal and opposite effects, resulting in a pulse rate which is power limited as in free space propagation. This particular effect is examined more closely by Smith and Snitzer [22]. At shorter wavelengths, material dispersion predominates over the waveguide dispersion and vice versa as wavelength increases.

Taking a value of $\beta'' = 4 \times 10^{-23} \text{ sec}^2/\text{km}$ for a typical fiber in the vicinity of $\lambda = 0.8 \mu\text{m}$, and $\delta A = 0.01$ (20 dB down from the peak), equation (2.19) predicts a maximum pulse rate of $26/\sqrt{L}$ Gbits/sec.

Since equation (2.19) assumes that the input pulse width has been optimized to minimize the output pulse width, a more general expression of pulse spreading [13] is

$$\frac{\tau_o}{L} = \beta''/\tau_i \quad (2.21)$$

where τ_i is the input pulse width.

This can be rewritten as

$$\frac{\tau_0}{L} = 2\pi c \beta'' \frac{\delta\lambda}{\lambda^2} \quad (2.22)$$

where $\delta\lambda$ is effective spectral width of source
 λ is wavelength of source

This expression gives pulse spreading as a function of wavelength, spectral width and wavenumber dispersion β'' . A plot of dispersion as a function of spectral width is presented in Fig. 2.9.

Fig. 2.9 illustrates the advantage of using laser sources having narrow spectral widths. LED's typically have $\delta\lambda = 20$ to 60 nm while lasers have $\delta\lambda < 5$ nm.

To this point only material and waveguide dispersion effects have been considered. For single-mode fibers, this would have been sufficient. However, single-mode fiber technology and systems are still under development and not considered feasible for the proposed radio telescope project. Multimode fibers are commercially available and are being used in a number of existing telecommunication systems. Since multimode fibers are the logical choice for the radio telescope project, we must also examine the dispersion caused by the propagation of numerous modes in fibers.

2.3.2 Multimode Dispersion

2.3.2.1 Step-Index Profile

The analysis of multimode fibers ($V > 2.405$) is

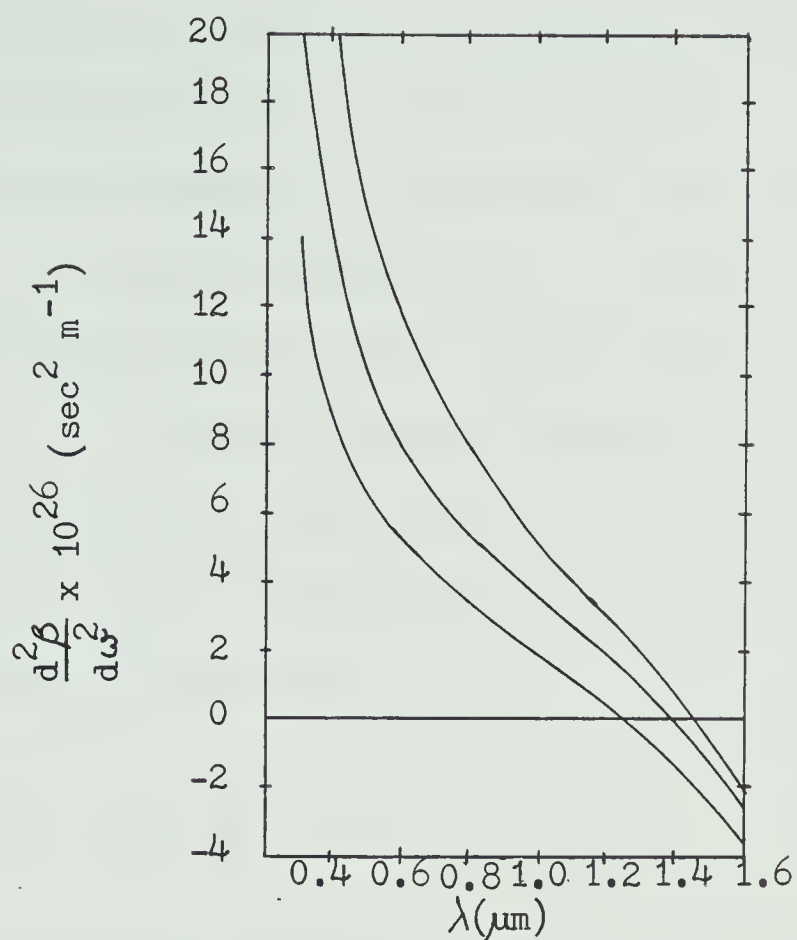


Fig. 2.8 Calculated wavenumber dispersion β'' as a function of λ for several optical fibers of varying core-cladding index difference and core diameters (After Kapron & Keck [21]).

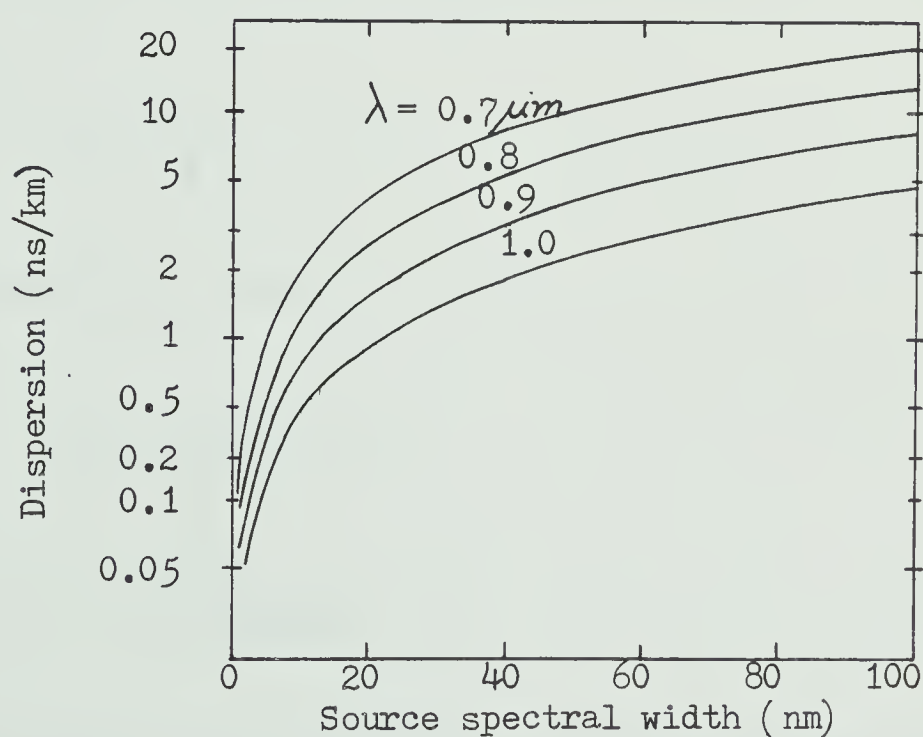


Fig. 2.9 Dispersion as a function of source spectral width and center wavelength (After [13])

difficult because of unknown power distribution among the various modes. The modal excitation depends on launching conditions at the input. Also, the modes are coupled in a complicated fashion and power distribution is constantly changing [13]. An approximate analysis based on ray theory, is often used in a first analysis. In this approximation, it is assumed that the distortion is caused by the difference in propagation time for rays of different angles.

From Fig. 2.3, it can be seen that the propagation time t_2 for the reflected ray will be

$$t_2 = \frac{L}{V_p \cos \psi} \quad (2.23)$$

where V_p is the propagation velocity in the core (phase velocity)
 L is the axial length

The propagation time t_1 for an axial ray would be

$$t_1 = \frac{L}{V_p}$$

The time delay τ_M is then $t_2 - t_1$, or

$$\begin{aligned} \tau_M &= \frac{L}{V_p} \left(\frac{1}{\cos \psi} - 1 \right) \\ &= \frac{Ln_1}{c} \left(\frac{1}{\cos \psi} - 1 \right) \end{aligned} \quad (2.24)$$

The maximum time delay will occur at the maximum angle of ψ , which corresponds to the critical angle for reflection given by Snell's law,

$$\cos \psi_c = \frac{n_2}{n_1}$$

The maximum time delay estimate is then

$$\tau_M = \frac{L}{c} \frac{n_1}{n_2} (n_1 - n_2) \approx \frac{Ln_1 \Delta}{c} \quad (2.25)$$

where Δ is the relative index difference

A typical, multimode fiber with refractive indices of core and cladding of 1.5 and 1.49, respectively, has a maximum time delay of

$$\begin{aligned} \tau_M &= \frac{1}{3 \times 10^5} \cdot \frac{1.5}{1.49} (1.5 - 1.49) \\ &= 33.5 \text{ nsec/km.} \end{aligned}$$

This would permit a bandwidth of about 14.9 MHz in 1 km of fiber, based on the Nyquist rate.

Equation (2.25) is known to be pessimistic since it depends on n_1 and n_2 in only a gross way. The analysis should also account for the amount of waveguide and material dispersion suffered by each mode and for the fact that various modes suffer various degrees of attenuation. In particular, slower modes, which correspond to more energy propagating in the cladding material, are attenuated more than faster modes, which propagate mostly in the core. Thus, while this introduces more loss of power, the effects of dispersion are reduced. There is also a certain amount of mode mixing present which tends to reduce dispersion. These factors will be discussed later.

The previous discussion has considered only the group-delay differences between the highest and lowest-order modes. Miller et al [8] examined the dependence of group-delay on wavelength for each propagating mode M . The time difference between output power components separated by $\delta\lambda$ is given by

$$\begin{aligned} \tau = \delta\lambda \frac{d\tau}{d\lambda} = \frac{\lambda \delta\lambda}{c} & \left\{ - \frac{d^2 n_1}{d\lambda^2} \left[1 + \Delta \frac{(M+1)^2}{(M+1)_{\max}^2} \right] + \right. \\ & \frac{(M+1)^2}{16n_1 a^2} - \frac{dn_1}{d\lambda} \frac{(M+1)^2 \lambda}{8n_1^2 a^2} + \\ & \left. \left(\frac{dn_1}{d\lambda} \right)^2 \frac{\lambda^2 (M+1)^2}{16n_1^3 a^2} \right\} \quad \text{sec/m} \end{aligned} \quad (2.26)$$

Considering only the spread at the highest mode, this simplifies with good approximation to [8]

$$\tau = - \frac{\lambda \delta\lambda}{c} \frac{d^2 n_1}{d\lambda^2} + \frac{2n_1}{c} \frac{\delta\lambda}{\lambda} \Delta \quad (2.27)$$

The first term shows the effect of material dispersion and the second term gives the output pulse spreading due to the wavelength dependence of the group delay when $dn_1/d\lambda$ and $d^2 n_1/d\lambda^2$ are both zero. Fig. 2.10 shows the dependence of n , $dn/d\lambda$ and $d^2 n/d\lambda^2$ on wavelength for pure silica glass.

The amount of pulse spreading predicted by equation (2.27) can easily be determined. Considering an LED with an r.m.s. spectral width of 36 nm with centre wavelength of $0.9 \mu\text{m}$, Fig. 2.10 yields $n_1 = 1.451$, $d^2 n_1/d\lambda^2 = 1.6 \times 10^{10}$. Pulse spread is then

$$\begin{aligned}
\tau &= - \frac{(0.9 \times 10^{-6})(36 \times 10^{-9})}{3 \times 10^5} (1.6 \times 10^{10}) + \\
&\quad \frac{2(1.451)}{3 \times 10^5} \frac{(36 \times 10^{-9})}{(0.9 \times 10^{-6})} \Delta \\
&= -1.73 \times 10^{-9} + 3.87 \Delta \times 10^{-7} \text{ sec/km}
\end{aligned}$$

Considering a fiber with $\Delta = 0.01$, this becomes

$$\tau = -1.73 \text{ nsec/km} + 3.87 \text{ nsec/km}$$

or $\tau = 2.14 \text{ nsec/km}$

If we consider a laser diode operating at $0.9 \mu\text{m}$ with a spectral width of 2 nm, the pulse spread becomes

$$\begin{aligned}
\tau &= - \frac{(0.9 \times 10^{-6})(2 \times 10^{-9})}{3 \times 10^8} (1.6 \times 10^{10}) + \\
&\quad \frac{2(1.451)}{3 \times 10^8} \frac{(2 \times 10^{-9})}{(0.9 \times 10^{-6})} (0.01) \\
&= -0.096 \times 10^{-9} + 0.1225 \times 10^{-9} \\
&= 0.0265 \text{ nsec/km}
\end{aligned}$$

It is clear that the multimode dispersion as given by eq. (2.25) is much greater than the wavelength-dependent dispersion of individual modes as given by the second term of eq. (2.27) for a typical LED, and very much greater than that for a laser diode.

2.3.2.2 Graded-Index Profile

The dispersion in multimode fibers can be reduced by adjusting the index of refraction to cause the various modes to have the same (or nearly the same) group velocity [11]. This is illustrated in Fig. 2.11 which shows various optical ray paths that are constrained by the expression

$$\int_1 n(r) dl = \text{constant}$$

where dl is an element of length along the ray profile
 r is the radial distance from the axis
 $n(r)$ is the refractive index as a function of radial distance

With this configuration, all meridional rays will arrive at the receiver at the same time, regardless of the path traversed.

Considerable improvement in pulse distortion is realized with a parabolic profile, in which

$$n(r) = \begin{cases} n_1[1 - \Delta(r^2/a^2)] & , r \leq a \\ n_2 = n_1(1 - \Delta) & , r \geq a \end{cases} \quad (2.28a)$$

$$(2.28b)$$

This results in a fiber with a time delay spread in the impulse response [23] of

$$\tau \approx \left(\frac{L}{2c}\right) n_1 \Delta^2 \quad (2.29)$$

For a sufficiently narrow pulse traversing a fiber with $n_1 = 1.5$ and

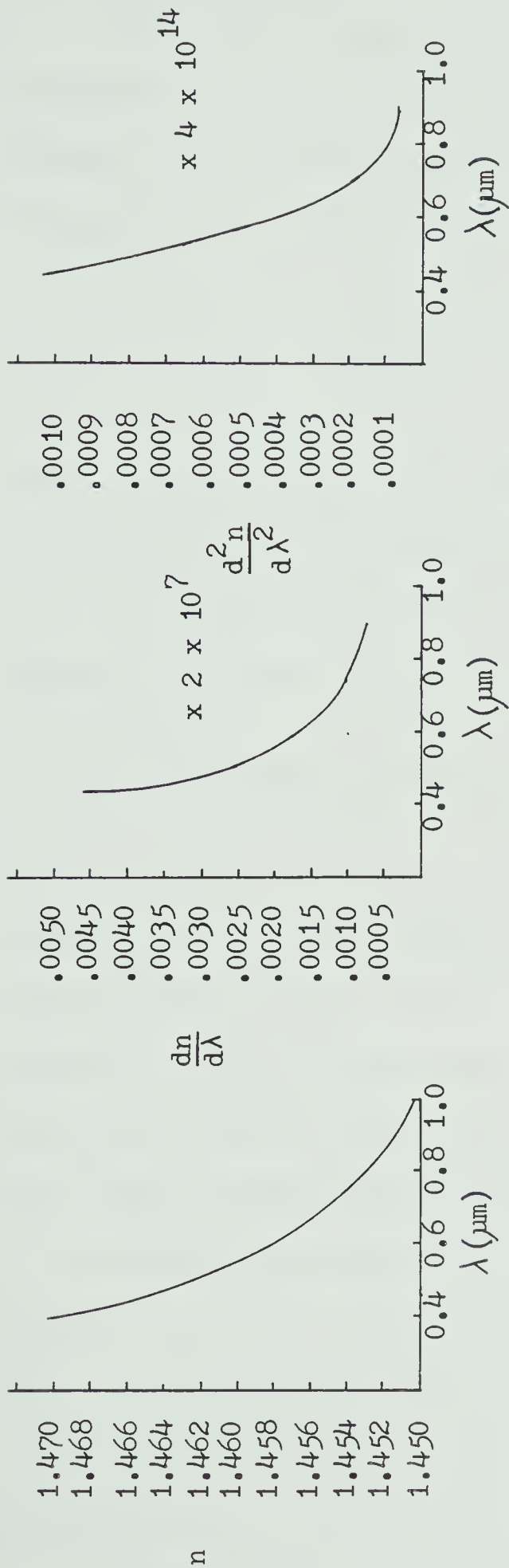


Fig. 2.10 Wavelength dependence of fused silica glass
 (a) dependence of index n (b) dependence of $dn/d\lambda$
 (c) dependence of $d^2n/d\lambda^2$ (After Miller, Marcatili and Li [8]).

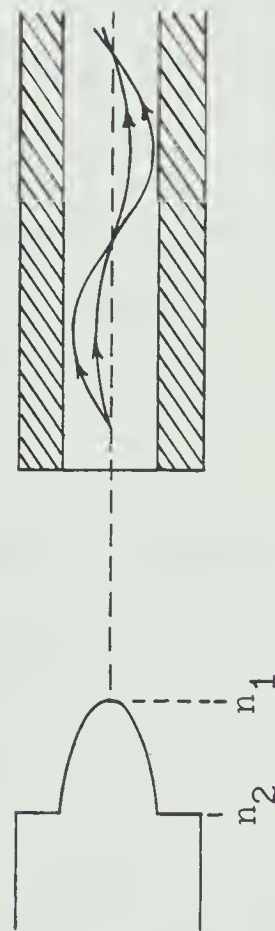


Fig. 2.11 Meridional ray propagation in a graded-index fiber (After [13]).

$\Delta = 0.01$, eq. (2.29) predicts an output pulse width of 0.25 nsec/km.

The time delay per unit length between the longest path, which corresponds to the helical path at the interface of core and cladding surfaces, and the shortest path, which corresponds to the axial path in the centre of the core [24] is

$$\tau \approx 1.5 \frac{n_1 \Delta^2}{c} \quad (2.30)$$

Again, using the example of a fiber with $n_1 = 1.5$ and $\Delta = 0.01$, eq. (2.30) predicts a maximum time delay of 0.77 nsec/km.

Appendix A discusses results by other researchers into pulse spreading in fibers with various refractive index profiles.

2.3.3 Dispersion-Limiting Techniques

Rather than using only a graded-index of refraction, methods for making the step-index multimode fiber more attractive for communications purposes have been described in the literature. One method [25] relies on equalizing the modal delay in the fiber by causing the carrier to drift in the detector according to the expected modal delay and modal field pattern at the detector. Another method [6] would be to couple the light into a smaller cone than the numerical aperture. This will result in a reduced spread in transit time. It has also been shown in Fig. 2.9 that a laser source with a relatively narrow spectral width would suffer less dispersion than a broadband source, such as an LED.

Marcuse [26] has developed guidelines for the design of multimode, step-index fibers with intentional fluctuations of the

refractive index of the core. Coupling coefficients are calculated for a variety of cases which can be used to calculate an "improvement factor", which indicates the reduction of Gaussian pulse length relative to its uncoupled length.

Jeunhomme and Pochelle [27] have determined mode coupling effects due to externally applied deformations which can be used to "design" given amounts of mode power transfer.

The dispersion-limiting method which has received the most attention involves mode coupling along the fiber [20,26,28,29,30,31]. Structural imperfections along the fiber axis (e.g. refractive index variation, diameter fluctuations, strain birefringence) will cause coupling among the various modes. As the energy propagates along the fiber, energy moves back and forth among the modes, ultimately averaging out the single mode propagation time differences to cause a "net delay" that depends on the weighted average of the delays of all the modes. The coupled modes then tend to have a common mean velocity of propagation.

If the coupling spectrum is flat, the velocity spread from the mean velocity will increase as $\sqrt{LL_c}$, where L_c is the length where mode coupling reaches an equilibrium state (and is greater than a kilometer for most low-loss fibers). This indicates that the delay varies as \sqrt{L} rather than directly with length (beyond L_c). L_c is referred to as the coupling length.

Personick [30] has shown that the multimode delay distortion in conventional, clad (step-index) multimode fibers is

$$\tau_M = 0.289 \frac{n\Delta}{c} \sqrt{LL_c} \quad , L > L_c \quad (2.31a)$$

$$= 0.289 \frac{n\Delta}{c} L \quad , L \leq L_c \quad (2.31b)$$

Experimental evidence for the validity of eq. 2.31 has been established and is discussed in Appendix B.

2.3.4 Summary

The total dispersion in a multimode fiber can be expressed [32] by

$$\tau_T = \left[\tau_M^2 + (\tau_D^2 - \tau_W^2) \right]^{1/2} \quad (2.32)$$

where τ_M is multimode dispersion
 τ_D is material dispersion
 τ_W is waveguide dispersion

The negative effect of waveguide dispersion is again noted.

The dispersion-limited maximum bit rate for digital transmission, and maximum bandwidth for analog transmission can be expressed as [24,28]

$$R_{b_{\max}} \text{ (bits/sec)} = \frac{1}{2\tau_T} B_{\max} \text{ (Hz)} \quad (2.33)$$

where τ_T is total dispersion from eq. (2.32).

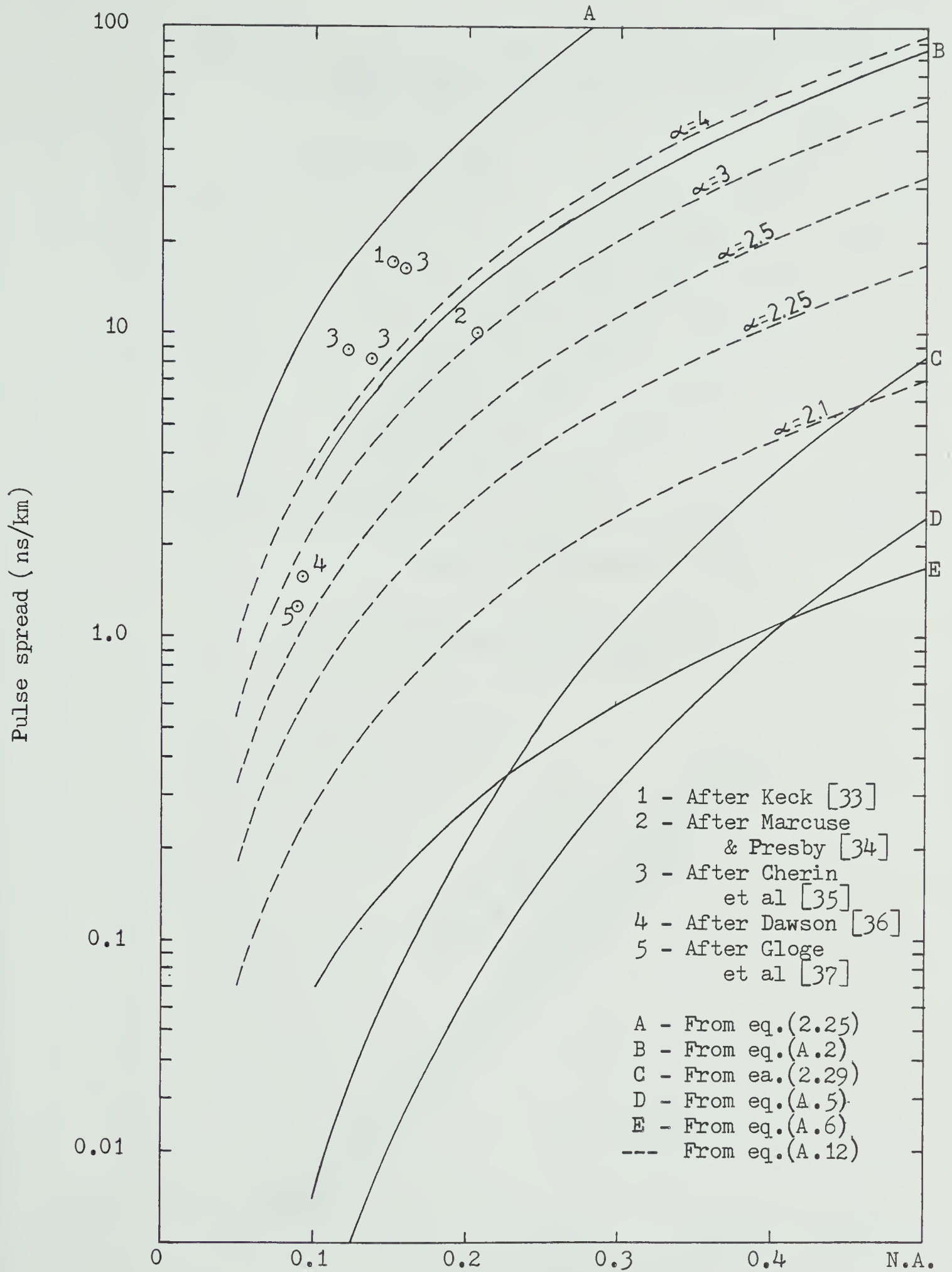


Fig. 2.12 Multimode dispersion τ_M . Curves A & B represent step-index fibers; curves C, D & E represent parabolic-index fibers; dashed-line curves represent graded-index fibers (profile factor α).

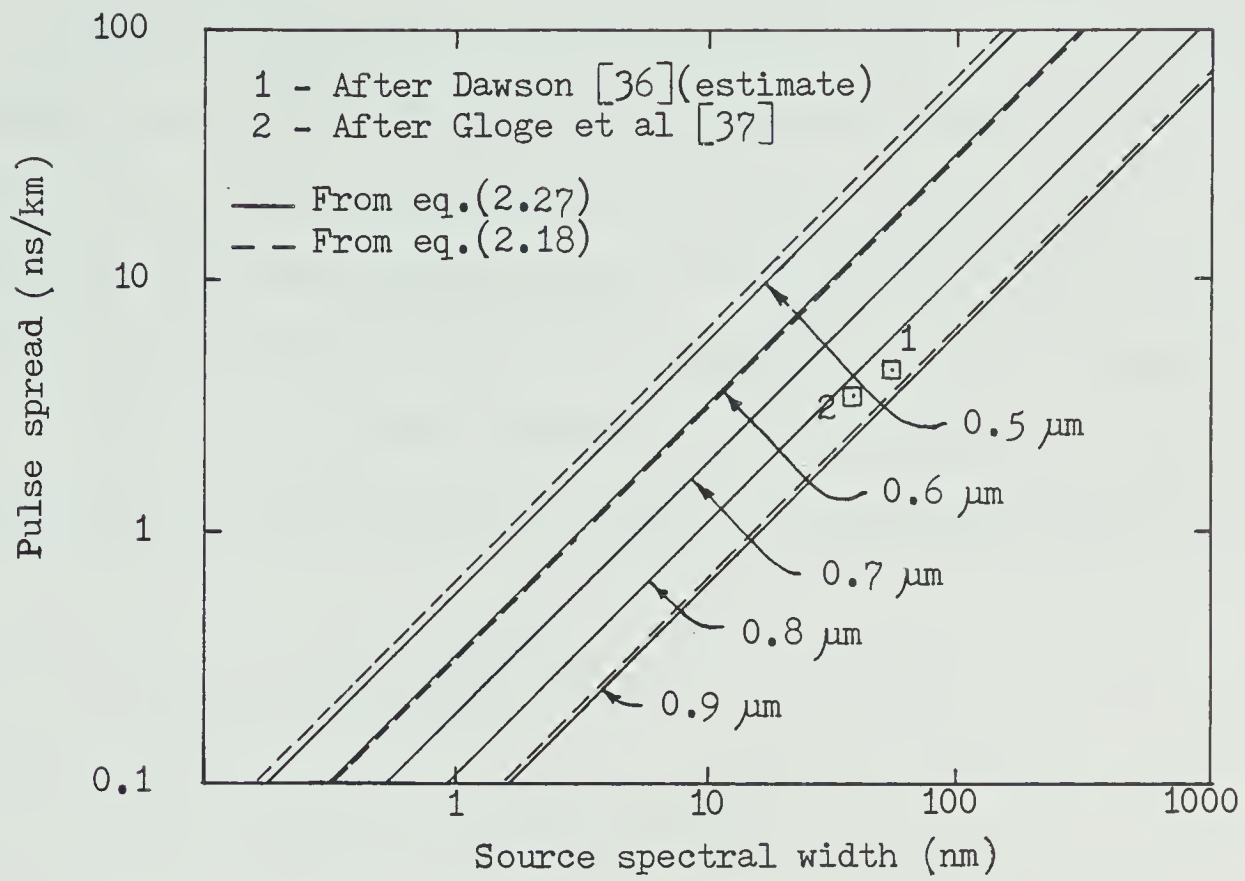


Fig. 2.13 Material dispersion τ_D

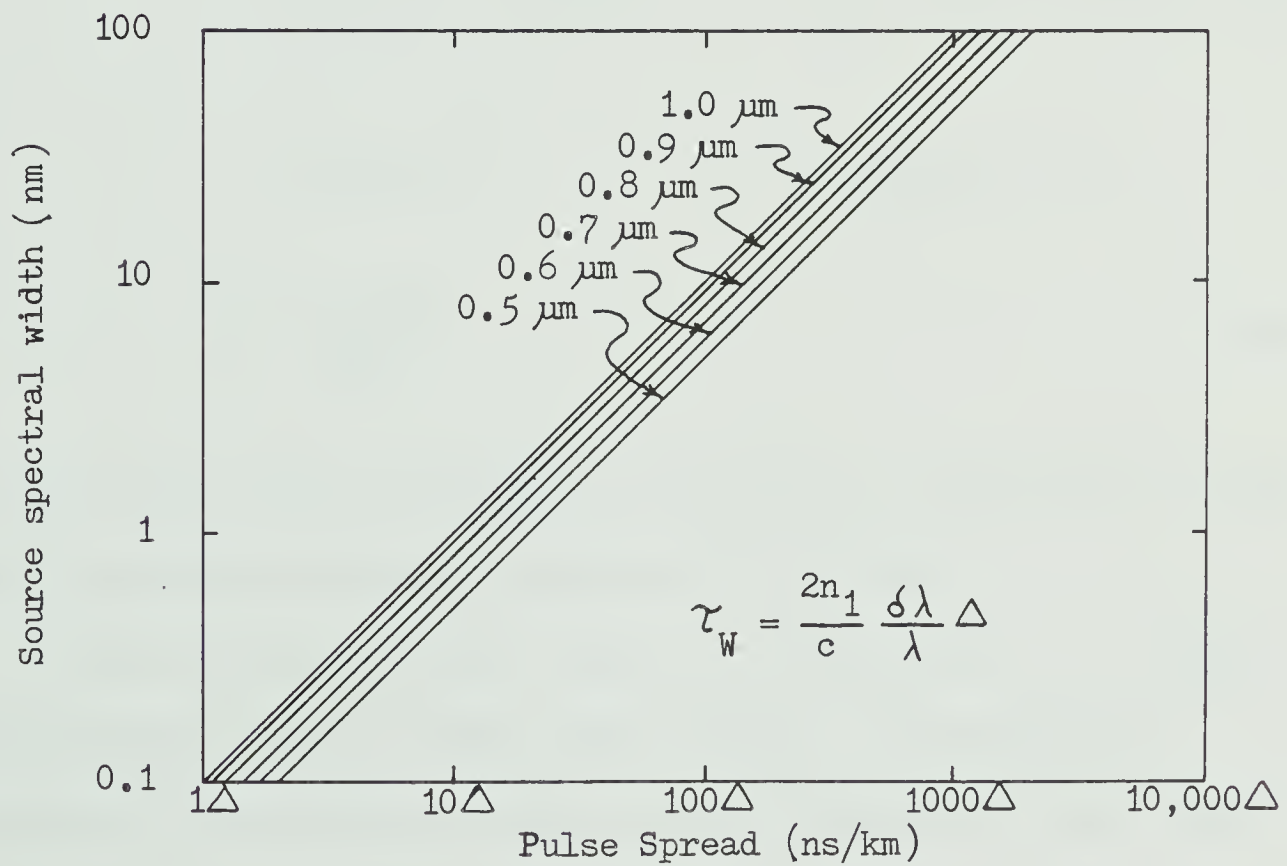


Fig. 2.14 Waveguide dispersion τ_W

Graphs of τ_M , τ_D and τ_W are presented in Figs. 2.12, 2.13 and 2.14 for fused silica fibers. Fig. 2.12 portrays multimode dispersion as a function of numerical aperture for step-index and graded index fibers. The various curves were plotted using the analytical results of the different researchers discussed in the foregoing pages and Appendix A.

The more universal parameter, numerical aperture, was used instead of the relative index difference Δ using the following approximation:

$$\begin{aligned}
 \text{N.A.} &= [n_1^2 - n_2^2]^{1/2} \\
 &= [(n_1 - n_2)(n_1 + n_2)]^{1/2} \\
 &= [n_1(n_1 - n_2) + n_2(n_1 - n_2)]^{1/2} \\
 &\approx [2n_1(n_1 - n_2)]^{1/2} && \text{for weakly guiding fibers} \\
 &= [2n_1^2 \Delta]^{1/2} && \text{using eq. (2.8)}
 \end{aligned}$$

$$\text{or,} \quad \Delta = \frac{(\text{N.A.})^2}{2n_1^2} \quad (2.34)$$

The error using this approximation was found to be negligible over the range of numerical apertures considered (0.1 to 0.5).

The curves were plotted using $n_1 = 1.455$ which is an average index for fused silica as seen in Fig. 2.10(a). The wavelength dependence of the refractive index did not introduce any significant error.

Experimental results described in Appendix E have been plotted for comparison with the theoretical. It is apparent that the only curve that can be used safely for design with step-index fibers is curve (A) which is a plot of eq. (2.25). Curve (B) for the square fiber is seen to be in error by several nanoseconds per kilometer when compared with experimental results. It is also apparent that graded-index fibers yield very inconsistent results, depending largely on the actual profile factor α . Basing a design on even the most pessimistic parabolic curve (curve (E) for $N.A. \leq 0.21$; curve (C) for $N.A. \geq 0.21$) could be catastrophic. It is, therefore, mandatory that either the index profile factor be known with considerable precision, or the manufacturer specify the maximum dispersion. Samples may have to be tested and the dispersion distribution determined for the ensemble of cables required.

Fig. 2.13 shows material dispersion as a function of source spectral width. The solid lines were plotted using the first part of eq. (2.27) and using values of $d^2n/d\lambda^2$ for fused silica from Fig. 2.10(c). The dashed lines were plotted using equation (2.18) with values of $kd^2\beta/dk^2$ from Fig. 2.7.

The dispersion characteristics in Fig. 2.8 were compared with the above results and were found to be virtually identical to those portrayed by the solid lines. However, plotting two experimental values (one estimated) suggests that the solid lines may be overly optimistic. Certainly, one measured value and one estimated value form a weak basis for substantiation of analytical results. Since they do provide some evidence, they must be considered accordingly.

The advantage of using longer wavelength sources is apparent from the graph. Using the curve for eq. 2.27, an LED with a spectral width of 40 nm suffers a material dispersion of 22 nsec/km at $0.5 \mu\text{m}$ and only 2.0 nsec/km at $0.9 \mu\text{m}$. This is one reason for current interest in developing optical sources and photodetectors which operate at longer wavelengths.

Fig. 2.14 illustrates waveguide dispersion as a function of source spectral width according to the second part of eq. (2.27). The delay is seen to be a function of relative index difference Δ . As a rough rule of thumb, Δ can be considered to be 0.01, although, in all likelihood, it will probably be smaller. As is the case for material dispersion, waveguide dispersion is found to increase with frequency, but it does so at a much slower rate. Keeping in mind the counteracting effects of the two dispersions, these results are generally consistent with Fig. 2.8.

Although mode mixing has been demonstrated to reduce dispersion in relatively long fibers, the improvement depends upon the actual length and the coupling length L_c . This latter parameter may not be known with any precision, so it would appear most prudent to design using the most pessimistic criteria, ie: linear increase in dispersion with length. For the proposed radio telescope, with a maximum run length of 2.5 km, this approach would seem reasonable. For systems with longer runs of fiber, the coupling length should be either specified by the manufacturer or measured.

2.4 Attenuation

Attenuation losses in optical fibers can be attributed to the following mechanisms [8]:

- Material absorption
- Material scattering
- Waveguide scattering
- Radiation due to bends
- Cladding design effects

2.4.1 Material Absorption

Material absorption is a combination of both intrinsic and impurity absorption. Intrinsic absorption is believed to be due to strong absorption bands [13] in the infrared and particularly the ultraviolet regions, whose "tails" extend into the visible region. This mechanism, although small, is present even in "perfect" glasses.

The greatest contributor to material absorption is the presence of impurities. These are transition metal ions and their neighbors in the periodic chart (Cr, Mn, Fe, Co, Ni) [8,38] and hydroxyl ions OH^- . The absorption wavelength and bandwidth vary somewhat with the valence of the ion and the specific glass considered [8]. Table 2.1 [39] illustrates the typical absorption wavelengths and concentrations necessary (in parts per million) to achieve an attenuation of 1 dB/km (at $0.8\text{ }\mu\text{m}$) for the more important ions. It is seen that impurity concentration must be kept below the order of a few parts per billion to avoid significant attenuation effects.

Table 2.1

Contribution of Impurities in Glass to Absorption

Ion	Absorption Peak (μm)	Concentration, ppm for 1 dB/km Attenuation at $0.8\mu\text{m}$
Cu^{2+}	0.8	< 0.0008
Cu^{+}	0.2	>> 1
Fe^{2+}	1.1	> 0.0025
Fe^{3+}	0.3	>> 10
Cr^{3+}	0.65	< 0.002
OH^{-}	{ 0.72 0.95	0.15 at $0.72\mu\text{m}$ 1 at $0.95\mu\text{m}$

Present manufacturing seems to have the metallic ion losses well under control. The greatest problem is that of reducing the effects of the OH^{-} ion. The fundamental absorption peak of OH^{-} is around $2.7\mu\text{m}$ which is far beyond the range of interest for optical fibers. However, there are second and third overtones [8,40] located at $0.95\mu\text{m}$ and $0.72\mu\text{m}$. The relative magnitude of the absorption peak at $0.72\mu\text{m}$ is much lower than at $0.95\mu\text{m}$, so the major problem is at the latter wavelength. There is also a relatively small absorption peak at about $0.88\mu\text{m}$ due to the OH^{-} ion.

Keck, Maurer & Schultz [40] have determined that all absorption between $0.7\mu\text{m}$ and $1.1\mu\text{m}$ in a low-loss fiber (4 dB/km between 0.8 -

$0.85\mu\text{m}$ and at $1.05\mu\text{m}$) can be attributed to OH^- bands to within ± 0.7 dB/km.

2.4.2 Material Scattering

Material scattering losses can be attributed [8,41,42] to linear effects such as Rayleigh and Mie scattering and to such nonlinear effects as stimulated Raman and Brillouin scattering.

Inhomogeneities, such as fluctuations in glass density [38] are always formed in the waveguides during production. No way has yet been suggested for decreasing these. Rayleigh scattering is due to inhomogeneities which are small compared to the wavelength of the light. Most of the scattered light escapes from the core into the cladding or beyond [43], where it is dissipated. Rayleigh scattering varies as λ^{-4} and, for well made glasses, eg. fused-silica, will result in a loss of less than 1 dB/km at $1.0\mu\text{m}$ [8].

Inhomogeneities which have physical dimensions in the same order of magnitude as the wavelength cause Mie scattering [8]. Care in manufacturing should eliminate most large inhomogeneities, rendering Mie scattering insignificant.

Below a certain threshold, nonlinear effects will have negligible influence on transmission. Such effects do, however, constitute an upper limit on the power level that can be used, such as, for example, in long-distance transmission.

Raman scattering involves the interaction of light with atoms or molecules in the transmission medium [44]. Depending on the energy state of these particles, the scattered light may result in higher or lower frequencies. If interaction occurs with more macroscopic

density fluctuations rather than with microscopic atoms or molecules, Brillouin scattering can occur [44]. For stimulated Raman scattering, the maximum useable power is given by [8]

$$P_{\max} \simeq 4 \times 10^{-2} l_f \sigma^2 \quad \text{watts} \quad (2.35)$$

where l_f is the transmission loss of the fiber (dB/km)
 σ is the full width at half-maximum power density for the guided wave in the fiber (in μm)

This equation assumes the spectral width is equal to or less than 10 nm. For LED sources ($\Delta\lambda \geq 0.03 \mu\text{m}$), P_{\max} will be two to four times greater than that given by eq. (2.35).

Considering a multimode fiber in which the half power density bandwidth is $50 \mu\text{m}$ and the attenuation at the wavelength of interest is 5 dB/km,

$$\begin{aligned} P_{\max} &\simeq 4 \times 10^{-2} (5)(50)^2 \\ &= 500 \text{ watts.} \end{aligned}$$

Clearly, the use of low-loss, multimode fibers eliminates any potential nonlinear effects due to stimulated Raman scattering.

Stimulated Brillouin scattering is found to be dependent upon source spectral width. For a monochromatic source, the maximum useable power is given by [8]

$$P_{\max} \simeq 8 \times 10^{-5} l_f \sigma^2 \quad \text{watts} \quad (2.36)$$

assuming that the stimulated gain coefficient is not a function of wavelength. For a multifrequency source of bandwidth $B(\text{MHz})$ or $\delta\lambda(\text{nm})$,

$$\begin{aligned} P_{\max} &\simeq 3 \times 10^{-6} l_f \sigma^2 B \quad \text{watts} \\ &\simeq 8 \times 10^{-1} l_f \sigma^2 \quad \text{watts.} \end{aligned} \quad (2.37)$$

Considering again a multimode fiber with $l_f = 5 \text{ dB/km}$ and $\sigma = 50 \mu\text{m}$ excited by an LED with spectral width of 40 nm ,

$$P_{\max} \simeq 4 \times 10^5 \quad \text{watts.}$$

It is apparent that nonlinear effects due to stimulated Brillouin and Raman scattering will be negligible in low-loss, multimode fibers, particularly when broad spectral width sources are used.

Tests have determined [13] that power densities of at least 44 MW/cm^2 can be coupled into multimode fibers from a laser source with no observable non-linear attenuation. This is equivalent to 864 watts into a fiber with a core diameter of $50 \mu\text{m}$.

2.4.3 Waveguide Scattering

Waveguide scattering can result due to imperfections at the core-cladding boundary. Variations in core diameter will cause

transfer of power between modes [8]. If the transfer is between guided modes, this can be a beneficial effect as the various modes tend to average out their velocities of propagation, thus improving dispersion characteristics. This was discussed in section 2.3.3. However, if power is transferred from guided modes to the radiation field, there can be prohibitive loss of power. Assuming an r.m.s. core radius deviation of only $10^{-3}\mu\text{m}$, radiation losses of 10 dB/km [13] can be expected in a worst-case situation. Fortunately, such losses are not encountered in state-of-the-art low-loss fibers due to high-quality manufacture.

2.4.4 Physical Bends

Radiation losses occur at bends where a portion of the wavefront would otherwise require a velocity greater than that of light [8] to maintain phase coherence. The radiation attenuation coefficient has the form

$$l_r = \chi_1 \exp(-\chi_2 r) \quad (2.38)$$

where χ_1 and χ_2 are constants which are functions of the propagation characteristics and dimensions of the material and which are independent of r , the radius of curvature. The exponential dependence of l_r on r indicates that the attenuation can vary enormously with even a 2:1 range in r . Fig. 2.15 [13,38] illustrates the attenuation as a function of radius r for two waveguides. Fig. 2.15 implies that fibers with relatively large normalized frequency ν (described in section 2.2) do not radiate easily, since, with increasing ν , the

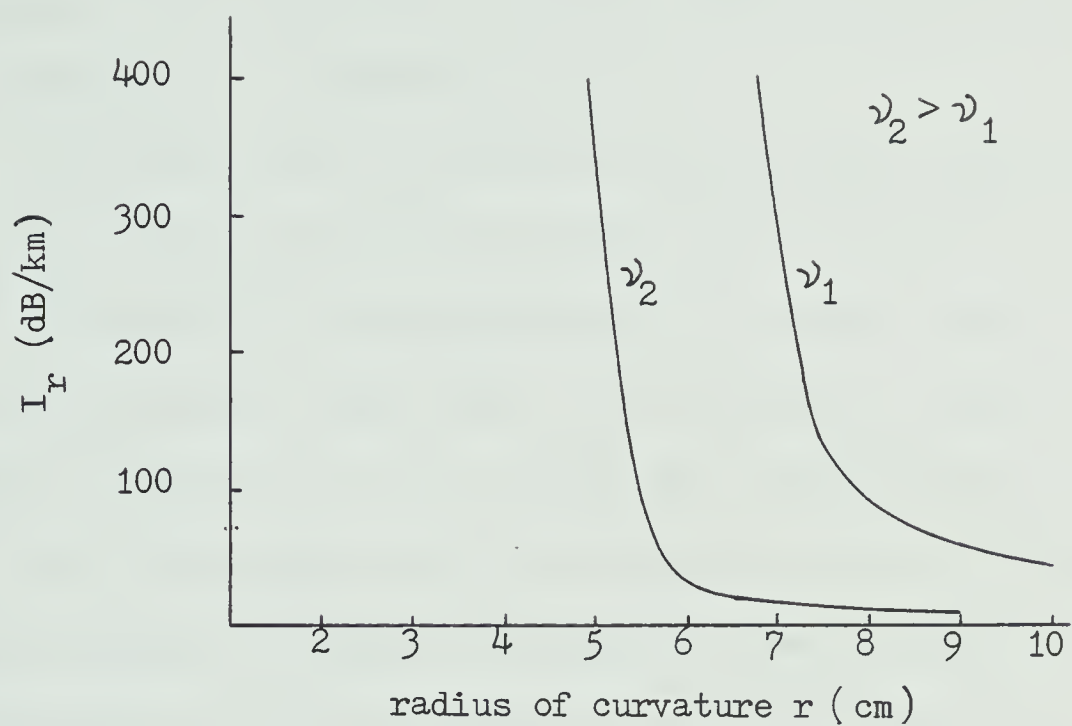


Fig. 2.15 Attenuation due to bends for two waveguides (After [13] and Bielawski [38]).

modes are more tightly bound to the core-cladding interface.

In order to see any appreciable increase in attenuation due to bending, it would be necessary to coil lengths of the order of a kilometer of optical fiber around a drum having a radius of several centimeters. For this reason, bending losses are generally considered to be unimportant for practical systems.

Array-type radio telescopes employing equal-length distribution lines usually have excess cable lengths stored in coils. If such a system is employed in the proposed radio telescope, lengths of over 2 km may be stored in such coils. It would then be important to consider bending losses and to ensure that coil diameters be greater than ~ 20 cm. It would probably be advisable to ensure that such coils be kept virtually circular to minimize the bending radius. Similarly, if excess cable lengths are stored in other configurations, bends must be constrained such that the bending radius is greater than ~ 10 cm.

2.4.5 Cladding Design Effects

Energy in the cladding as cladding modes, or simply energy scattered from guided modes, can couple back into the core and degrade the group-delay characteristics. For this reason, the cladding is often made deliberately lossy [8]. It is also possible to utilize a lossy jacket, but this can introduce losses in core-guided modes, particularly if the index of refraction in the jacket is greater than in the cladding. This is because some of the energy in the cladding would be refracted into the jacket resulting in excess loss.

Cherin & Murphy [45] have determined that cladding thickness is the dominant fiber parameter that plays a critical role in preventing

transmission loss due to a lossy jacket. They plotted transmission loss vs. a/b , where a and b are radius of core and cladding, respectively. Plots for a number of fibers of different core sizes and numerical apertures revealed that a cladding thickness of at least $20\text{ }\mu\text{m}$ was required to prevent any appreciable loss in core-guided modes due to a lossy jacket. Their model was based on a jacket loss of $4\text{ dB}/\mu\text{m}$.

2.4.6. Summary

When optical fibers were first being considered for long-distance communications, the objective was to attain attenuation levels as low as 20 dB/km [38]. This level was expected to permit economically feasible repeater spacings and be compatible with existing telecommunication system configurations.

In 1970, Corning Glass Works fabricated a fiber with a loss of 16 dB/km [28] and by 1971 had attained a level of 13 dB/km . In 1972, Corning announced the achievement of 4 dB/km at 0.85 and $1.06\text{ }\mu\text{m}$. In this fiber, losses between 0.6 and $0.9\text{ }\mu\text{m}$ were all below 12 dB/km . By 1973, a loss of 2 dB/km was attained. In 1974, Bell Telephone Laboratories reported a fiber with a loss of 1.1 dB/km at $1.02\text{ }\mu\text{m}$. In 1976, a fiber exhibited a loss of 0.47 dB/km at $1.2\text{ }\mu\text{m}$ with less than 1 dB/km at $0.95\text{ }\mu\text{m}$ [47]. Additional results are presented in Appendix C.

Typical plots of spectral attenuation are presented in Fig. 2.16 for various fibers. It can be seen that the attenuation generally decreases with increasing wavelength as λ^{-4} in accordance with the Rayleigh scattering effect. Other attenuation effects mostly due to absorption effects of the OH^- ion predominate around the $0.95\text{ }\mu\text{m}$ wavelength.

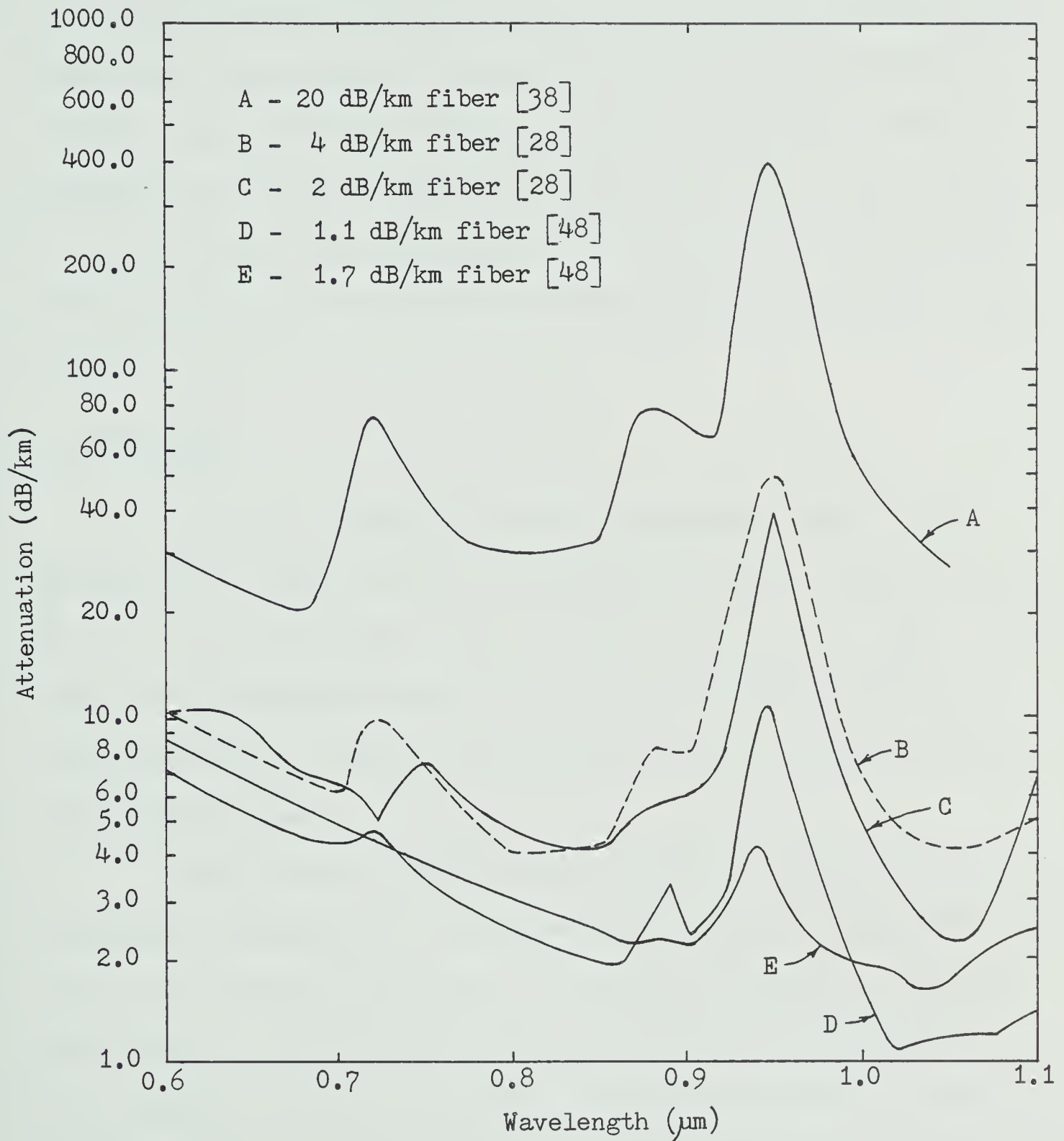


Fig. 2.16 Spectral attenuation of various optical fibers

For low-loss fibers, Fig. 2.16 indicates that the scattering losses predominate, with the hydroxyl ion absorption coming more under control as technology progresses.

For the radio telescope project, it is expected that optical fibers will be available in commercial cables with attenuations of 5 dB at $0.7\text{ }\mu\text{m}$ and 2 dB at $1.06\text{ }\mu\text{m}$ since these values are easily attainable in laboratory fibers as shown in Fig. 2.16. This seems to be consistent with the state-of-the-art (Appendix D). These values will be shown to be adequate for the system design proposed in this thesis.

2.5 Crosstalk

Analyses of crosstalk between single-mode fibers or those allowing only a small number of propagating modes have been performed by a number of researchers (see the bibliography in ref. [46]). It is likely that multimode fibers will be used in the proposed radio telescope system, so the following discussion will be restricted to the multimode case.

Some results of research into crosstalk in optical fibers is presented in Appendix E. As expected intuitively, cladding thickness is a very important contributor to crosstalk isolation. It is also interesting to note that increasing the numerical aperture of the fiber improves crosstalk isolation. Crosstalk isolation is also improved by distributing most of the optical energy that is coupled into the lower order modes. Under conditions of constant optical "launching" conditions, crosstalk increases approximately 2 dB per decade of length and increases about 7 dB when the wavelength is doubled.

Cladding thickness and numerical aperture are parameters that are established for the fiber at the time of manufacture. Optical launching conditions may be able to be varied to some degree through choice of optical source, method of coupling the source to the fiber, or other means. The parameters over which we have the most control are the system, or fiber length, and the optical wavelength of the source.

To determine the crosstalk for arbitrary cable lengths and at different wavelengths, it is tempting to consider the following expression [49] used for wire systems:

$$\text{FEXT (dB)} = X + 20 \log \frac{f}{f_o} + 10 \log \frac{L}{L_o} \quad (2.39)$$

where X is the known FEXT at frequency f_o and length L_o .

The frequency-dependent term implies a 6 dB increase in crosstalk per octave of frequency increase. However, Fig. H.6 indicates a decrease of ~ 7 dB per octave of frequency increase. This is logical since increasing the optical frequency tends to increase the confinement of the beam within the waveguide and thus reduce crosstalk coupling. The length-dependent term implies a 3 dB increase in crosstalk with every doubling of the length. Fig. H.4 indicates an increase of only 2 dB per decade, which is substantially more optimistic. These factors suggest that a more appropriate expression for FEXT might be

$$\text{FEXT (dB)} \simeq X + 2 \log \frac{L}{L_o} - 23.3 \log \frac{f}{f_o} \quad (2.40a)$$

$$\text{or} \quad \text{FEXT (dB)} \simeq X + 2 \log \frac{L}{L_0} + 23.3 \log \frac{\lambda}{\lambda_0} \quad (2.40b)$$

Considering a cable with inter-fiber crosstalk of -80 dB in 500 meters (at $0.6328 \mu\text{m}$), eq. (2.39) predicts a FEXT of ~ -78.6 dB in 2.5 km as opposed to -73 dB predicted by eq. (2.40).

The verification of eq. (2.40) would require crosstalk testing at various lengths and wavelengths, which, in principle, is simple to do.

2.6 Polarization

Light polarization is a property which, in general, can be used to advantage in communication systems since it is readily manipulated with optical devices. Possible applications include polarization modulation and multiplexing.

While photodetectors are generally insensitive to the polarization of incident light, sources are usually polarized to some extent, depending on the type of source. Semiconductor lasers have been found to emit plane polarized light [50,51], but the polarization varies from one device to another. Polarization perpendicular to the main plane has been observed, as has elliptical polarization. Different regions of a laser have been found to emit light with different polarizations. The factors governing this apparently random polarization are not presently known. However, systems can be constructed to use polarized light by simply passing randomly polarized light through suitable polarizing optics. For this reason, it is necessary to examine depolarizing effects in optical fibers.

Step-index fibers with high attenuation losses have been found to exhibit rapid depolarization effects due to mode mixing in very short lengths of fiber [52]. A study on a low-loss graded-index fiber [53] indicated some strong dependence between the degree of polarization of emergent light and the incident polarization, the degree of polarization of emergent light and temperature and the output polarization angle and incident polarization angle. However, this polarization sensitivity will probably not be of any consequence in the radio telescope project. Since the fiber tested was very short (45 cm), depolarization effects due to mode mixing in long fibers were negligible. It is not known at what length such depolarization effects will occur in graded-index fibers. If the proposed radio telescope is to use an "equal-length" optical waveguide feeder system, each fiber run will be about 2 1/2 kilometers long. This length should almost certainly ensure complete depolarization. For this reason, polarization modulation will not be considered in the transmission system for the radio telescope.

Regardless of the extent of depolarization in a fiber, a simple system, employing a perfectly polarized source transmitting light onto a photodetector through the fiber, will suffer no loss due to depolarization effects. This is because photodetectors are not polarization-sensitive.

Polarizing effects in input and output coupling devices will probably contribute the most toward polarization losses in systems. Considering the worst case of perfectly polarizing input devices and polarization-sensitive output devices, installation would be critical

only if the fiber was sufficiently short such that no depolarization occurred. In such a case, the polarization angle of the couplers should be aligned with one of the "privileged" axes of the fiber. This will ensure no loss due to polarization effects (unless the source is randomly polarized, which will then contribute a maximum loss of 3 dB).

In long fibers, which (presumably) experience total wave depolarization, the polarization angles of the couplers can be placed arbitrarily. There will be a 3 dB loss if the output coupler is perfectly polarization-sensitive and an additional 3 dB loss if the source is randomly polarized.

A block diagram of a basic optical fiber transmission system is presented in Fig. 2.17. Table 2.2 summarizes the critical parameters and system losses for various configurations of polarizing elements. It is assumed that, in the case of a polarized source, the polarization angle of the source is aligned with the input coupler to assure 100% coupling. The incident and output polarization angles τ and Ψ are defined at the input and output of the fiber, respectively.

Table 2.2

Polarization Effects & Losses

<u>Source</u>	<u>Input Coupler</u>	<u>Fiber</u>	<u>Output Coupler</u>	<u>Detector</u>	<u>Critical Parameters</u>	<u>Depolarization Loss (Max)</u>
Pol	Pol	Pol	Pol	Non-pol	τ, Ψ	—
Pol	Pol	Non-pol	Pol	Non-pol	—	3 dB
Non-pol	Pol	Pol	Pol	Non-pol	τ, Ψ	3 dB
Non-pol	Pol	Non-pol	Pol	Non-pol	—	6 dB



Fig. 2.17 Typical Optical Fiber Transmission System

2.7 Physical Properties

(a) Tensile Strength

Fibers are quite immune to mechanical fatigue. The tensile strength of glass fibers is of the order of 6.9×10^5 newtons/cm² [5]. However, due to the size and frequency of surface imperfections, failure can occur at much smaller values. Tensile tests performed at Bell Telephone Laboratories [5] indicated a breaking limit with masses of 450 grams on samples of individual fibers with core diameters of 100 μ m and cladding diameter of 142 μ m. This is equivalent to 2.785×10^4 newtons/cm² for the composite fiber.

Corning's 6-fiber CORGUIDE cable [12] has a minimum rated breaking limit of 50 kg. Tensile tests have indicated [5] that some fibers remain intact at loads up to 90 kg. During manufacture, all CORGUIDE optical fibers are subjected to tensile testing at 1.72×10^4 newtons/cm² [13]. Multi-kilometer lengths of fibers tested at this level are expected to withstand loads of 6.9×10^3 newtons/cm² for at least 20 years.

(b) Impact Resistance

Optical fibers are tested for resistance to impulsive forces by repeated dropping of a hammer of known weight from a

specified height. Corning's CORGUIDE cable [56] has an impact resistance for 200 impacts of 0.14 m.kg. This is generated by dropping a 1.35 kg, 2.5 cm diameter hammer from a height of 10.4 cm 200 times in one place. The cable can also withstand, without fiber breakage, from 4 to 24 impacts of 0.70 m.kg.

(c) Flexing & Twisting

Tests on Corning CORGUIDE cable samples [56] indicate no loss of fibers when subjected to sustained flexing back and forth over a 2.5 cm mandrel for 10,000 cycles. Similar performance has been achieved for 2000 cycles of a $\pm 90^\circ$ twist with a simultaneous 180° bend over a 2.5 cm diameter sheave. The bending radius of current CORGUIDE fibers before breakage occurs is about 1.7 mm.

(d) Environmental Properties

Although corrosion resistance of glass is generally better than its copper counterparts, the presence of moisture tends to reduce the molecular bonding strength of the fibers [57]. This increases the susceptibility of failure due to cracking when under tensile load. The plastic jacket or coating over the fibers will provide a degree of moisture protection, but fiber cables designed for buried applications should have additional protection with metallic and polyethylene cable sheaths and, possibly, cable filling jelly or powder.

One of the attractions of fiber optics, at least for the military, is its relative immunity to nuclear radiation. In the wavelength region from 0.8 to $1.05\text{ }\mu\text{m}$, studies of nuclear radiation

effects indicate a linear increase of attenuation with cumulative dosage at a rate of about 1 dB/km per kilorad [13]. A dose of 3 kilorads is considered a serious threat to human survival. Average worldwide background radiation yields an accumulated dose of 10 Rads over a twenty year period. Radiation immunity is therefore of no practical concern for the radio telescope application.

2.8 Summary

Optical fibers appear to be clearly capable of providing the transmission medium for the feeder system of the proposed radio telescope. The basic transmission characteristics of dispersion and attenuation have been shown to have improved sufficiently such that an optical fiber feeder system is practical. Crosstalk characteristics of cabled fibers appear to be more than adequate for this system. There should be no adverse effects due to polarization properties in optical fibers. Finally, the physical properties of optical fibers and cables indicate that practical systems can be installed, and expected to operate satisfactorily in the field.

CHAPTER 3

OPTICAL SOURCES

The sources generally considered most promising for optical fiber communications [6,19] are semiconductor electroluminescent devices-injection laser diodes (ILD's) and light-emitting diodes (LED's). Their desirable characteristics include small size, relatively low power requirements, the fact that the wavelength can be varied somewhat (depending on the material) and their relatively low cost.

These characteristics are particularly attractive for the proposed radio telescope. With some 2000 dipole antennas spread over a large area, a number of sources will be required, even assuming a certain amount of R.F. multiplexing. Of major importance are the device cost and power requirements, especially at remote locations. The small size is particularly suitable for equipment meant for pole mounting, especially in the unlikely event that each antenna were to have its own transmitting source and link to the observatory. With devices operating at different wavelengths, and since optical wavelength is largely independent of temperature (see ref. [51]), wavelength division multiplexing (WDM) becomes an appealing prospect.

The development of semiconductor diode sources for optical fiber communications has concentrated on the use of elements in groups III and V of the periodic table (see ref. [51]). The first practical devices were made from gallium arsenide (GaAs) and emitted light at a wavelength of about $0.9\text{ }\mu\text{m}$. This matched the transmission window of optical fibers very well. The addition of a third element such as

aluminum or phosphorous allowed the optical wavelength to be varied over a range of about $0.75 - 0.9 \mu\text{m}$, depending on the proportions of the elements. At the present time, the ternary alloy system $\text{Al}_x\text{Ga}_{1-x}\text{As}$ is the most highly developed for optical sources (see ref. [51]). With the improved dispersion characteristics of optical fibers at wavelengths around $1.1 \mu\text{m}$ and longer, sources using quaternary alloys are being developed to accommodate these longer wavelengths.

For the proposed radio telescope project, either laser diodes or light-emitting diodes could be employed in the optical transmission system since they are very similar devices. There are present advantages in cost and reliability with light-emitting diodes over laser diodes so it would appear preferable to use light-emitting diodes. It will be shown that they can offer satisfactory performance although laser diodes are technically superior.

3.1 Laser Diodes

3.1.1 General

A laser diode is basically a p-n junction situated within a Fabry-Perot optical cavity as described in ref. [58]. The resonant cavity is formed by cleaving two parallel facets along natural cleavage planes of the semiconductor crystal and perpendicular to the p-n junction. The other two sides perpendicular to the p-n junction are left rough to suppress unwanted modes that may otherwise develop in that direction. Gallium arsenide has a refractive index of 3.5 at $0.9 \mu\text{m}$ and a GaAs-air interface has a reflectivity of 30 - 35% [51]. This enables the cleaved facets to act as end mirrors in the Fabry-Perot resonant cavity. In order to reflect all the radiation from

one end, the reflectivity of the opposite mirror is made as close to 100% as possible. This is accomplished by coating the facet with an insulating material such as silicon monoxide or silicon dioxide [59] so as not to short-circuit the p-n junction and then applying a metallic coating such as aluminum, silver or gold.

Under forward bias conditions, current flows across the p-n junction and radiation is emitted. Stimulated emission, necessary for lasing, occurs when a spontaneously emitted photon collides with an electron that is about to emit a photon of the same energy. The two photons will then proceed to stimulate more emission and the process continues until a standing wave is formed within the cavity and coherent radiation is emitted. The laser gain mechanism is maintained once a threshold current has been exceeded to create a sufficiently high electron density. Since the photons tend to stimulate emission of the same wavelength, the gain mechanism serves to narrow the emission spectrum [39]. This is the reason the spectrum of a laser diode is about an order of magnitude narrower than that of an LED and typically less than 2.5 nm [60].

Early semiconductor lasers required high threshold current densities j_{th} to establish lasing. This resulted in considerable device heating and subsequent short operating lifetimes. Even with heat sinks, the devices could only tolerate pulsed operation with relatively low duty factors at room temperature. Typical lifetimes of from 10 - 1000 hours were observed at duty factors of 10^{-4} [60].

The development of laser diodes for continuous operation has been made possible by dramatically lowering the threshold current from typical values of 50,000 - 100,000 A/cm² [60] to below 1000 A/cm²

[58,61] for present devices. This has been accomplished largely by the use of epitaxial techniques to form p-n junctions [51] and by the use of multi-layer structures.

The simplest laser geometry, and that most suitable for optical fiber communications, is the symmetrical double heterojunction with a stripe contact [61]. Although there are a number of variations of this design [58], the basic principle is that the current distribution occurs over an area much narrower than the total width of the active region. A typical cross-section is represented in Fig. 3.1.

The stripe geometry provides a number of advantages over non-stripe:

(i) Filamentary operation is reduced [58]. Lasing filaments are narrow regions which, presumably due to inhomogeneities, begin to lase while surrounding regions are still below threshold. These contribute to device noise.

(ii) Multimode operation is reduced [58]. Uniform stripe-geometry lasers exhibit an increase in mode order with an increase in stripe width. Since dispersion increases with the number of modes, it is desirable to limit the number. The fundamental mode alone is obtained for stripe widths of about $12\text{ }\mu\text{m}$ or less.

(iii) The radiation is emitted from a small region, which simplifies coupling the radiation into fibers with low numerical aperture [61].

(iv) The operating current is low, usually less than 0.5 amp [60].

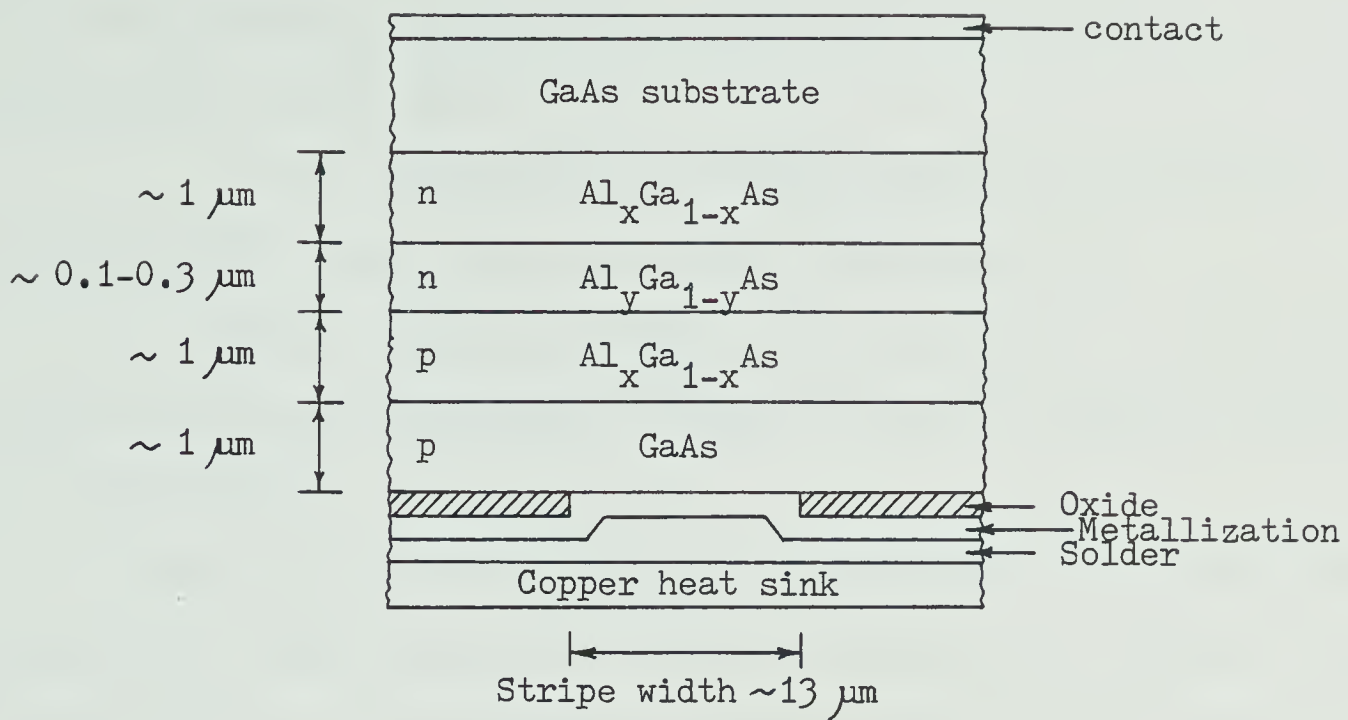


Fig. 3.1 Cross-section of a typical stripe-contact laser diode (After Kressel et al [61]).

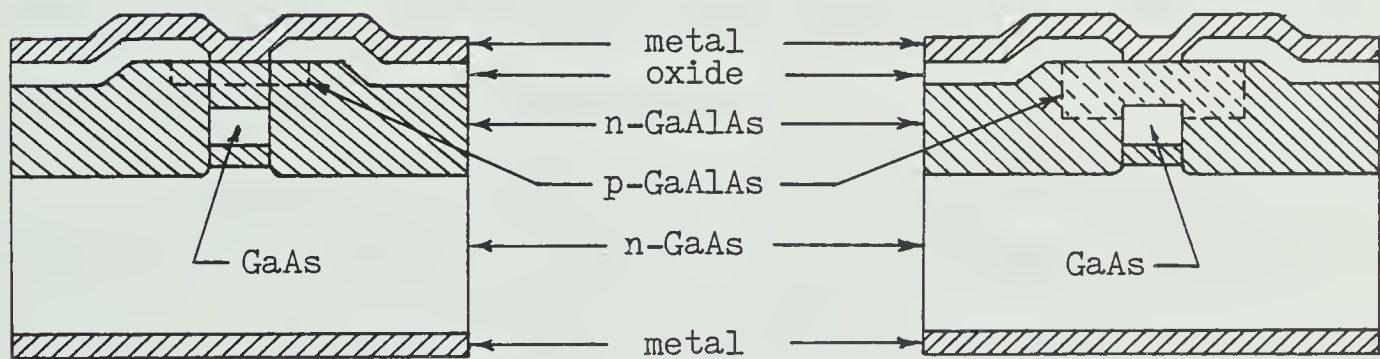


Fig. 3.2 Buried heterostructure (BH) injection laser diode (After Tsukada [62]).

(v) Thermal dissipation of the device is improved because the heat generating active region is imbedded in an inactive semiconductor medium [61].

(vi) Fabrication of reasonably defect-free areas is simplified due to the small size of the active area [61].

(vii) The active region is isolated from an open surface along its two major dimensions, a factor believed to improve long-term reliability [61].

The width of the stripe can be used to adjust the output power level [61]. Power levels of 5 - 10 mw, anticipated for optical fiber communications, are obtained with a stripe width of about $13\mu\text{m}$ [61], a dimension that is a suitable compromise between low operating currents and appropriate power output level.

A form of stripe-geometry laser that appears very promising is known as a buried heterostructure (BH) laser [62]. In this laser, the narrow GaAs active region is completely surrounded by GaAlAs as shown in Fig. 3.2.. The two types shown depend on the doping on the upper side of the active GaAs layer.

In BH lasers, as other stripe-geometry lasers, the heat source is the narrow active region that is surrounded by inactive semiconductor material. This is expected to be advantageous in the transfer of heat to the heat sink. It appears that CW operation of these lasers may be possible (at room temperature) without bulky heat sinks. The superior thermal characteristics of these devices is also expected to result in high reliability.

3.1.2 Laser Diode Performance

(a) Threshold Current Density

As described in ref. [58], the threshold current density j_{th} for laser diodes has decreased over two orders of magnitude since they were first introduced. A plot of this evolution until the early 1970's is indicated in Fig. 3.3. More recent development has yielded double heterojunction devices with threshold current densities as low as 475 A/cm^2 [61].

The threshold current density of heterojunction lasers is typically an exponential function of temperature as shown in Fig. 3.4. This indicates, for a DH laser, a variation from about 700 A/cm^2 to about 1400 A/cm^2 over the temperature range of -50°C to $+30^\circ\text{C}$, or a ratio of 1:2. This represents an important consideration for electronics compensation circuitry and power supply design.

(b) Efficiency and Power

The quantum efficiency η_q of an electroluminescent device is defined as the ratio of the number of photons emitted to the number of electrons flowing through it. This can be written as [51]

$$\eta_q = \frac{I/hf}{i/e} \quad (3.1)$$

where

- I is the optical power emitted
- i is the drive current
- hf is the photon energy
- e is the electron charge.

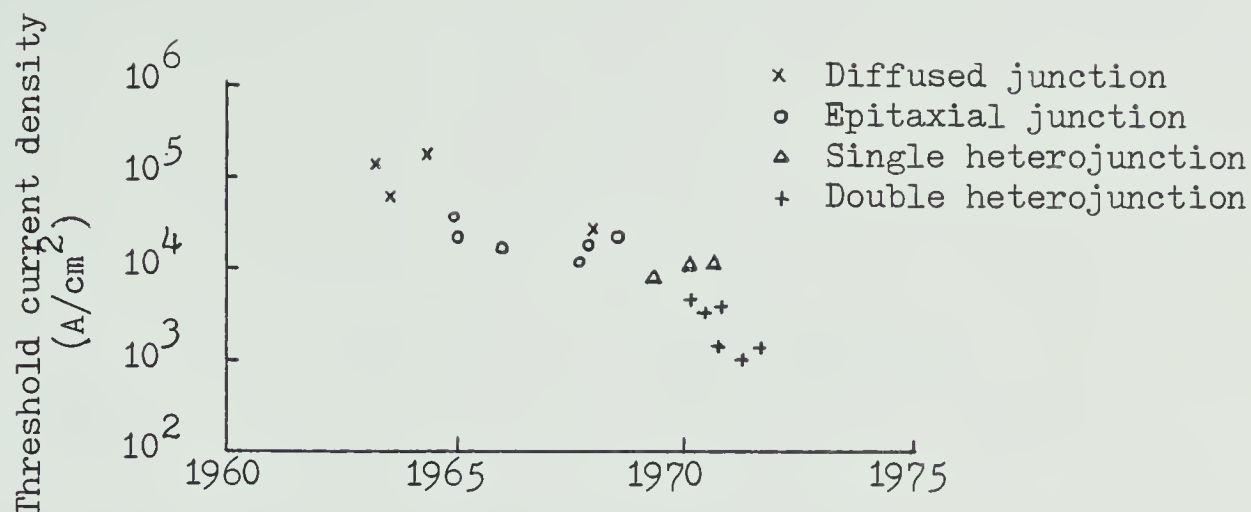


Fig. 3.3 Development of GaAs lasers since 1963, showing progressive reduction of reported threshold current densities at room temperature (After Gooch [51]).

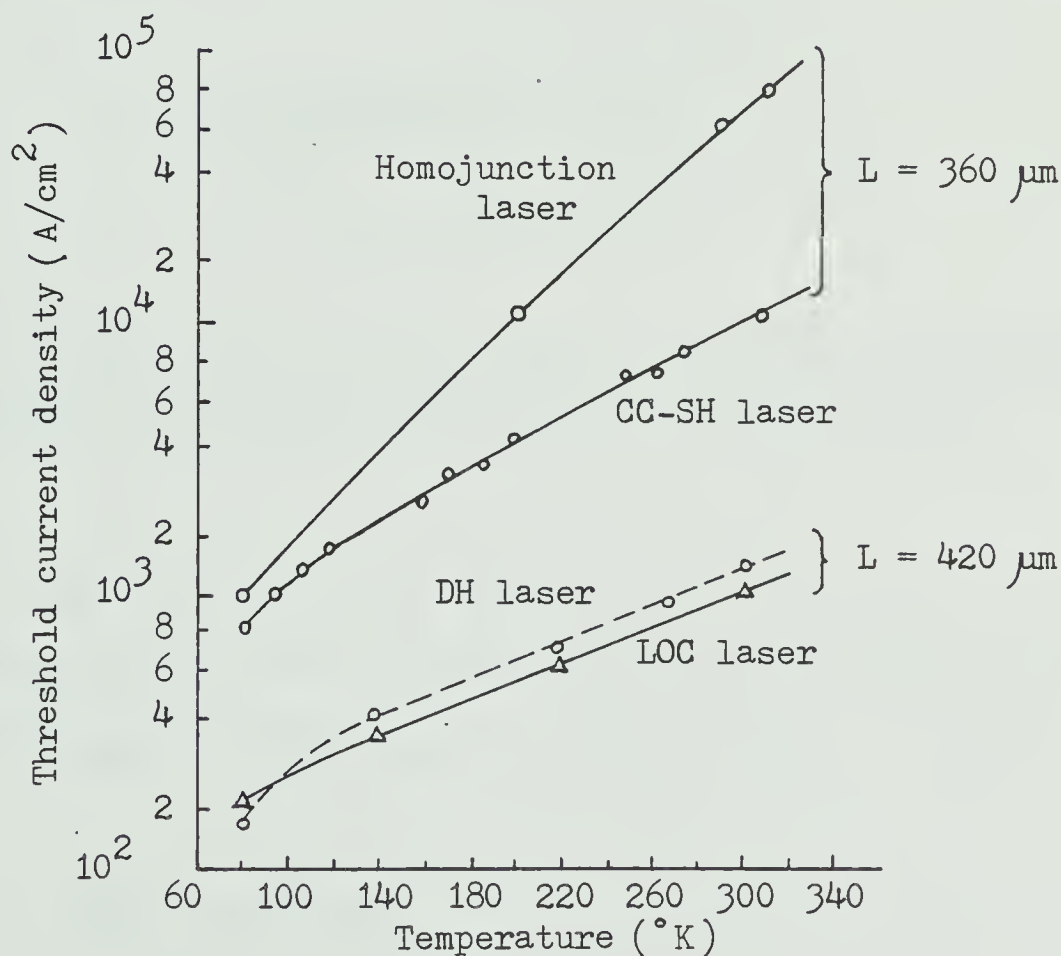


Fig. 3.4 Threshold current density as a function of temperature for homojunction, single-heterojunction (SH), double-heterojunction and large optical cavity lasers with cavity length L (After Kressel et al [60]).

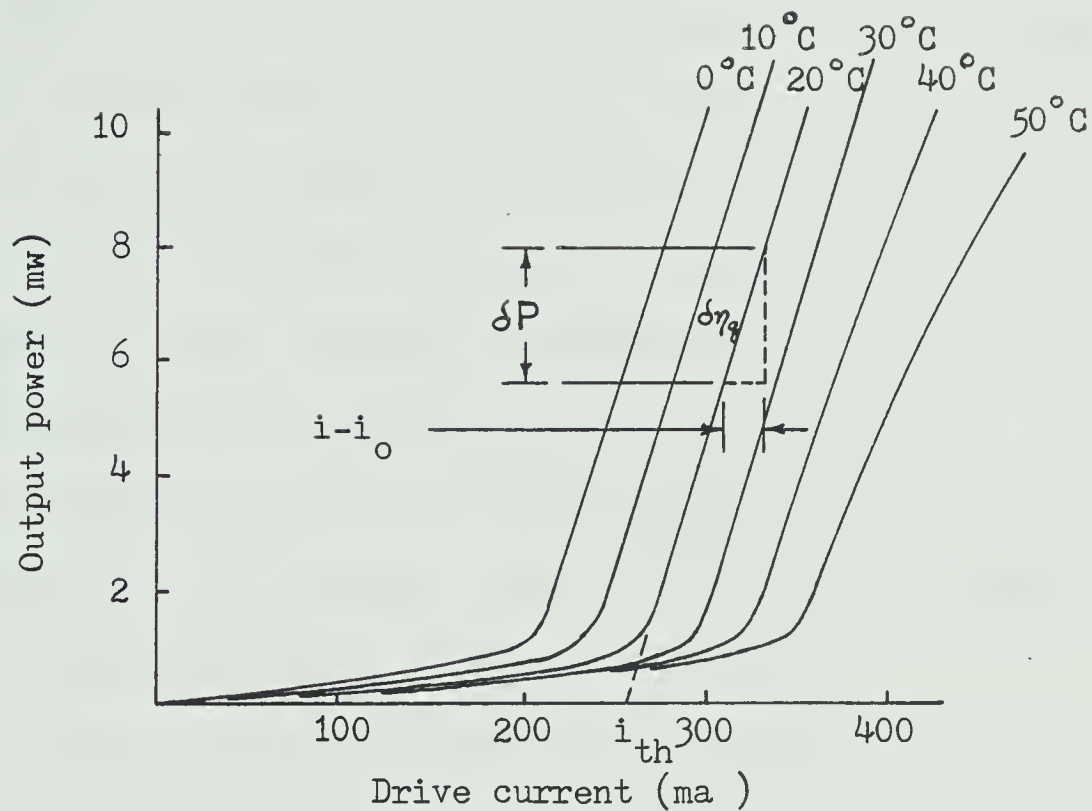


Fig. 3.5 Power emitted from one facet of a typical stripe-geometry aluminum gallium arsenide laser diode in CW operation at various temperatures (After Kressel et al [61] and O'Brien [64]).

A more convenient term, which relates the slope of the output power characteristic above threshold and the bias voltage v_s , is the differential quantum efficiency $\delta \eta_q$ shown in Fig. 3.5 and given by [51]

$$\delta \eta_q = \frac{\delta P}{(i - i_0) v_s} \quad (3.2)$$

Internal quantum efficiencies of good quality DH laser diodes approach 100% at cryogenic temperatures and 60 - 70% at room

temperature [60]. Differential quantum efficiencies approach 50% at room temperature, indicating low internal absorption losses. In the case of heterojunction lasers, the differential quantum efficiency is relatively independent of temperature, as compared to homojunction lasers [60]. This is a welcome characteristic, since a temperature control or compensation scheme adopted for use with the radio telescope would not need to be so critical. The bias point (assuming an analog, class A system) on the characteristic curve of Fig. 3.5 can be allowed to wander somewhat with temperature, providing the dynamic range remains within the linear region above threshold. (This also presumes that the variation in optical signal power is acceptable at the receiver, ie: adequate signal-to-noise ratio, within the range of the automatic gain control, etc.)

Power conversion efficiency is the ratio of optical power output to the electrical power input [60]. For SH lasers, the power conversion efficiency can reach about 10% and, for some LOC lasers, can reach as high as 20% while operating in a pulsed mode at a duty cycle of a few percent. In 1971, a power conversion efficiency of 7% was determined for a laser at an output power of 120 mw operating at a current density of 5000 A/cm^2 . (Threshold current density was 2000 A/cm^2 .)

A typical output power characteristic curve as a function of temperature is shown in Fig. 3.5 for commercial RCA DH lasers. Because of this heavy dependence of threshold current on temperature, the laser should be operated at some fixed temperature within its operating temperature range. A small thermoelectric heat pump could maintain the laser heat-sink temperature to within a few tenths of a degree over

the expected ambient temperature range.

Peak output powers of 100 - 200 mw have been achieved [60] under CW operation at 300°K. However, reliable operation with lifetimes of the order of 10,000 hours [61] have been reported with output power of only a few milliwatts. Fig. 3.5 indicates that output power of 10 mw can be obtained at drive currents less than 400 ma with some commercial DH laser diodes. Devices with threshold currents less than 150 ma have also been reported [8], which yield 10 mw output power for drive currents less than 200 ma. More recently, stripe-geometry BH lasers have been constructed which exhibit threshold currents that range from 15 ma to 20 ma at 20°C [65]. Light output power of 0.5 mw was obtained with input signals 3 ma above threshold.

(c) Beamwidth

Efficient coupling to optical fibers demands that the source beamwidth be as narrow as possible, preferably within the numerical aperture of the fiber. Beamwidth is inversely proportional to the width of the emitting region [61]. In the plane perpendicular to the junction, a typical full-width half-maximum (FWHM) beamwidth is 30° - 50° [61]; in the plane parallel to the junction, it is usually less than 15° [60] and typically 5° - 10° [61]. The beamwidth has been found to vary slightly with diode topology and internal geometry [61].

One of the disadvantages of the DH laser is that it has a typically broader beamwidth than the SH or homojunction laser due to its narrower active region.

(d) Modulation

One of the merits of laser diodes is that they do not require sophisticated external modulators. They are easily modulated directly by varying the drive current. Most applications reported in the literature involve biasing the laser just below threshold and pulsing the driving current to effect digital modulation. However, the output characteristic of a laser diode, as portrayed in Fig. 3.5 is observed to have a reasonably linear region above threshold, and is thus suitable for direct analog modulation [8,66].

Since the signal-to-noise ratio of an AM channel increases with the modulation depth [66], it would seem desirable to maximize this parameter. There is, however, a certain nonlinearity in the laser's output characteristic [66]. This necessitates that the modulation depth be kept reasonably small, so as to avoid harmonic and intermodulation distortion. The extent of this distortion will probably also vary somewhat with the type of device and operating point. Selection of devices for the radio telescope would then require preliminary testing to determine harmonic distortion levels, unless they are specified by the manufacturer.

The recombination lifetime of the injected carriers is about 2 ns [51] during spontaneous emission (below threshold) and less than 1 ns for stimulated emission (above threshold). Laser diodes are thus capable of being directly modulated at high speed by variation of the injected current. This implies that wide bandwidths are possible with direct analog modulation [66]. The modulation efficiency (modulation depth of the light intensity as a function of modulating frequency) is flat with increasing modulating frequency up to values of

a few tenths of a gigahertz to several gigahertz, where a resonant peak occurs [8,66]. Near this peak, narrow band signals can be modulated with very little energy. Wide band signals must be restricted to the flat portion of the spectrum below this peak to avoid distortion. Above this resonant frequency, the efficiency falls off rapidly. Direct modulation rates up to 800 Mbits/s [67] have been reported in the literature. Some of the newer stripe-geometry BH lasers have predicted modulation capabilities up to 2 GHz [65].

(e) Noise

Laser noise has been the subject of some study [6,68]. Near threshold, the noise level can be considerably higher than that associated with quantum (shot) noise. Just how much higher depends on the signal level and the coherence time of the noise, which in turn, depends on the proximity to threshold. The noise level, for conditions well above threshold, is greatly reduced, in most practical cases, to that of quantum noise. This is borne out by the fact that there is no mention of laser noise contribution in any of the literature describing practical optical fiber systems.

(f) Reliability

Failure in laser diodes has generally been attributed to two basic mechanisms — catastrophic failure and gradual degradation [58,60]. Catastrophic failure is manifested by structural damage to the facets of the optical chamber and is related to the power density within the cavity. Thus, lasers with thin optical cavities, such as DH lasers, are much more prone to this type of failure than SH or SCH

lasers. This mechanism is largely associated with pulsed operation, such as digital modulation.

Lasers operating in the CW mode are primarily subject to gradual degradation [58]. This is characterized by a gradual decrease in quantum efficiency concurrent with an increase in threshold current density [60]. This degradation is believed to be due to metallurgical imperfection density and to the formation of non-radiative recombination centers. Device fabrication and assembly are thus important factors in laser life. Reduced-strain electrical contacts have permitted an increase in lifetime from tens of hours to several thousand hours at room temperatures indicating that stresses and strains are important considerations in device reliability [58]. Stresses can be reduced in DH lasers by the use of $\text{Al}_x\text{Ga}_{1-x}\text{P}_y\text{As}_{1-y}$ heterojunctions. Such lasers have lower room temperature current thresholds and have predicted lifetimes greater than 100,000 hours [58].

In 1975, it was reported [69] that long-life lasers, with output powers between 1 and 20 mw were being tested by RCA and Bell Telephone Laboratories. These devices were promising CW operation of 100,000 hours at room temperature. The Bell devices emit 5 - 10 mw of light at about $0.9\ \mu\text{m}$ with an input power of 0.2 watts. RCA's aluminum-gallium-arsenide lasers emit 20 mw at $0.8\ \mu\text{m}$ with an input power of 0.5 watts. The RCA devices were rated by industry personnel at 50,000 - 100,000 hours of CW operation at room temperature, but RCA researchers were reluctant to claim lifetimes longer than 10,000 hours.

Bell Telephone Laboratories have reported [70] that lasers used in their Chicago lightwave project have accumulated more than 75,000 hours of operating time without incurring a failure in the sense of having zero output. One failed due to an instability which rendered it unusable. An updated report on this project indicated one laser failure out of a total of 120,000 accumulated hours. The mechanism of this failure was not given. Life tests on similar lasers conducted at 70 °C indicate a mean-time-to-failure (MTTF) of 10.5 years for devices operating at 22 °C ambient. Lifetime tests on units manufactured more recently indicate an MTTF of 100 years when operated at 22 °C ambient. This temperature is maintained by the use of a thermoelectric cooler attached to the device.

3.2 Light-Emitting Diodes

Despite the relatively large power output, narrow spectral widths and narrow beamwidths of laser diodes, their relatively low reliability and high cost has served to focus increased attention on light-emitting-diodes (LED's) as sources for optical fiber communication systems [71]. While their performance is otherwise generally inferior to that of laser diodes, LED's are most adequate for many system applications.

3.2.1 General

An LED is essentially a p-n junction diode forward-biased to effect spontaneous radiation as described in ref. [51]. The main difference between an LED and a laser diode is that the LED does not (usually) contain a Fabry-Perot optical cavity. Thus, the radiation is spontaneous, and therefore, incoherent.

Incoherent radiation is characterized by many spatial modes. In order to couple reasonable amounts of power into an optical fiber, then, multimode fibers are required. As will be discussed in the section on coupling, the amount of power I_c coupled into a fiber by a small, incoherent source can be given by [8]

$$I_c = \Lambda \cdot A \cdot \Omega_a \quad (3.3)$$

where Λ is the radiance (brightness) of the source ($\text{W}/\text{sr}\cdot\text{cm}^2$)
 A is the area of emission
 Ω_a is the external solid acceptance angle of the fiber.

This indicates that an important parameter, for efficient coupling, is the radiance, or brightness, of the source.

Another important parameter is the beamwidth. Since an optical fiber can accept only radiation that falls within its numerical aperture, radiation at larger angles is absorbed into the cladding. Incoherent radiation, as a result of spontaneous carrier recombination, is essentially omnidirectional [51]. Although the radiation pattern is modified somewhat by the internal geometry and structure of the device [6], only a small portion of the radiation from an LED can be coupled into a fiber.

LED's are designed to minimize internal absorption, allow high operating current densities and maximize coupling efficiency into fibers [61]. Two types of structure are generally used — surface-emitters and edge-emitters.

(a) Surface-Emitters

Burrus [72] has developed LED's specifically for optical fiber communications purposes in which the coupled radiation is obtained from the direction normal to the plane of the p-n junction. A "well" is etched through the substrate to accommodate a fiber, which is then butted against the junction and cemented into place with epoxy. The junction's linear dimensions are made to be of the same order of magnitude as the diameter of the fiber core. The recombination region is placed adjacent to a heat sink to allow high operating current densities. A typical Burrus-type surface-emitting LED is shown in Fig. 3.6.

(b) Edge-Emitters

Edge-emitter LED's utilize heterojunction structures similar to laser diodes [61] as shown in Fig. 3.1. The heterojunctions provide a certain measure of internal waveguiding of the spontaneous emission. This tends to modify the radiation pattern [6], improving its directionality in the plane perpendicular to the junction. Like the stripe-geometry laser diodes, the lateral width of the emitting region is adjusted to match the fiber dimensions ($\sim 50\text{-}100\text{ }\mu\text{m}$) [61].

A modified structure, termed a "restricted edge-emitting diode" or REED, has recently been developed [73]. This device is basically an LOC laser operated in the spontaneous mode. Since the output power is found to decrease with increased diode length (due to internal reabsorption of the emitted radiation), increased power and efficiency result from diodes that are constructed with the active area restricted, as much as possible, to the radiant edge.

3.2.2 LED Performance

(a) Radiance and Current Density

Early homostructure surface-emitting (Burrus) devices yielded radiance values over 100 W/sr/cm^2 , as indicated in Table 3.1 [74]. It is seen that the radiance is a relatively linear function of current density and inversely proportional to the active area. Since the largest radiant intensity (product of emitting area and radiance) was obtained with diodes having a diameter of $50 \mu\text{m}$, this was determined to be optimum. A comparison of diffused (homostructure), SH and DH diodes was made [74] with active diameters of $50 \mu\text{m}$ and is presented in Table 3.2. The increased efficiency of the SH and DH devices is apparent.

An edge-emitting LED was reported in 1971 having a radiance of 25 W/sr/cm^2 at 600 ma for an active area of $7 \times 10^{-4} \text{ cm}^2$ [8]. For purpose of comparison, the radiance of a number of commercially-available LED's (Monsanto MV-50, HP 5082-4400, GE SSL-22, BTL Zn91203, TI TIL-23) was measured [74] at the manufacturer's maximum rated current. Using emitting-area values estimated visually, the radiance values ranged between 0.01 and 0.26 W/sr/cm^2 at current densities of $6 - 25 \text{ A/cm}^2$. These are some two to four orders of magnitude lower than the surface-emitters described in Table 3.2, which were designed specifically for fiber communications.

In 1976, RCA Laboratories reported the development of high-radiance LED's [75]. These devices are edge-emitters and feature a narrow active region. The radiance of these devices has been increased to over $1000 \text{ W/cm}^2\text{.sr}$.

Table 3.1
Effect of Area on Radiance

Contact Diameter (μm)	Contact Area (cm^2)	Drive Current * (mA)	Current Density (kA/cm^2)	Radiance ($\text{W}/\text{sr}/\text{cm}^2$)
13	0.13×10^{-5}	100	75	80 - 117
25	0.49×10^{-5}	150	30	27 - 46
50	1.96×10^{-5}	300	15	16 - 30
100	7.85×10^{-5}	300	1.75	4 - 7

* Drive current $\approx 2/3$ x saturation current

Table 3.2
Comparison of Absolute Radiance Values For Three Types of Diodes

Diode Type	Contact Diameter (μm)	Contact Area (cm^2)	Drive Current * (mA)	Current Density (kA/cm^2)	Radiance ($\text{W}/\text{sr}/\text{cm}^2$)
Homostructure	50	1.96×10^{-5}	300	15	30 - 40
Single-heterostructure	50	1.96×10^{-5}	200	10	55 - 70
Double-heterostructure	50	1.96×10^{-5}	150	7.5	60 - 100

* Drive current $\approx 2/3$ saturation current

It is interesting to compare the radiance of an LED with that of a laser. An LED with an efficiency of 1%, operating at a current density of 5 A/cm^2 with an applied voltage of 2 V will have a radiance of approximately 0.01 W/sr/cm^2 [51]. Increasing the current density to 5000 A/cm^2 , the radiance would be about 10 W/sr/cm^2 . A laser, operating at a current density of 5000 A/cm^2 with a junction area of 10^{-2} cm^2 would emit 10 watts from a source area of $0.1 \text{ cm} \times 2 \text{ }\mu\text{m}$ into a solid angle of about 0.25 sr. This is equivalent to a radiance of about $2 \times 10^6 \text{ W/sr/cm}^2$.

Of course, radiance is not an indication of total power output I_t which is the product of radiance Λ , emitting area A and radiating solid angle Ω_r , or

$$I_t = \Lambda \cdot A \cdot \Omega_r \quad (3.4)$$

For optical fiber communications purposes, the amount of power that can be coupled into the fiber is more important than total power output. In this respect, if an LED has a higher total power, but a lower radiant intensity (product of emitting area and radiance) per unit solid angle than a laser diode, it will not couple as much power into the fiber as the laser will. Coupling efficiencies and techniques will be discussed further in section 5.0.

(b) Efficiency and Power

While internal quantum efficiency for an LED may approach 100% at cryogenic temperatures, it is around 50% at room temperatures [51]. However, the external quantum efficiency is

limited by internal reabsorption of the emitted radiation. This radiation spans a broad spectral range (about 40 nm) and is virtually omnidirectional. Typical external quantum efficiency is less than 10%, with the remaining 90% being dissipated as heat [19], which must be removed to prevent damage to the device.

Efficiency is also highest at high drive currents up to, say, 100 mA [76]. Lowering the current to 10 mA reduces the efficiency to about 65% (of what it was at 100 mA) and at 1 mA it drops to about 20%. The tradeoff is reliability. A rule of thumb is that the failure rate jumps an order of magnitude for each doubling of the drive current [76].

Surface-emitter and edge-emitter diodes provide several milliwatts of power in the 0.8 - 0.9 μm spectral range at drive currents of 100 - 200 mA (2000 - 4000 A/cm^2) and at modulating frequencies of 100 - 200 MHz [61]. In the 1.0 - 1.1 μm range, surface-emitting diodes have yielded about 1 mW of output power for devices with InGaAs structures [77].

A typical characteristic of output power as a function of drive current for an LED will look like Fig. 3.7, which is seen to be of the same form as Fig. J.4. Actual power/current values will vary with the radiance and type of device. The values shown in Fig. 3.7 are representative of a Burrus-type surface-emitter with a radiance of about 60 $\text{W}/\text{sr}/\text{cm}^2$ emitting from a surface of diameter 50 μm into a cone of about 130° or 3.62 sr [74,78]. Overall power efficiency is about 1 - 2%.

The output characteristic of a typical edge-emitter is shown in Fig. 3.8 along with that of a REED device to emphasize its higher efficiency.

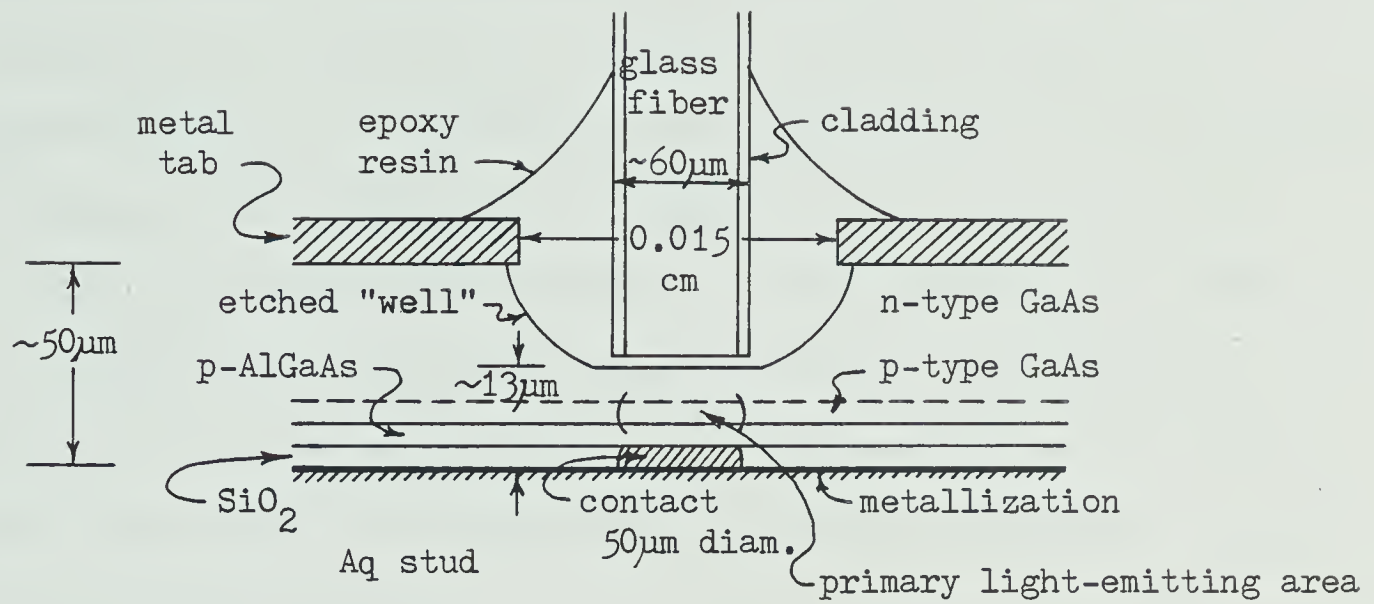


Fig. 3.6 Cross-section of surface-emitting LED (After Burrus and Ulmer [72]).

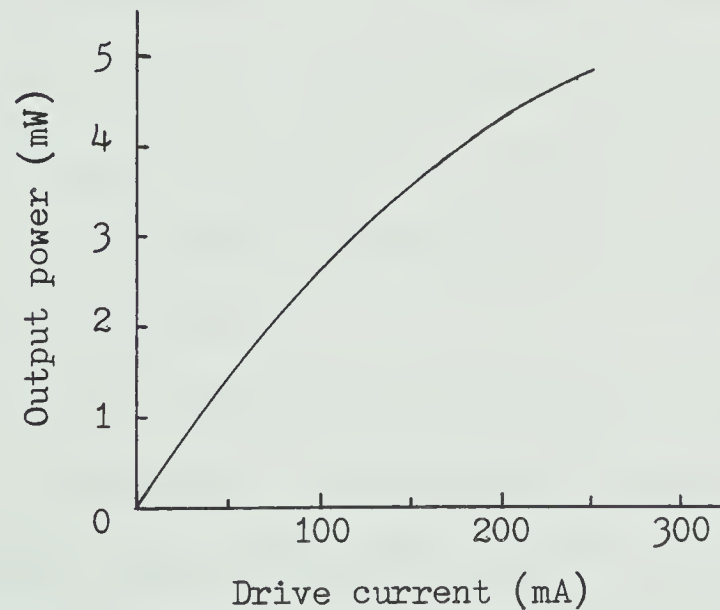


Fig. 3.7 Output characteristic for Burrus-type surface-emitting LED (After Barnoski [78]).

Due to their small emitting area and improved directionality, edge-emitters are generally more efficient at coupling to fibers than surface-emitters. Typical coupling loss into a step-index fiber with a numerical aperture of 0.14 is about 17 - 20 dB for (Lambertian) surface-emitters, 12 - 16 dB for edge-emitters and 3 dB for lasers [61]. RCA's edge-emitters [75] have demonstrated coupling losses of only 9 - 11 dB since they have a relatively narrow beamwidth ($\sim 25^\circ$ FWHM) and the fibers had a microlens formed on the end. Coupling will be discussed in more detail in chapter 5. Edge-emitters, with somewhat lower output power, can couple power into a fiber comparable to that of some surface-emitters.

(c) Modulation

In a recent paper, Lee [79] has indicated that the risetime of an LED decreases as junction capacitance decreases. For a GaAs diode, the risetime was about 5.5 ns for a junction capacitance of 200 pF and 3.5 ns for 20 pF. The risetime was also found to decrease with increased driving current density. It was also reported that higher modulation rates (digital) were achieved by lowering the driving circuit output impedance.

The lower limit on risetime is set by the chromatic delay of the device [80]. In general, it is found that shorter wavelengths are delayed more than longer wavelengths when the device is modulated. For a typical LED with a spectral width of 40 nm, this chromatic delay is about 200 - 300 ps within the half-power points of the LED spectrum. This delay, although small, is an internal or intrinsic type of dispersion.

Light-emitting diodes typically have risetimes of about 5 ns or less, indicating modulation frequencies in the hundreds of megahertz. The Burrus-type surface-emitters have exhibited [81] risetimes of 4-6 ns for homostructures, 8-11 ns for SH and 10-12 ns for DH diodes in a 50 ohm circuit. All three structures had risetimes of about 1 ns when the modulation source impedance was 2-4 ohms, which approximately matched the diodes' internal impedance.

While many state-of-the-art LED's have been modulated at frequencies up to about 200 MHz (-3 dB point) [6,8,61,63], many have lower limits. Modulation efficiency was measured by Burrus et al [82] with surface-emitting LED's. It was found that the -3 dB point occurred at about 40 MHz for homojunction GaAs devices, 36 MHz for SH AlGaAs devices and 30 MHz for DH AlGaAs devices. The Plessey Company has developed high-radiance GaAs [63] and InGaAs [83,84] surface-emitters for optical fiber communications. The GaAs diodes emit at about 0.9 μm and the InGaAs diodes emit at 1.06 μm . A plot of the modulation characteristic shown in Fig. 3.9 indicates constant modulation response to almost 500 MHz with suitable doping for GaAs devices. InGaAs diodes reveal 3 dB modulation bandwidths of about 150 MHz, with capability up to 250 MHz. The edge-emitting REED devices introduced by Kressel and Ettenberg [73] had modulation capability of 50 - 60 MHz (at -3 dB point). The more recent edge-emitters developed by RCA Laboratories [75] have exhibited modulation at frequencies greater than 150 MHz.

While laser diodes are capable of much higher modulating frequencies than LED's, it seems apparent that the modulation performance of LED's would be more than satisfactory for the radio

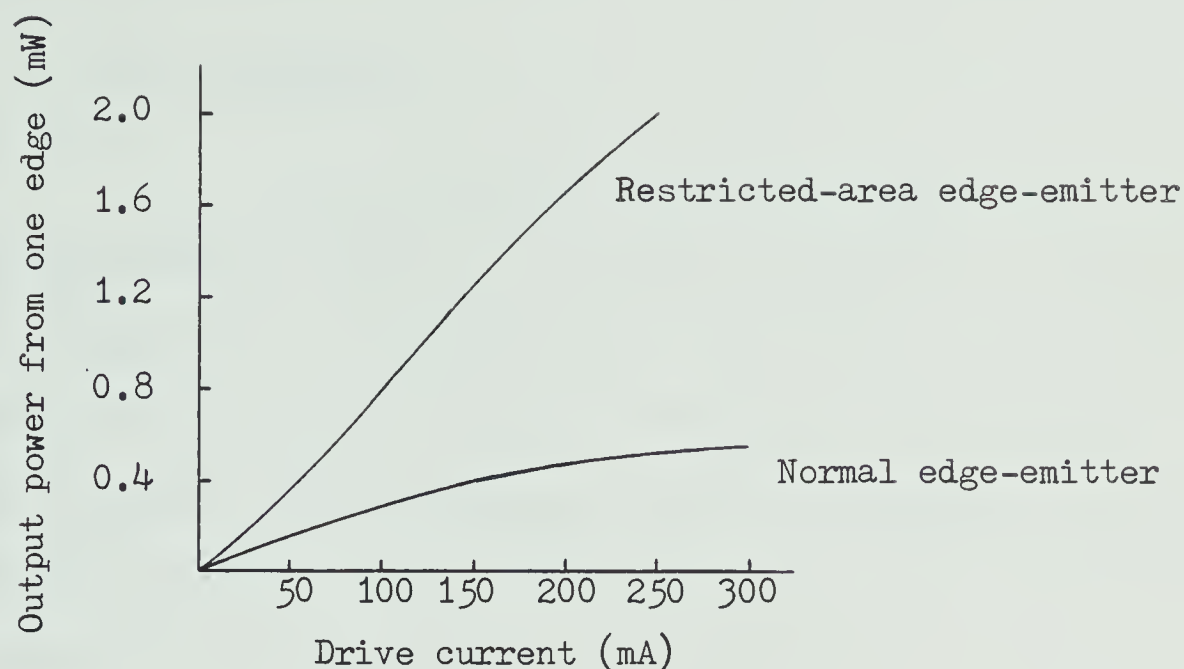


Fig. 3.8 Power emitted as a function of drive current for a normal and a restricted edge-emitting LED (After Kressel and Ettenberg [73]).

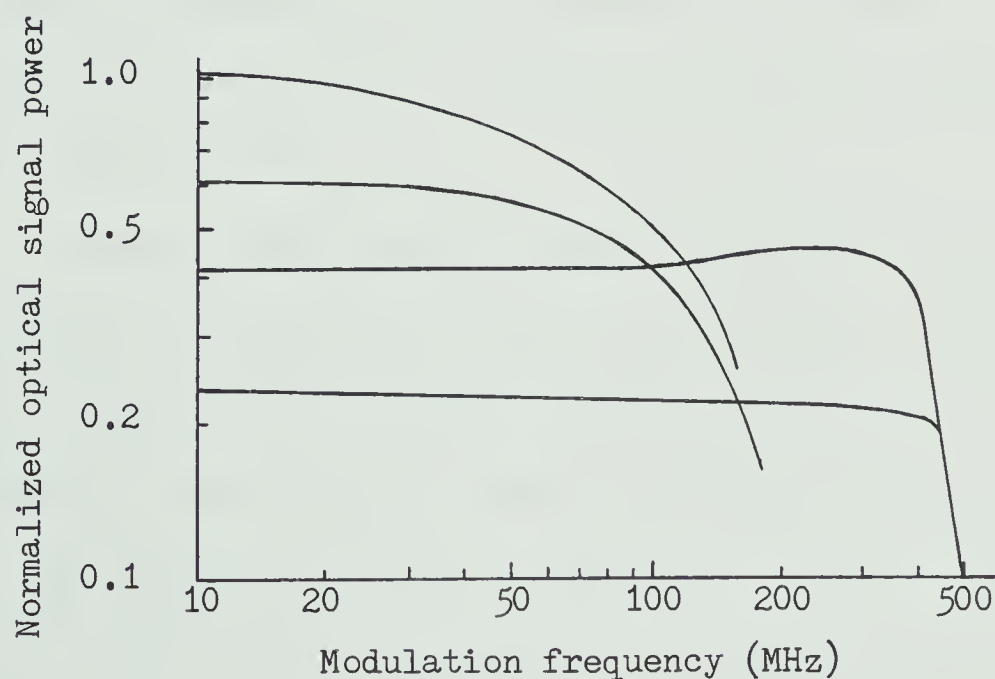


Fig. 3.9 Modulation characteristics of highly-doped GaAs and InGaAs high-radiance diodes (After Goodfellow and Mabbitt [63]).

telescope transmission system.

(d) Linearity

The relationship between the output power and the driving current for LED's is relatively linear over a large range [8]. This allows direct analog modulation to be easily accomplished. The extent of the linearity (or, more accurately, the nonlinearity) is very important and would probably require measurement to determine the levels of distortion. Variations in the output characteristic from unit to unit may require some control.

LED's have been tested for nonlinear distortion in various broadband analog systems (see Appendix F). Studio-quality video has been demonstrated over optical fiber links indicating good LED linearity performance, depending on modulation index. By reducing modulation index, distortion levels of -50 dB and lower can be attained. Since harmonic distortion in LED's appears to increase with increasing temperature (see Appendix F), a relatively cool and constant temperature should be advantageous.

A technique was recently reported [83] for extending the linear range of an LED by the use of a shunt diode. Increases in relative optical output of 20% to 60% was indicated. This was accomplished, however, at the expense of additional driving current.

The linearity of photodiodes appears to be excellent. Since the second- and third-harmonic distortion is expected to be approximately proportional to the square and cube of the fundamental, respectively, photodiodes operating with relatively low incident optical powers should exhibit virtually negligible distortion.

(e) Noise

The minimum noise generated by an LED will be quantum noise, or shot noise [68] associated with carrier recombination. Lee & Burrus [84] found that the noise in a photodetector illuminated by an LED exceeded the quantum noise contributed by the photodetector itself by a factor that decreased roughly as the reciprocal of the modulating frequency. Quantum noise was dominant at frequencies above about 100 KHz and, in the better diodes, about 10 KHz. Lee & Burrus concluded that much of the excess noise was due to contacts and could be reduced or eliminated by improved fabrication. Since their measurements were made at a current level of 150 μ A in the photodetector, the lower current levels expected with LED's in fiber communication systems should render the additional $1/f$ noise negligible at even lower frequencies.

(f) Reliability

Since LED's are basically laser diodes without the optical cavity, the failure mechanism is essentially the same as the gradual degradation of the lasers. The surface-emitter diodes developed by Burrus & Miller [81] are capable of operating lifetimes to half-power of about 10,000 hours at a drive current of 150 ma and a current density of 7500 A/cm². In 1973 the Plessey Company [71] had built diodes with a projected half-power life of 15,000 hours starting at 500 μ W output, and showing less than 1% degradation in power over 1000 hours. In 1976 a lot of AlGaAs LEDs maintained constant power output to within 5% in 14,000 hours of operation [61].

In 1977, it was reported [85] that LED's had been operating at bias levels of 10^4 A/cm² and that power degradation was less than 5% after 20,000 hours. Temperature-accelerated aging tests on these devices have led to predictions of 10^7 hours of continuous operation at room temperature.

3.3 Summary

Both laser diodes and light-emitting diodes appear to be satisfactory optical sources for the proposed transmission system. While laser diodes offer superior technical performance to LED's, LED's have reliability and cost advantages over laser diodes. For the near future, it is expected that these advantages would demand the use of LED's for the feeder system. Serious consideration for using laser diodes in the feeder system of the proposed radio telescope system will require good device reliability and a reasonably attractive cost. Judging by the development of semiconductor devices in general over the past few years, there is good reason for such optimism. It has been forecast [86] that current prices of about \$1000 for some lasers will drop to below \$20 and possibly to below \$10 by 1988.

CHAPTER 4

PHOTODETECTORS

4.1 General

Optical radiation is converted into electrical signals by photodetectors. These are square-law devices that respond to the intensity of the incoming radiation averaged over a few optical cycles [87]. Performance requirements of photodetectors for use in optical fiber transmission systems include [8]: high response or sensitivity at the wavelength of the source; sufficient bandwidth or speed of response to accommodate the required information rate; minimum additional noise introduced by the detector; low susceptibility of performance characteristics to changes in ambient conditions.

Photodetectors are classified into three general types -- photoemitters, photoconductors and photovoltaic devices. Photoemitters are principally vacuum photodiodes, gas-filled phototubes and photomultipliers. These devices utilize an external photoelectric effect, in which electrons are emitted into a vacuum or gas from a material which has absorbed optical radiation. While time constants involved are adequate to permit modulation into the microwave frequencies, quantum efficiency is low, typically about 30 - 40% as an upper limit [87]. Increased sensitivity can be obtained with photomultiplier tubes, but these are bulky, expensive and require elaborate high-voltage power supplies. In view of these limitations, photoemitters will not be considered further. Photoconductors are bulk

semiconductor devices whose conductivity varies with the generation of hole-electron pairs due to the absorption of optical radiation. These devices are largely limited to infrared wavelength ($> 1 \mu\text{m}$) operation and require near-cryogenic cooling [87, 88]. These devices are not considered suitable for optical fiber communications purposes. Photovoltaic detectors are basically semiconductor devices with a p-n junction (usually reverse-biased) across which photon-generated electrons and holes diffuse to be collected as photocurrent [87]. These devices include p-n junction photocells, p-n-p phototransistors, avalanche photodiodes, p-i-n photodiodes and Schottky-barrier devices [88]. The most promising devices for optical-fiber transmission systems currently are p-i-n photodiodes and avalanche photodiodes. Some of the attributes of photodiodes are small size, ruggedness, simplicity, high response speeds and low cost. Photodiodes will be considered further below.

4.2 Photodiodes

(a) Materials

For operation within the band of interest for optical fiber communications, three semiconductor materials are currently used — silicon, germanium or gallium arsenide [8]. Silicon is generally used from about $0.4 - 1.0 \mu\text{m}$ wavelengths due largely to its highly developed technology and also to its relatively low dark current (this will be described later). Gallium arsenide is useful only to $0.9 \mu\text{m}$, whereas germanium can be used to beyond $1.5 \mu\text{m}$. Due to the narrow bandgap, germanium diodes exhibit larger dark currents than silicon diodes, which results in higher noise levels.

(b) Non-avalanche Photodiodes

The most efficient photodiodes are those with a p-i-n structure as shown in Fig. 4.1. These diodes are seen to be comprised of heavily doped p and n regions separated by a layer of intrinsic material. Under reverse-biased conditions, an electric field is set up within the intrinsic region which becomes the depletion region. At the shorter wavelengths of operation, this region can be quite narrow and it is not particularly difficult to obtain good efficiency and also fast rise times for wide bandwidth operation. However, at the longer wavelengths, the light penetrates deeply into the material, requiring wider depletion regions [8, 87] for good efficiency. Since this results in increased carrier transit times, there is a tradeoff between quantum efficiency and speed of response (or bandwidth). Some compromise between these two is realized if the light is allowed to enter the depletion region from the side as shown in Fig. 4.1 (b).

(c) Avalanche Photodiodes

If the reverse-bias of a photodiode is increased to a point just below the avalanche or breakdown voltage, a considerable increase in sensitivity is achieved. This is because the electron-hole pairs created by the absorption of optical radiation create new electron-hole pairs through impact ionization [8, 87]. This gain mechanism is a function of the bias voltage, reaching a maximum at the breakdown voltage.

Cross-sections of typical front and side-illuminated silicon avalanche photodiodes are shown in Fig. 4.2.

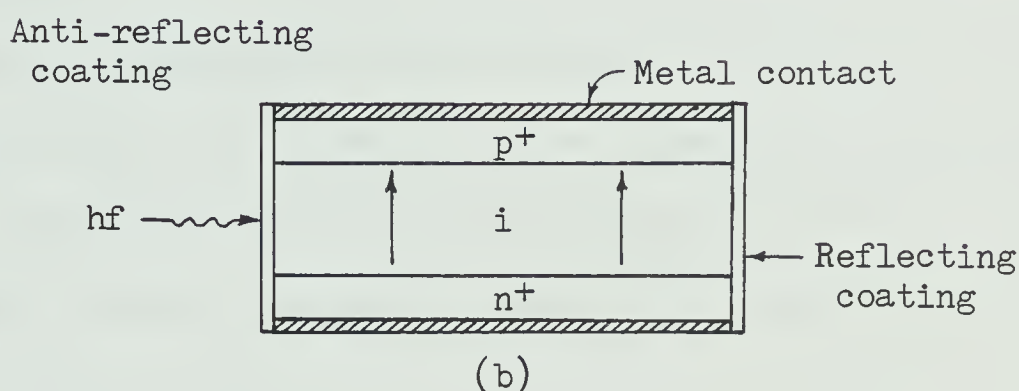
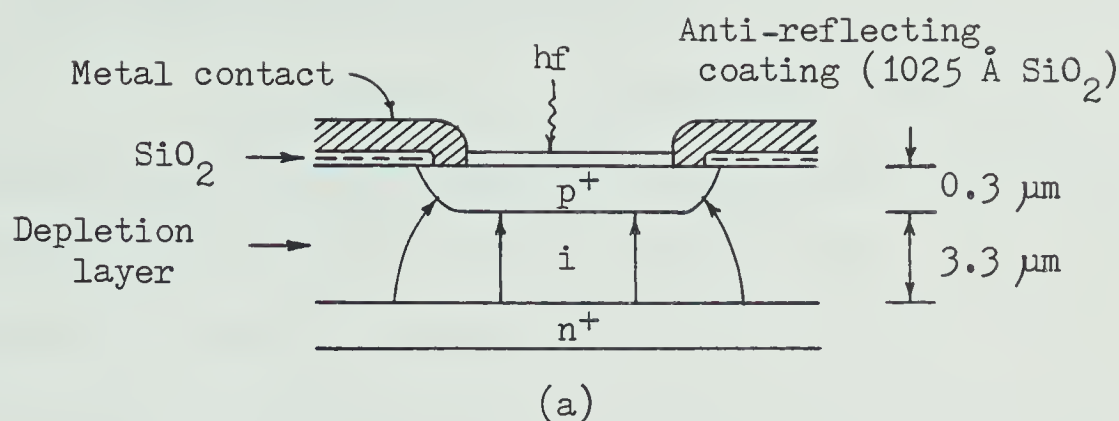


Fig. 4.1 Construction of nonavalanching p-i-n photodiodes (a) Front-illuminated silicon photodiode optimized for $\lambda = 0.633 \mu\text{m}$ (b) Side-illuminated silicon photodiode (After Miller, Li and Marcatili [8]).

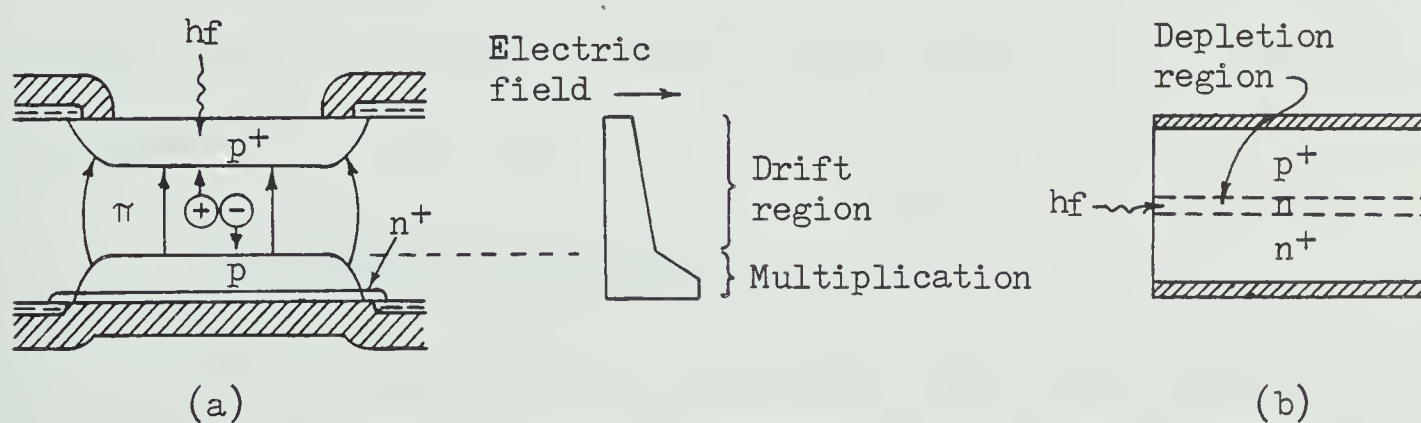


Fig. 4.2 Construction of avalanche photodiodes (a) Front-illuminated silicon avalanche photodiode - electric fields in the drift and multiplication regions are also shown (b) Side-illuminated silicon avalanche photodiode (After Miller, Li and Marcatili [8]).

(d) Responsivity and Efficiency

Responsivity is a measure of the sensitivity of the photodetector and is the ratio of output current or voltage to the incident optical flux in watts or lumens [88]. The spectral responsivity is simply the responsivity as a function of wavelength. Typical curves are shown in Fig. 4.3 for silicon and germanium photodetectors.

Quantum efficiency of p-i-n silicon photodiodes is typically greater than 85% [8, 87], while for p-i-n germanium photodiodes, it is around 60% (measured at the peak responsivity) [87]. The relationship between quantum efficiency $\eta(\lambda)$ and spectral responsivity $\rho(\lambda)$ is given by [88]

$$\eta(\lambda) = \frac{1.23985 \times 10^{-6} \rho(\lambda)}{\lambda} \quad (4.1)$$

Often, in the case of devices with internal gain (ie: photo-multipliers, avalanche photodiodes), the responsivity includes the gain, so it is necessary to note this when examining or using such devices.

(e) Risetime and Bandwidth

The speed of response of a solid-state photodetector to incident light is governed ultimately by the time it takes for the generated electrons and holes to be collected in the diode [88]. This is a function of the RC time constant of the diode and input amplifier circuitry.

The a.c. equivalent circuit of a photodiode is shown in Fig. 4.4 and consists of a photocurrent generator i_{ph} , diode junction capacitance C_j , series resistance R_s and shunt resistance R_j .

The risetime t_r will be about [89]

$$t_r = \frac{1}{3B} \quad (4.2)$$

where B is the 3 dB bandwidth of the diode, and

$$B = \frac{1}{2\pi(R_i + R_s)(C_j + C_i + C_{stray})} \quad (4.3)$$

where R_i is the amplifier input resistance
 R_s is the diode series resistance
 C_j is the diode junction capacitance
 C_i is the amplifier input capacitance
 C_{stray} is additional stray capacitance

Response time is generally determined with a load resistance R_i of 50 ohms and subnanosecond values are not uncommon [8] with diode capacitances in the order of 1 pF. This suggests bandwidths in the order of hundreds of megahertz. In the case of avalanche photodiodes, response times are in the same order of magnitude as for non-avalanching diodes and gain-bandwidth products are reported in the 20 - 100 GHz range [8, 87]. The maximum achievable gain is determined by the gain-bandwidth product at high modulating frequencies [87]. Although stable gain has been achieved up to values of 10^4 at room temperature (in silicon diodes)[87], typical values are in the order of 200 - 500 [89].

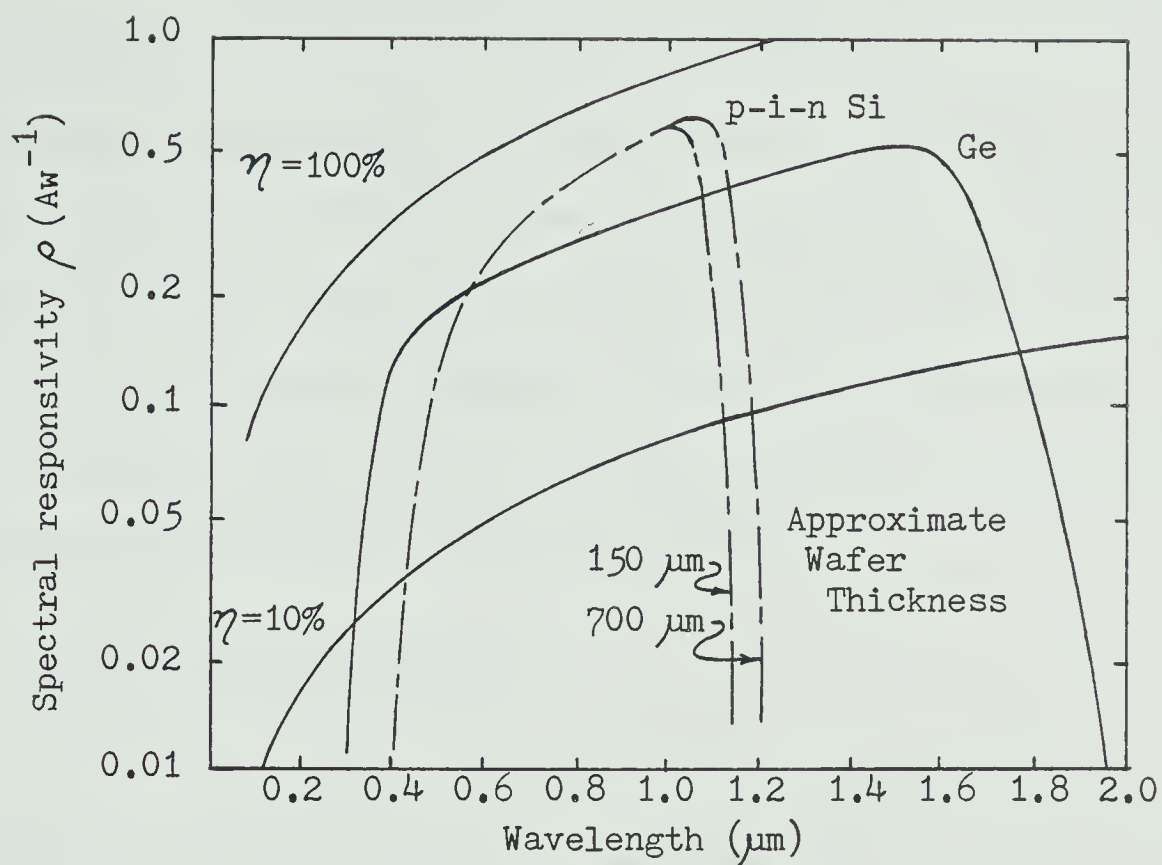


Fig. 4.3 Spectral response of p-i-n silicon and germanium photo-detectors (After RCA Handbook [88]).

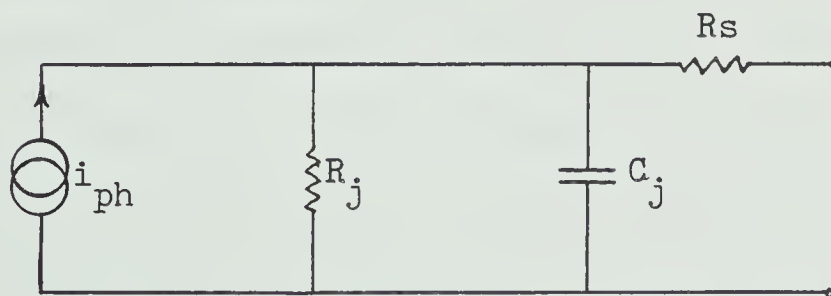


Fig. 4.4 Equivalent circuit of a photodiode (After Melchior, Fisher and Arams [87]).

(f) Temperature Stability

With the exception of avalanche photodiodes, whose avalanche point varies as a function of temperature [59], the performance characteristics of solid-state photodetectors are not greatly susceptible to variations in ambient conditions [8]. The optical detector circuits will be located in the observatory building and in remote equipment housings. Unless adequate temperature control is provided for these circuits, non-avalanching photodiodes may be the only feasible devices that can be used.

(g) Noise Performance

The noise performance of any detection system is dependent on the detection method employed. This can incorporate either direct, heterodyne or homodyne detection [90]. A direct detection system receives the transmitted signal directly and produces an output signal proportional to the intensity of the transmitted signal averaged over a few carrier cycles [90]. In a heterodyne detection system, the received signal is mixed with a local oscillator signal to produce an intermediate frequency (IF) signal which carries the modulation information. This IF signal is filtered to remove unwanted mixing products and then is fed to the detector which produces an output signal proportional to the square of the sum of the electric fields of the received signal and the local oscillator signal [90]. A homodyne detection system differs from a heterodyne system only in that the local oscillator is of the same frequency as the carrier. Instead of an IF signal resulting from the mixing process, the modulation information is now available at baseband [90].

Heterodyne and homodyne detection systems require that the transmitted carrier which undergoes modulation be a single frequency. This would necessitate the use of lasers which offer a high degree of monochromaticity and would preclude the possibility of using LED's as transmitting sources. The very small optical wavelengths present a problem in maintaining uniform phase between the local oscillator and the received signal across the surface of the photomixer. Ross [91] has indicated that, if this phase nonuniformity is present, beat currents at one part of the surface will be out of phase with beat currents at another part, resulting in signal loss. Any corruption of the wavefront during its passage through the transmission medium will add to the difficulty of performing heterodyne (or homodyne) detection. No practical systems involving heterodyne or homodyne detection at optical frequencies have been built so far as is known.

In view of the foregoing, it is evident that the difficulty, additional complexity and cost of utilizing heterodyne or homodyne detection systems appears to preclude their consideration for the proposed telescope system. The following noise considerations will then be based on the use of a direct detection system. The receiver is assumed to begin with an avalanche photodiode with quantum efficiency η and avalanche current gain G . This photodiode is followed by a baseband amplifier which presents a load resistance R to the photodiode and which has a noise figure F_a . The various noise components in a photodetector and the signal-to-noise ratios for each component are discussed in Appendix G.

The signal-to-noise ratio for each individual noise component will now be calculated and plotted for an analog transmission system having a bandwidth of 50 MHz, such as could be the case for the proposed radio telescope. Determining the SNR performance on a per-component basis aids in appreciating the relative effect of each on the total. The total signal-to-noise ratio is simply determined by adding the various SNR components on a reciprocal power basis.

Assuming the use of a low-noise p-i-n photodiode, such as a United Detector Technology PIN-020, typical parameters would be $i_D = 100$ pA and $i_L = 50$ pA. At a wavelength of $0.8 \mu\text{m}$, peak responsivity is 0.42 amp/watt, which corresponds to a quantum efficiency of 65% according to eq.(4.1). A modulation index of 100% is assumed for simplicity of calculation, as is an input amplifier noise figure of 10 dB. If the source is an LED having spectral width of about 40 nm ($\delta f \simeq 20 \times 10^{12}$ Hz), and the number of spatial modes Y reaching the detector is at least 5, $Y\delta f$ will be at least 10^{14} . When these parameters are substituted into equations (M.2) to (M.8), the following results:

$$\langle i_s^2 \rangle = 1/2 \left[\eta \frac{e}{hf} G m p_o \right]^2 = 0.0878 p_o^2 G^2 \quad (4.4)$$

$$\langle i_Q^2 \rangle = 2e \frac{e}{hf} \eta p_o G^2 F_d B = 6.72 \times 10^{-12} p_o G^{2.5} \quad (4.5)$$

$$\langle i_T^2 \rangle = 4 \frac{kT}{R} B F_a = \frac{8.08 \times 10^{-12}}{R} \quad (4.6)$$

$$\langle i_D^2 \rangle = 2e i_d G^2 F_d B = 1.6 \times 10^{-21} G^{2.5} \quad (4.7)$$

$$\langle i_L^2 \rangle = 2ei_L B = 8 \times 10^{-22} \quad (4.8)$$

$$\langle i_B^2 \rangle = 2 \left[\frac{e}{hf} G \eta p_o \right]^2 \frac{B}{Y \delta f} \left[1 - 1/2 \frac{B}{\delta f} \right] \cong 1.76 \times 10^{-7} G^2 p_o^2 \quad (4.9)$$

The signal-to-noise ratio for each noise component follows directly.

$$\begin{aligned} [SNR]_Q &= \langle i_s^2 \rangle / \langle i_Q^2 \rangle = 1.31 \times 10^{10} p_o / \sqrt{G} \\ &= 101.2 + 10 \log p_o - 5 \log G \\ &= 71.2 + p_o(\text{dBm}) - 5 \log G \end{aligned} \quad (4.10)$$

$$\begin{aligned} [SNR]_T &= \langle i_s^2 \rangle / \langle i_T^2 \rangle = 1.09 \times 10^{10} p_o^2 G^2 R \\ &= 100.4 + 20 \log p_o + 20 \log G + 10 \log R \\ &= 40.4 + 2 p_o(\text{dBm}) + 10 \log R + 20 \log G \end{aligned} \quad (4.11)$$

$$\begin{aligned} [SNR]_D &= \langle i_s^2 \rangle / \langle i_D^2 \rangle = 5.49 \times 10^{19} p_o^2 / \sqrt{G} \\ &= 197.4 + 20 \log p_o - 5 \log G \\ &= 137.4 + 2 p_o(\text{dBm}) - 5 \log G \end{aligned} \quad (4.12)$$

$$[SNR]_L = \langle i_s^2 \rangle / \langle i_L^2 \rangle = 1.10 \times 10^{20} p_o^2 G^2$$

$$\begin{aligned}
&= 200.4 + 20 \log p_o + 20 \log G \\
&= 140.4 + 2 p_o(\text{dBm}) + 20 \log G \quad (4.13)
\end{aligned}$$

$$[\text{SNR}]_B = \langle i_s^2 \rangle / \langle i_B^2 \rangle = 5 \times 10^5 = 57 \text{ dB} \quad (4.14)$$

These results are plotted in Fig. 4.5 for a non-avalanching photodetector ($G = 1$). It can be seen that the maximum signal-to-noise ratio is limited by the beat noise, in this case 57 dB. This was determined on the basis of the number of spatial modes Y being 5. Hubbard [92] indicates that Y could be as high as 5000 using GaAs LED's and multimode fibers. (This is consistent with the example on page 22 of Chapter 2.) This would result in a signal-to-beat noise ratio $[\text{SNR}]_B$ of 87 dB instead of 57 dB.

Assuming that an $[\text{SNR}]_B$ of 57 dB represents a worst-case condition, it is apparent that the system is then limited by thermal and quantum noise. The leakage and dark currents have virtually no effect whatever — at least, not until the input resistance is in the hundreds of megohms range. Using a value of R of 1 megohm, the system is seen to be quantum-noise limited for input signals down to around -25 dBm, where thermal-noise begins to affect the performance. From around -35 dBm and down, the system is thermal-noise limited. With 1 megohm input resistance, the input power must be greater than -50 dBm in order to have a positive signal-to-noise ratio, which may or may not be significant in itself. This will be discussed in chapter 7.

The situation is seen to change dramatically when avalanche gain is introduced. Fig. 4.6 portrays the performance of the previous system example when a gain of 10 is used in eqs. (4.10)-(4.13). The

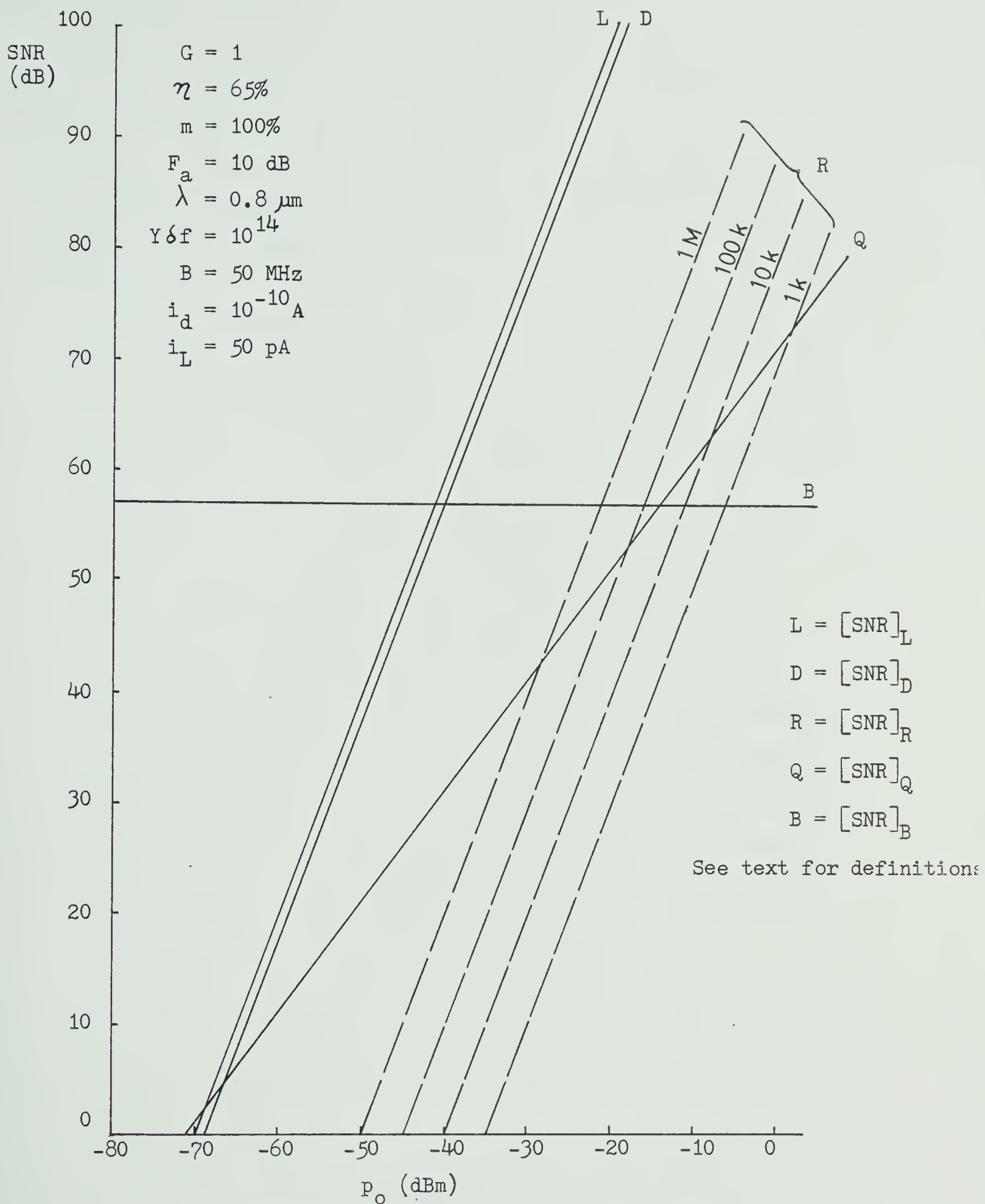


Fig. 4.5 Signal-to-component noise ratio versus incident power for a photodetector with unity gain

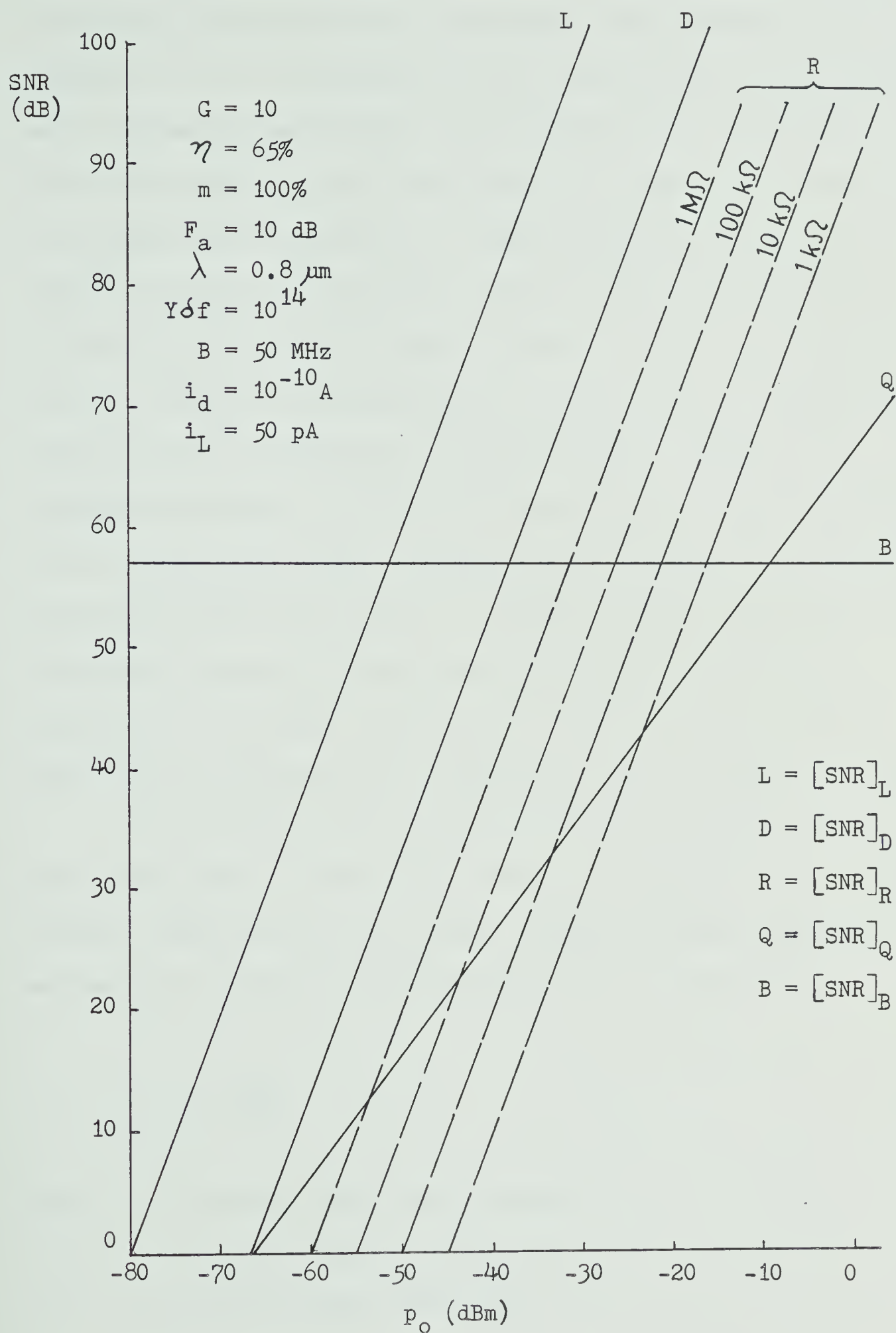


Fig. 4.6 Signal-to-component noise ratio versus incident power for a photodetector with a gain of 10.

quantum and dark-current noise performance components are seen to be degraded by 5 dB over the previous case with no gain. On the other hand, the leakage and thermal-noise performance has been improved by 20 dB. Using again an input resistance of 1 megohm, the system is now quantum-noise limited down to about -50 dBm, at which point thermal- and dark-current effects begin to enter. This system is now able to yield positive signal-to-noise ratios for inputs as low as about -60 dBm, so an improvement of some 10 dB in "threshold" has resulted from the application of avalanche gain. However, an examination of Figs. 4.5 and 4.6 will reveal that any additional gain will not result in further lowering of this "threshold" due to increasing quantum and dark-current noise. It becomes apparent, then, that for each value of input resistance and incident power, there is an optimum gain below which thermal noise effects limit the SNR and above which the quantum noise performance begins to degrade the SNR.

The advantage of using large photodiode load resistances is obvious from Figs. 4.5 and 4.6 to obtain high signal-to-noise ratios. However, consideration of the signal bandwidth suggests that this resistance be limited by the capacitance C to a value [92.],

$$R > \frac{1}{4CB} \quad (4.15)$$

where R is the diode load resistance
 C is the total load capacitance
 B is the signal bandwidth.

In studies on digital optical receivers, Personick [93] and Goell [94] have deplored this practice since it results in increased noise

at the receiver input. They suggest (and also Hubbard [92] is quick to point out) that larger values of load resistance can be used to improve the noise performance at the input, with the resulting bandwidth distortion being improved at a later stage with equalization.

Assuming a system with a bandwidth of 50 MHz and a total input capacitance of 5 pF, such as might be obtained with a United Detector Technology PIN-020A photodiode and an RCA CA3040 video amplifier, eq.(4.15) implies a maximum load resistance of 4k ohms. This system, while not utilizing any avalanche gain, can still accept signals (for positive SNR) down to ~ -38 dBm from Fig. 4.5. It is also apparent, however, that the system is thermal-noise limited from about -10 dBm and down and, therefore, is not optimum. It is clear that the system can be improved either with avalanche gain or by increasing the load resistance. An increase to 40k ohms would provide an improvement in SNR of up to 10 dB (depending on the input power) and in "threshold" of 5 dB. The advantages to be gained by using this technique would have to be weighed against the feasibility, economics and the increase in noise of the necessary equalization circuitry. This subject is discussed further in ref.[95].

An alternate method, which would allow the preferred larger values of load resistance, while adhering to the conditions of eq.(4.15) would be the use of positive feedback or bootstrapping. This technique can be used to neutralize the total capacitance at the input of the amplifier [96]. Since little use has been made of this idea, nothing more will be said at this time.

(h) Linearity

Nonlinear distortion in photodiodes appears to be sufficiently low as to allow the feasibility of high-quality analog transmission systems. Test results on p-i-n and avalanche photodiodes indicate that second and third harmonic distortion is in the order of 60 dB and 100 dB, respectively, below the level of the fundamental [see Appendix H]. This suggests that the linearity of photodiodes is excellent. Since the second- and third-harmonic distortion is expected to be approximately proportional to the square and cube of the fundamental, respectively, photodiodes operating with relatively low incident optical powers should exhibit virtually negligible distortion.

4.3 Summary

Both avalanche and non-avalanche p-i-n photodiodes appear to be suitable devices for the proposed optical fiber transmission system. Silicon photodiodes offer high efficiency over the wavelength range considered, rapid risetimes and excellent linearity. Noise performance, based on a direct detection system, has been discussed at length and will be seen later to be satisfactory. While avalanche photodiodes offer improved noise performance over p-i-n photodiodes, they are very temperature-dependent. The use of p-i-n photodiodes would appear to be preferable to using avalanche photodiodes if at all possible.

CHAPTER 5

COUPLING

One of the greatest problems associated with optical fiber communication is in coupling the light energy among the various components. The coupling areas can be categorized basically as:

1. Source-to-fiber coupling
2. Fiber-to-fiber coupling and splicing
3. Fiber-to-detector coupling

The major part of the discussion will be concerned with source-to-fiber coupling. By reciprocity, much of this will be applicable to fiber-to-detector coupling. Fiber-to-fiber coupling and splicing will be discussed last. In all cases, the emphasis is on coupling efficiency. For the first and third categories, much of the emphasis is on potential optical signal multiplexing.

In the area of source-to-fiber coupling, a number of techniques have been outlined in the literature. These techniques can be categorized as follows:

1. Direct coupler
2. Prism-film coupler
3. Birefringent coupler
4. Grating coupler
5. Tapered-film coupler

Strictly speaking, some of these techniques are not source-to-fiber couplers, but rather source-to-waveguide couplers. However, it is a relatively easy matter to complete the coupling from the waveguide to the fiber. The following sections will elaborate on these techniques.

5.1 Direct Coupler

The most straightforward and obvious way of coupling an optical source to a fiber is to physically place the source in direct, or near, proximity to the fiber with due precision. A number of researchers have addressed this problem. Coupling light from surface-emitter and stripe-geometry LED's into step-index fibers with and without a focusing lens is described in Appendix I. A number of relationships among the various parameters are presented there. In essence, it is shown that the radius of the LED should be less than, or equal to the radius of the fiber core for optimum coupling efficiency. A lens can improve coupling efficiency for cases when the radius of the source is less than, or equal to the diameter of the fiber core. Increasing the numerical aperture of the fiber also provides increased coupling efficiency, since light is accepted over a wider range of incident angle.

A summary of examples of various coupling configurations as calculated in Appendix I is presented in Table 5.1. For the electrical power required, an electrical power input, jv_s , of 2×10^4 watts/cm² was used, where j is the current density (amps/cm²) and v_s is the voltage (volts) across the LED. It can be seen that focusing provides about a tenfold improvement in overall efficiency, even though the actual coupled power is less than that provided without focusing, since the source effective area is reduced with a lens.

Parabolic-index fibers can accept only one-half the number of modes from an LED that step-index fibers can accept [15], and therefore only one-half the power [97]. Most practical systems, however,

Table 5.1

Summary of Results of Analyses for Disc and Stripe Geometries With
and Without a Lens (After Yang and Kingsley [98])

Source Geometry	Power Into Fiber	Electrical Power Required	Overall Efficiency
<u>Disc</u> , diam = $2a$	$4\pi^2 \Lambda U a^2 \sin^2 \theta_c / 2$ $36 \mu\text{W}$	$\pi j v_s a^2$ 0.4 W	$\sim 0.01\%$
<u>Focused Disc</u> , diam = $2\Gamma \tan \theta_c$ lens, diam = $2a$ focal length = Γ	$\sim \pi^2 \Lambda U a^2 \tan^2 \theta_c$ $31 \mu\text{W}$	$\pi j v_s \Gamma^2 \tan^2 \theta_c$ 0.031 W	0.1%
<u>Rectangular Stripe</u> width = $2a$ length = $n_0 a \cot \theta_c$	$8.64 \Lambda U a^2 n_0 \tan \theta_c / 2$ 0.4 mW	$2 j v_s a^2 n_0 \cot \theta_c$ 6.2 W	0.01%
<u>Focused Rectangular Stripe</u> width = $2\Gamma \tan \theta_c$ length = $\frac{2n_0 \Gamma^2 \tan \theta_c}{a \left[1 - \left(\frac{\Gamma \tan \theta_c}{a} \right)^2 \right]}$	$3\pi \frac{\Lambda U n_0 \Gamma a \tan^2 \theta_c}{\left\{ 1 - \left[\left(\frac{\Gamma \tan \theta_c}{a} \right)^2 \right] \right\}}$ 0.26 mW	$0.4 j v_s n_0 \frac{\Gamma^3}{a} \tan^2 \theta_c$ 0.28 W	$\sim 0.1\%$

such as the proposed radio telescope antenna feeder system, will utilize parabolic-index fibers for their improved dispersion characteristics. Results of a study into coupling light from an LED into parabolic-index fibers are presented in Appendix J. It has been found that coupled power is relatively insensitive to source-fiber separation and particularly for fibers with small values of Δ (or numerical aperture). Tolerance to source-fiber offset tended to increase with source-fiber separation.

Considering the total power coupled into the fiber as a function of source radius, it was determined that the maximum power occurs at a source-core radius ratio of 0.8 (see Appendix J). In addition, the maximum coupled power relative to the electrical drive power of the diode was found to occur at a source-core radius ratio of 0.2. As a compromise between these two values, a source with radius of one-half that of the fiber core would seem to be reasonable. For this case with the radius of the source being less than the radius of the fiber core, a lens would improve the coupling efficiency as before.

Since lasers are considerably brighter sources than LED's and since their spatial emission pattern is very much narrower than LED's, they can couple much more power into a fiber. The usual technique is to use a fiber with a lens formed on the end by a number of processes including melting, etching and photoresist exposure techniques [99].

Coupling efficiency between a GaAlAs stripe-geometry laser and four low-loss optical fibers was determined experimentally [99]. The laser had a rectangular aperture of $15\text{ }\mu\text{m} \times 0.5\text{ }\mu\text{m}$ and had angular

divergence much smaller than the acceptance angle of the fibers. A lens was melted onto the ends of the four fibers whose physical characteristics were as shown in Table 5.2. The laser-to-fiber coupling efficiency for each fiber was determined for the cases of no lens and with a lens and the results are presented in Table 5.3.

Although the coupling efficiency with fiber A appears to be considerably greater than with any other fiber, the lens formed on fiber A was more efficient than on any other fiber and thus admitted more light [99]. For the other fibers, though, the efficiency is seen to be roughly proportional to the numerical aperture, which is to be expected. The improvement in efficiency by using a lens on the end of the fiber is seen to be about 35% or 1.5 dB for the graded-index fibers and 62% or 4 dB for the step-index fiber.

A major problem with direct coupling is the alignment of the source with respect to the fiber, either with or without physical optics, to ensure maximum light coupling. Another problem is encountered if more than one source requires coupling to the same fiber to facilitate color, or wavelength division multiplexing, for example. Such a multiplexing technique would expand an optical fiber system's capacity by the number of optical carriers that could be "stacked" within the fiber's optical bandwidth. For the radio telescope project, this could prove to be a desirable option.

The following coupling techniques involve the coupling of light into a waveguide from which it can be coupled into an optical fiber. In general, the source-to-waveguide and waveguide-to-fiber coupling is not as critical as direct source-to-fiber coupling. The source-to-waveguide coupling occurs over a length of many optical

wavelengths and coupling a waveguide of thickness less than 1 μm to a fiber whose core is, say, 50 μm is also not very critical (relatively speaking!).

Table 5.2

Fibers Used To Measure Coupling Efficiency

<u>Fiber</u>	<u>Core Composition</u>	<u>Index Profile</u>	<u>Numerical Aperture</u>	<u>Core Diameter</u>
A	SiO_2	step	0.1707	55 μm
B	$\text{B}_2\text{O}_3\text{:SiO}_2$	partially graded	0.148	50 μm
C	$\text{GeO}_2\text{:SiO}_2$	graded	0.1707	46 μm
D	$\text{B}_2\text{O}_3\text{:SiO}_2$	graded	0.162	42 μm

Table 5.3

Laser-to-Fiber Coupling Efficiency in Percent

	<u>Fiber</u>			
	<u>A</u>	<u>B</u>	<u>C</u>	<u>D</u>
Flat End	24	13	17	10
Lens	63	19	26	15

5.2 Prism-Film Coupler

One of the first methods of coupling light into a thin waveguide was by utilizing a prism in the configuration shown in Fig. 5.1. This has been described in a number of references [19,100,101,102,103,104,105,106] and a brief description will be presented here.

An optical waveguide is formed by depositing a thin (usually a fraction of a micrometer) film onto a substrate that serves both as a waveguide boundary and provides structural rigidity for the film. In order for the film to act as a waveguide, its index of refraction must be larger than those of the substrate on the bottom and the air on top. This is shown in Fig. 5.2 along with the three cases of light propagation. According to Snell's law,

$$n_a \sin \phi_a = n_f \sin \phi_f = n_s \sin \phi_s \quad (5.1)$$

where n_a , n_f and n_s are the indices of refraction of air, film and substrate, respectively, and ϕ_a , ϕ_f and ϕ_s are the angles between the light ray and the normal in each of the air, film and substrate, respectively.

If the incident angle ϕ_a is too small, the light will be refracted according to eq. (5.1) and pass through the film and into the substrate as shown in Fig. 5.2 (a). Increasing ϕ_a beyond $\sin^{-1}(n_a/n_f)$ will result in light being reflected from the top surface and not entering the film at all. However, light may still enter (or leave) the waveguide from the substrate as in Fig. 5.2 (b) until the angle ϕ_s reaches $\sin^{-1}(n_s/n_f)$ at which point no more light may enter, or

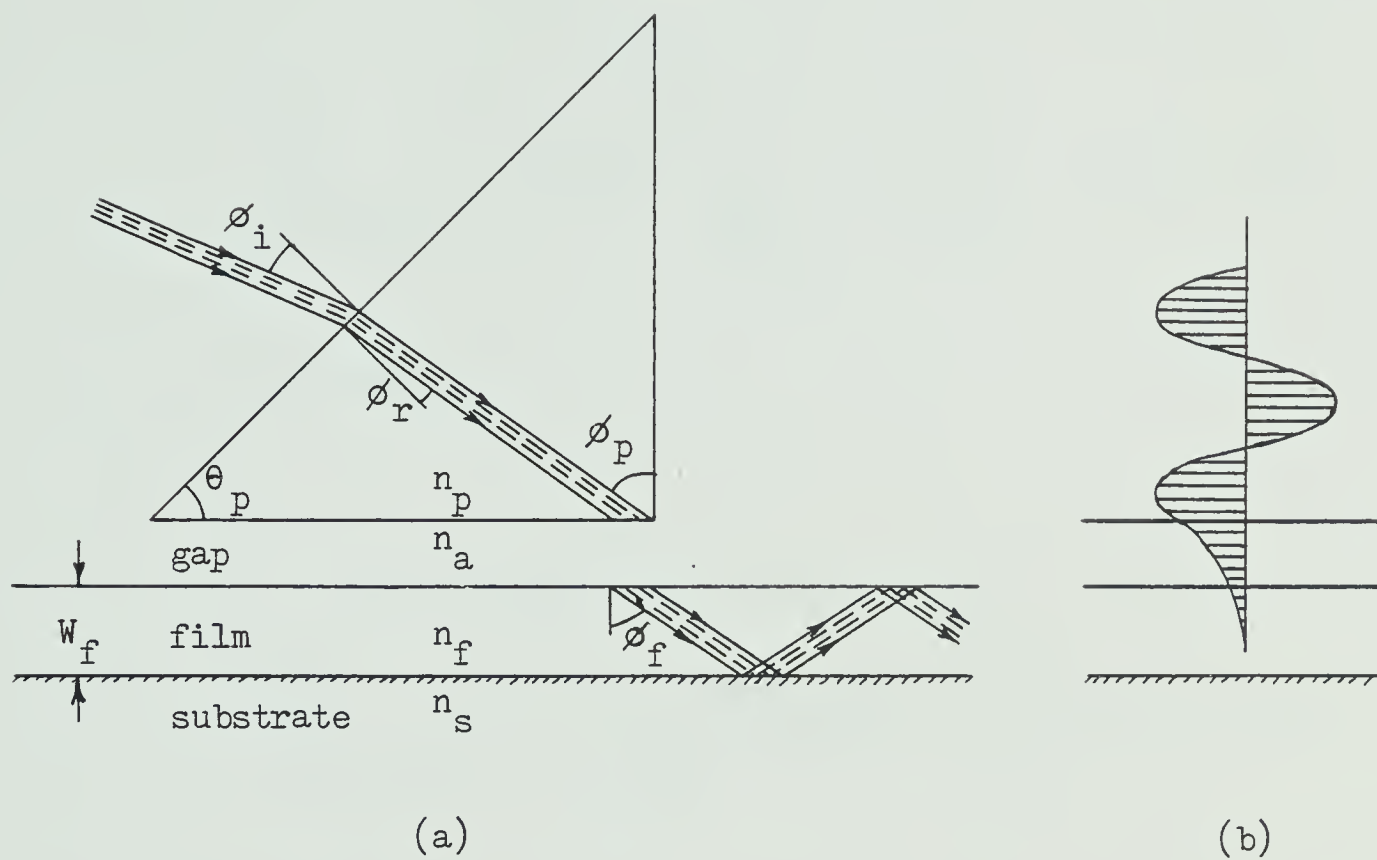


Fig. 5.1 Prism-film coupler (a) physical configuration (b) standing-wave field distribution in prism (After Tien [101]).

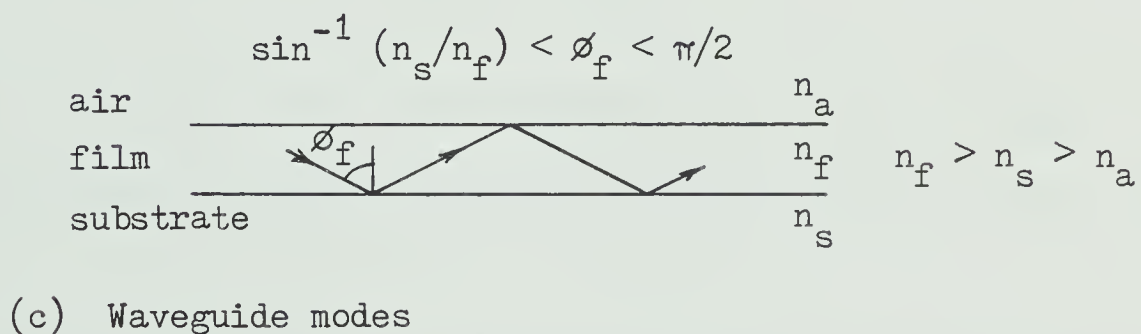
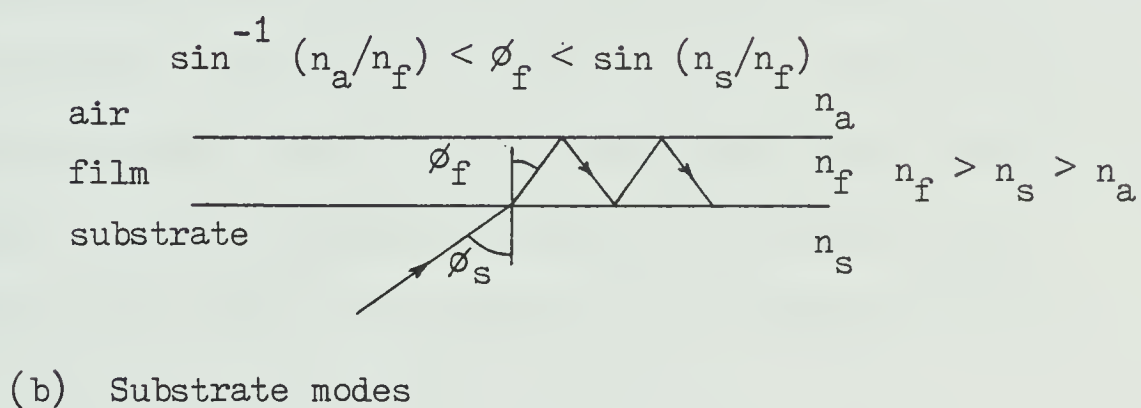
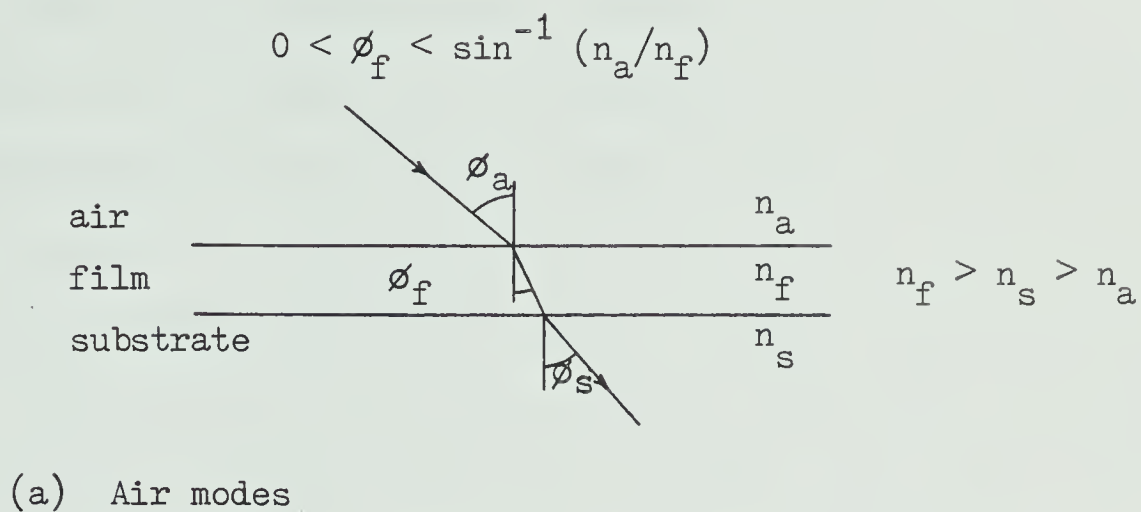


Fig. 5.2 Thin-film optical waveguide showing the three cases of optical propagation (After Tien [101]).

leave, the film. This is the condition required for propagation within the film and the modes that characterize this are known as waveguide modes. This case is shown in Fig. 5.2(c).

Light can be coupled into a waveguide by the use of a prism that is displaced from the film by a small air gap in the order of $1/8$ to $1/4$ of the optical wavelength in air [19] as shown in Fig. 5.1(a). The prism has a refractive index n_p which is greater than that of the film n_f . The incoming optical beam is totally reflected at the prism-air gap interface and thus establishes a standing wave within the prism as indicated in Fig. 5.1(b). This standing wave extends below the base of the prism in an exponentially decreasing pattern known as the evanescent field. If the prism is close enough to the waveguide to allow this evanescent field to excite waveguide modes, coupling will occur. This coupling mechanism is known as "frustrated total reflection" or FTR [106]. The condition for waveguide modes to propagate within the film is given by [101]

$$2k_o n_f W_f \cos \phi_f - 2\Phi_{fs} - 2\Phi_{fa} = 2M\pi \quad (5.2)$$

where $k_o = \omega/c = 2\pi/\lambda$, W_f is the thickness of the film, $-2\Phi_{fs}$ and $-2\Phi_{fa}$ are the Goos-Haenchen shifts [101] and M is the order of the mode.

The Goos-Haenchen shifts represent phase changes due to total reflection at the waveguide boundaries. Further discussion on this phenomenon can be found in [100,102,106,107,108]. These phase shifts can be determined directly from the following equations [101]:

$$\Phi_{fs} = \tan^{-1} \left[(n_f^2 \sin^2 \phi_f - n_s^2)^{1/2} / n_f \cos \phi_f \right] \quad (5.3 \text{ a})$$

$$\Phi_{fa} = \tan^{-1} \left[(n_f^2 \sin^2 \phi_f - n_a^2)^{1/2} / n_f \cos \phi_f \right] \quad (5.3 \text{ b})$$

for TE waves and

$$\Phi_{fs} = \tan^{-1} \left[n_f^2 (n_f^2 \sin^2 \phi_f - n_s^2)^{1/2} / n_s^2 n_f \cos \phi_f \right] \quad (5.3 \text{ c})$$

$$\Phi_{fa} = \tan^{-1} \left[n_f^2 (n_f^2 \sin^2 \phi_f - n_a^2)^{1/2} / n_a^2 n_f \cos \phi_f \right] \quad (5.3 \text{ d})$$

for TM waves.

Equation (5.2) states that, given the set of physical waveguide parameters such as film thickness and indices of refraction of the film and substrate, a particular waveguide mode can be launched by simply varying the angle of refraction ϕ_f within the film. Figures 5.3 (a) & (b) illustrate, for two different wavelengths, the relationship among the angle of refraction in the film ϕ_f , the thickness of the film and the mode of the propagated wave. These curves are based on the use of a zinc sulfide film (refractive index of 2.4 @ 0.532 μm , 2.3 @ 1.064 μm) on a glass substrate (refractive index 1.52 @ 0.532 μm , 1.51 @ 1.064 μm). The wavelengths used, 0.532 μm and 1.064 μm , represent two diverse wavelengths within the available optical fiber bandwidth. Although zinc sulfide would probably not be used in a practical film waveguide due to relatively high attenuation, it is considered adequate for this study since its index of refraction should be approximately representative of those materials that would be used for this application.

Figures 5.3 (a) & (b) indicate that a film can support many different modes, depending on the angle of refraction ϕ_f . For the example given, a film of thickness $0.25\text{ }\mu\text{m}$ can support four modes of $0.532\text{ }\mu\text{m}$ radiation: the TM_1 mode for an angle ϕ_f of 43° , the TE_1 mode for an angle of 50° , the TM_0 mode for an angle of 66.5° , and the TE_0 mode for an angle of 70.8° .

At this point it is evident that, for a given waveguide thickness, light of different wavelengths can propagate if the correct angle of propagation in the waveguide is set. This characteristic would obviously facilitate wavelength division multiplexing. In order to minimize the problem of exciting unwanted modes, it would seem preferable to use as thin a waveguide as possible to restrict the number of modes. If we consider only the modes for which $M = 0$ in equation (5.2), Figs. 5.3 (a) & (b) can be redrawn as shown in Fig. 5.4. This figure shows the TE_0 and TM_0 modes as a function of refraction angle ϕ_f and wavelength λ for waveguides of different thickness W_f . It can be seen that a waveguide of thickness $0.1\text{ }\mu\text{m}$ will support only TE_0 modes over most of the range of wavelengths. The TM_0 mode is only supported at short wavelengths up to about $0.6\text{ }\mu\text{m}$. At this point the angle ϕ_f reaches cutoff. The thicker waveguides can support both TM and TE modes over the range considered.

It is apparent, from Fig. 5.4, that the angle vs. wavelength curve becomes more nonlinear as the film thickness diminishes. The TE_0 curve for $W_f = 0.2\text{ }\mu\text{m}$ is much more linear than the TM_0 curve for $W_f = 0.2\text{ }\mu\text{m}$ or the TE_0 curve for $W_f = 0.1\text{ }\mu\text{m}$. Also the angular discrimination is more critical at the longer wavelengths. This nonlinearity will not be a detriment; in fact, it should be an

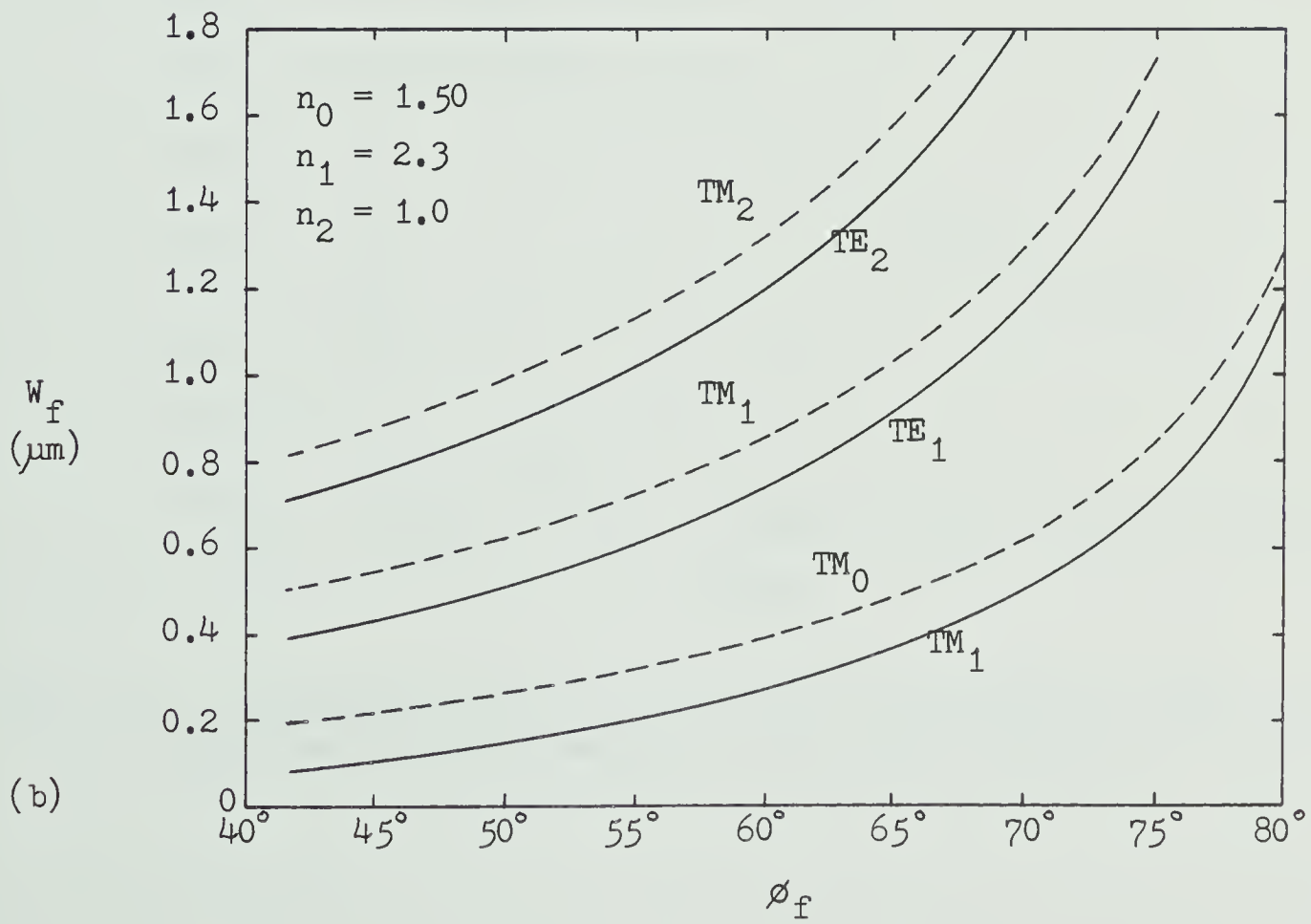
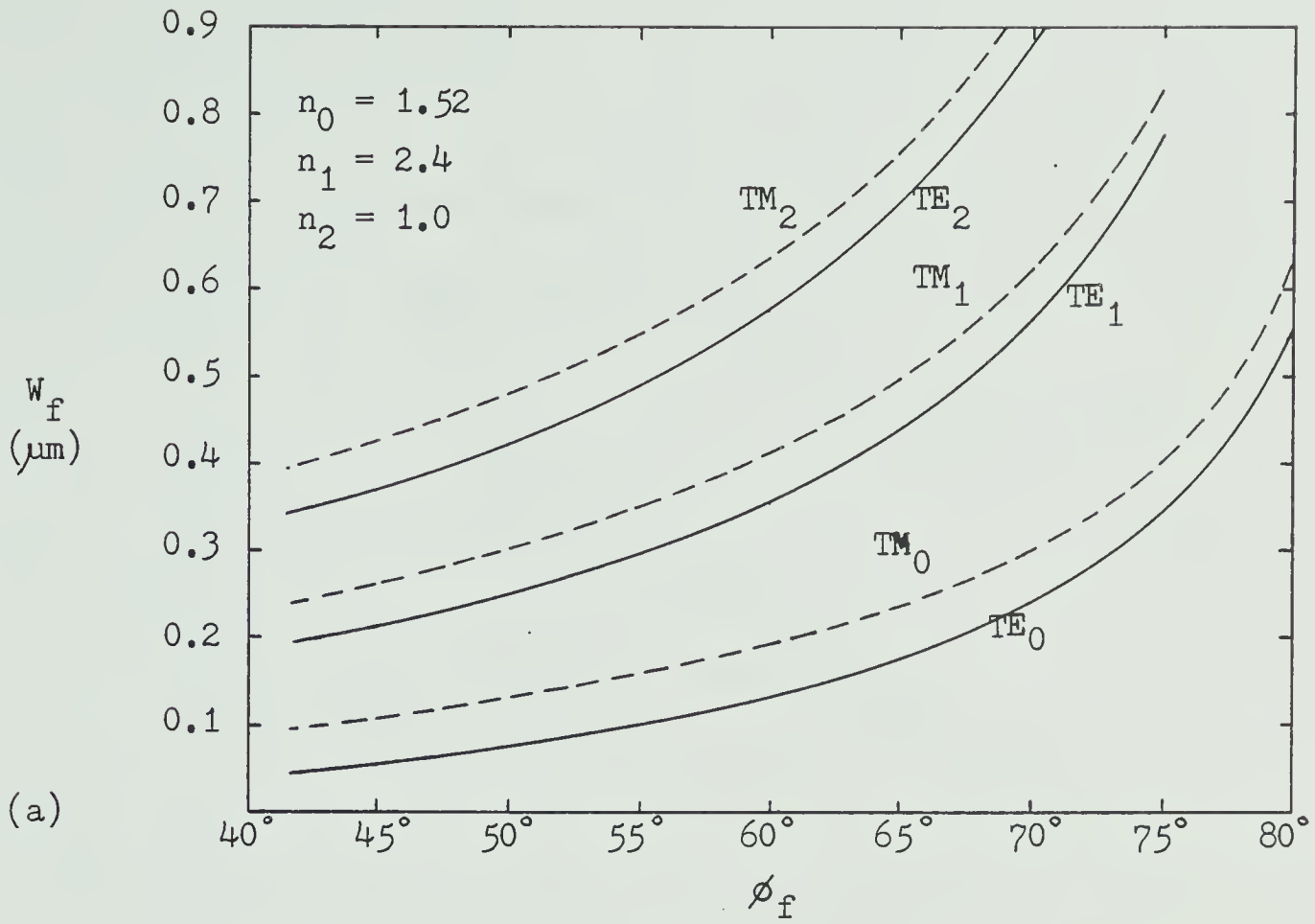


Fig. 5.3 Waveguide mode characteristics as a function of film thickness and angle of refraction for (a) $0.532 \mu\text{m}$ (b) $1.06 \mu\text{m}$.

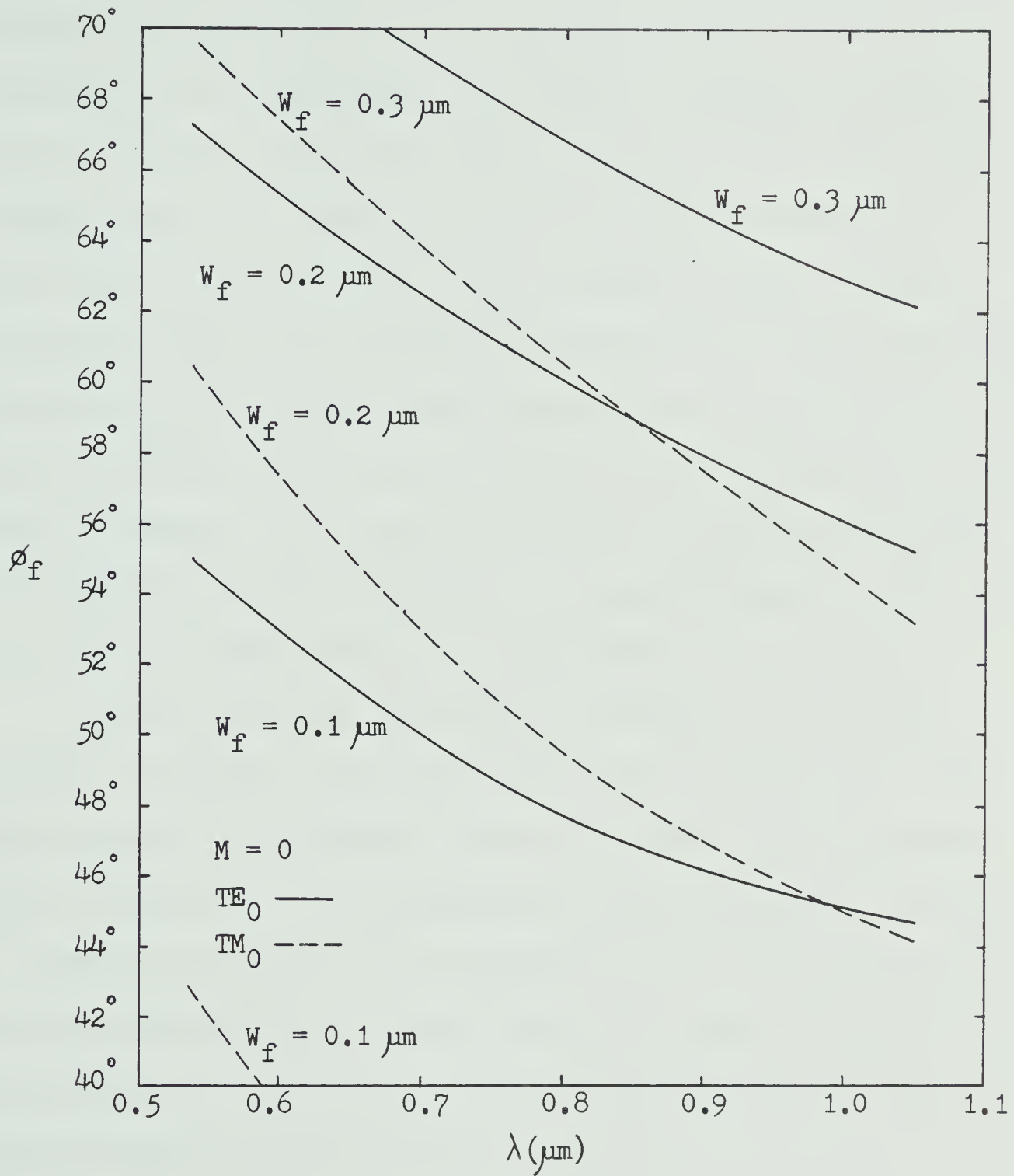


Fig. 5.4 Propagation angle as a function of wavelength for TE₀ and TM₀ modes in film waveguides of different thickness.

advantage in allowing more power to be coupled from wideband sources at the longer wavelengths due to the lower slope of the curve. If we consider a source of center wavelength $0.9\ \mu\text{m}$ and a source of center wavelength $0.6\ \mu\text{m}$, each with the same spectral width of $50\ \text{nm}$ (for convenience), it can be readily seen that the wavelength extremes of the $0.9\ \mu\text{m}$ source are much closer to the $W_f = 0.1\ \mu\text{m}$ curve than those for the $0.6\ \mu\text{m}$ source. If the $0.9 \pm 0.05\ \mu\text{m}$ radiation is coupled into the film at 46.2° , the wavelength extremes (maximum & minimum) are only $\pm 0.6^\circ$ off the required angle for those wavelengths. A look at the $0.6\ \mu\text{m}$ source shows that the $0.6 \pm 0.05\ \mu\text{m}$ maximum and minimum wavelengths are in error by about $\pm 1.7^\circ$. This would probably result in somewhat lower coupling efficiency at shorter wavelengths (with comparable spectral widths) than longer wavelengths. This appears to be an area in which little, if any, research has been done.

As stated earlier, the angle of propagation in the film waveguide is related to the angle in the prism and therefore to the angle of entry into the prism, which is the final control parameter (refer to Fig. 5.1). The relationships among the angle of incidence ϕ_i , the angle of refraction in the prism ϕ_r , the angle between the light ray and the perpendicular in the prism ϕ_p , the angle of the prism θ_p , and the angle of propagation in the film ϕ_f as a function of the various indices of refraction are:

$$\phi_i = \sin^{-1}[n_p \sin \phi_r] \quad [5.4]$$

from Snell's Law,

$$\phi_r = \phi_p - \theta_p \quad (5.5)$$

from simple geometry, and

$$\phi_p = \sin^{-1}[(n_f/n_p)\sin \phi_f] \quad (5.6)$$

from Snell's Law.

Fig. 5.5 illustrates graphically the relationship among angle of incidence ϕ_i , prism angle θ_p , prism index of refraction n_p and angle between light ray and perpendicular in the prism ϕ_p . This is determined for the case of TE_0 modes at the wavelengths of $0.532 \mu\text{m}$ and $1.064 \mu\text{m}$ propagating in a film $0.1 \mu\text{m}$ in thickness with index of refraction 2.4. The choice of variable for the abscissa ϕ_p allows us to see the angles of the ray within the prism at the two wavelength extremes. The angle of propagation for each wavelength within the film is, of course, constant. This graph assists one in appraising the relationship among the various parameters. For wavelength division multiplexing, it is probably desirable to maximize the spread of incident angle over the wavelength range of interest. This would facilitate physically clustering light sources of different wavelengths such that the light from each one would enter the prism at its required angle ϕ_i and yet the maximum physical separation between sources would ease the physical placement. It can be seen, for example, that a prism with angle $\theta_p = 30^\circ$ and index of refraction 2.5 allows an incident angle of 72° at $0.532 \mu\text{m}$ and 31° at $1.06 \mu\text{m}$ for a spread of 41° . These curves showing the angular spread between the $0.532 \mu\text{m}$ and $1.06 \mu\text{m}$

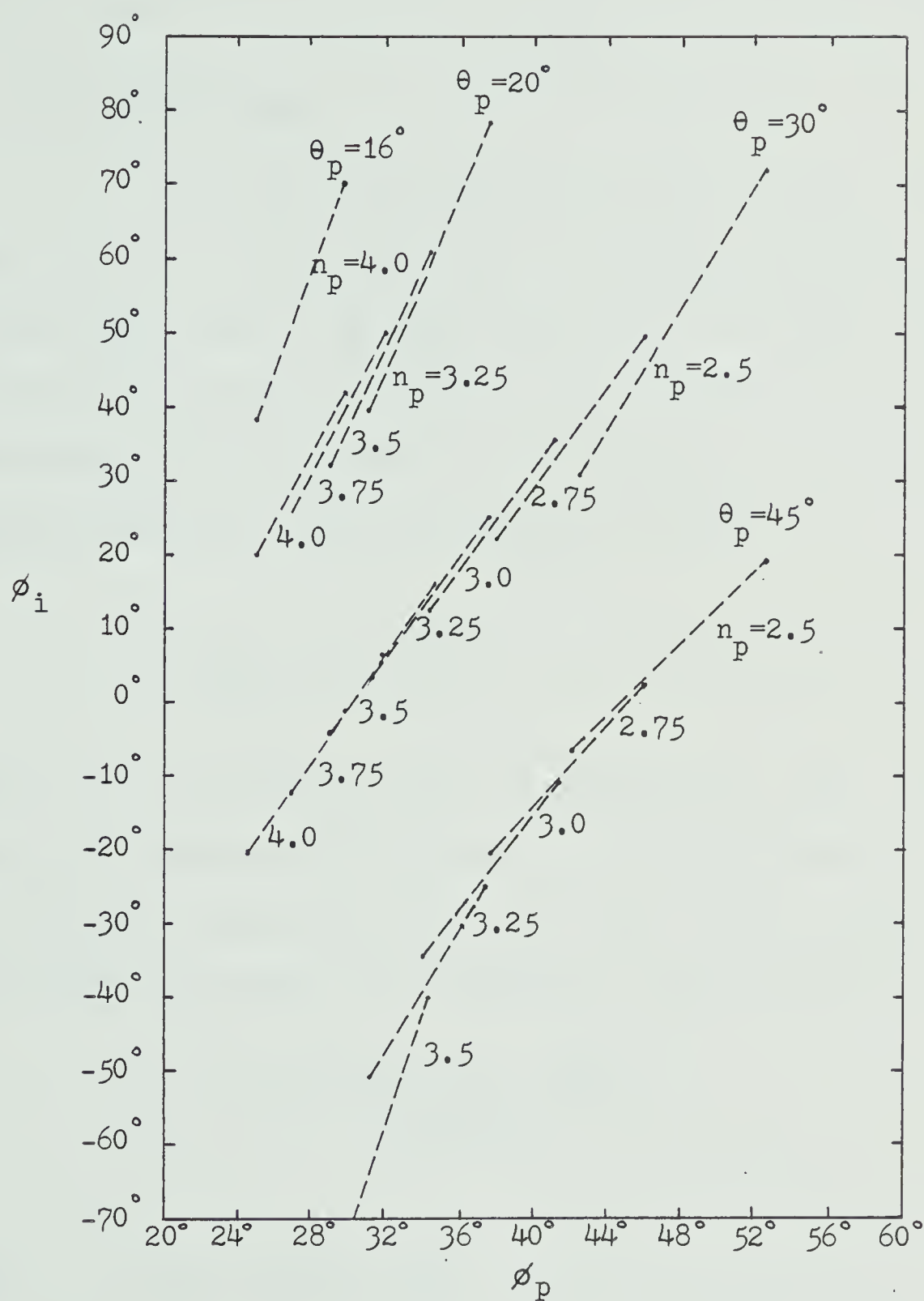


Fig. 5.5 Angle of incidence for TE_0 modes in prisms of various angles θ_p and indices of refraction n_p . The upper value represents the case of $0.532 \mu\text{m}$ wavelengths and the lower value represents $1.06 \mu\text{m}$.

wavelengths can also be shown as a continuous function of prism index of refraction n_p . Fig. 5.6 illustrates the cases for prisms of angle 20° , 30° and 45° .

Coupling_Efficiency

It has been established [101] that, to couple the maximum light from a prism into a waveguide, a rectangular prism must be used and the leading edge of the light beam must be as close as possible to the rectangular corner of the prism. If the horizontal distance between the leading and trailing edges of the light beam is given by L_1 , the coupling efficiency η_c can be represented by [101]

$$\eta_c = \frac{2}{SL_1} [1 - e^{-SL_1}]^2 \quad (5.7)$$

where S is a coupling parameter. By maximizing eq. (5.7) with respect to SL_1 , the optimum coupling length $SL_1 = 1.25$ is determined as well as the optimum coupling efficiency $\eta_c = 81\%$. All the properties of the coupler then depend on the parameter S , which is given by [101]

$$S = e^{-2p_2 W_g} \frac{\sin 2\bar{\phi}_{fa} \sin 2\bar{\phi}_{pa}}{W_{eff} \tan \phi_f} \quad (5.8)$$

where

$$W_{eff} = \frac{1}{W_f} + \frac{1}{p_1} + \frac{1}{p_2}, \quad (5.9)$$

the effective waveguide width due to the Goos-Haenchen shifts,

$$p_1 = [\beta^2 - (k_0 n_0)^2]^{1/2}$$

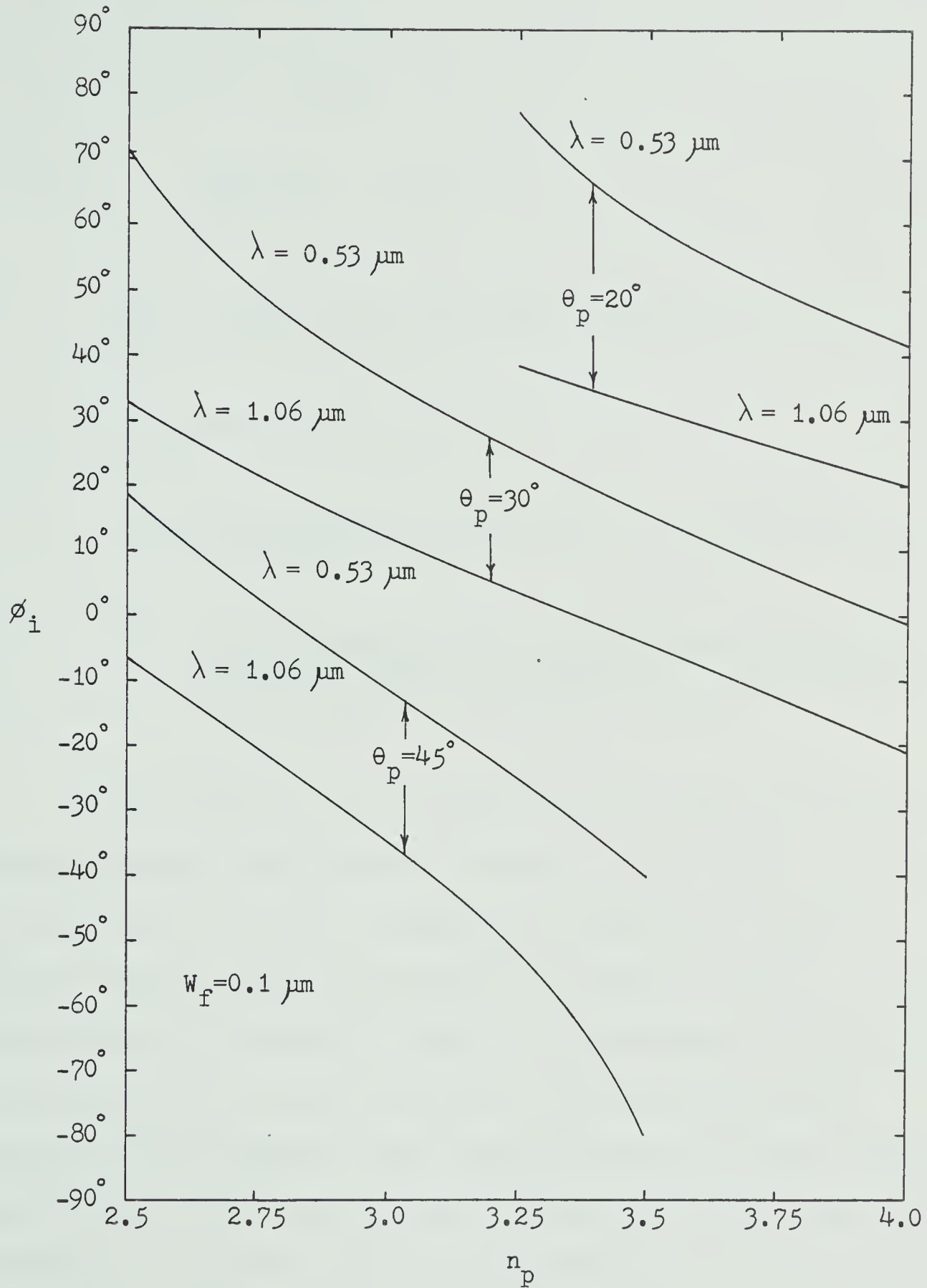


Fig. 5.6 Angle of incidence for TE_0 modes as a function of prism index of refraction for prisms of different angles for prism-film coupling.

$$= \frac{2\pi}{\lambda} \left[(\beta/k_o)^2 - n_o^2 \right]^{1/2} \quad (5.10a)$$

$$p_2 = [\beta^2 - (k_o n_2)^2]^{1/2}$$

$$= \frac{2\pi}{\lambda} \left[(\beta/k_o)^2 - n_2^2 \right]^{1/2} \quad (5.10b)$$

$$\frac{\beta}{k_o} = n_f \sin \phi_f = \frac{c}{V_p}, \text{ the effective refractive index}$$

Φ_{fa} is given in eq. (5.3)

Φ_{pa} is determined from eqs. (5.3) by substituting the subscript p for f.

W_g is the air-gap spacing between the prism and the waveguide (typically one-quarter to one-eighth of the wavelength of the light in vacuum).

At this point, it will be interesting to examine the effects of source spectral width and beam divergence on the coupling efficiency as dictated by eq. (5.7). Throughout the literature, lasers are virtually the only sources considered for waveguide coupling. If any consideration is to be given to LED's, it is necessary that the effects of spectral width and beam divergence on coupling efficiency be examined. If we consider a light source of center wavelength $1.064 \mu\text{m}$ coupled through a prism of refractive index $n_p = 3.0$ with an air gap spacing $W_g = 0.1 \mu\text{m}$ into a thin film waveguide of thickness $0.1 \mu\text{m}$, index of refraction $n_f = 2.3$ and propagating a TE_0 mode, the internal angles of refraction in the prism will be 33° and in the film will be about 44° which is equivalent to $\beta/k_o = 1.60$. From eqs. (5.9) and (5.10) $p_1 = 3.288 \mu\text{m}^{-1}$ and $p_2 = 7.376 \mu\text{m}^{-1}$ resulting in $W_{\text{eff}} = 0.540 \mu\text{m}$.

These parameters can then be substituted into eq. (5.3) which, for TE modes, yields $\Phi_{fa} = 0.6455$ and $\Phi_{pa} = 0.4744$. These, in turn, can be substituted into eq. (5.8) to give $S = 0.3425 \mu\text{m}^{-1}$. Since the optimum coupling length $SL_1 = 1.25$ was established earlier, $L_{1\text{opt}} = 3.65 \mu\text{m}$.

If we consider first the spectral dependency and choose arbitrary spectral widths of 10 nm, 20 nm, 30 nm and 40 nm, Table 5.4 can be determined from eqs. (5.9) and (5.10). The maximum and minimum values are associated with the wavelength extremes on either side of the center wavelength. It is interesting to note that, after substituting each of the various values of S into eq. (5.7) along with $L_{1\text{opt}} = 3.65 \mu\text{m}$, the coupling efficiency is essentially constant at 81%. This implies that spectral width is not a critical consideration in coupling efficiency. Table 5.4, however, shows that the coupling efficiency is very dependent on the parameter L_1 , the horizontal distance between the leading and trailing edges of the beam at the base of the prism. From a minimum coupling loss of about 1 dB at $L_{1\text{opt}} = 3.65 \mu\text{m}$, the loss increases logarithmically with L_1 . It is therefore desirable to keep this distance as close as possible to $L_{1\text{opt}}$ unless there is a considerable margin available in the overall system power budget. Since a laser can be focused to small areas more readily than LED's, this would be a strong argument for the use of lasers over LED's for this type of coupler. It is interesting to note that practical coupling length for use with air gaps of 0.1 to 0.3 μm is roughly 10 μm to 100 μm , with 50 μm being common [109].

Let us now examine the effect of beam divergence on coupling efficiency. For simplicity and consistency the same parameters as in

the previous example will be used. The only parameter that will be variable will be the angle of refraction in the waveguide. The beam divergence $\delta\phi_f$ is assumed to be distributed equally on either side of the nominal angle of propagation ϕ_f . That is, the leading edge of the beam will present an angle of propagation of $\phi_f + \delta\phi_f/2$ in the waveguide and the trailing edge an angle of $\phi_f - \delta\phi_f/2$. Utilizing eqs. (5.7) through (5.10) and (5.3), Table 5.5 can be compiled. At angles of divergence somewhat larger than 5° , the trailing edge angle becomes smaller than the cutoff angle so only part of the beam can be coupled. Table 5.5 indicates that as long as cutoff is avoided, the coupling efficiency is not dramatically affected by beam divergence over the range considered.

The discussion to this point has involved a prism-film coupler with a uniform separation gap. By varying this gap between the prism and the film waveguide, it has been determined [8,110,111] that greater coupling efficiencies are possible. Miller [8] has calculated the optimal gap geometry with which 100% coupling is theoretically possible. Ulrich [110] has examined the use of the linearly tapered gap which has a theoretical coupling efficiency of 96%. Experimentally, he achieved an efficiency of 88%. Zlenko and Sychugov [111] examined a gap with a parabolic profile which they determined by computer calculations to allow a theoretical coupling efficiency of 98.7%. A subsequent experiment yielded an efficiency of 90%.

While a uniform gap coupler can achieve a theoretical efficiency of 81% as an input coupler, when it is used as an output coupler it can achieve a theoretical efficiency of 100% [101]. This is because the uncoupled light at the input is immediately lost upon

Table 5.4

Coupling Efficiency as a Function of Spectral Width

$\delta\lambda$		10 nm		20 nm		30 nm		40 nm		Coupling Loss	
		min	max	min	max	min	max	min	max		
p_1		3.273	3.303	3.257	3.319	3.242	3.335	3.227	3.351		
p_2		7.341	7.410	7.307	7.446	7.273	7.481	7.240	7.517		
W_{eff}		0.542	0.538	0.544	0.536	0.546	0.534	0.548	0.531		
S_{min}		0.3391	0.3416	0.3354	0.35	0.3318	0.3537	0.3283	0.3581		
η_c	L_1	3.65	0.814	0.814	0.814	0.814	0.814	0.814	0.814	0.9 dB	
	(μm)	10	0.551	0.548	0.555	0.537	0.56	0.533	0.564	0.528	2.6 dB
		100	0.059	0.0585	0.06	0.057	0.06	0.0565	0.061	0.056	12 dB

Table 5.5

Coupling Efficiency as a Function of Beam Divergence

$\delta\phi_f$	1°		2°		5°		10°	
β/k_o	1.583	1.612	1.569	1.626	1.524	1.668	1.447	1.736
p_1	2.987	3.486	2.717	3.706	1.591	4.308	0	5.161
p_2	7.247	7.466	7.140	7.571	6.791	7.884	6.176	8.380
W_{eff}	0.573	0.521	0.608	0.502	0.876	0.459	∞	0.413
Φ_{fa}	0.6343	0.6567	0.6230	0.6678	0.5887	0.7007	—	0.7546
Φ_{pa}	0.4634	0.4854	0.4522	0.4963	0.4180	0.5286	—	0.5812
S	0.3296	0.3502	0.3151	0.3569	0.2274	0.3668	—	0.3608
η_c	0.814	0.814	0.812	0.814	0.766	0.813	—	0.814

reflection from the base of the prism, whereas the propagating light in the waveguide can all be coupled out provided that the coupling length is sufficiently long. This length has not been discovered in the literature.

5.3 Birefringent Coupler

Brandt [112] has investigated the use of birefringent materials to couple light into a waveguide. A birefringent material is one whose index of refraction varies with the angle of the light ray in the material. A plot of refractive index as a function of angle is found to trace out an ellipse, whose major axis, termed the "optic axis", passes through the points of highest refractive index. This point of highest refractive index is termed the ordinary index n_{or} which is the value the material would have if it were isotropic. The index of refraction at the minor axis is termed the extraordinary index n_{ex} . Fig. 5.7 illustrates this property. The value of refractive index at any other angle can be determined from

$$n(\psi)^2 = n_{ex}^2 n_{or}^2 / (n_{or}^2 \sin^2 \psi + n_{ex}^2 \cos^2 \psi) \quad (5.11)$$

where ψ is angle of the light ray measured from the optic axis.

A coupler made from suitable birefringent material can be positioned directly on a waveguide without the requirement of having an air gap if the refractive index of the waveguide n_f falls between the range of the ordinary and extraordinary indices n_{or} and n_{ex} . Fig. 5.8 shows such a prism of birefringent material coupling light into a film waveguide. By suitably positioning the optic axis with

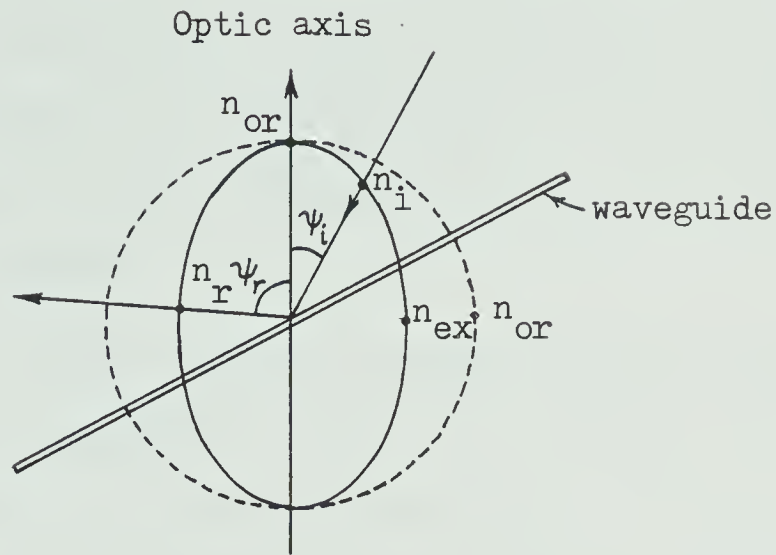


Fig. 5.7 Refractive-index ellipsoid for birefringent material with a waveguide superimposed at an angle to the optic axis. The dashed circle represents the ordinary index; n_i & n_r are the indices seen by the incident and reflected rays (After Brandt [112]).

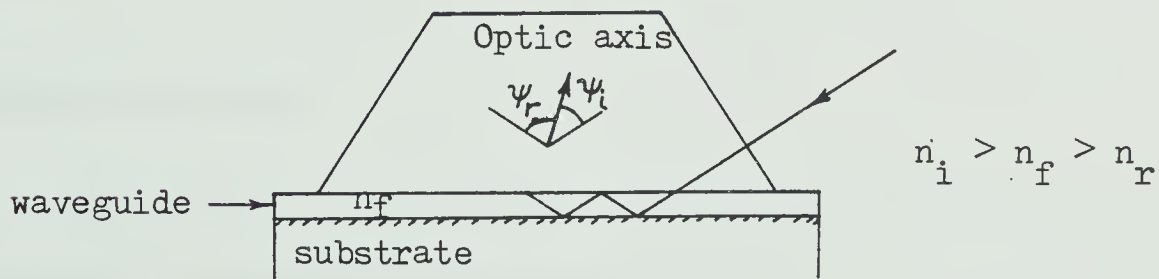


Fig. 5.8 Schematic of a birefringent coupler. The angles ψ_i and ψ_r represent the angles between the optic axis and the incident and refracted beams (After Brandt [112]).

respect to the prism-waveguide interface, the light beam will experience a different index of refraction at the angle of incidence than at the angle of reflection. This is illustrated in Fig. 5.7, where it can be seen that n_i is greater than n_r . If the refractive angle of the waveguide n_f falls between n_i and n_r , the light will be coupled into the waveguide.

This type of coupler has the advantage that the incident light beam does not require focusing to a small spot. Brandt [112] reports coupling beams as wide as 1 cm without difficulty. An oddity with this coupler is that only TM polarized light can be coupled so a polarized source would require aligning and an unpolarized source would lose an immediate 3 dB of power. The major disadvantage of birefringent couplers is that coupler materials require careful choosing so that the ordinary and extraordinary indices span the index of refraction of the waveguide. In addition, careful orientation of the prism and close control of the waveguide index and thickness are required for success. In view of the foregoing, birefringent couplers are not considered for the optical fiber transmission system.

5.3 Grating Coupler

Light can be coupled into a thin-film waveguide by the use of a diffraction grating on the waveguide. Essentially, there are two techniques for accomplishing this. One way is to simply focus the beam onto the top of the grating at an appropriate angle. The other way is to couple the incoming light beam from the reverse direction through the substrate. This latter coupler is known as a "reverse coupler". These couplers are discussed in Appendix K.

The grating coupler is a distributed coupler just as the prism coupler is, and much of the concepts and theory developed for the latter can be applied here. The grating equation which governs the coupling of light as a function of refractive index (or phase velocity), angle of incidence, optical wavelength and grating periodicity is (see Appendix K)

$$c/v_p = \sin \theta_i + \frac{m\lambda_o}{g} \quad (5.12)$$

Just as the prism-film coupler can be used to multiplex numerous light signals into a waveguide by providing the correct angle of incidence according to the wavelength, so can a grating coupler be used to multiplex light signals. This fact is obvious from an examination of eq. (5.12). In order to determine the approximate relationship between angle of incidence and wavelength, the following example is considered from the experiments by Boivin [113]. A grating with periodicity $g = 0.5 \mu\text{m}$ is formed on a thin film of refractive index 1.62 which is attached to a substrate of refractive index 1.46. The value of c/v_p used will be 1.55 and this will be assumed to be constant over the range of wavelengths considered. A plot of angle of incidence versus wavelength is presented in Fig. 5.9. This graph should be meaningful for both normal and reverse-coupler gratings, at least in so far as to show the range of angles (in a refractive index medium of $n = 1.0$) required for wavelength-division multiplexing.

The coupling efficiency of gratings can approach 100% in theory (see Appendix K), but experimental results tend to range from

40% to 70%.

Although grating couplers may be easier to fabricate than prism-film couplers, this thesis will assume the use of the latter couplers in view of their demonstrated coupling efficiency advantage.

Since coupling light from a source or sources into a film waveguide is only half of the source-to-fiber coupling problem, we must now address the other half. Fortunately, an excellent method of coupling light from a waveguide to a fiber or vice-versa is available with the tapered-film coupler.

5.5 Tapered-Film Coupler

A tapered-film coupler consists of a thin film waveguide that tapers down to the substrate as shown in Fig. 5.10. This type of coupler utilizes the cutoff property of an asymmetrical optical waveguide [114]. A waveguide mode, upon entering the tapered region from the film, is coupled to the radiation modes of the substrate (see Fig. 5.2 (b)). As was discussed in the section on prism-film couplers, a waveguide mode requires a minimum guide thickness in order to propagate. As the waveguide narrows in the tapered region, this minimum width is not sustained and the propagating energy is coupled into the substrate. A more comprehensive discussion of tapered film couplers is found in [114] and [115] both from a modal and a ray-optics approach. A brief description of operation using ray optics will be presented here.

A light ray propagating in the film waveguide has an angle of incidence of θ_f with respect to the normal to the film-substrate interface. As this ray enters the tapered region, this angle becomes

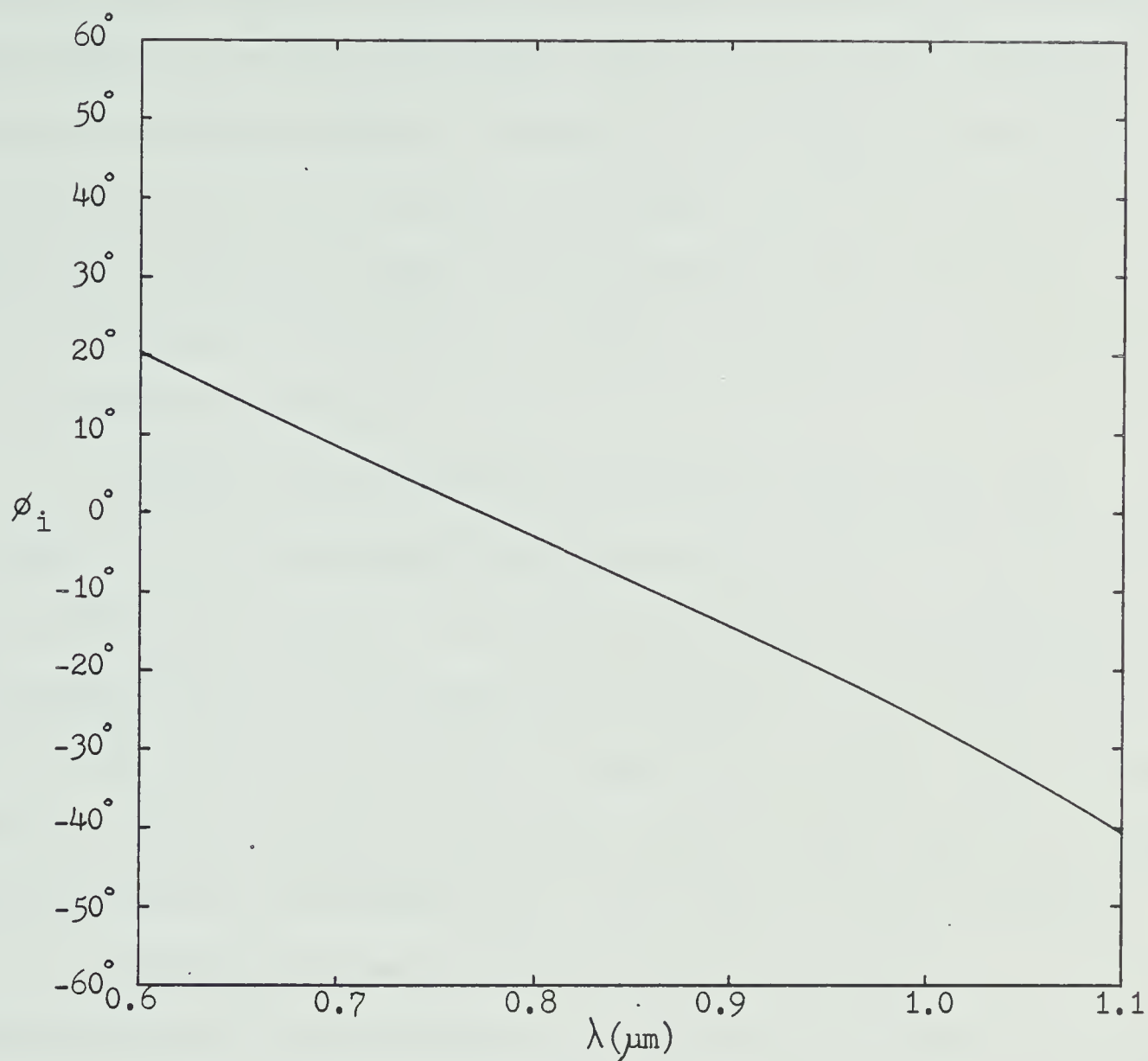


Fig. 5.9 Angle of incidence as a function of wavelength for a grating coupler with periodicity $g = 0.5 \mu\text{m}$, $c/V_p = 1.55$ and $m = 1$.

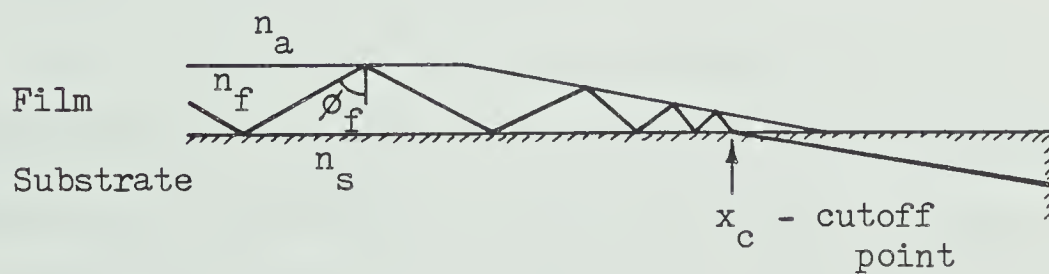


Fig. 5.10 Tapered-film coupler (After Tien and Martin [114])

progressively smaller with each reflection from the film-air interface. Eventually, at point x_c this angle becomes smaller than the critical angle of the film-substrate interface $\theta_c = \sin^{-1}(n_f/n_s)$ and the ray is refracted into the substrate according to Snell's Law (eq. 5.1) Radiation into the air above the film does not occur since the critical angle of the film-air interface is smaller than that of the film-substrate interface.

Theory predicts [114] that over 80% of the output light energy should be concentrated in an angle less than 15° below the film-substrate interface. Tien and Martin [114] have experimentally determined that it is an easy matter to couple all the light energy out of the film and within the 15° predicted by theory. Using tapered films as input couplers, they coupled 25% of a laser beam into a glass film and 40% of a laser beam into a film made of organic material.

The beam that exits from the substrate is found to be relatively wide in the dimension of the substrate thickness [115,116]. By experimenting with glass films of different amounts of taper, it was found [115] that a narrower beam is associated with a longer taper. By way of comparison, a taper with ratio 30:1 resulted in a spread between half-intensity points of about 13° whereas a taper with ratio 500:1 resulted in about a 3° spread.

While the previous discussion has been restricted to the case of a single mode, the multimode case has also been examined. Funayama et al [116] coupled a laser into various waveguide modes using a prism-film coupler and examined the output from a tapered-film coupler. It was found that the various modes appeared at slightly different angular positions. Using the tapered-film as an input

coupler, they achieved a coupling efficiency of over 40% and over 50% on two different samples using a $0.6328\text{ }\mu\text{m}$ laser. The maximum efficiency was determined to coincide with the positioning of the laser beam at the center of the taper.

5.6 Splicing and Connecting

Another problem associated with optical fiber communications is the splicing and coupling of fibers, particularly in a field environment. Conventional wire cables can be repaired in a relatively dirty environment using ordinary hand tools such as wire cutters, pliers and soldering irons. Optical fibers present an entirely different approach. The size and nature of the individual fibers necessitates special tools for stripping jacketing, making precision breaks or cuts and joining the fibers. The environment must be well-lit and clean to prevent foreign material from contaminating the fiber ends. Techniques will require more care and precision since minute misalignments can cause relatively large losses.

There are essentially three sources of loss related to the characteristics of fibers to be joined [13]:

1. Mismatch in fiber core diameters
2. Mismatch in peak numerical aperture
3. Mismatch in refractive index profile.

Fig. 5.11 shows that two fibers differing in core diameter from the nominal by +1% and -1%, respectively, but identical in every other way and joined perfectly, will exhibit a loss upon joining of 0.17 dB. Similarly, the same figure shows that two fibers differing in peak numerical aperture by $\pm 1\%$, but identical in every other way and joined perfectly, will also exhibit a 0.17 dB joint loss.

Figure 5.12 shows the loss incurred upon joining two fibers with different refractive index profiles. The profile exponent α is the same as is used in eq. (A.8) where $\alpha = \infty$ represents a step-index fiber and $\alpha = 2$ represents a parabolic profile. A joint between a fiber characterized by $\alpha_2 = 2.2$ and a fiber with a profile characterized by $\alpha_1 = 2.0$ will exhibit a loss of 0.20 dB. A joint between a step-index fiber and a parabolic-index fiber results in a loss of 3.0 dB.

These losses are encountered when propagating a signal from a fiber of larger core diameter, peak numerical aperture or profile exponent to one with a smaller core diameter, peak numerical aperture or profile exponent. The same joint measured in the opposite direction will exhibit no loss due to these effects. It is also to be noted that these effects are additive.

In addition to the fiber characteristic related losses, there are technique- or hardware-related losses [13]:

1. Lateral misalignment of fiber cores.
2. Angular misalignment of fiber axes.
3. Separation of fiber ends.
4. Scattering and Fresnel reflection at fiber ends.

Lateral misalignment or offset, of fiber cores can arise from hardware inaccuracies as well as outside diameter variations. Figure 5.13 shows the loss due to lateral misalignment of two step-index fibers. The effect of angular misalignment is shown in Fig. 5.14. For low losses, approximately 1° misalignment can be tolerated. The effect of separation between fiber ends is illustrated in Fig. 5.15 for two identical step-index fibers of $85\text{ }\mu\text{m}$ core diameter and numerical aperture

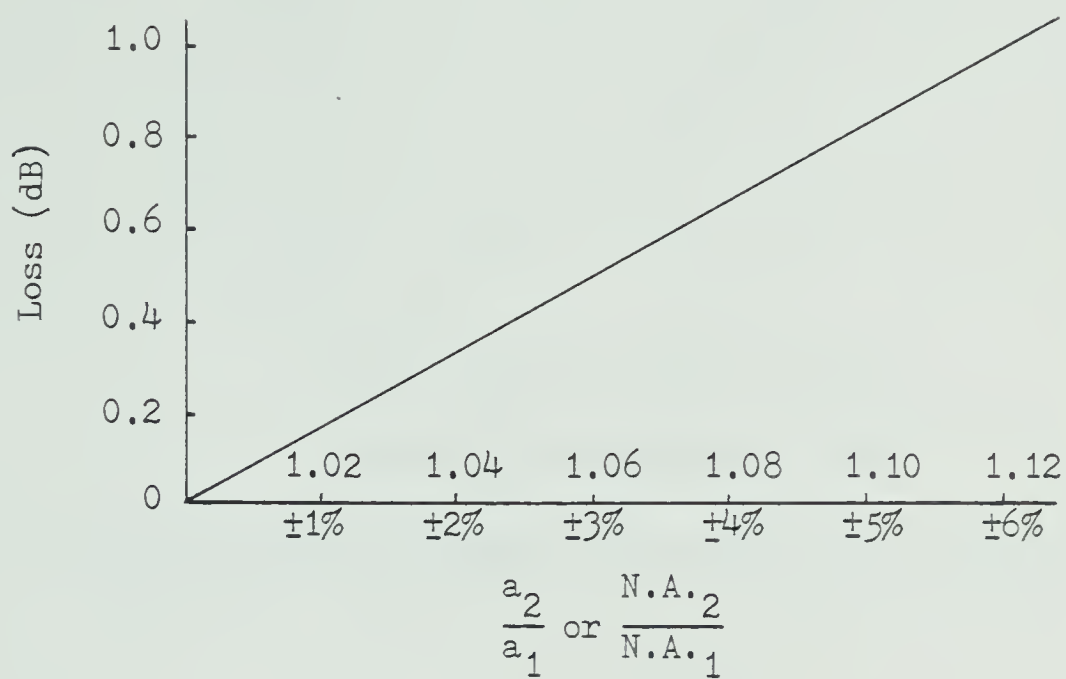


Fig. 5.11 Loss caused by mismatches in fiber core diameters or numerical aperture. The two effects are additive (After [13]).

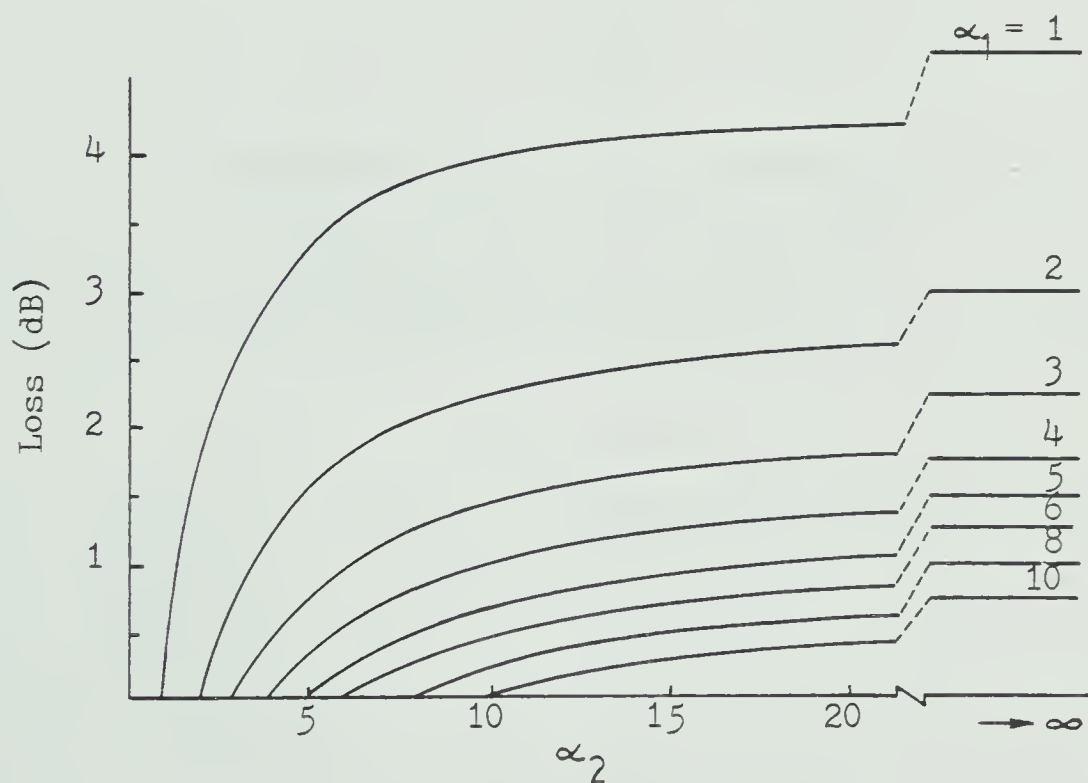


Fig. 5.12 Loss caused by mismatch in refractive-index profiles (After [13]).

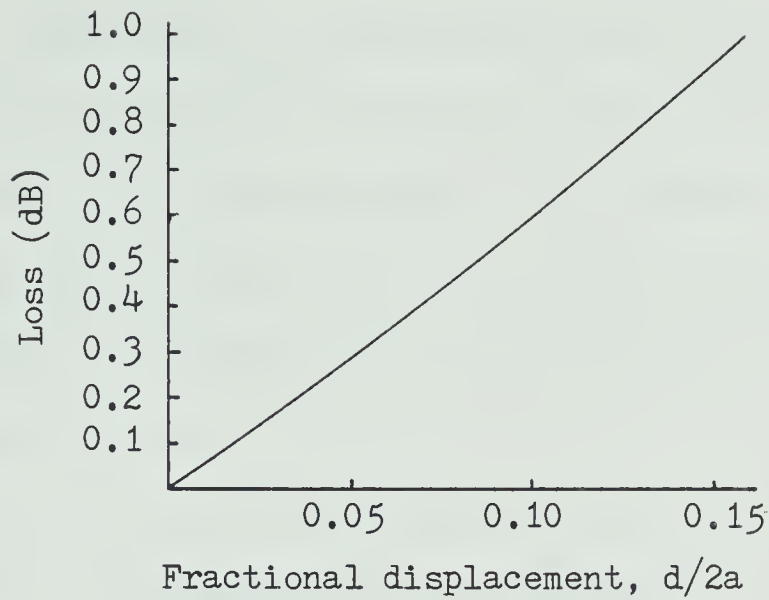


Fig. 5.13 Loss caused by lateral misalignment of centers of identical step-index fibers (After [13] & Dalglish [117]).

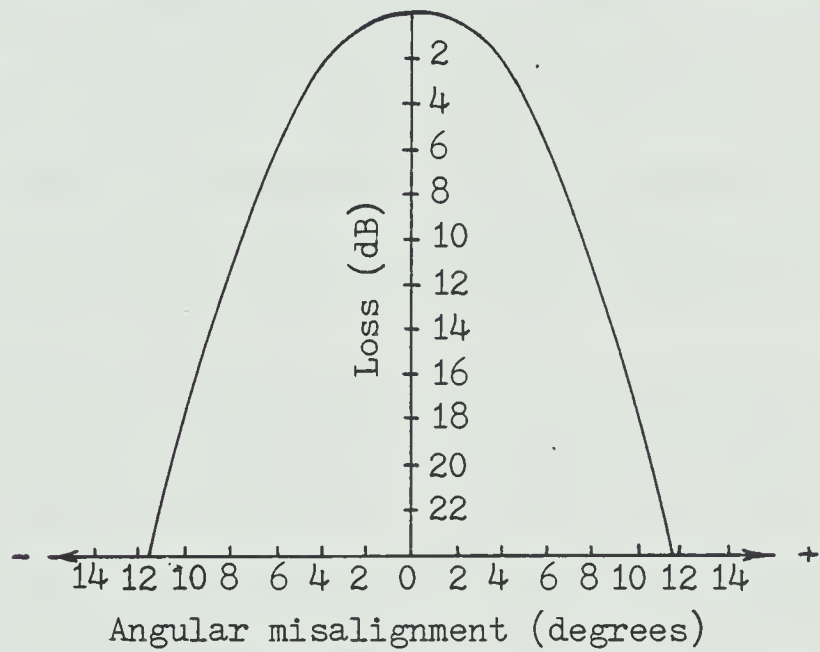


Fig. 5.14 Loss caused by angular misalignment of axes of identical step-index fibers (After [13]).

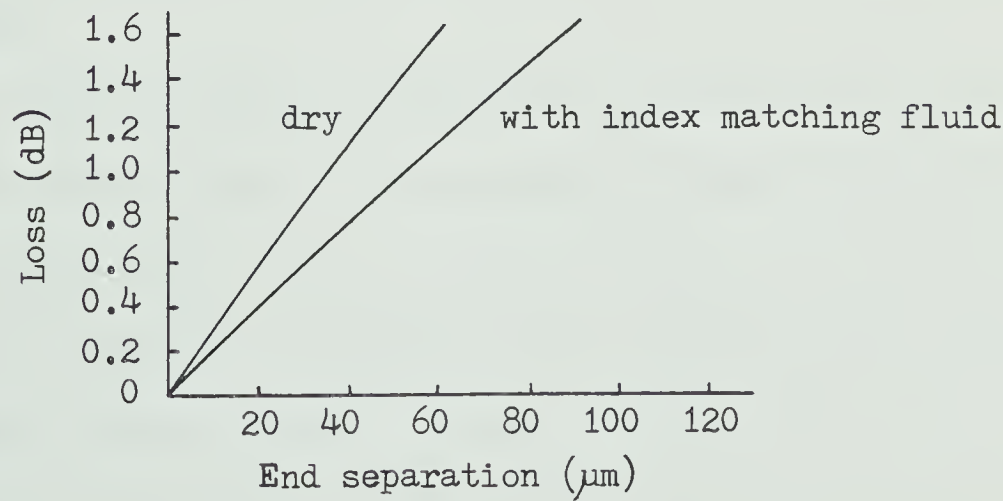


Fig. 5.15 Loss caused by separation of the ends of perfectly aligned identical step-index fibers (After [13]).

N.A. = 0.14. Separations of a few micrometers produce a perceptible loss. Fiber ends that are not finished smoothly result in scattering losses and Fresnel reflection losses. This problem is minimized by using index matching fluid at the joint. Even perfectly smooth ends will give Fresnel reflection losses of ~ 0.4 dB per joint in the absence of index matching fluid.

Similar results for graded-index fibers have recently been published [118]. Two experiments were performed — one using a fiber with a $50\text{ }\mu\text{m}$ core and $100\text{ }\mu\text{m}$ cladding diameters and the other using a fiber with a $55\text{ }\mu\text{m}$ core and $110\text{ }\mu\text{m}$ cladding diameters. Both fibers had a numerical aperture in air of 0.20. Besides measuring losses as a function of only lateral misalignment (offset), angular misalignment or end separation alone, the researchers also determined loss as a function of:

1. Normalized offset at various normalized separations.
2. Angular misalignment at various normalized separations.
3. Angular misalignment and various normalized offsets at constant separation.

Figure 5.16 is a plot of losses due to the three basic technique-related causes.

Fiber ends are generally prepared by scribing the fiber at the point of the desired break and then applying tension to the fiber. Mechanical stresses will cause the fiber to break at the scribed point with a very flat end face. Siemens AG has reported [119] a method of producing smooth ends on fibers by using a temperature shock cutting method. Heat is applied for a short time to any point along the fiber, then the fiber is given a little pull or push and it breaks at the

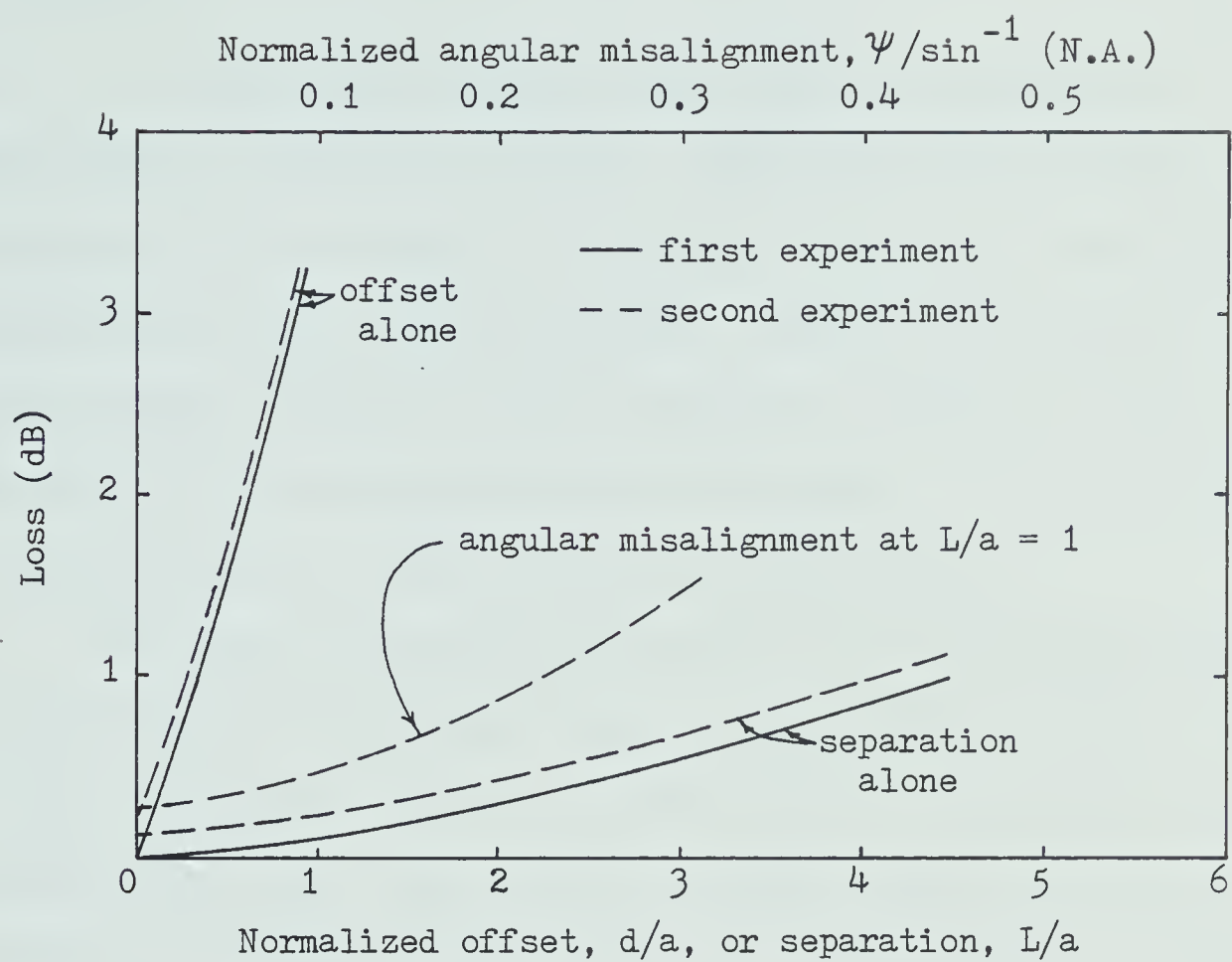


Fig. 5.16 Loss in dB vs. normalized offset d/a , separation L/a , and angular misalignment $\psi/\sin^{-1}(\text{N.A.})$ for graded-index fibers (After Chu and McCormick [118]).

point of thermal stresses. The end surfaces are reported to be extremely smooth and perpendicular to the fiber axis.

Splices

Experimental splices made to date can generally be categorized as mechanical or fused. Mechanical splices involve positioning the two fibers to be joined in some form of self-aligning mechanical structure, butted together, usually in the presence of an index-matching substance and then permanently fastened in some manner. Fused splices involve precision butting together of the two fiber ends and heating so as to cause the fiber to fuse together.

The use of precision-sleeve splices has been reported [120,121] for the joining of individual fibers. Fibers that have been stripped of their cladding are fed into a short piece of tubing which has a precision inner bore. Each end has a tapered alignment section to simplify the placement of the fibers. The fibers are then fastened by either crimping the sleeve on the fiber [120] or by the application of an adhesive [121]. Crimped splices of step-index fibers have reportedly exhibited losses of from 0.85 to 1.0 dB without index matching fluid and from 0.25 to 0.35 dB with index matching fluid. The glued splices have exhibited average losses of 0.25 dB for step-index fibers and 0.21 for graded-index fibers. Tensile strength tests on the crimped splices indicated that crimping did not weaken the fiber. Similar results were reported for the glued splices.

Bell Telephone Laboratories have introduced a loose-tube splice which uses a square tube whose inner dimensions are slightly larger than the optical fibers to be joined [122]. The tube is filled

with epoxy and the fibers are inserted in each end. Bending the fibers causes the tube to self-align the fibers. The fibers are then pushed together and held until the epoxy sets. Tests using this type of splice indicated average losses of less than 0.1 dB using graded-index fibers.

Bell Telephone Laboratories have configured a number of fibers into single-layer tapes [123,124]. These tapes have been successfully spliced by stripping away the tape material to reveal the individual fibers, simultaneously fracturing all the fibers with a hand-held tool, positioning the fibers in V-shaped grooves with index-matching epoxy and clamping in place until the epoxy sets. Splices involving tapes of individual fibers revealed losses of the order of 0.25 dB [125].

Another type of splice reported by Bell Telephone Laboratories uses no adhesives or mechanical clamps [55]. This splice involves placing one or more fibers to be connected in an aligning mechanism and then compressing an aluminum washer over the fibers such that the aluminum yields around a portion of each fiber. The pressure is below the breaking strength of the fiber and the aluminum is permanently bonded to the fibers without bonding to the aligning substrate. Index-matching fluid is retained in the washer by sealing off the hole on top and bottom. Experimental results of typical splices revealed an average of 0.25 dB loss for single-fiber splices and 0.33 dB loss for 3-fiber splices. Splices of this kind were found to have sufficient intrinsic strength to be used as splices of cable subgroups.

Fibers have been fused together to form splices. Fibers with good, flat end faces are butted together using some alignment

mechanism and then heated to cause the glass to melt and fuse together. One method reported uses a d.c. arc for a heat source [126] and another method uses a CO_2 laser [127]. Splices using the electric arc method exhibited average losses of 0.26 dB on step-index fibers with numerical apertures of 0.14. Splices made with the laser averaged less than 0.5 dB.

Connectors

In addition to splices, which are permanent connections, optical fiber cables will also require connectors which can be rematable. The precise aligning of fibers and the necessary precision in preparing end faces poses problems for connectors. Corning [128] has constructed connectors with fibers in a hexagonal array. This was accomplished in the laboratory by stripping the jacketing off the cable, inserting the fibers as a unit into a ferrule where they are bonded together and finishing the mating faces of each ferrule on metallographic polishing paper. Connectors for joining 61-fiber cables were fabricated and exhibited losses of less than 1 dB. The fibers were low-loss and had numerical apertures of 0.14. The losses included Fresnel reflection losses since no index-matching fluid was used.

Bell-Northern Research has developed single-fiber connectors for use with plastic-coated multimode fibers [117]. This is a variation of their crimped precision sleeve used for splices. The connector plug has tapered funnels leading to a central alignment bore. Longitudinal position of each fiber is accurately located by using a special fixture. Both the plug and its mating jack are mounted

separately on a fixture. Crimping the stainless steel tubing onto the fibers' plastic coating holds the fibers in place. When mated, the fibers are separated by a small gap. By using index matching fluid, typical losses average 0.8 dB [129].

Corning Glass Works and Deutsch Company have developed a connector for fiber-optic cables that exhibits losses of 0.3 dB [130]. Each individual fiber of the cable is held in place by cylindrical rods built into the connector housing, providing the necessary alignment accuracy. This connector is made to accommodate Corning's six-fiber CORGUIDE cable.

Amphenol RF and ITT Cannon reported in May, 1975 [131] that they could supply fiber-optic connectors. Amphenol RF have since marketed an eight-channel connector [132] which can accommodate individual fibers with diameters as small as $127\text{ }\mu\text{m}$. Total loss is reported to be 1.5 dB maximum per contact. This is due to keeping end separation from $2.5\text{ }\mu\text{m}$ to $33\text{ }\mu\text{m}$, axial misalignment (offset) to $5\text{ }\mu\text{m}$ and maintaining angular displacement less than 1° . ITT Cannon is presently marketing single-fiber connectors with typical losses of 2 dB and possible losses of 1 dB. These connectors will accommodate fibers with diameters from 100 to $150\text{ }\mu\text{m}$.

5.7 Summary

A number of techniques for coupling light into optical fibers have been examined. For the case of coupling a single optical source to a fiber, a direct coupler is the straightforward solution. More complex couplers allow the coupling of light from a number of sources into a fiber using wavelength-division multiplexing. The highest coupling

efficiencies have been attained using a prism-film coupler to couple light into a thin-film waveguide. An excellent method of coupling the light from the thin-film waveguide to a fiber is to use a tapered-film coupler. This combination of prism-film and tapered-film couplers will be assumed for the optical feeder system.

Various loss mechanisms in optical fiber connection have been examined. Splice losses in the order of 0.25 dB have been reported by different sources. Rematable connectors exhibit losses in the order of 1 dB or less.

It seems that coupling light among the various optical elements will, in principle, not be a serious problem in the optical feeder system.

CHAPTER 6

MODULATION AND MULTIPLEXING

Any system requiring the transmission of a multiplicity of signals over a common route is faced with a potential multiplexing situation. Considering the great number of antennas and the distances of transmission involved in the proposed radio telescope, some form of multiplexing appears necessary to minimize the cost of transmission line. From an economic standpoint, it must be recognized that such reductions of transmission line can result in increased complexity and costs of filters (in the case of FDM), mixers, couplers, splitters, frequency- or time-stable reference oscillators, etc.

In order to appreciate the quantities of transmission line involved under various multiplexing arrangements, it is necessary to examine some of the possible feeder system configurations.

6.1 Feeder System Configurations

The radio telescope, as currently envisaged, would be comprised of 2848 half-wave antenna dipoles (assuming a maximum density array, with no physical tapering) in a tee-shaped array, as shown in Fig. 6.1 [3]. There would be 1248 dipoles in the east-west subarray, 1568 in the north-south subarray and 32 in the common region of overlap. The dipole spacing would be $0.625\lambda_t$ centre-to-centre in the east-west direction and $0.5\lambda_t$ in the north-south direction where λ_t is the wavelength of the telescope signal (~ 24.27 m).

Each dipole would be supported above a plane reflecting screen at a distance of $0.125\lambda_t$.

It is assumed that the antenna signals will be brought to a location central to each group of antennas, where they will be multiplexed onto an optical fiber for transmission to the observatory. It is further assumed that the observatory will be located adjacent to the junction of the subarrays of the tee. The signals may be conveyed from the antennas to each central transmitting location (CTL) via coaxial cable or optical fiber and these will be termed "branch" feeders. The optical fiber transmission lines from the CTL's to the observatory will be termed "primary" feeders.

For purposes of calculating representative transmission feeder lengths, the array will be considered to contain the maximum number of dipoles (2848). Also, for simplicity of calculation, the array will be divided into rectangular groupings of various sizes containing various numbers of dipoles. Fundamental to this approach is the intention of conveying each antenna signal to the observatory. This implies no previous correlation of antenna signals out in the array. The grouping is only done for purposes of multiplexing, so the grouping configuration is not particularly important.

The types of antenna grouping that will be considered are shown in Fig. 6.2. In the north-south subarray, (A) refers to groups comprising eight dipoles in the lateral dimension, (B) refers to groups comprising four dipoles in the lateral dimension, (C) refers to groups with two dipoles in the lateral dimension and (D) refers to groups with only one dipole in the lateral dimension. The east-west subarray, having only four dipoles in its lateral dimension,

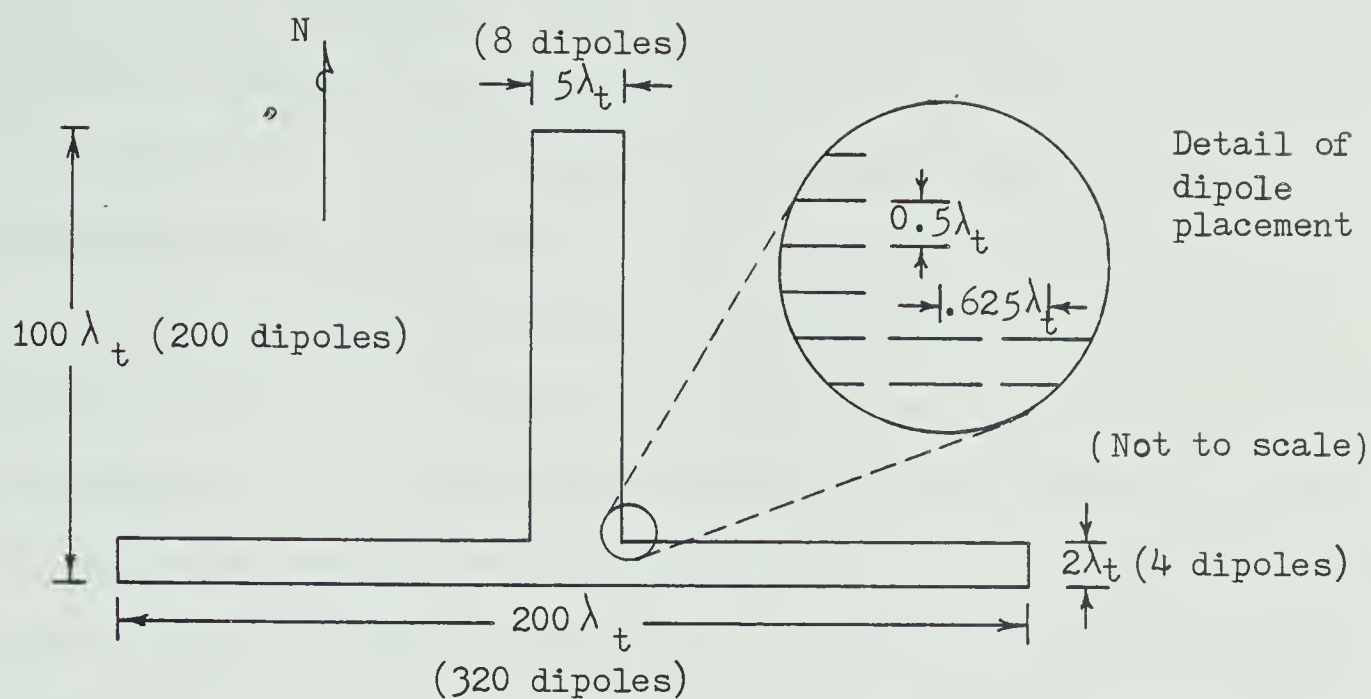


Fig. 6.1 Tee array configuration (After McLarnon [3]).

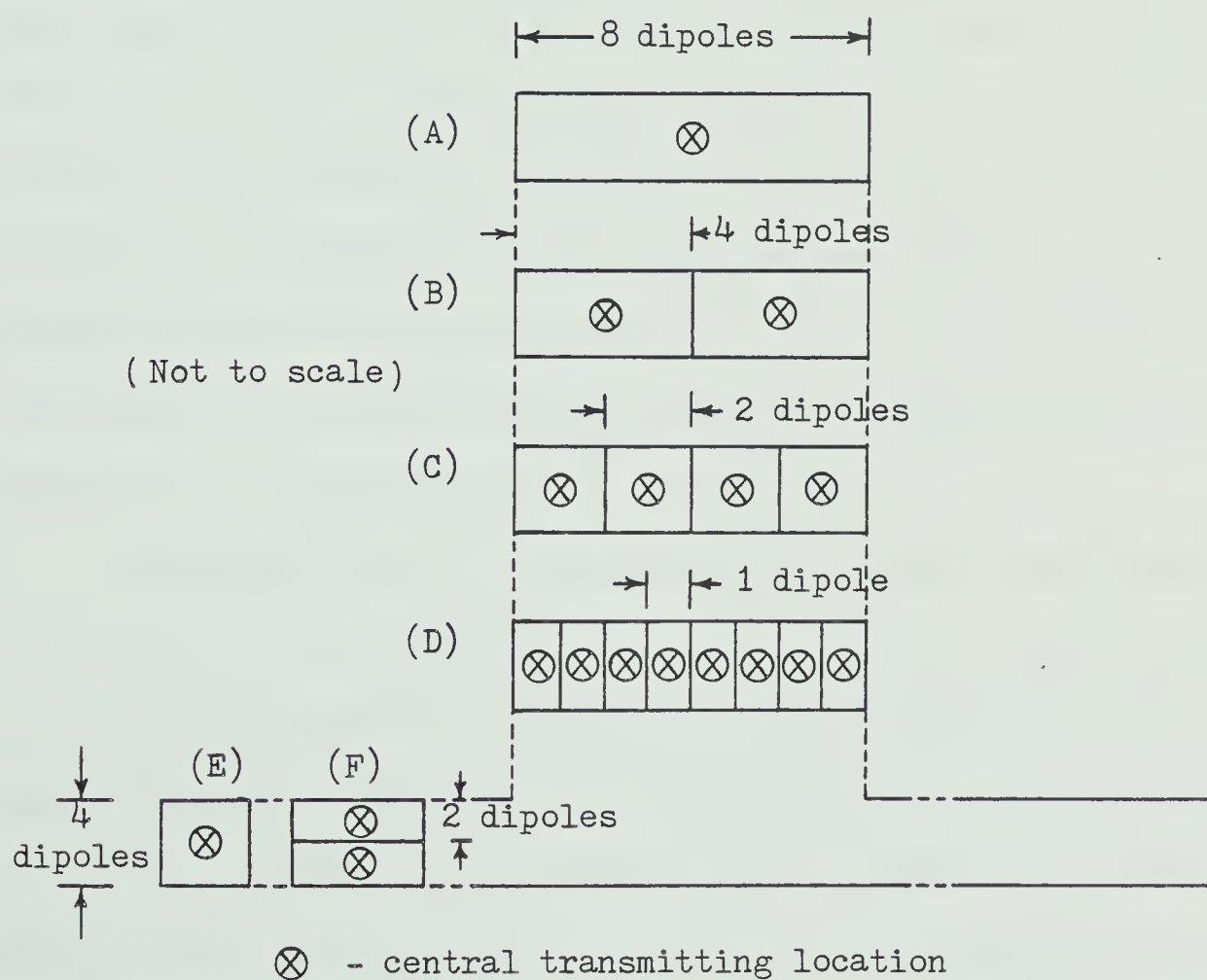


Fig. 6.2 Possible antenna groupings within the array.

will be divided according to group (E), with these four dipoles in the lateral dimension, and group (F), which has only two dipoles in the lateral dimension. The longitudinal length in each case will ultimately be set by the multiplexing capability.

This thesis will not address the problem of the physical placement of the optical fibers other than to mention a number of considerations. An underground trench may not be suitable since it is common experience in the telephone companies that underground cable plant is subject to water ingress. This could be catastrophic since experiments by Bell-Northern Research [133] indicate phenomenal increase in attenuation (~ 1000 dB/km) due to mechanical deformation by the ice around fibers. Water, as indicated in section 2.7, tends to cause physical deterioration of fibers. Ordinary aerial cable construction where communications cables are tied to a high-strength (usually steel) messenger cable might be a solution. This also would have to be waterproof or at least water-resistant. A metallic messenger could be a lightning hazard and it is not inconceivable that damage could result to even a dielectric optical fiber cable, perhaps due to extreme heating of the messenger.

Assuming the use of a cable such as Corning's CORGUIDE [11], which contains six (6) individual fibers and has an outside diameter of 5 mm, we can estimate the quantity of fiber required for the telescope project. Using only three (3) of these six (6) fibers for transmission purposes (the remainder could be spares), 550 cables would more than suffice to feed each of the 1600 dipoles in the north-south subarray and the overlap region. The 1248 dipoles in the east-west subarray would require 416 cables making a total of some 966

cables for the total array. With a number of multiplexed antenna signals, the number of cables decreases proportionately.

For purposes of analysis, the branch feeders within the antenna groups are presumed to be laid north-south and east-west in a Cartesian co-ordinate system. The branch feeder quantities are determined separately from the primary feeders since, depending upon factors such as economics and practicability, the branch feeders may be optical fibers or coaxial cables. For both branch and primary feeders, "minimum length" and "equal length" quantities are included. The "minimum length" quantity represents the shortest total length of transmission line required to convey the signals among the various locations in the array. The only consideration given is that the transmission line follow an approximately Cartesian co-ordinate system. No consideration has been given to the problems of phase and delay. "Equal length" quantities represent the total length of transmission line required when each individual transmission line is the same length as that required for the longest transmission line. The terms "minimum length" and "equal length" are exemplified in Appendix L.

The equal length technique obviously overcomes the phase and delay problems inherent in the minimum length system above, which would require extensive additional signal processing in the observatory, if it is practical at all. The equal-length technique, while obviously the most costly in terms of transmission line, has been used in a number of radio telescopes since it allows the greatest flexibility and minimizes decorrelation losses and excitation errors [3]. This thesis will assume the use of an equal-length feeder system.

An operating frequency of 12.36 MHz corresponds to a wavelength of about 24.27 meters. For the purpose of determining transmission line length, the (approximate) distances that are used are as shown in Fig. 6.3.

Transmission line quantities are presented in Table 6.1 for primary feeders and Table 6.2 for branch feeders. A sample calculation is included in Appendix L for the case of a 24 channel system.

The numbers listed in Tables 6.1 and 6.2 indicate the lengths of transmission line required for the various antenna dipole groupings considered. Since grouping (B) in the north-south subarray and grouping (E) in the east-west subarray has been considered for all channel groups (except for a 2-channel system), this combination has been used in a plot of transmission line length as a function of the number of channels multiplexed. This plot is presented in Fig. 6.4 with primary and branch feeders shown separately for a minimum-length and equal-length feeder configuration.

Fig. 6.4 clearly shows the advantages of multiplexing larger numbers of channels. For an equal-length system, some 865 km of transmission line is required for an 8-channel system whereas only about 245 km is required for a 48-channel system. Beyond about 28 channels, the total length of transmission line is virtually constant since any decrease in primary feeder length is offset by an increase in branch feeder length. From the viewpoint of transmission line saving, a 48-channel system is considered to be a reasonable maximum.

It should be emphasized that the transmission line quantities have been determined for a one-way, working-system configuration. No provision has been made for additional lines that may be required to

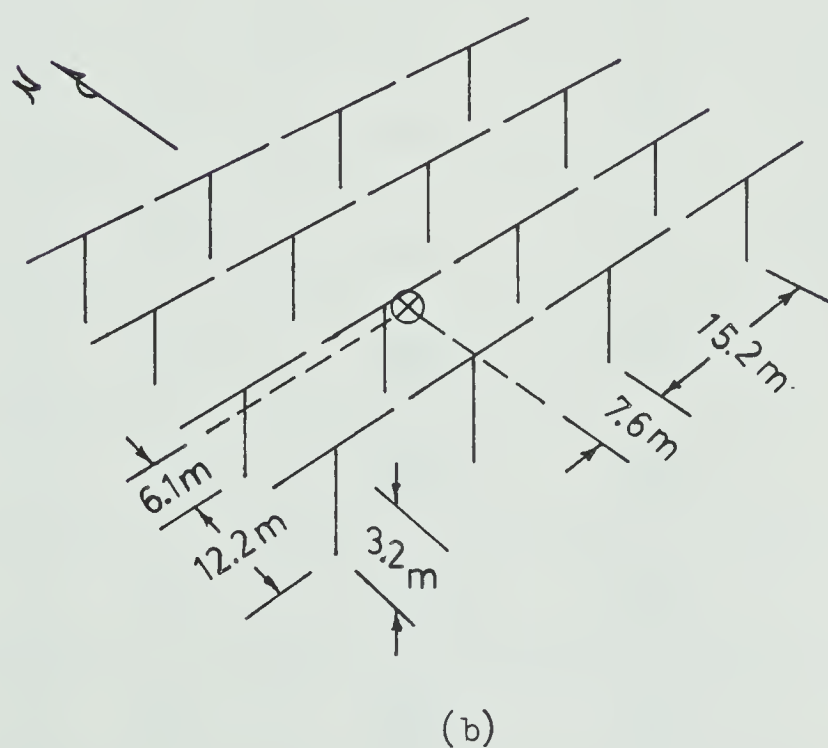
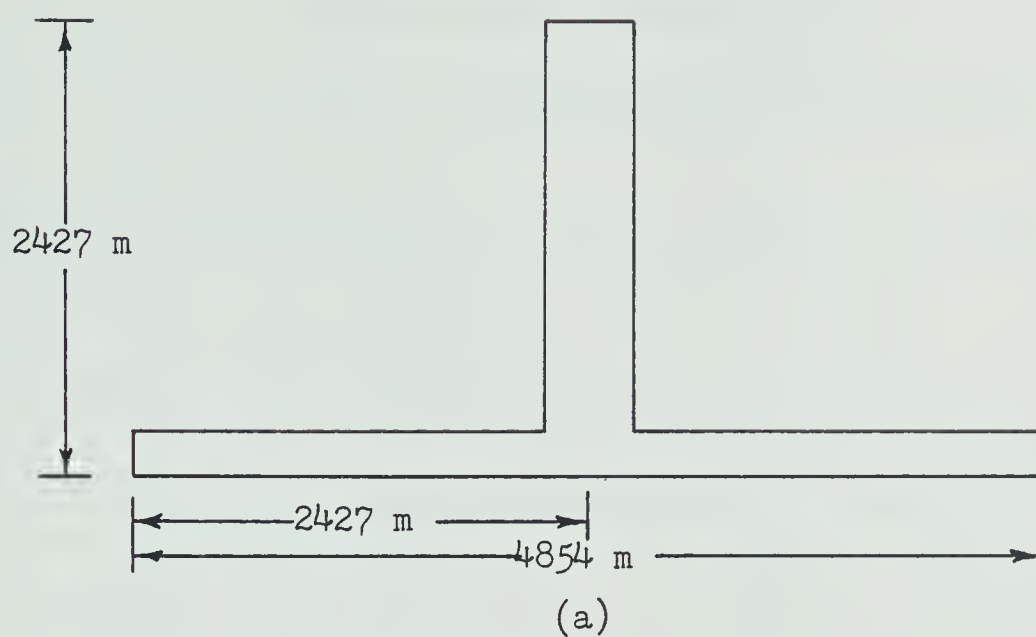


Fig. 6.3 Dimensions used to determine transmission line lengths
(a) overall array (b) inter-element.

Table 6.1

Primary Feeder Quantities (km)

Equal Lengths & Minimum Lengths (in brackets)

No. of Channels	N - S E - W	(A)	(B)	(C)	(D)
		(A)	(B)	(C)	(D)
2	(F)	—	—	—	3379.5 (1696.3)
4	(E)	—	1679.9 (846.0)	1683.2 (844.6)	—
	(F)	—	1682.0 (848.7)	1685.3 (847.4)	—
8	(E)	—	838.6 (422.3)	839.6 (421.3)	—
	(F)	—	835.7 (420.9)	836.7 (419.9)	—
12	(E)	—	558.1 (281.1)	563.0 (282.5)	—
16	(E)	—	417.5 (210.1)	416.6 (208.9)	—
20	(E)	—	333.4 (168.1)	332.2 (166.7)	—
24	(E)	287.4 (142.8)	291.4 (145.5)	—	—
28	(E)	239.9 (119.9)	240.0 (120.9)	—	—
32	(E)	206.0 (103.0)	206.2 (103.9)	—	—
36	(E)	184.2 (92.1)	186.7 (94.0)	—	—
40	(E)	166.7 (83.4)	166.7 (84.0)	—	—
48	(E)	143.9 (71.2)	143.5 (71.6)	—	—

Table 6.2

Branch Feeder Quantities (km)
Equal Lengths & Minimum Lengths (in brackets)

No. of Channels	N - S E - W	(A)	(B)	(C)	(D)
2	(F)	—	—	—	26.5 (26.5)
4	(E)	—	74.0 (48.7)	61.2 (46.3)	61.2 (43.9)
	(F)	—	74.0 (50.5)	48.1 (48.1)	61.2 (45.7)
8	(E)	—	91.4 (69.8)	82.9 (67.4)	—
	(F)	—	91.4 (67.9)	91.4 (65.5)	—
12	(E)	—	108.8 (74.4)	117.6 (78.4)	—
16	(E)	—	126.2 (87.1)	152.4 (94.5)	—
20	(E)	—	147.8 (97.4)	187.1 (110.6)	—
24	(E)	195.4 (114.4)	169.5 (106.2)	—	—
28	(E)	212.7 (125.1)	191.1 (116.0)	—	—
32	(E)	212.7 (129.9)	212.7 (125.2)	—	—
36	(E)	234.4 (136.1)	234.4 (133.3)	—	—
40	(E)	256.0 (142.2)	256.0 (144.2)	—	—
48	(E)	299.4 (159.0)	299.4 (163.6)	—	—

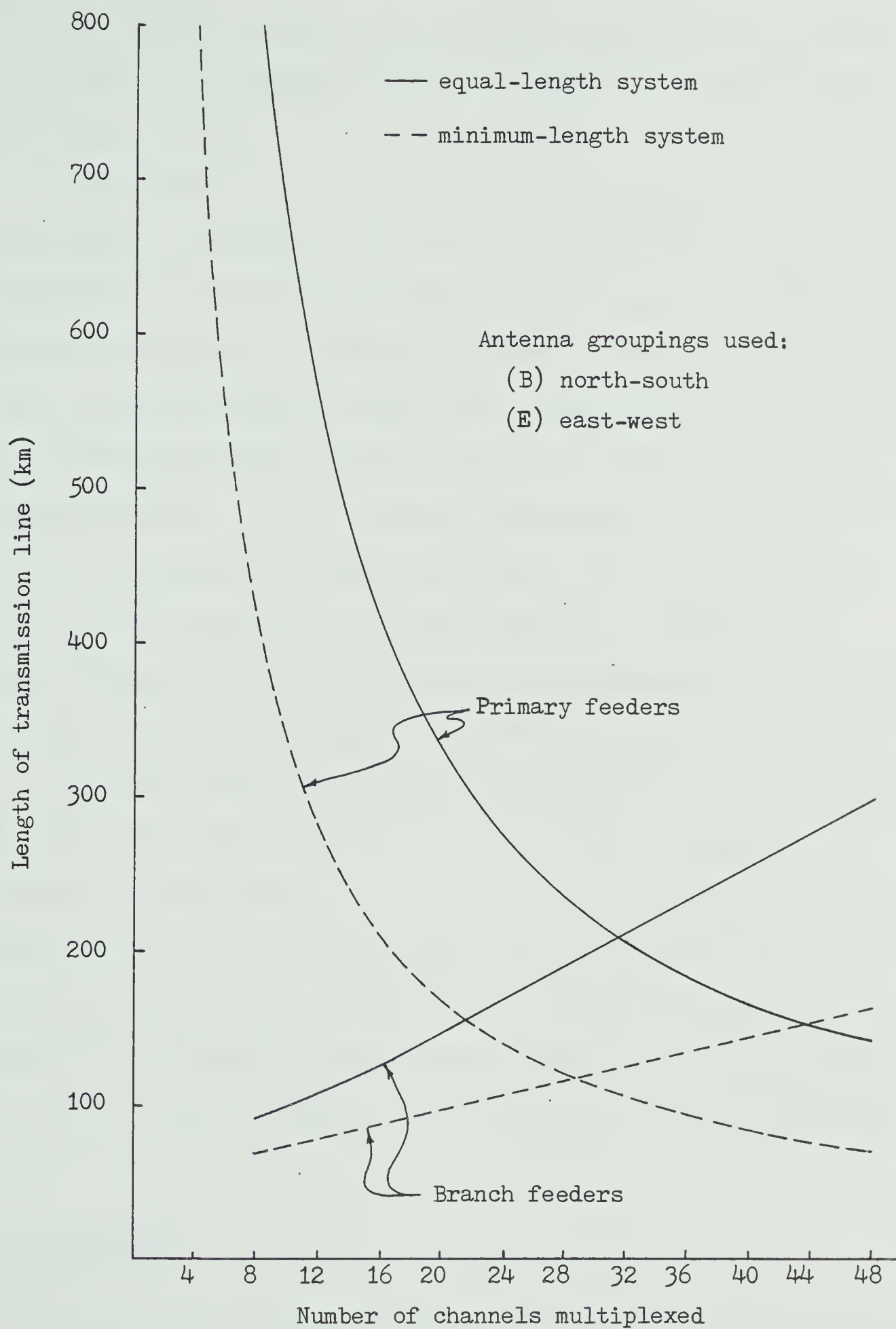


Fig. 6.4 Transmission line requirements as a function of the number of channels multiplexed.

convey local oscillator or synchronization signals from the observatory to the central transmitting locations. Similarly, no spare lines have been included.

The foregoing has been presented as an appreciation of the quantities of transmission line required for an array of the size and type planned for the radio telescope. Various dipole groupings have been considered for different numbers of channels multiplexed as has a minimum-length and equal-length configuration. Primary and branch-feeder quantities have been determined separately to allow maximum versatility for final design. Depending on factors such as costs and signal processing techniques, it may be decided, for example, to use optical fiber primary feeders and coaxial-cable branch feeders. In all likelihood, the branch feeders would probably be coaxial cable carrying the r.f. (electrical) signal to the CTL. This would save converting the r.f. antenna signal to optical form at the antenna and then converting it back to electrical form at the CTL for r.f. multiplexing. In any event, since the transmission line represents a major cost of any array, it is desirable to keep these quantities to a minimum. To accomplish this without forfeiting versatility and signal processing capability, it is required that as many antenna signals as possible be multiplexed onto the transmission lines.

6.2 Modulation

The types of modulation that are available for consideration are analog, pulse and digital [90]. Analog modulation methods are

characterized by a continuous variation of some carrier signal parameter such as amplitude, frequency, phase or polarization with an applied, continuous, modulating signal. Pulse modulation methods are characterized by the variation of some pulse parameter, such as amplitude, position or width, of a carrier pulse train. This variation is made to represent the instantaneous amplitude of a sampled analog signal and, as such, can assume an infinitum of values within the amplitude range. Digital modulation methods, on the other hand, are characterized by some carrier signal parameter, such as amplitude, frequency, phase or polarization, being encoded into a digital signal which represents either a quantized instantaneous value of a sampled analog signal or a data signal already in digital form.

The trend in communications is toward the use of digital modulation systems. This is due, in part, to the inherent simplicity of the digital signal and its associated advantages in generation, transmission and reception and also to the proliferation of economical digital integrated circuitry. In this light, the first modulation system to be considered will be a digital system.

6.2.1 Digital Modulation

Digital modulation is basically characterized by an information bit stream containing the presence or absence of bits within allocated time slots. There are two main categories of digital modulation — pulse code modulation (PCM) and differential pulse code modulation (DPCM).

A pulse code modulation system for use in the telescope project might be represented as shown in Fig. 6.6. The analog signal

from each antenna dipole could receive initial improvement such as amplification and filtering. This signal would then be sampled at a rate equal to, or greater than, the Nyquist rate (twice that of the highest frequency component), resulting in a signal having a pulse-amplitude-modulated (PAM) waveform. Each pulse of this PAM waveform would then be quantized to a discrete value, depending on the pulse amplitude and the number of discrete values allowed in the quantizing scheme. This particular value is then encoded into a digital binary "word" which emerges from the modulator. In this manner, the analog signal is transformed into a stream of digital pulses, the rate of which is determined by the sampling rate and the number of bits required to encode the amplitude information. This digital output can be transmitted directly over wire facilities, or can be used to modulate an analog carrier for radio or optical transmission. Depending on the carrier parameter being modulated, the following systems are possible [90]:

- PCM/IM (PCM/AM) — PCM Intensity (Amplitude) Modulation, also called PCM/ASK, amplitude shift keying. The carrier intensity (amplitude) is set at a maximum to represent a "one" bit and at minimum to represent a "zero" bit of binary code of information signal sample amplitude.

- PCM/FM — PCM Frequency Modulation, also called PCM/FSK, frequency shift keying. The carrier frequency is set at one of two possible values to represent a "one" or "zero" bit of binary code of information sample amplitude.

- PCM/PM — PCM Phase Modulation, also called PCM/PSK, phase shift keying. The carrier phase angle is set at a phase angle of zero or π radians with respect to a phase reference to represent "one" or "zero" bit of binary code of information signal amplitude.

- PCM/PL — PCM Polarization Modulation — linear type: The carrier is set in vertical polarization to represent the "one" bit and horizontal polarization to represent the "zero" bit of binary code of information signal sample amplitude; circular type: The carrier is set in right circular polarization to represent a "one" bit and left circular polarization to represent a "zero" bit of binary code of information sample amplitude.

The antenna signal, at the input to the sampler in Fig. 6.6, will contain frequency components up to the highest frequency of interest, ie: $f_h = 12.46$ MHz. The minimum sampling rate, or Nyquist rate [134], that an analog signal can be sampled at, and yet be totally reconstructed back to its analog form is twice that of the highest frequency component present in the signal. This Nyquist rate requires that the signal be bandlimited by an ideal (low pass) rectangular filter with an impulse response [135]

$$v(t) = \frac{\sin 2\pi f_h t}{2\pi f_h t} \quad (6.1)$$

Since ideally bandlimited waveforms are physically unrealizable, sampling, in principle, always introduces a certain amount of distortion due to aliasing. In practice, this distortion becomes negligible when the signal is effectively bandlimited and

the sampling rate chosen accordingly. In telemetry systems, the sampling rate may be three [136] to five [137] times that of the highest frequency component of the signal. Conventional PCM systems used in the North American telephone network sample voice channels at 8 KHz, providing a useable bandwidth of 3.5 KHz [49]. This corresponds to a sampling rate of ~ 2.29 times that of the highest useable frequency.

Assuming the minimum sampling rate of twice that of the highest frequency component, a rate of ~ 25 MHz would be required to extract the antenna signal information. Depending upon aliasing distortion due to non-ideal filters, a somewhat higher sampling rate would probably be required. At three times the rate of the highest frequency component, a sampling frequency of ~ 37.5 MHz would be required.

In order to transmit a pulse train at a rate of 25 Mb/s the transmission system would require a maximum dispersion of about 20 ns. If the pulse train was at 37.5 Mb/s, the dispersion should be no more than 13 ns. If the PAM samples were quantized and encoded into digital words of, say, 5 bits to represent $2^5 = 32$ possible quantized amplitude values, the transmission line rate would now be 125 Mb/s or 187.5 Mb/s, depending on the sampling rate (assuming return-to-zero RZ binary digit coding). This would correspond to a maximum allowable dispersion of 4 nsec or 2.6 nsec, depending on the sampling rate. Since the transmission line runs are some $2\frac{1}{2}$ kilometers in length, this would require a maximum dispersion of 1.25 nsec/km or 1 ns/km assuming a linear increase in dispersion with length. This is currently attainable for multimode, graded-index fibers at $0.85\text{ }\mu\text{m}$ wavelengths. Even if the digital code words contained, say 3 bits to

represent only $2^3 = 8$ possible quantized amplitude values, the dispersion could only be relieved by a factor of about 2. This would still only allow a maximum of about 4 antenna signals to be time-division multiplexed over an optical fiber. In view of the foregoing, the PCM system concept was abandoned.

A differential pulse code modulation system can be represented as shown in Fig. 6.7. In this system, the signal that is sampled and coded is the difference between the input signal and a prediction signal based on past samples [49]. When this difference signal is coded into a single binary digit, this DPCM system is known as a delta modulation (Δ -mod) system.

DPCM is used in applications such as video transmission, where successive information samples are highly correlated [49]. In such a case, for the same signal-to-distortion ratio S/D , DPCM can result in a lower digital rate than PCM. However, for signals with a noise-like flat spectrum, as expected in the radio telescope, there is little or no correlation between successive samples. In this case, for the same S/D ratio as PCM, DPCM will require a higher digital rate [49]. Sampling at a higher rate provides the needed correlation between samples, but since the digital rate is increased proportionately, the trade is an inefficient one. For this reason, DPCM or Δ -modulation is not considered as being particularly advantageous over PCM in this application.

6.2.2 Pulse Modulation

A pulse modulation system for use in the telescope project would be comprised essentially of the same elements as the

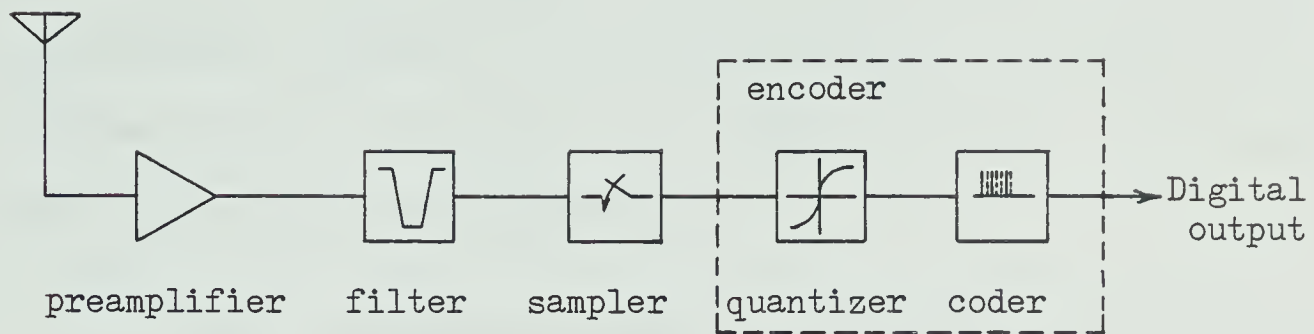


Fig. 6.5 Basic PCM transmitter.

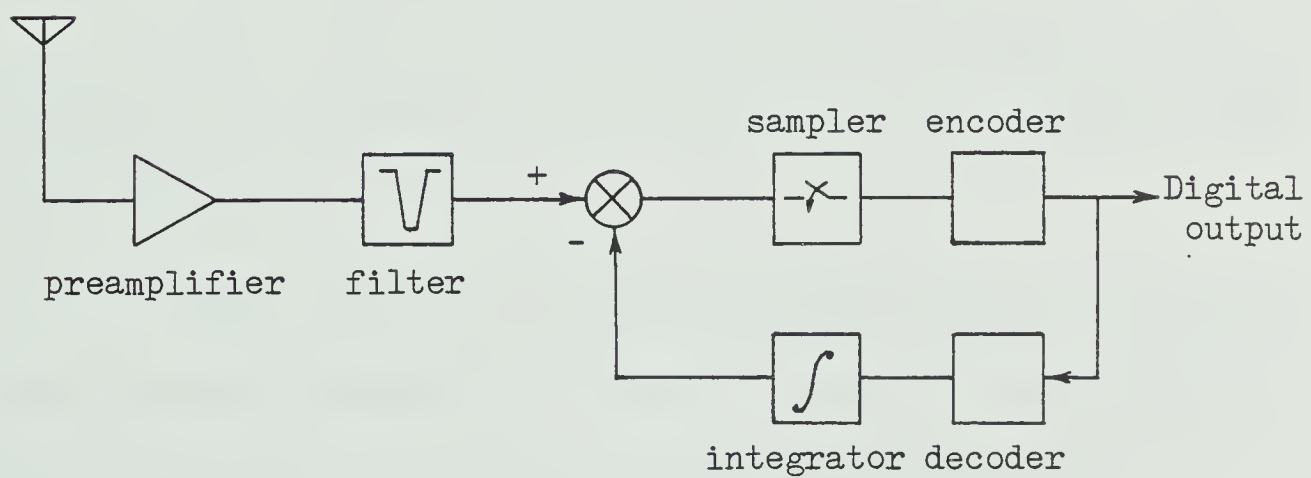


Fig. 6.6 Basic DPCM transmitter (After [49]).

digital system in Fig. 6.5. The quantizer may, or may not, be required but the main difference lies in the encoder. In a pulse modulation system, the encoder performs the modulation of some parameter of a carrier signal or pulse train with the instantaneous (or quantized) amplitude of the sampled waveform. Depending on the parameter chosen to represent these sample amplitudes, the following modulation methods are possible [90]:

- PAM — continuous or quantized Pulse Amplitude Modulation — pulsed carrier electric field amplitude is set proportional to information signal sample amplitude.

- PFM — continuous or quantized Pulse Frequency Modulation — pulsed carrier frequency is set proportional to information signal sample amplitude.

- PIM — continuous or quantized Pulse Intensity Modulation — pulsed carrier intensity is set proportional to information signal sample amplitude.

- PDM — continuous or quantized Pulse Duration Modulation — pulsed carrier duration, with respect to start of sample period, is set proportional to information signal sample amplitude.

- PPM — continuous or quantized Pulse Position Modulation — time delay of initiation of a short-duration carrier pulse is set proportional to information signal sample amplitude.

- PRM — Pulse Rate Modulation — number of short-duration carrier pulses per unit time period is set proportional to information signal sample amplitude.

In the previous section on digital modulation, it was established that the sampling rate would be at least 25 MHz and possible 37.5 MHz or higher. Assuming that the lower rate would be satisfactory, this suggests that the maximum allowable dispersion from transmitter to receiver would be about 20 nsec, except for PRM. On the longest transmission line run of 2 1/2 kilometers, this dispersion corresponds to 8 nsec/km (assuming linear increase in dispersion with length). If the sampling rate was 37.5 MHz, the maximum dispersion would be limited to about 13 nsec or 5.2 ns/km for the 2 1/2 km runs. In Chapter Two it has been shown that this amount of dispersion is well within the capabilities of present fibers. This indicates that a PAM (or PIM) modulation system is a viable method of transmission for the telescope project. PFM would not be possible, since the carrier frequencies of optical sources can not readily be varied in accordance with some modulating signal. In a PDM system, the modulating signal information is determined by the position of the trailing edge of the carrier pulses. Accurate information transmission then requires rapid pulse rise and fall-times. This, in effect, increases the bandwidth requirement of the system and, therefore, reduces the allowable dispersion. For this reason, a PDM system (and, similarly, a PPM system) is not considered a logical contender for the telescope project. A PRM system would obviously also suffer more from dispersion than the PAM signal since it necessarily transmits pulses at a rate higher than the PAM frequency.

While a PAM (or PIM) system would be a satisfactory transmission scheme, multiplexing would not appear to be feasible. Increasing the number of signals to be transmitted would again increase the transmission line rate and, therefore, the dispersion problem.

Transmitting a single signal via PAM (or PIM) would also require considerably more complicated hardware than, say, an intensity-modulated (IM) analog system.

Since pulse-modulation methods have not yielded a satisfactory solution for a multiplexed transmission system, analog methods will be examined next.

6.2.3 Analog Modulation and Frequency Division Multiplexing

Analog modulation techniques which are available include the following [90]:

- PL — analog Polarization Modulation — linear type: angle of linear carrier polarization with respect to reference axis is set proportional to information signal amplitude; circular type: ratio of carrier intensity in right-to-left polarization states is set proportional to information signal amplitude.

- IM — analog Intensity Modulation — carrier intensity is set proportional to information signal amplitude.

- FM — analog Frequency Modulation — carrier instantaneous frequency is set proportional to information signal amplitude.

- PM — analog Phase Modulation — carrier phase angle is set proportional to information signal amplitude.

- AM — analog Amplitude Modulation — carrier electric field amplitude is set proportional to information signal amplitude.

Polarization modulation is not being considered since it was

established in section 2.6 that polarized signals become rapidly depolarized in optical fibers.

Intensity modulation is being presumed for the optical signal transmission section in Fig. 1.2. As has been discussed in the chapter on sources, the output power (not the amplitude) of light sources is proportional to the driving current. Also, the output current from a photodetector was seen to be proportional to the input power (intensity). In this respect, an intensity-modulation system is the only logical choice for the optical section, regardless of whether the driving, or modulating, input be continuous (ie: analog) or discrete (ie: pulsed or digital).

6.2.3.1 Frequency and Phase Modulation

Frequency modulation is a widely used technique for transmitting high-quality signals, such as high-fidelity and stereophonic radio broadcasting and the audio portion of television. The advantages of FM (over AM) are well-known and the principles are covered in a great many textbooks on communication systems.

Considering the use of FM for the telescope project suggests a minimum modulation index m of ~ 0.5 for noise performance at least equal to that achievable with a DSB-AM system. Assuming a baseband modulating signal f_m of 12.5 MHz, the required bandwidth, as determined by Carson's rule [134], would be

$$B = 2(m + 1)f_m$$

$$= 37.5 \text{ MHz}$$

This bandwidth would require a maximum transmission line dispersion of about 13.3 nsec or 5.32 nsec/km for the 2 1/2 km runs. This is well within the capabilities of contemporary optical fibers. Reducing the modulation index to, say, 0.2 would still require a bandwidth of 30 MHz, which would not substantially improve the multiplexing capabilities. It would, however, result in a system having 7.4 dB lower signal-to-noise ratio than a DSB-AM system, according to eq. (9.3-1) of ref. [134]. Similarly, an increase in modulation index to, say, 1.0 would result in a required bandwidth of 50 MHz which would limit the maximum possible dispersion to about 10 nsec or 4 nsec/km for the 2 1/2 km runs. While a modulation index of 1.0 would provide some 6.5 dB S/N improvement over DSB-AM, possibilities of multiplexing more than two or three 50 MHz channels onto contemporary fibers would be questionable. Future fibers, however, will undoubtedly exhibit much lower dispersion rates, permitting a number of such relatively wide bandwidth channels to be multiplexed.

The foregoing discussion has been based on modulation by a single sine wave, and on the use of Carson's rule which determines the bandwidth required to pass at least 98% of the power in an FM signal. In practice, a modulating waveform is rarely sinusoidal. Plotkin [138] has compiled curves relating modulation index m and distortion D due to band-limiting for the two extreme cases of sinusoidal and white-noise modulation down as low as a modulation index of 1.0. For the white-noise case, Plotkin has determined the following approximate relationship:

$$B = \left[\frac{m^2}{6.834} (-10 \log_{10} D - 10 \log_{10} m^2) \right]^{1/2} - 0.05m + 0.75 \quad (6.2)$$

where

$$D = \frac{P_{FM} - P'_{FM}}{P_{FM}}$$

and P_{FM} is the power in the unmodulated carrier or unbandlimited signal

P'_{FM} is the power in the bandlimited FM signal.

Curves are plotted using eq. (6.2) for distortion values down to -80 dB in Fig. 6.7. For comparison purposes, the bandwidth as specified by Carson's rule is shown as a dotted line. Since the modulating signals from the dipole antennas will be virtually white noise, these curves can be used to relate the modulation index to the required bandwidth for a specified distortion requirement. Surprisingly, for a modulation index less than about 1.0, the bandwidth required is less than that specified by Carson's rule — at least for distortion levels down to -80 dB. As the modulation index increases above 1.0, the required bandwidth exceeds that specified by Carson's rule, particularly for distortion values of -50 dB or lower.

It was stated in section 1.1 that the amplitude error of the radio telescope is required to be in the order of 2%. For the output of a two-element correlator to have amplitude errors of 2% requires that each of the inputs have amplitude errors of about 1% (assuming ideal correlation). This is equivalent to a distortion of -40 dB. An examination of Fig. 6.7 reveals that this distortion criterion can be met with a bandwidth less than that dictated by Carson's rule.

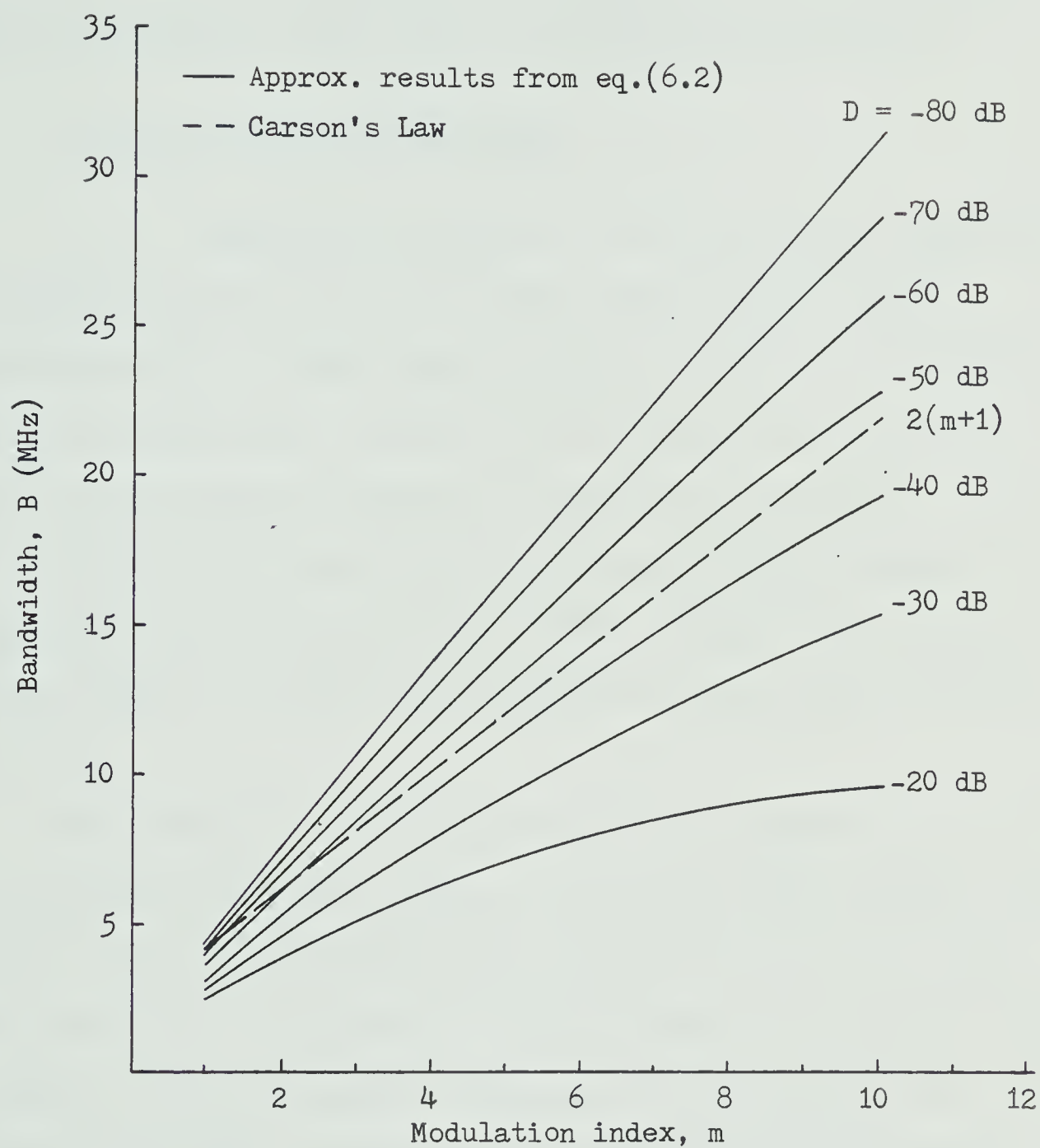


Fig. 6.7 Frequency modulation bandwidth for noise modulation (After Plotkin [138]).

For a modulation index of 1.0, Carson's rule specifies a bandwidth of 4 times the highest modulating frequency while Fig. 6.7 indicates a requirement of about 3 times the highest modulating frequency. This marginal decrease in bandwidth would not make an FM system appear much more attractive than it does with sinusoidal modulation.

6.2.3.2 Amplitude Modulation

Amplitude modulation is one of the oldest modulation techniques known and, yet, it is still widely used in modern applications such as FDM telephony systems, television video transmission and radio broadcasting. Details of AM techniques are described in detail in the numerous textbooks on communications systems. The options that are available include double-sideband transmitted-carrier (DSBTC), double-sideband suppressed-carrier (DSBSC), single-sideband suppressed-carrier (SSBSC or just SSB) and vestigial sideband (VSB) as shown in Fig. 6.8.

Both DSBTC and DSBSC occupy a spectral bandwidth twice that of the baseband modulating signal. In the case of the proposed radio telescope, the baseband signal might extend out to about 12.5 MHz. This would result in a frequency translated spectrum of about 25 MHz in bandwidth about the carrier frequency. By a suitable choice of carrier frequencies, a number of these signals can be multiplexed for transmission to the observatory. Again, the problem of dispersion must be considered. A 25 MHz bandwidth will require a transmission line dispersion less than about 20 nsec, or 8.0 nsec/km for the 2 1/2 km run. Assuming the use of a 200 MHz.km graded-index fiber

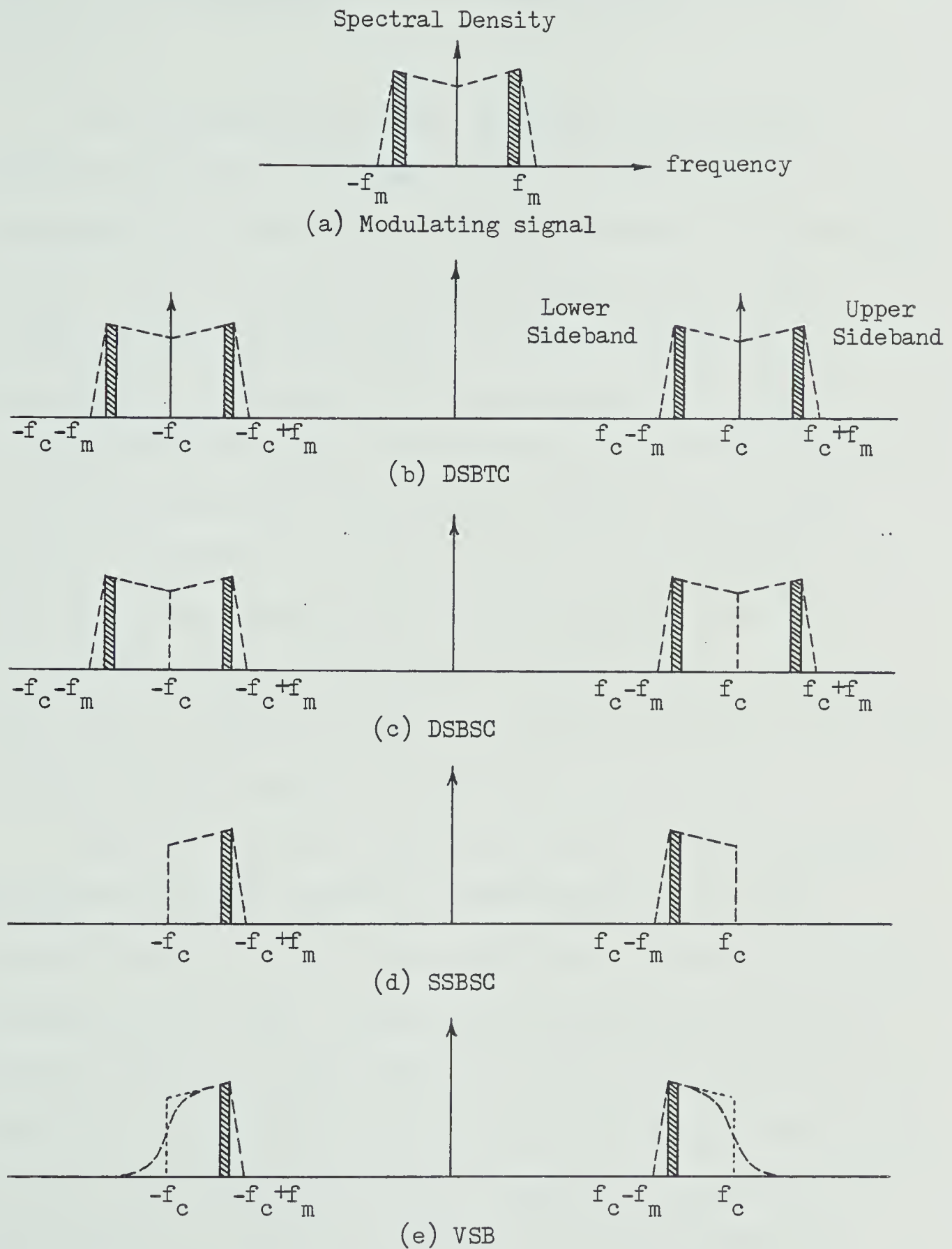


Fig. 6.8 Amplitude modulation waveforms (a) Modulating signal (b) Double-sideband, transmitted carrier (c) Double-sideband, suppressed carrier (d) Single-sideband, suppressed carrier (e) Vestigial-sideband.

(dispersion about 2.5 nsec/km), this would allow a maximum of three signals to be multiplexed into the 80 MHz available on a 2 1/2 kilometer run.

If the baseband signal does not contain low-frequency components, there is no spectrum to provide a gradual cutoff characteristic and hence there would be no advantage to VSB modulation over SSB. Fig. 6.8 shows the effect of modulating the entire baseband, as shown in dotted lines, or merely a portion of the baseband, shown in solid line and cross-hatched. In the case of the proposed radio telescope, the signals of interest are considered to lie in a narrow band of some 200 KHz in width around a center frequency of 12.36 MHz. In this case, it would seem desirable to filter out all other frequencies except those within this narrow passband, and multiplex these signals onto the optical transmission system. Such a system employing SSB "passband" modulation could have a frequency spectrum similar to that in Fig. 6.9..

Fig. 6.9 illustrates that the (center-to-center) frequency separation δf_c between channels is determined by the allowable crosstalk criterion (in this case, x decibels) and the type and order of bandpass filter used. McLarnon [3] determined that, in order to maintain an excitation phase error of 0.1° rms, the maximum allowable crosstalk was -55 dB for the filters and -60 dB for the coaxial cable. An optical fiber transmission line is expected to easily meet the -60 dB criterion. Section 2.5 indicated that the far-end fiber crosstalk should be much lower than -70 dB in the 2 1/2 km transmission runs. In this respect, it would seem logical to consider filters with comparable performance. This would also provide a factor of 5

improvement in excitation phase error, from 0.1° rms down to 0.02° rms according to McLarnon [3].

It is not within the scope of this thesis to provide a major investigation into the optimum type of filters to use in the multiplexing system, but a cursory examination would seem in order. It is known that, in general, attenuation and phase (ie: group delay) characteristics tend to offset one another [139]. Filters with flat passbands, such as the Butterworth, tend to have relatively severe phase and group-delay distortion which becomes even worse as the order of the filter is increased to improve its attenuation characteristic. Allowing an increase in the amount of amplitude ripple in the passband, as in the Chebyshev filter, tends to further improve the attenuation skirt steepness characteristic, but also results in deterioration of the phase characteristic. Since the preservation of phase and relative delay throughout the 200 KHz passband is an important consideration for a correlation array such as the proposed radio telescope, it is necessary to give due consideration to the phase as well as the amplitude characteristic.

There is a class of filters known as Gaussian filters which provide a highly linear phase characteristic across the passband [139]. As expected, the attenuation characteristic is Gaussian in shape. Within this class is the Bessel filter, or maximally-linear phase filter. This filter produces a virtually flat phase characteristic within the passband and an attenuation characteristic slightly improved over the basic Gaussian filter except near the cutoff frequency.

Another filter, known as a transitional filter, combines the

attenuation discrimination characteristics of the Butterworth and the group-delay characteristics of the Gaussian filters [139]. A transitional filter which is Gaussian to 12 dB is seen to exhibit relatively flat group delay (linear phase) well beyond the 3 dB frequency cutoff [139].

If the governing criterion is phase integrity, with a certain allowable amplitude distortion, the Bessel or Maximally-Linear Phase filter would seem a likely choice. If the system can tolerate some phase and group delay distortion and it is required that the amplitude distortion be kept to an absolute minimum, a Butterworth filter would be an eligible choice. If minimum phase distortion and maximum frequency discrimination are required, a transitional filter should be considered. Table 6.3 is provided which lists the bandwidths required for these three types of filter as a function of attenuation discrimination and the number of reactive elements. These bandwidths were determined from data obtained from graphs [4,139] using a nominal passband of 200 KHz. Table 6.4 presents essentially the same information but in a different manner. In this table, the type of filter along with the minimum number of reactive elements is given which can provide a specific amount of attenuation in a given bandwidth. The bandwidths are arbitrarily chosen from 0.5 MHz to 2.0 MHz to represent potential multiplexed channel bandwidths.

Assuming the use of a 200 MHz.km optical fiber (ie: ~ 2.5 nsec/km dispersion), the longest transmission line runs of 2.5 km would have a total bandwidth available of 80 MHz. If the multiplexed signals are allowed to occupy only the spectrum above 12.36 MHz for convenience, this still leaves some 68 MHz of bandwidth. Allowing a bandwidth

Table 6.3

Bandwidth vs. Attenuation Discrimination

For 3 dB Bandwidth Separation of 200 KHz

Attenuation	Butterworth		Bessel		Transitional (Gaussian to 12 dB)	
	No. of Poles	B (MHz)	No. of Poles	B (MHz)	No. of Poles	B (MHz)
-70 dB	8	0.54	10	0.92	10	0.60
	7	0.62	9	0.96	9	0.68
	6	0.76	8	1.04	8	0.74
	5	1.00	7	1.14	7	0.88
	4	1.50	6	1.32	6	1.08
	3	--	5	1.60	5	1.46
			4	--	4	--
-65 dB	8	0.52	10	0.86	10	0.56
	7	0.58	9	0.90	9	0.64
	6	0.70	8	0.96	8	0.70
	5	0.88	7	1.04	7	0.82
	4	1.30	6	1.20	6	1.00
	3	--	5	1.42	5	1.30
			4	1.90	4	1.90
-60 dB	8	0.48	10	0.84	10	0.55
	7	0.54	9	0.85	9	0.60
	6	0.62	8	0.88	8	0.65
	5	0.80	7	0.94	7	0.76
	4	1.12	6	1.08	6	0.90
	3	2.00	5	1.28	5	1.16
			4	1.66	4	1.64
-55 dB	8	0.44	10	0.78	10	0.52
	7	0.50	9	0.80	9	0.56
	6	0.58	8	0.84	8	0.62
	5	0.72	7	0.88	7	0.70
	4	0.98	6	0.98	6	0.82
	3	1.62	5	1.12	5	1.04
			4	1.44	4	1.40

Table 6.4

Channel Spacing vs. Filter Types (minimum poles & zeros req'd) -- 0 dB Ripple in Passband!

Attenuation	0.5 MHz	0.6 MHz	0.8 MHz	1.0 MHz	1.5 MHz	2.0 MHz
-70 dB	Butterworth 9 Poles	Butterworth 8 Poles	Butterworth 6 Poles	Butterworth 5 Poles Bessel 9 Poles	Butterworth 4 Poles Bessel 6 Poles	Butterworth 4 Poles Bessel 5 Poles
		Transitional 10 Poles	Transitional 8 Poles	Transitional 7 Poles	Transitional 5 Poles	Transitional 5 Poles
-65 dB	Butterworth 9 Poles	Butterworth 7 Poles	Butterworth 6 Poles	Butterworth 5 Poles Bessel 8 Poles	Butterworth 4 Poles Bessel 5 Poles	Butterworth 4 Poles Bessel 4 Poles
		Transitional 10 Poles	Transitional 8 Poles	Transitional 6 Poles	Transitional 5 Poles	Transitional 4 Poles

Table 6.4 (continued)

Attenuation	0.5 MHz	0.6 MHz	0.8 MHz	1.0 MHz	1.5 MHz	2.0 MHz
-60 dB	Butterworth 8 Poles	Butterworth 7 Poles	Butterworth 5 Poles	Butterworth 5 Poles Bessel 7 Poles	Butterworth 4 Poles Bessel 5 Poles	Butterworth 3 Poles Bessel 4 Poles
		Transitional 9 Poles	Transitional 7 Poles	Transitional 6 Poles	Transitional 5 Poles	Transitional 4 Poles
-55 dB	Butterworth 7 Poles	Butterworth 6 Poles	Butterworth 5 Poles Bessel 9 Poles	Butterworth 4 Poles Bessel 6 Poles	Butterworth 4 Poles Bessel 4 Poles	Butterworth 3 Poles Bessel 4 Poles
		Transitional 9 Poles	Transitional 7 Poles	Transitional 6 Poles	Transitional 4 Poles	Transitional 4 Poles

of 2 MHz for each channel, up to 34 signals can be multiplexed into this band. Restricting the channel bandwidth to 1 MHz would allow up to 68 multiplexed signals. Continued reduction in channel bandwidth results in even greater multiplexing capability albeit at greater complexity in filtering.

Fig. 6.10 shows representative spectra for two SSB-FDM transmission systems which could be used in the proposed radio telescope. The first system uses a 2 MHz channel bandwidth, while the second uses 1 MHz. In each case, the multiplexed signals are obtained by mixing the baseband signal f_m (12.36 ± 0.1 MHz) with a carrier signal f_c and filtering out either the sum or difference of the two frequencies, depending on which is required. Both systems use carrier frequencies in integral multiples of 2 MHz and 1 MHz, respectively, from 14 MHz through 36 MHz and 37 MHz, respectively. Each carrier frequency is used to multiplex two baseband signals into the FDM spectrum — one translated to the sum of the carrier and baseband frequencies and the other to the difference of the frequencies. In the 2 MHz channel system, the 14 MHz carrier is used to multiplex channel 1 ($14 - 12.36 \pm 0.1 = 1.64 \pm 0.1$ MHz) and channel 13 ($14 + 12.36 \pm 0.1 = 26.36 \pm 0.1$ MHz), the 16 MHz carrier multiplexes channel 2 (3.64 ± 0.1 MHz) and channel 14 (28.36 ± 0.1 MHz), and so on up to 36 MHz and channels 12 and 24. The 1 MHz channel system is obtained in a similar manner for 48 channels.

The lower carrier frequency, 14 MHz, was chosen to be higher than the highest modulating frequency (12.36 ± 0.1 MHz). This allows the complete (positive and negative) baseband spectrum to be translated across the zero frequency axis for convenience. If

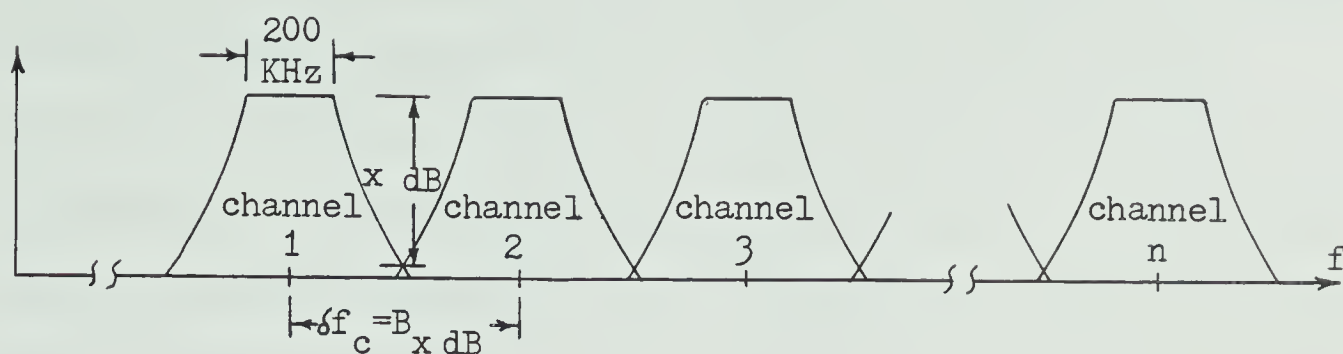


Fig. 6.9 Typical "passband" SSB-FDM modulation spectrum for an n -channel transmission system.

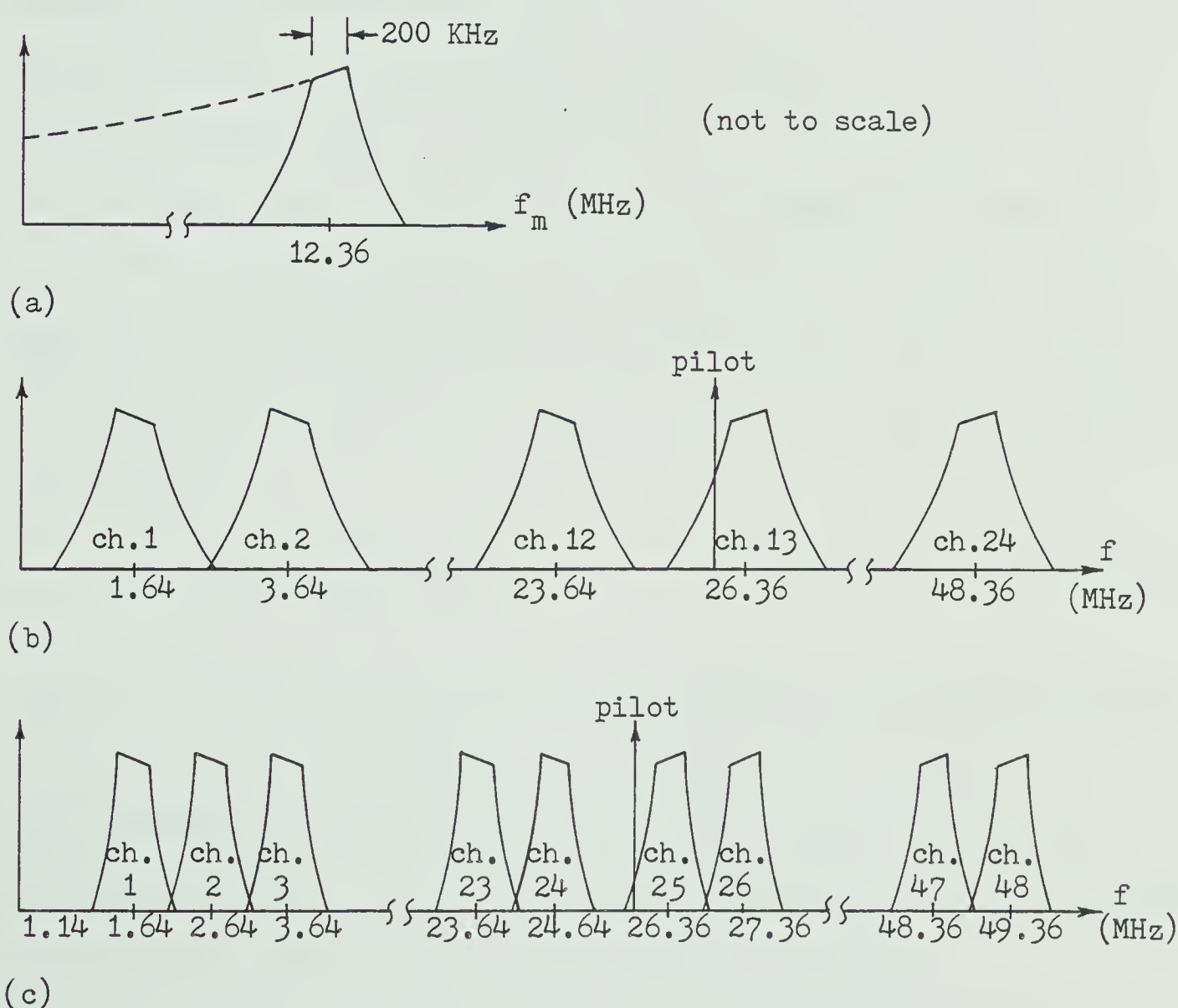


Fig. 6.10 Typical spectra of two passband, SSB-FDM systems
 (a) baseband (modulating) signal (b) 2 MHz channel spacing system
 (c) 1 MHz channel spacing system.

practical considerations deem that channel 1 be higher than 1.64 MHz, higher carrier frequencies can be chosen. The upper carrier frequencies, 36 MHz and 37 MHz, were determined on the basis of image interference. In the 2 MHz channelsystem, a carrier at, say, 40 MHz would be required to multiplex the baseband up to channel 26 (52.36 MHz). Demultiplexing this channel back to baseband at the receiver requires that the FDM spectrum be mixed with a local, 40 MHz carrier, synchronized to the 40 MHz carrier at the transmitter. The problem occurs when this carrier is allowed to mix with that portion of the spectrum containing channels 13 (26.36 MHz) and 14 (28.36 MHz). The difference between the carrier and these channels is 13.64 MHz and 11.64 MHz, respectively. A portion of these bands will pass through the baseband filter, and interfere with the baseband of channel 26.

This image interference can be avoided in two ways. One way would be to limit the difference between the upper and lower carrier frequencies to be less than, or equal to, twice the highest modulating frequency, or

$$f_{cu} - f_{cl} \leq 2f_m \quad (6.3)$$

Another way would be to filter the FDM spectrum at the receiver before the mixer so as to eliminate those channels which would result in image interference. While this method would require an additional filter per channel, it would provide the maximum "fill" since it would be a relatively easy matter to add additional channels.

In order for the multiplexed signals to be synchronously demodulated, it is common practice to include carrier pilots along with the multiplexed signals. This is shown in Fig. 6.10 for the two

FDM systems represented. The 1 MHz system is clearly preferable to the 2 MHz system since the pilots and their harmonics are largely out of the passband. There would then be less of an interfering effect into the signal information of interest. Since this is a correlation array, the pilots would have to be filtered out prior to the correlation stage. Two baseband channels with translated pilots within the band when correlated would yield erroneous results.

Using the assumption of a 200 MHz.km fiber (2.5 nsec/km dispersion), the optical transmission line runs of 2 1/2 kilometers have an available bandwidth of 80 MHz. It was just mentioned that this allows a bandwidth of about 68 MHz above 12.36 MHz to be available for multiplexed channels. The desirability of providing increased channel capacity beyond a certain point becomes questionable. From Fig. 6.4 it can be seen that adding channels beyond about 40 will result in an increase in required transmission line, due to the additional lengths of the branch feeders. If these branch feeders are coaxial cable, increasing the length will add to the excitation errors which are inherent with coaxial cable [3]. In this respect, 48 channels would appear to be a reasonable maximum since such a system would provide sufficient multiplexing capability and still demand a minimum of transmission line. It would also keep the number of mixers in the system reasonably low. While practicalities in hardware design may require that the system have fewer channels, the system design approach will be the same. This thesis will assume a transmission system for the proposed radio telescope based on the use of a 48-channel FDM system. In addition, it will be assumed that pilot tones will be transmitted along with the information on a per-

channel basis for synchronous demodulation at the receiver. As will be discussed in chapter seven, this is not the only solution, nor is it necessarily more advantageous. It is felt that this problem may be best solved at the time of the hardware design. At any rate, it should not be particularly consequential to the overall system design presented here.

The previous discussion has considered r.f. multiplexing in the feeder system. Since optical multiplexing is also possible, this will be examined next.

6.3 Optical Multiplexing

6.3.1 Antenna Signal Distribution

At the present time, the only methods available for multiplexing optical signals are time division multiplexing (TDM) using digital or pulse modulation and wavelength division multiplexing (WDM) using optical sources of different wavelength. Digital and pulse modulation have been eliminated from further consideration so WDM is the only remaining choice. The practicality of using sources of different wavelength was addressed in chapter 5.

Since the fundamental advantage of multiplexing is to save transmission line, this will now be examined. For a 48-channel system, Tables 6.1 and 6.2 indicate that the total length of primary and branch feeders is about the same for grouping (A) or (B). This thesis will assume that the configuration will be comprised of grouping (A) in the north-south subarray and grouping (E) in the east-west subarray. Fig. 6.2 shows schematically the physical layout of the array. Since the number of CTL's is fixed, the length of

branch feeder transmission line is also fixed. If we now multiplex the optical signals from a number of CTL's, a saving in primary feeder transmission line will result, albeit at the expense of additional system complexity. Without this optical multiplexing, the length of optical fiber transmission line is approximately

North-South	$33 \times 2 \frac{1}{2} = 82.5$ km (equal-length primary feeders)
East-West	$2 \times 13 \times 2 \frac{1}{2} = 65$ km (equal-length primary feeders)
Total	<hr/> 147.5 km

Introducing WDM necessitates introducing physical multiplexing locations. It will be assumed that these locations will be situated at the center of the group of CTL's that feed them, since this will result in the minimum quantity of equal-length feeders. These locations will be termed optical multiplexing locations (OML's). Since additional optical fiber feeders will be required between the CTL's and the OML's, these feeders will be termed "secondary" transmission feeders (STF's). Their (equal) lengths in the subsequent discussion are determined from Fig. 6.3. When used in a WDM system, the primary transmission feeders (PTF's) will be assumed to run from the OML's to the observatory.

A 2, 4 or 6 channel WDM system will be considered. The approximate lengths of optical fiber transmission line required for each system is presented below. The saving over the non-optical multiplexed system is also indicated.

	<u>2-Channel</u>	<u>4-Channel</u>	<u>6-Channel</u>
N-S PTF	$16 \times 2 \frac{1}{2} = 40 \text{ km}$	$8 \times 2 \frac{1}{2} = 20 \text{ km}$	$6 \times 2 \frac{1}{2} = 15 \text{ km}$
E-W PTF	$2 \times 6 \times 2 \frac{1}{2} = 30 \text{ km}$	$2 \times 3 \times 2 \frac{1}{2} = 15 \text{ km}$	$2 \times 2 \times 2 \frac{1}{2} = 10 \text{ km}$
N-S STF	$2 \times .09 \times 16 \approx 2.9 \text{ km}$	$4 \times .28 \times 8 \approx 9.0 \text{ km}$	$6 \times .46 \times 5 \frac{1}{2} \approx 15 \text{ km}$
E-W STF	$2 \times .09 \times 12 \approx 2.2 \text{ km}$	$4 \times .28 \times 6 \approx 6.7 \text{ km}$	$6 \times .46 \times 4 \approx 11 \text{ km}$
Total	$\sim 75 \text{ km}$	$\sim 51 \text{ km}$	$\sim 51 \text{ km}$
Saving	$\sim 72.5 \text{ km}$	$\sim 96.5 \text{ km}$	$\sim 96.5 \text{ km}$

It is evident that a substantial saving of transmission line can result from optical multiplexing — a 2-channel system saves virtually half, while a 4-channel system can save about two-thirds of that required for a non-optical multiplexed system. It is interesting to note that a 6-channel system does not result in any saving of transmission line over a 4-channel system. This is due to the additional lengths of secondary transmission feeders required. In this respect, there is no point examining an 8-channel WDM system.

It was mentioned previously that a saving in transmission line must be weighed against the additional system complexity. A 2-channel WDM system will require 28 optical multiplexers, a 4-channel system will require only 14, and a 6-channel system will require only 10. If the extra cost of the optical multiplexing is less than the saving of the optical fiber transmission line, it is clearly economical. This design will assume the use of a 4-channel WDM system. While this involves four more optical multiplexers than a 6-channel system, the amount of transmission line saved is about the same. Also, fabrication of the optical multiplexers will be less difficult with fewer channels.

6.3.2 Local Oscillator Distribution

Since local oscillator signals are required at each CTL for multiplexing the antenna signals, the advantages of using optical multiplexing for the local oscillator distribution system will now be examined.

The amount of transmission line required for a local oscillator distribution system can be determined in a manner similar to the previous for the antenna signal distribution system. If we assume that an equal-length local oscillator distribution system will be used, the requirement would be the same as what was required for the antenna signal transmission feeders, or about 147.5 km. Just as the total length of the antenna signal transmission feeders was reduced by multiplexing, the total length of local oscillator distribution feeders can be reduced by splitting. If this splitting is done at the OML, these distribution feeders can be categorized as primary local oscillator feeders (PLOF's) and secondary local oscillator feeders (SLOF's), consistent with the terminology for the antenna signal transmission feeders.

If we consider a 2, 4 or 6-way split at the OML, the approximate lengths of distribution line, as shown below, will be identical to those just calculated for the optical multiplexed situation.

	<u>2 Way Split</u>	<u>4 Way Split</u>	<u>6 Way Split</u>
N-S PLOF	40 km	20 km	15 km
E-W PLOF	30 km	15 km	10 km
N-S SLOF	2.9 km	9 km	15 km
E-W SLOF	<u>2.2 km</u>	<u>6.7 km</u>	<u>11 km</u>
Total	~ 75 km	~ 51 km	~ 51 km
Saving	~ 72.5 km	~ 96.5 km	~ 96.5 km

In order to remain consistent with the antenna signal transmission section, and since a 6-way split is seen to be not particularly advantageous over the 4-way, a 4-way splitting system will be used in this design. This presumes that the cost of the 14 splitters is more than offset by the saving of ~96.5 km of optical fiber. Assuming a minimum cost of 10¢ per meter, the splitters should cost no more than about \$689 apiece for a capital cost tradeoff advantage. Since present fiber costs are more than an order of magnitude higher than this, the splitter method seems clearly to be the most economical.

6.4 Summary

Antenna signal multiplexing has been examined on the basis of reducing transmission line quantities. For the tee-array configuration considered, 48 channels seems to be a reasonable upper limit for r.f. multiplexing. Additional multiplexing in the optical domain up to about 4 optical channels provides further transmission line reduction. Various modulation techniques were examined to provide the desired

r.f. multiplexing capability. The frequencies of interest (12.36 ± 0.1 MHz) effectively ruled out digital and pulse modulation systems. Similarly frequency modulation was rejected in favor of amplitude modulation. The narrow frequency band of interest (200 KHz) is ideally suited for amplitude modulation and frequency-division multiplexing. A single-sideband, suppressed-carrier modulation system was finally chosen to provide 48 FDM channels as the basic r.f. carrier signal. Assuming a channel spacing of 1 MHz, a number of filters appear to be satisfactory, although the specific choice may best be made at the time of hardware design. The 48-channel r.f. carrier signal will modulate an optical source and the subsequent optical multiplexing will be accomplished via wavelength-division multiplexing (WDM) as discussed in chapter 5.

CHAPTER 7

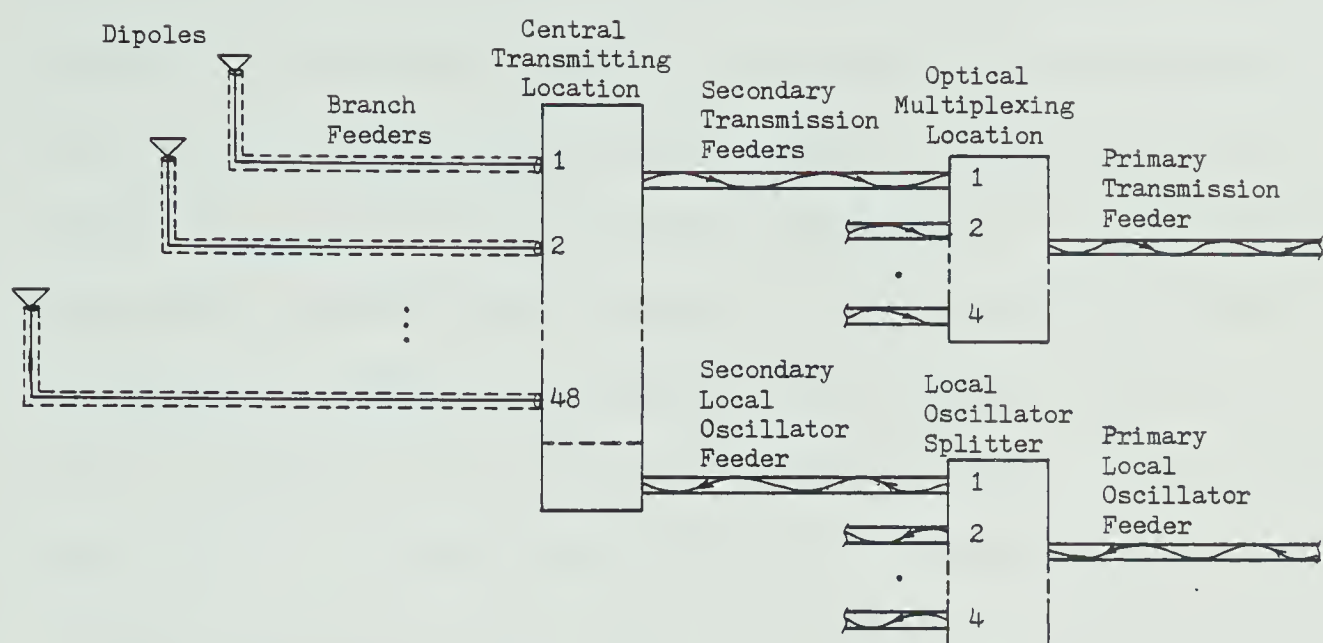
TRANSMISSION SYSTEM DESIGN

In order to ensure the viability, and assess the performance of an optical fiber transmission system in the radio telescope array, we must first design the system. In view of the material presented in the previous chapters, it is apparent that an optical fiber transmission system design will involve many considerations. Many of these considerations will be subject to the state-of-the-art of available components. In this respect, it is deemed advisable to present a representative system design -- that is, one which is consistent with the development of the previous chapters, and yet which can be modified to accommodate changes in technology. The entire transmission system will be presented. The major transmission considerations, however, will be directed toward the optical portion.

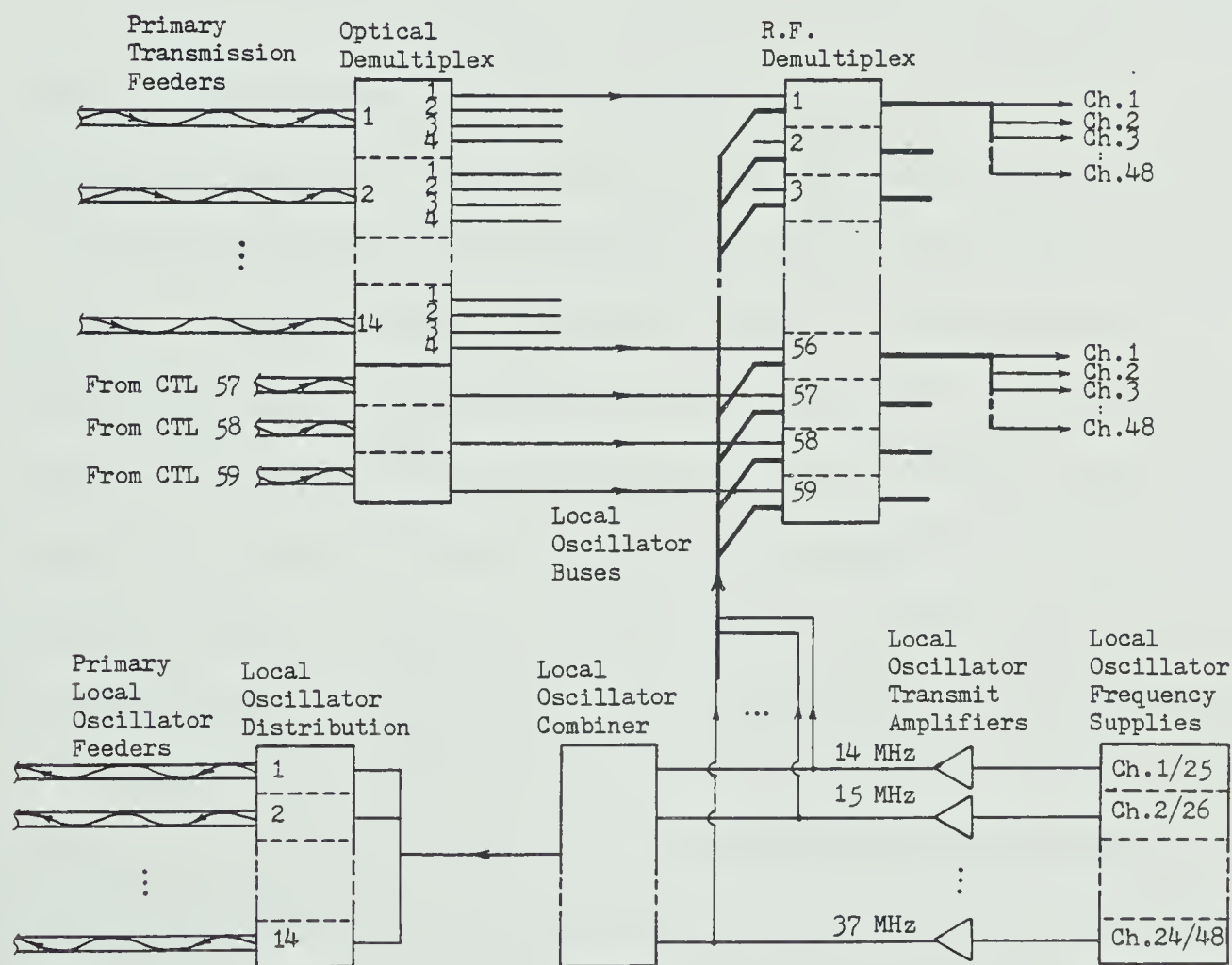
7.1 System Configuration

7.1.1 General

A block diagram of the transmission system configuration is shown in Fig. 7.1. The transmitting section is shown in Fig. 7.1(a).



(a) Transmitting Section



(b) Receiving Section

Fig. 7.1 Transmission system configuration

The signal from each antenna is conveyed to the CTL via coaxial cable branch feeders. At the CTL, signals from 48 antennas are multiplexed together and converted into an optical signal for transmission to the OML via the secondary transmission feeders. At the OML, optical signals from 4 CTL's are multiplexed and transmitted down the primary transmission feeder to the receiver. A local oscillator signal is received at the OML via the primary local oscillator feeder and split into four signals in the local oscillator splitter. The four identical local oscillator signals are fed via the secondary local oscillator feeders to the CTL's where they are processed and used in the multiplexing of the antenna signals.

Fig. 7.1(b) shows the receiving section of the transmission system. The receiving section is located in the observatory at the junction of the tee. The signals formed from each incoming primary feeder are optically demultiplexed into their four constituent optical signals. Each of these constituent signals is then converted into electrical form, where it is r.f. demultiplexed into its 48-channel group. Associated with the receiving section are the local oscillator frequency supplies. These frequencies are combined into one FDM signal which is converted into an optical signal for distribution out to each of the 59 CTL's in the array. This distribution will be examined next.

Each CTL requires local oscillator signals to facilitate channel multiplexing. Since the antenna signal phase integrity is of prime importance for a correlation array as used for the proposed radio telescope, these identical local oscillator signals are required at the receiver to permit synchronous demodulation [135]. This, in turn, requires that the carrier phases of the multiplexed signals be

known precisely at the receiver, such that the phase of the local oscillator signals can be matched precisely before mixing. In view of this, this design will provide generation of these local oscillator signals at the receiver and distribution of them via optical transmission lines to the CTL's. This will require that the local oscillator transmission lines be equal-length so as to maintain phase coherence for all local oscillator frequencies at all CTL's in the array.

Another local oscillator arrangement is possible. A single, highly stable frequency can be generated at the receiver and transmitted to the CTL's in the array. This arrangement would not require equal length feeders. It would be sufficient to use near minimum-length feeders, such that the differences in lengths were in precise integral wavelengths of the single frequency. This would maintain identical phases at each CTL. This approach would require a frequency synthesizer at the receiver and at each CTL to derive the necessary local oscillator frequencies. This type of system would also require only a single pilot frequency to be transmitted to the receiver from each CTL for synchronization.

It is not within the scope of this thesis to analyze and compare the relative merits and demerits of using the frequency synthesis approach as opposed to generating and transmitting all 48 local oscillator frequencies. It is being mentioned only as an alternative. Aside from economics, the major considerations of each method is the accuracy of reproducing the antenna signals at the receiver with the correct phase relationships. For the purposes of this representative design, it is assumed that the necessary phase and frequency accuracy will be attained using the method proposed, ie: independent local oscillator signal generation, transmission and

synchronization.

7.1.2 Transmitting Section

7.1.2.1 Central Transmitting Location (CTL)

A typical CTL configuration is shown in Fig. 7.2.

The antenna signals from the branch feeders are amplified to a level suitable for mixing, filtered to pass the band of interest (12.36 ± 0.1 MHz) and then fed to a mixer. The mixer performs the amplitude modulation operation by multiplying the antenna signal with a local oscillator signal. The output signal is then filtered to remove the unwanted sideband and is then fed into a combiner. Here, all 48 channels which have been modulated to occupy different slots in the spectrum, are combined into one 48-channel FDM signal. The output of the combiner is fed into an optical source. The output of the optical source is connected to a secondary transmission feeder via a suitable coupler.

The local oscillator signals used in the mixers are distributed to the CTL in optical form via a secondary local oscillator feeder (SLOF). The optical signal is converted to electrical form in the optical detector which is attached to the SLOF via a suitable coupler. This electrical signal is an FDM waveform containing all 24 local oscillator frequencies. This FDM signal is amplified and fed to a bank of local oscillator filters. These filters extract the local oscillator frequencies and feed them to the various mixers.

The 48-channel FDM waveform out of the combiner is considered to occupy the spectrum from 1.14 - 49.86 MHz as shown in Fig. 6.10. Each 200 KHz signal is allowed a 1 MHz channel spacing. McLarnon [3]

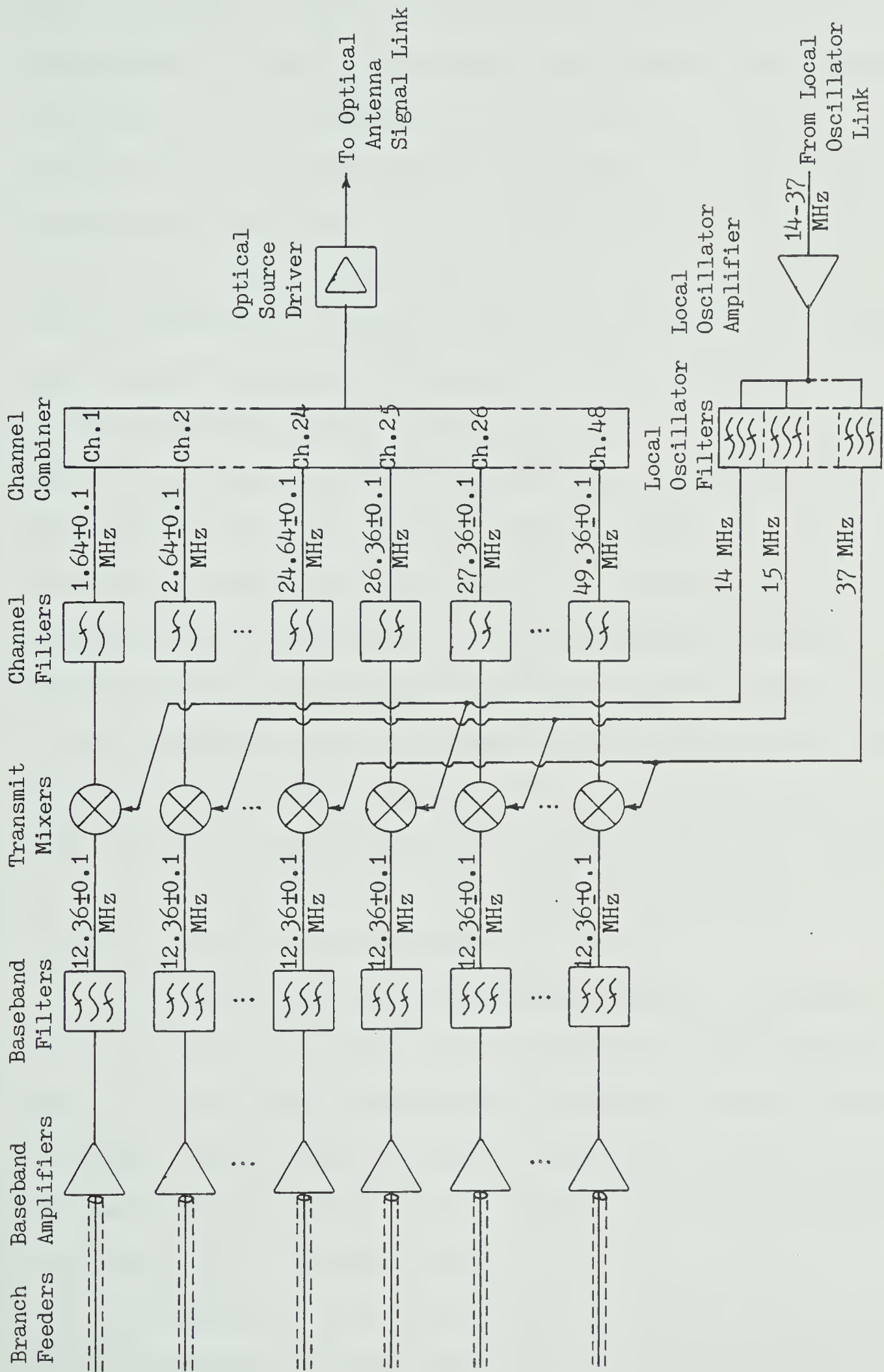


Fig. 7.2 Central transmitting location configuration

established that, in order to constrain phase excitation errors of the array to 0.1° rms, 55 dB baseband filter separation was required and 60 dB inter-cable separation. Table 6.2 shows that 55 dB separation can be met with a 4-pole Butterworth, 6-pole Bessel or 6-pole transitional filter. The type of filter will be left for a future study. Section 6.3.3.2 outlined the basic considerations. For the purposes of this design, a Butterworth filter will be assumed, since this was suggested by McLarnon [3]. This presumes that any delay distortion introduced by the filters will be equalized at some point. Even though a 4-pole Butterworth filter will satisfy our basic criterion of 55 dB separation, it was suggested in section 6.3.3.2 that, by adding one more pole, over 70 dB separation can be achieved. As mentioned earlier, the optical fibers are expected to provide more than 70 dB crosstalk isolation. In this respect, using a 5-pole Butterworth filter will make better utilization of the cable isolation. Theoretically, this should also allow an improvement in phase excitation error by a factor of 5 down to 0.02° rms as indicated in section 6.3.3.2. In view of the foregoing, the baseband filters will be assumed to be 5-pole Butterworth filters.

The function of the mixer is straightforward — to multiply the incoming 12.36 ± 0.1 MHz antenna signal with a local oscillator signal to achieve basic double-sideband, suppressed carrier (DSB-SC) modulation. Specific mixer features or characteristics will not be addressed since no experimental work was done. The noise performance of the mixer will be discussed later.

The purpose of the channel filter is to remove the unwanted sideband produced by the mixer and to pass the desired sideband on to

the channel combiner. Since the sidebands will be separated at the center frequencies by twice the baseband center frequency, or 24.72 MHz, the channel filters can be relatively simple, with shallow attenuation skirts. The channel filters also could be low-pass for channels 1 through 24 and high-pass for channels 25 through 48, eliminating the need for more costly and complex bandpass filters. This presumes that the FDM spectrum from 1.14 - 49.86 MHz has not been contaminated with significant amounts of additional noise or intermodulation products from the mixer stage.

No specific criteria will be demanded of the channel combiner. Its function is straightforward — to accept the 48 single-sideband channels modulated up to their required frequency assignment and to combine them into a 48-channel waveform which occupies the 1.14 - 49.86 MHz spectrum. Depending on the combining process, further filtering may or may not be required. For the purposes of this design, it is assumed that the combining process is linear and no perceptible intermodulation products will result. In this case, no additional filtering is required.

The optical source driver and the rest of the optical transmission system will be examined later.

The 24-channel FDM local oscillator signal received from the optical detector must be amplified to a level suitable for further processing. The local oscillator amplifier is a wideband, low-noise amplifier that amplifies the entire 24-channel spectrum from 14 to 37 MHz. Amplification prior to splitting the frequencies requires only one amplifier, with possibly some subsequent individual frequency level adjustment. It is assumed that the amplifier's

linearity is sufficient to keep intermodulation distortion negligible.

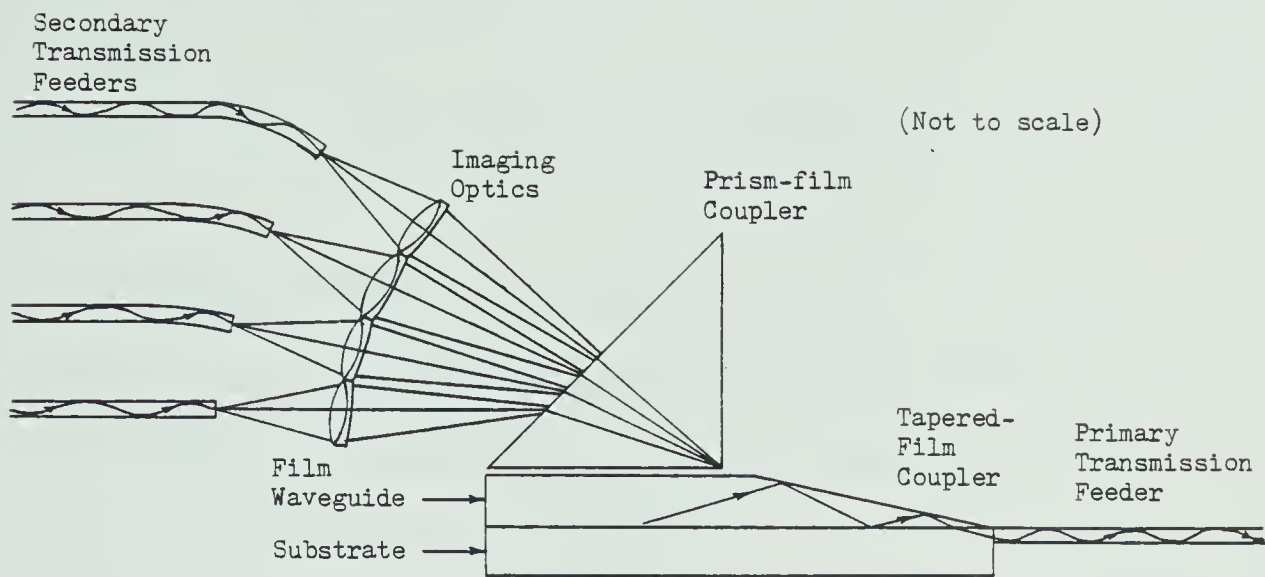
The local oscillator filters are a bank of 24 filters that accepts the 24-channel FDM local oscillator waveform from the local oscillator amplifier. Since the frequencies of interest are single-frequency tones, the filters can be very narrow slot filters or phase-locked loops (PLL's). While final decision on the type and design of these filters will be based on the phase and frequency accuracy that can be attained, it will be assumed that phase-locked loops will be used.

The optical detector and the rest of the optical local oscillator distribution system will be examined later.

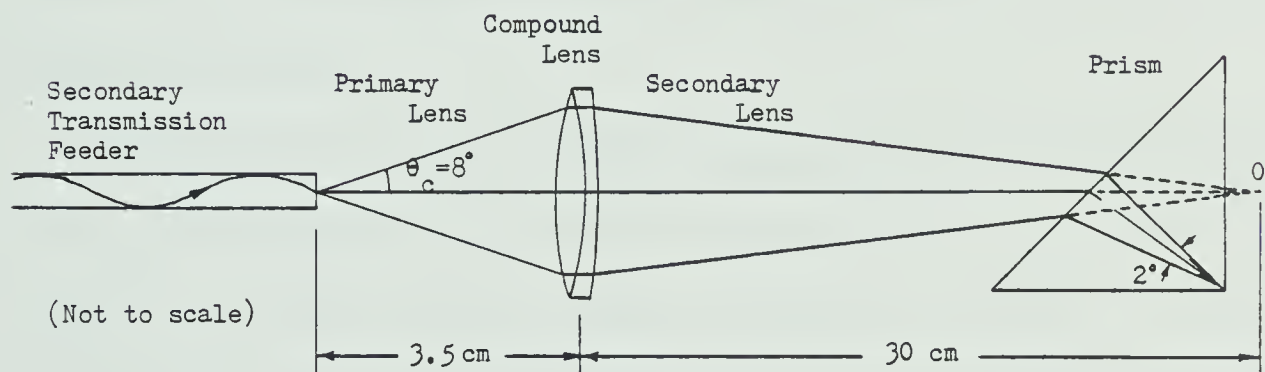
7.1.2.2 Optical Multiplexing Location (OML)

A typical OML configuration is shown in Fig. 7.3. The four incoming secondary transmission feeders are shown converging toward a prism-film coupler in Fig. 7.3(a). The light outputs from the feeders pass through imaging optics and into the prism such that the beams converge at the apex. From here, they are coupled into a thin-film waveguide. The waveguide is tapered so as to form a tapered-film coupler between the waveguide and the attached primary transmission feeder. A prism-film coupler has been selected for this design due to its present efficiency advantage over other couplers. It is also a realizable means of achieving wavelength-division-multiplexing and has been analyzed in detail in section 5.2.

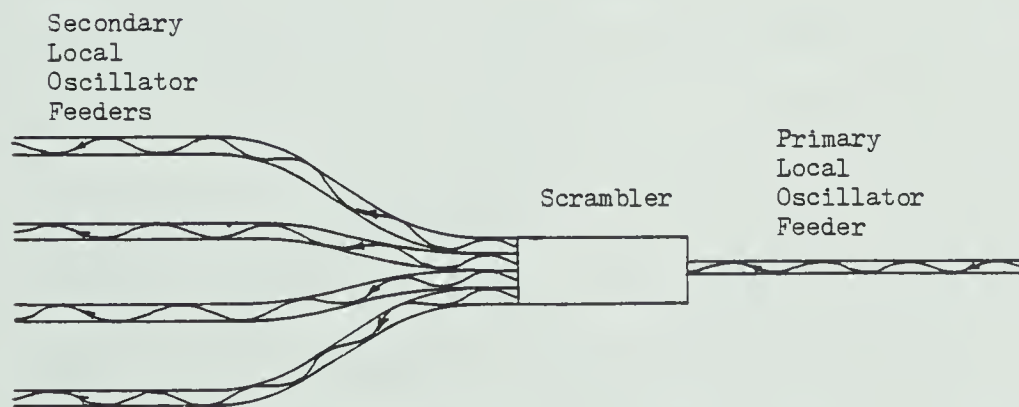
The light that exits from an optical fiber will be constrained within a narrow cone of illumination whose angle θ_c from the axis is a function of the numerical aperture N.A. of the fiber. Since a typical N.A. is 0.14 in contemporary fibers, the light power will be



(a) Optical Multiplexer



(b) Expanded view showing possible imaging optics and representative dimensions



(c) Local oscillator splitter

Fig. 7.3 Optical multiplexing location configuration

concentrated in a cone of angle

$$\theta_c = \sin^{-1}(\text{N.A.}) = \sin^{-1}(0.14) \approx 8^\circ$$

about the axis. This cone is much too broad for efficient coupling. A compound lens will serve to focus the light energy into a narrower cone as shown in Fig. 7.3(b). This lens can be sufficient for adequate coupling provided that it intercepts all of the light from the fiber and that it focuses the light into a sufficiently narrow beam.

Appendix M demonstrates that this arrangement is feasible for coupling light at four wavelengths of 0.70, 0.78, 0.86 and 1.06 μm into a prism-film coupler.

Now that the four incoming optical signals are wavelength-division multiplexed into the film waveguide, the next step is to couple this energy into the primary transmission feeder. It was indicated in section 5.5 that 100% of the light energy in a waveguide has been recovered in practice using a tapered-film coupler, so this method will be chosen. The taper ratio will be assumed to be 30:1 or greater, resulting in a spread between half power points of 13° or smaller. Since the acceptance cone of the fiber feeder is about 16° , this should be adequate for very efficient coupling. This is an area requiring experimental work. The primary transmission feeder can be bonded to the substrate at the correct position by a suitable adhesive.

The incoming local oscillator feeder is fed into a scrambler whose output is coupled to the four secondary local oscillator feeders, as shown in Fig. 7.3(c). It should be mentioned that there have been no known studies or experimentation done on couplers of this nature

for single-strand optical fibers. However, there has been considerable work in this area using optical fiber bundles [57]. Much of this work has been oriented to military applications, such as data buses on aircraft and ships. Work is presently underway by the U.S. Navy on what is expected to be single-fiber couplers.

An experimental WDM system has been reported by Miki and Ishio [140]. They coupled the optical outputs from three LED's into a fiber and recovered the individual signals at the far end. The light from each LED was fed via a short fiber to three cylindrical lenses which were clustered together. The output from these lenses was coupled through an objective lens into a step-index multimode fiber. This multiplexing arrangement introduced a loss of 12 dB. The demultiplexer involved coupling the light output from the fiber through an objective lens into a prism and then using an additional objective lens to focus the recovered spectral signals into separate fibers attached to photodetectors. This demultiplexer introduced a loss of 7 dB. The LED's operated at center wavelengths of 784 nm, 825 nm and 858 nm. With spectral halfwidths of 30 nm, there was considerable spectrum overlap. The resulting interference was overcome by the use of "interchannel interference cancellers". This basically involved coupling a portion of the electrical input of one detection amplifier to the electrical output of the adjacent channel detection amplifier using opposite sign. While this arrangement provides a simple means of achieving WDM, the system described introduced a loss of some 19 dB with a step-index fiber or an equivalent loss of about 22 dB with the design considered in this thesis. It therefore is not considered a viable alternative for the proposed radio telescope feeder system.

7.1.3 Receiving Section

7.1.3.1 Optical Demultiplexing

The optical demultiplexing equipment is shown in Fig. 7.4. The light output from the primary transmission feeder is passed through suitable imaging optics to focus the light through a substrate onto a tapered-film coupler. The light energy in the film waveguide is coupled into a prism using a basic prism-film coupler. In the prism, the four wavelength components are separated and they are directed through imaging optics onto photodetectors. The photodetectors then convert the optical signal into an electrical signal for subsequent processing by the r.f. demultiplexers.

The light output from the primary transmission feeder has been established previously as being effectively in a 16° cone. Since the output light from a tapered-film coupler was found to be within a 13° cone for taper ratios of 30:1, by reciprocity the input beam should also be focused with this in mind. If the taper ratio can be altered to output a 16° cone of light from the waveguide, then the imaging optics for an input coupler need only be a simple convex lens. If only large ratio tapers are available, then the imaging optics will require the use of a compound lens as was considered for the optical multiplexer section. It will be assumed here that a single lens is sufficient for adequate focusing.

The prism-film output coupler is assumed to be identical to the prism-film input coupler used in the optical multiplexer. The various wavelengths of light propagating in the film waveguide will be coupled into the prism and out to the photodetectors. The output

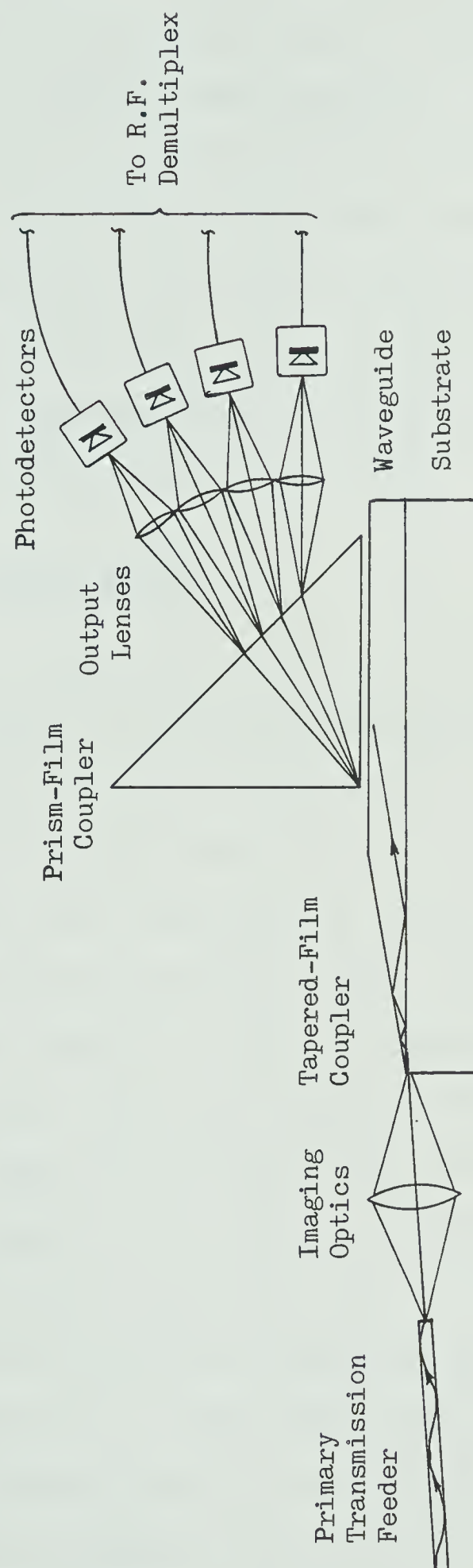


Fig. 7.4 Optical demultiplexing configuration

beam width and angular divergence is not known, particularly if the light sources are LED's with their wide spectral width. Experimental work will be required to determine these parameters. For this reason, an additional set of lenses is considered between the prism and photodetectors. The output angles at the center wavelength of the beams will be the same as those for the input prism-film coupler. The distances between the lenses and the prism and between the lenses and photodetectors will probably require experimental optimization.

The photodetectors will be discussed later.

7.1.3.2 R.F. Demultiplexing

The r.f. demultiplexing section is shown in Fig. 7.5. The r.f. amplifier provides the gain for the 48-channel FDM signal immediately following its conversion from optical to electrical form. The amplifier will have sufficient gain to present a suitable signal level to the mixer stage, thus overcoming the losses in the band-splitting filters and signal distribution stages. Intermodulation distortion in amplifiers results in crosstalk into the various channels of an FDM signal. This causes amplitude and phase deterioration of the channel signals which degrades the accuracy of the telescope. For the purposes of this thesis, it is assumed that intermodulation distortion is negligible.

Since only 24 local oscillator frequencies were used to multiplex the 48 channels into a single FDM waveform, it is necessary to split the upper 24 channels away from the lower 24. As an example of why this is necessary, channels 1 and 25 will be considered. If the entire 48-channel group was mixed with the 14 MHz local oscillator

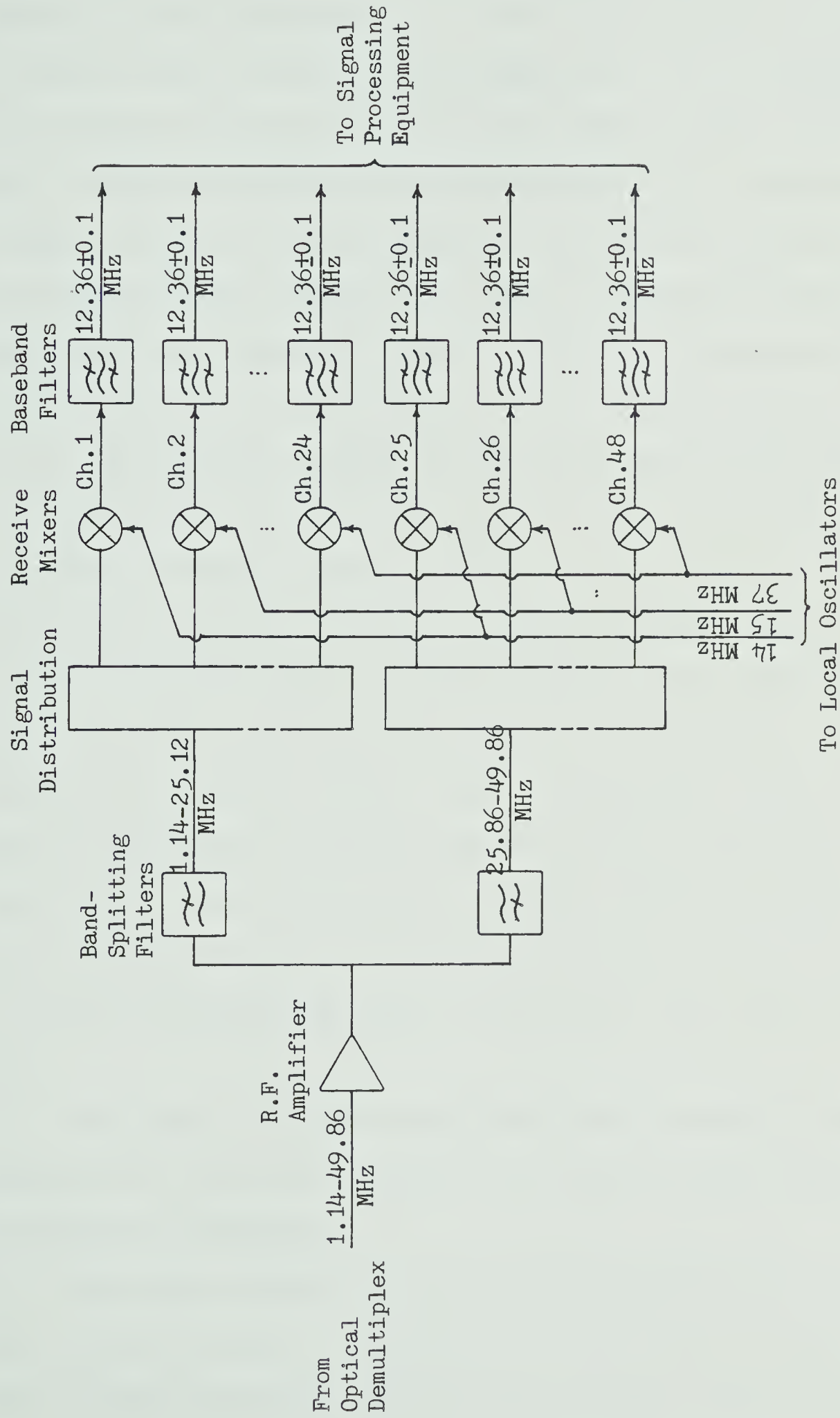


Fig. 7.5 R.F. demultiplexing configuration

signal, channels 1 and 25 would both be present at the baseband frequency of 12.36 ± 0.1 MHz. This is due to the difference products of channel 1 and the local oscillator signal ($14 - 1.64 = 12.36$ MHz) and of channel 25 and the local oscillator signal ($26.36 - 14 = 12.36$ MHz). To avoid this problem, the band-splitting filters separate the upper 24 from the lower 24 channels. These filters are high-pass and low-pass filters, respectively. Since the separation between channel 24 and 25 is more than 1 MHz (at the center frequencies), these filters need not have as sharp a cutoff as do the channel filters. The frequency separation between the center of channel 24 and the -70 dB point of channel 25 is $25.86 - 24.64 = 1.22$ MHz, representing a bandwidth ratio of $1.22/0.1 = 12.2$. Based on a Butterworth configuration, a 3-pole filter will provide >65 dB isolation between the upper and lower 24 channels for a bandwidth ratio of 12.2 [4]. Increasing the complexity of the filter to 4-poles increases the isolation to 87 dB. This is unnecessary, however, since the 3-pole filter provides 70 dB isolation at a bandwidth ratio of 14.7. This filter should be adequate since its -70 dB point will fall at $24.64 + 1.47 = 26.11$ MHz, which is still out of the 200 KHz information bandwidth by some $26.36 - 0.1 - 26.11 = 0.15$ MHz.

The signal distribution stage splits the incoming 24 channel waveform into 24 identical replicas of the input and feeds them to the mixers for demodulation.

The mixers multiply the 24 channel FDM waveforms with the local oscillator signals to produce basic double-sideband, suppressed-carrier (DSB-SC) modulation. Since this is the same type of operation

as performed by the mixers in the transmitting section, they can be identical for economic reasons.

The products from the mixers consist of the sum and difference of the local oscillator frequency and the various components of the 24 channel groups. The only product that will fall in the original baseband, however, is the difference product of the local oscillator signal containing only (hopefully) the original information signal, ie: 12.36 ± 0.1 MHz, baseband filters are required that are identical to those in the central transmitting locations. The signals present at the outputs of these filters are then available for any necessary equalization and subsequent processing.

7.1.3.3 Local Oscillator

The local oscillator section as shown in Fig. 7.6 consists of local oscillator frequency supplies, local oscillator combiner and local oscillator distribution stages. The local oscillator section generates the various signals required for multiplexing and demultiplexing the r.f. antenna signals and distributes these signals to the various CTL's in the array.

The local oscillator frequency supplies consist of 24 signal generators with integral frequencies from 14 through 37 MHz. Each generator requires sufficient power output capability to feed 2 mixers in each of the 59 r.f. demultiplex stages. In addition, it must provide sufficient signal for the 14 optical source drivers to enable distribution of the local oscillator signals throughout the array.

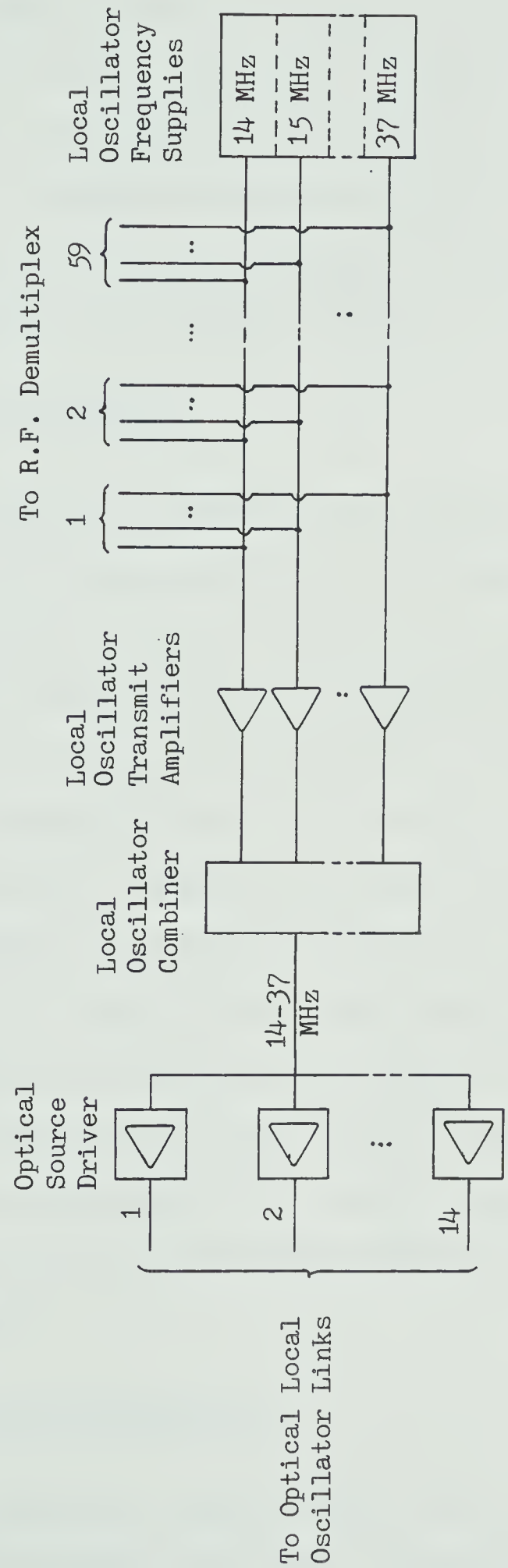


Fig. 7.6 Local oscillator distribution

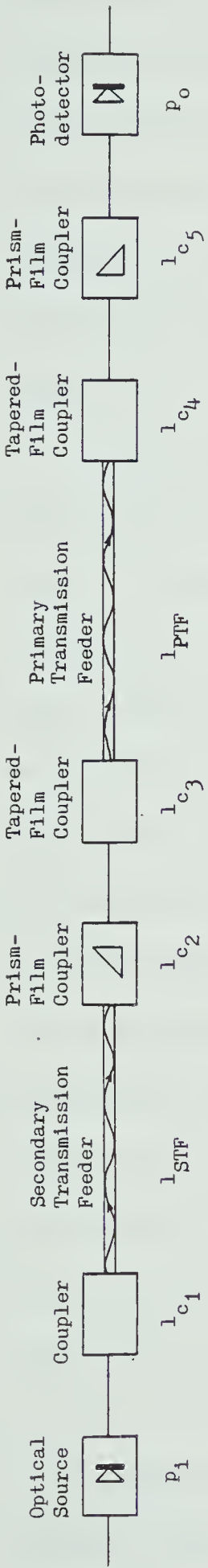
The local oscillator combiner accepts the 24 local oscillator signals and combines them into a single 24-channel FDM signal with bandwidth 14 - 37 MHz. This signal is then fed to the optical source drivers. The optical source drivers amplify the signals sufficiently to intensity modulate the optical sources. The optical sources convert the electrical signals to optical form for transmission over the primary local oscillator feeders to the remote locations.

7.2 Optical Link Design

The transmission configuration proposed for the radio telescope feeder system will require two optical links — one to carry the antenna signal information from the central transmitting locations (CTL's) to the observatory, and the other to carry the local oscillator signals from the observatory to the CTL's. The optical links will include all equipment between, and including, the optical sources and photodetectors. The effect of using laser diodes versus LED's and p-i-n photodiodes versus avalanche photodiodes (APD's) will be determined from a study of the system noise performance which, in turn, is dependent on the link power budget. The power budget is basically a compilation of link gains and losses to determine the (optical) power available at the receiver. Any excess power available over that required for a particular level of performance is termed the link margin.

7.2.1 Antenna Signal Link

The optical antenna signal link can be represented schematically as shown in Fig. 7.7. The optical sources considered



Power Budget

	Laser Diode			LED		
	5 mW	0.7 μm	1.06 μm	0.7 μm	1.06 μm	
System Gains, P_1		7 dBm	7 dBm	7 dBm	7 dBm	
System Losses (dB)						
L_{c1}	6			15		
L_{c2}	3			3		
L_{c3}	1			1		
L_{c4}	4			4		
L_{c5}	2			2		
Total Coupling Loss		16	16		25	25
Source Degradation		3	3		3	3
Temp. Degradation		3	3		3	3
Splices, Connections		2	2		2	2
Feeders		5 dB/km	2 dB/km	5 dB/km	2 dB/km	
L_{STF}	288 m	1.44	0.6	288 m	1.44	0.6
L_{PTF}	2.5 km	12.5	5.0	2.5 km	12.5	5.0
Total Feeder Loss		13.94	5.6		13.94	5.6
Received Power, P_o		-31 dBm	-22.6 dBm		-40 dBm	-31.6 dBm

Fig. 7.7 Optical antenna signal link and power budget

will be stripe-geometry DH laser diodes and edge-emitting LED's. These devices are chosen since they are representative of the latest state-of-the-art devices designed for optical fiber communications. Both the laser diodes and the LED's will be assumed to emit 5 mW of optical power. Lasers can emit more power than this, but operating lifetime in continuous mode is enhanced by lower power operation. Edge-emitting LED's are capable of emitting at least 5 mW in continuous mode [75].

The elements contributing to system losses are the source-to-fiber coupler, secondary transmission feeder, prism-film (input) coupler, tapered-film (output) coupler, primary transmission feeder, tapered-film (input) coupler, and the prism-film (output) coupler. These losses are labelled l_{c1} , l_{STF} , l_{c2} , l_{c3} , l_{PTF} , l_{c4} and l_{c5} , respectively. In section 5.1 it was reported that laser-to-graded-index fiber coupling was as high as 26% or -6 dB. This figure will be used for l_{c1} for the case of the laser diode. In section 3.2.4, coupling losses of 9 to 11 dB were reported for edge-emitting LED's into step-index fibers. Since we are considering the use of a graded-index fiber with index profile $\alpha \simeq 2$ (parabolic), an additional loss of 3 dB will be allocated. This is because, in section 2.1, it was mentioned that a step-index fiber can accept twice as many modes as a parabolic-index fiber. For this design, an overall LED-to-graded-index fiber coupling loss of 15 dB will be used for l_{c1} .

At the OML, there are two additional losses — l_{c2} and l_{c3} . Input coupling efficiencies of prism-film couplers using lasers have exceeded 80% (-1 dB). There has been no work discovered on coupling light from a fiber into a prism-film coupler. However, if the fiber

considered is assumed to have a numerical aperture of 0.14, the cone of light output from the fiber will fall within $\sin^{-1}(0.14) \simeq 8^\circ$ of the axis. This is seen to be very comparable with typical laser beamwidths (at least in one dimension). In this respect, a coupling loss of 3 dB will be assumed for l_{c2} . This loss should be virtually the same for both cases of using a laser diode and an LED source, since we are concerned with coupling the light from the fiber into the prism-film waveguide. It was determined in section 5.2 that source spectral width is not of great concern in coupling efficiency. The tapered-film output at the OML has been reported in section 5.5 to achieve virtually 100% efficiency. A value of 1 dB will be assumed for l_{c3} . This will allow a coupling efficiency as low as 80%.

At the receiver, there is a tapered-film input coupler with loss l_{c4} and an output prism-film coupler with loss l_{c5} . The tapered-film input coupler has been reported in section 5.5 to achieve efficiencies of over 40 and 50%. This design will assume a loss of 4 dB (40% efficiency) for l_{c4} . Output prism-film couplers have been constructed with efficiencies of 100% given sufficient coupling length. For the configuration considered in this design, a loss of 2 dB will be assumed for l_{c5} .

These coupling losses l_{c1} through l_{c5} will be assumed to be fixed regardless of the particular wavelength of interest. However, the optical fiber losses in the primary and secondary transmission feeders (PTF and STF) are not independent of wavelength. With present availability of optical fibers, it is reasonable to consider using a fiber with attenuation of 2 dB/km or lower at 1.06 μm wavelength. This design will use this value. Since we are also considering using

optical sources with wavelengths down to around $0.7\ \mu\text{m}$, an examination of Fig. 2.16 indicates that an attenuation of 5 dB/km should be reasonable at this wavelength. This value will also be used. The length of the primary and secondary transmission feeders will be taken as 2.5 km and 288 meters, respectively. The PTF losses l_{PTF} will then be $2.5 \times 5 = 12.5$ dB at $0.7\ \mu\text{m}$ and $2.5 \times 2 = 5$ dB at $1.06\ \mu\text{m}$. The STF losses l_{STF} will be $0.288 \times 5 = 1.44$ dB at $0.7\ \mu\text{m}$ and $0.288 \times 2 \approx 0.6$ dB at $1.06\ \mu\text{m}$.

In addition to these losses, it is customary to allocate additional margin losses to account for degradation of source output power with time, degradation of system performance as a function of temperature and losses due to splices and connectors. These margin losses will be taken as 3 dB, 3 dB and 2 dB, respectively. This will allow the source output power to degrade to 50% of the nominal, will allow temperature effects to degrade performance by 50% and will allow two connectors and two splices assuming 0.5 dB loss for each connector and splice.

At this point, the link power budget can be calculated and the received optical power at the detector can be determined. This is shown in Fig. 7.7. For the case of using a laser diode, the received signal varies from -22.6 dBm to -31 dBm and, for the LED, from -31.6 dBm to -40 dBm over the range from $1.06\ \mu\text{m}$ to $0.7\ \mu\text{m}$, respectively. For this system, it can be seen that the 9 dB power disadvantage suffered by the LED system is due to l_{c_1} , the source-to-fiber coupling loss.

It would be preferable, from the standpoint of economics and system complexity, to use LED's for the optical sources and p-i-n

photodiodes for the photodetectors. In order to determine the feasibility of this arrangement, it is necessary to examine the system performance with these components. Since this is an analog system, performance is measured in terms of signal-to-noise ratio SNR. Fig. 4.5 shows SNR as a function of received optical power for a p-i-n photodiode. As discussed in section 4.2(g), using a load resistance of 4k ohms, positive SNR's were available down to about -38 dBm. It was also indicated in section 4.2(g) that, in order to improve this system, higher values of load resistance or avalanche gain should be used. Since we are trying to avoid the use of avalanche photodetectors, the option is to increase the load resistance. It was pointed out, in section 4.2(g), that higher values of load resistance will result in the input signal being distorted due to the relatively large RC time constant of the receiver. This would have to be overcome by equalization. Although the previous work in this area by various researchers has been limited to digital receivers, it should be applicable to analog systems. However, this area will require further investigation and, probably, experimentation. For the purposes of this thesis, it will be assumed that such equalization will be achieved.

The example in section 4.2(g) considered an optical source operating at a center wavelength of $0.8\text{ }\mu\text{m}$. Using the responsivity curve provided by the photodetector manufacturer, an efficiency of 65% was determined using eq. (4.1). This curve approximated that of Fig. 4.3 to a large extent, except that the responsivity fell off dramatically beyond about $0.9\text{ }\mu\text{m}$, effectively rendering this particular device inadequate at $1.06\text{ }\mu\text{m}$. Using eq. (4.1), the device efficiencies were

determined to be 71%, 65%, 55% and 10% at $0.7\ \mu\text{m}$, $0.8\ \mu\text{m}$, $0.9\ \mu\text{m}$ and $1.06\ \mu\text{m}$, respectively. The efficiencies are seen to be decreasing as wavelength increases. This phenomenon can be used to advantage in the SNR calculations, in that variations among the SNR values for the three shorter wavelengths turn out to be quite insignificant. With this in mind, we can again perform the calculations for a system operating at $0.8\ \mu\text{m}$ and they will suffice, for all practical purposes, for all three wavelengths. It will also be assumed that a suitable detector will be available for operation at $1.06\ \mu\text{m}$ and for which the calculations will also suffice. This is a relatively unimportant assumption since, if no suitable device is available, this longer wavelength can be avoided by selecting devices with spectra closer together and allowing a certain amount of overlap. This would, however, create more problems in coupling, due to the narrower angular separation of the beams.

The noise performance curves of Figs. 4.5 and 4.6 are repeated as Figs. 7.8 and 7.9, respectively, for convenience. The received signal levels are shown for the LED and laser diode. For a p-i-n photodiode (Fig. 7.8), and with a load resistance of 4K ohms, positive SNR's are possible down to about -38 dBm. However, in order to obtain positive SNR's down to the lowest received level of -40 dBm, a load resistance of 10K ohms is required. It can also be seen from Fig. 7.8 that a variation in received optical power of 8.4 dB over the wavelengths considered results in a variation in SNR of some 17 dB, assuming thermal noise limited operation. This may require some compensation for the radio telescope feeder system, depending on final system design.

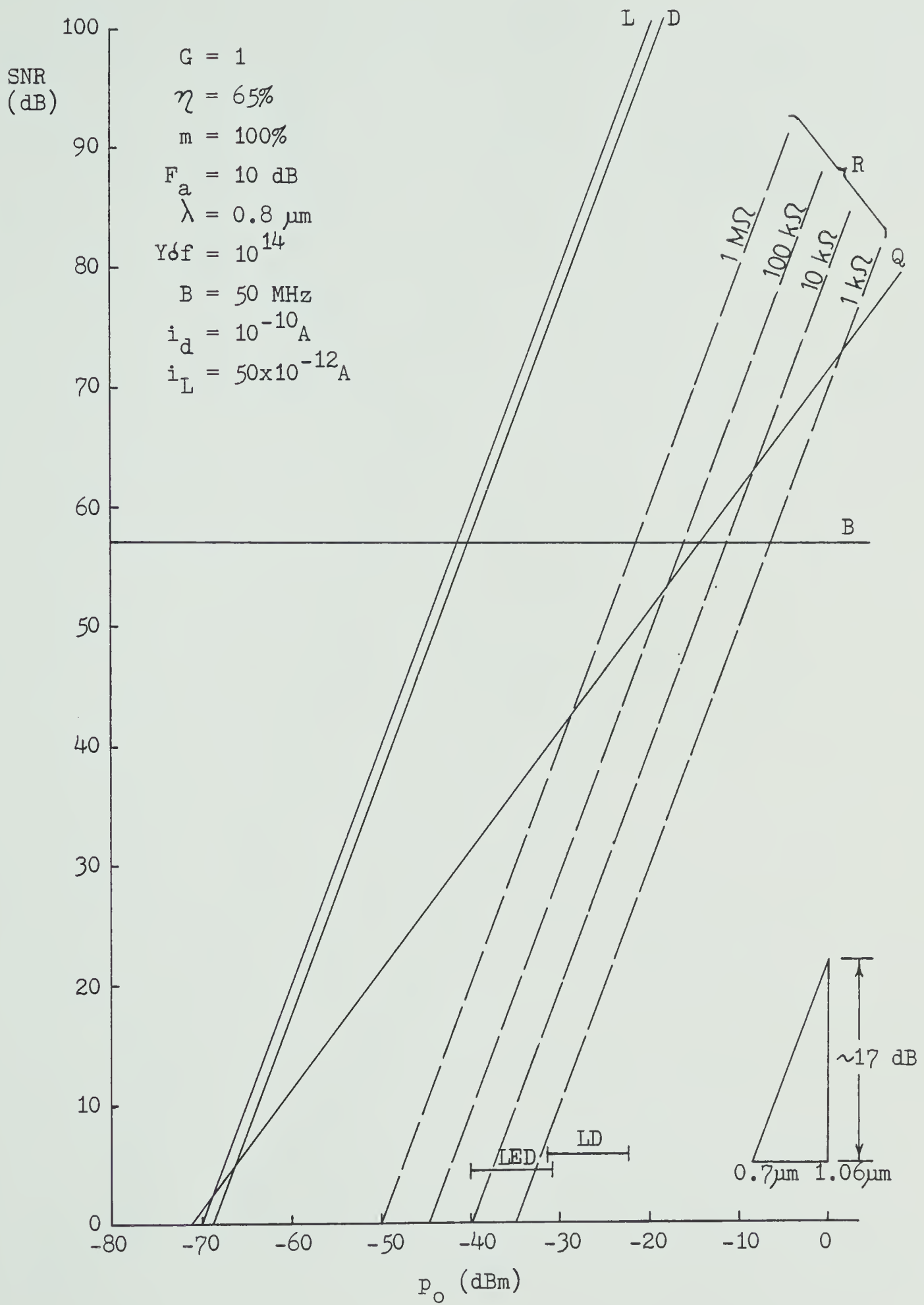


Fig. 7.8 Signal-to-component noise ratio versus incident power for a photodetector with unity gain.

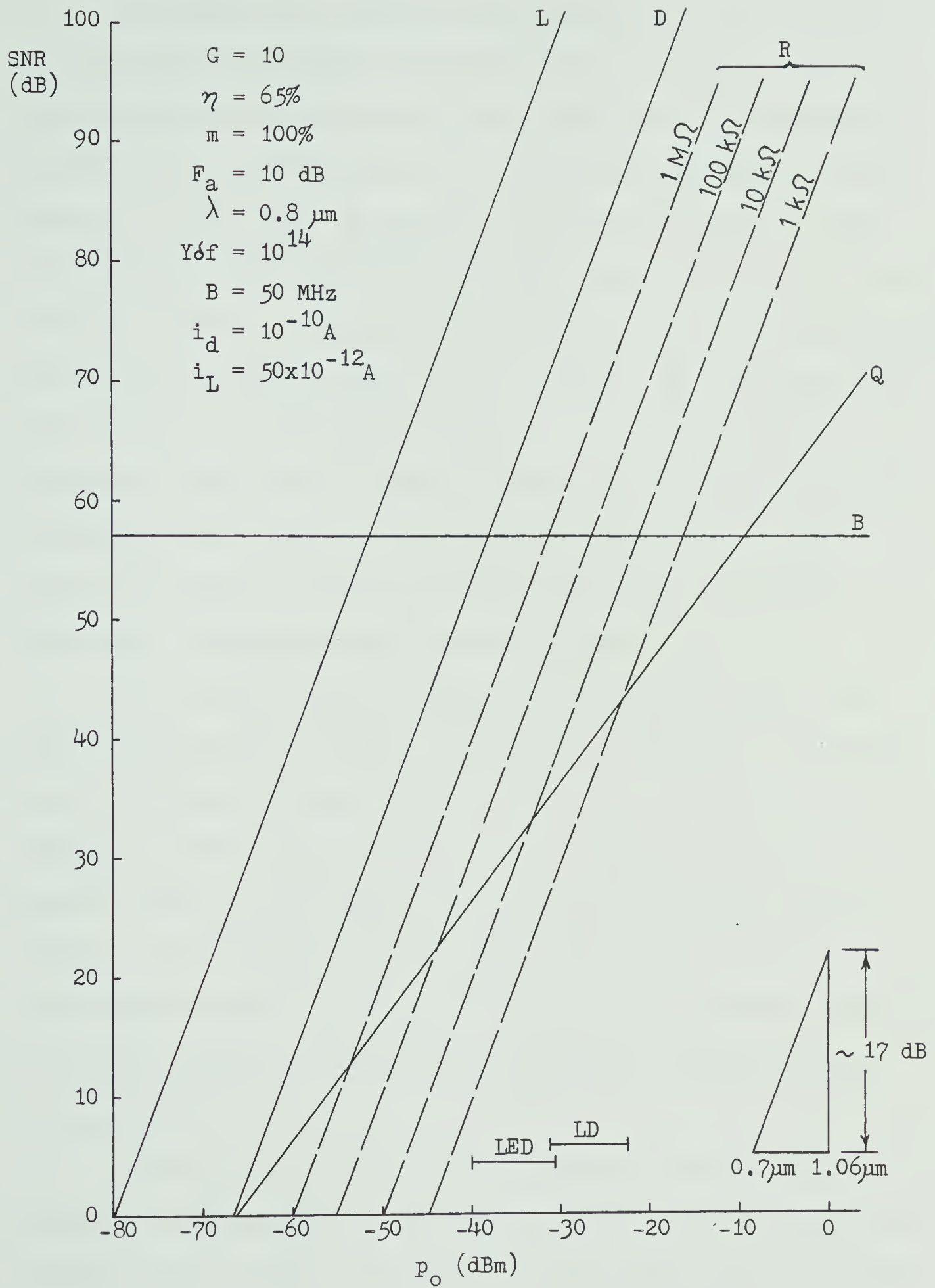


Fig. 7.9 Signal-to-component noise ratio versus incident power for a photodetector with gain of 10.

If higher SNR is desired without using very large values of load resistance, avalanche photodetectors are necessary. Using the same parameters as in the case for unity gain (the p-i-n photodiode), but including an avalanche gain of 10, the resulting SNR curves will appear as in Fig. 7.9. The received levels for the LED and laser diode are shown also. In this case, with a load resistance of 4k ohms, positive SNR values are possible down to about -48 dBm, a 10 dB improvement over the unity-gain case. For the LED, the SNR would range from about 15 dB at 0.7 μm to 32 dB at 1.06 μm . Increasing the load resistance to only about 7k ohms will bring the 1.06 μm LED system to the quantum noise limit of some 35 dB SNR, while the 0.7 μm LED system would still be thermal noise limited at about 18 dB SNR. At this point, a few words should be said about SNR.

The proposed radio telescope is a correlation array. This implies an improvement in SNR of 3 dB for each correlation, assuming the noise is purely random among the antennas. In addition, the signals of interest are at very low levels, deeply imbedded in galactic noise, to the extent that the SNR at the antenna input is negative. In this respect, transmission system SNR is not of overriding importance. However, since any additional noise contribution will further degrade the SNR, every effort should be made to keep it to a minimum.

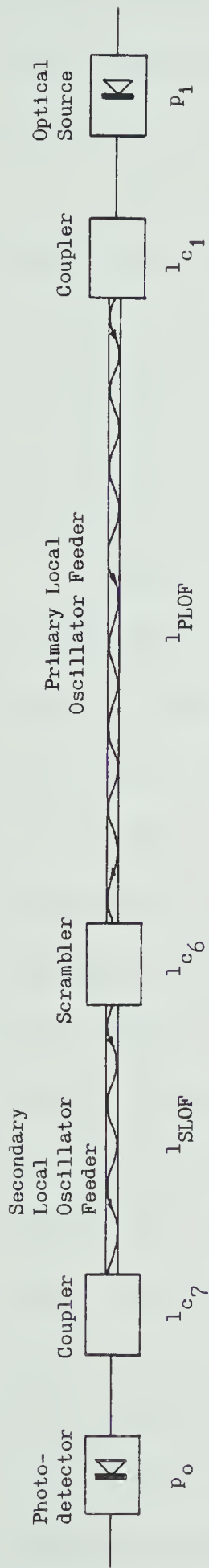
It has been seen that system SNR can be traded off against receiver load resistance (in the thermal noise controlled region) for specific values of input optical power. This thesis will not attempt to optimize this tradeoff. Basically, the largest value of load resistance should be selected whose effects can be economically

equalized. This will result in higher SNR and better device efficiency — ideally at the quantum noise limit. It will also allow more consideration to be given to using p-i-n photodiodes over avalanche photodiodes.

7.2.2 Local Oscillator Link

The optical local oscillator link is shown schematically in Fig. 7.10. The only items that are different from the optical antenna signal link in Fig. 7.7 are the scrambler and the photodetector coupler. Existing scramblers, used with optical fiber bundles, have been constructed of Pyrex rods in various lengths with the input and output fiber bundles butted against the ends [141]. Throughput losses of 1.5 - 2.5 dB were reported using this configuration. Assuming the scrambler is circular with diameter sufficient to accomodate the four secondary local oscillator feeders, as shown in Fig. 7.3(c), it can be shown, using basic geometry, that the feeders cover some 68% of the end of the scrambler. This implies that 1.6 dB is lost through the uncovered area. Since experimental work is necessary to determine optimum splitter configurations and their efficiencies, it will be assumed that there will be a 10 dB drop in level from the PLOF to each of the four SLOF's. The loss due to the scrambler l_{c6} will then be 10 dB.

The coupler between the secondary local oscillator feeder (SLOF) and the photodetector will be assumed to be a direct contact coupler. All the light energy that is output from the SLOF fiber will be constrained within a narrow cone of angle $\sin^{-1}(\text{N.A.}) \simeq 8^\circ$ about the axis assuming a fiber with numerical aperture of 0.14. Photo-



Power Budget				
	Laser Diode		LED	
		1.06 μm		1.06 μm
System Gains, P _i	5 mw	7 dBm	5 mw	7 dBm
System Losses l _{c1} l _{c6} l _{c7}	6		15	
	10		10	
	0.5		0.5	
Total Coupling Loss		16.5		25.5
Source Degradation		3		3
Temp. Degradation		3		3
Splices		2		2
Feeders l _{SLOF} l _{PLOF}	288 m	2 dB/km	288 m	2 dB/km
	2.5 km	0.6	2.5 km	0.6
Total Feeder Loss		5.0		5.0
Received Power, P _o		5.6		5.6
		-23.1 dBm		-32.1 dBm

Fig. 7.10 Optical local oscillator link and power budget

detectors are relatively insensitive to the angle of incidence of incoming light so a direct contact coupler should ensure virtually 100% coupling efficiency. For design purposes, a coupler loss l_{c7} of 0.5 dB will be allowed to account for any mismatch.

All other components are identical to those in Fig. 7.7. The power budget for the local oscillator link is determined directly and is shown in Fig. 7.10. The received power is seen to be almost the same as for the antenna signal link. This allows essentially the same arguments to be applied as for the antenna signal link. In this case, however, SNR assumes more significance.

The local oscillator signals must be extracted from the accompanying noise in the subsequent electrical detection stage. Since the SNR can not be enhanced through correlation, it must be sufficiently high to permit accurate detection and tracking. Tracking is required to synchronize the voltage-controlled oscillators in the phase-locked loop filters in order to maintain the high degree of frequency and phase accuracy required at the modulators. Since only a single optical carrier is required, a $1.06\text{ }\mu\text{m}$ source has been assumed, since the longer wavelength devices encounter lower losses. Fig. 7.7 indicates that a received level of -32.1 dBm, using an LED, results in an SNR of about 12 dB, assuming a load resistance of 4k ohms. Increasing the resistance to 40 k ohms will allow an SNR of 22 dB. Using a laser diode would result in an SNR of about 30 dB or 40 dB, assuming a load resistance of 4k and 40k ohms, respectively. As mentioned in section 4.2, it is advisable to use as high a value of load resistance as possible to attempt quantum noise-limited operation, and yet low enough that the resulting bandwidth distortion can be adequately improved with equalization.

7.3 System Noise Temperature

7.3.1 Antenna Signal Link

One of the most important factors requiring consideration in a radio telescope is its sensitivity. Since the antenna signal is essentially white noise, the sensitivity is a measure of how small a change in input noise power can be detected [3]. This, in turn, can be represented as a noise temperature.

The noise temperature T_{sys} of a receiving system is given by [49]

$$T_{\text{sys}} = T_{\text{ant}} + T_e \quad (7.1)$$

where T_{ant} is the noise temperature of the antenna
 T_e is noise temperature of the subsequent equipment.

McLarnon [3] has determined that the noise temperature of the antenna is about 1.4×10^5 °K at 12.36 MHz. In order to obtain maximum sensitivity for the system, the noise temperature contribution T_e must be considerably lower than T_{ant} , since T_{ant} is a system constant. McLarnon has indicated that if T_e is 10% or less of T_{ant} , the feeder system will contribute minimal degradation. Therefore, 1.4×10^4 °K will be considered as the maximum acceptable value for T_e in the following analysis.

To determine T_e for the system, it is necessary to consider all gains, losses and noise contributions of the various components in the transmission feeder system. This system can be represented schematically as shown in Fig. 7.11. In this diagram, the transmitter

is comprised essentially of all components in the CTL up to the optical source, the receiver is the r.f. demultiplexer, and the optical link is as shown in Fig. 7.7, including the optical source through to the photodetector. For this system, the noise temperature T_e is given by [49]

$$T_e = T_{e_{bf}} + \frac{T_{e_t}}{G_{bf}} + \frac{T_{e_o}}{G_{bf}G_t} + \frac{T_{e_r}}{G_{bf}G_tG_o} \quad (7.2)$$

where $T_{e_{bf}}$, T_{e_t} , T_{e_o} and T_{e_r} are the effective noise temperatures of the coaxial cable branch feeder, transmitter, optical link and receiver, respectively; G_{bf} , G_t and G_o are the gains of the branch feeder, transmitter and optical link, respectively. The effective noise temperature is related to the equipment noise figure F by the relationship [49]

$$T_e = T_o(F - 1) \quad (7.3)$$

where T_o is the ambient temperature of the equipment. For purposes of calculation, the ambient temperature of the outdoor equipment, ie: branch feeders and transmitter, will be assumed to be at a maximum of $+50^\circ\text{C}$. The ambient temperature of the receiver will be assumed to be $+30^\circ\text{C}$. The effective noise temperatures of the various subsystems will now be determined, in order that T_e can be calculated.

Branch Feeder

For the 48-channel, equal-length feeder system considered here, the length of the branch feeders is $83.6 + 18.3 + 3.2 = 105.1$ meters, which is determined from the E grouping in the east-west subarray. The branch feeders will be assumed to be RG-62 A/U coaxial cable with an attenuation of 3.12 dB/100 meters at 12.36 MHz and 20°C . This cable will be used here since it was selected by McLarnon [3] as being one of the most promising for an all-coaxial cable feeder system. The branch feeders will exhibit a loss of $3.12(1.051) = 3.28$ dB at 20°C . Allowing for temperature effects, a value of 4 dB will be used. This corresponds to a noise temperature

$$\begin{aligned} T_{e_{bf}} &= 323(\log^{-1}0.4 - 1) & (10 \log 0.4 = -4 \text{ dB}) \\ &= 4.9 \times 10^2 \text{ }^{\circ}\text{K} & \text{at } 50^{\circ}\text{C} \end{aligned}$$

Transmitter

The transmitter is shown in block diagram form in Fig.

7.12. The effective noise temperature T_{e_t} can be determined from

$$T_{e_t} = T_{e_1} + \frac{T_{e_2}}{G_1} + \frac{T_{e_3}}{G_1 G_2} + \frac{T_{e_4}}{G_1 G_2 G_3} + \frac{T_{e_5}}{G_1 G_2 G_3 G_4} \quad (7.4)$$

where T_{e_1} , T_{e_2} , T_{e_3} , T_{e_4} and T_{e_5} are the effective noise temperatures of the input amplifier, baseband filter, mixer, channel filter/combiner and optical source driver, respectively; G_1 , G_2 , G_3 and G_4 are the

respective gains of the input amplifier, baseband filter, mixer and channel filter/combiner. The channel filter and combiner are assumed to be pure loss devices and are "lumped" together to simplify calculations. Since the input amplifier noise temperature is a controlling parameter as seen from eq. 7.4, the noise figure will be assumed to be 5 dB. The input amplifier should also have as high a gain as practicable to minimize the noise contribution of the subsequent circuitry. It will be shown that a gain of 50 dB will be a reasonable minimum, so this value will be used. The baseband filter and channel filter insertion losses will be assumed to be 5 dB and 3 dB, respectively. The mixer will be assumed to exhibit a loss of 3 dB but, for noise calculation purposes, will be assumed to have a noise figure of 20 dB at the signal levels required. The channel combiner will be assumed to exhibit a loss of 24 dB (0.5 dB for each of the 48 channels combined). The optical source driver will not require the high degree of noise performance that the input amplifier required. A noise figure of 10 dB will be allowed. It will be seen that a gain of 50 dB for the optical source driver will be a reasonable minimum, so this value will be used.

The performance parameters assumed above are well within the state-of-the-art for circuitry at the frequencies of interest. It is expected that the loss and noise figures assumed for the design are very conservative. In this respect the design will represent a "worst-case" design and better performance can be expected from the working system. Using the above figures and substituting in eq. (7.3), the following parameters are determined:

$$T_{e_1} = 323(3.16 - 1) = 7 \times 10^2 \text{ }^\circ\text{K} \quad (10 \log 3.16 = 5 \text{ dB})$$

$$T_{e_2} = 323(3.16 - 1) = 7 \times 10^2 \text{ }^\circ\text{K}$$

$$T_{e_3} = 323(100 - 1) = 32 \times 10^3 \text{ }^\circ\text{K} \quad (10 \log 100 = 20 \text{ dB})$$

$$T_{e_4} = 323(501 - 1) = 16.2 \times 10^4 \text{ }^\circ\text{K} \quad (10 \log 501 = 27 \text{ dB})$$

$$T_{e_5} = 323(10 - 1) = 2.9 \times 10^3 \text{ }^\circ\text{K} \quad (10 \log 10 = 10 \text{ dB})$$

$$G_1 = 10^5 \quad (10 \log 10^5 = 50 \text{ dB})$$

$$G_2 = 0.3 \quad (10 \log 0.3 = -5 \text{ dB})$$

$$G_3 = 0.5 \quad (10 \log 0.5 = -3 \text{ dB})$$

$$G_4 = 2 \times 10^{-3} \quad (10 \log 2 \times 10^{-3} = -27 \text{ dB})$$

Substituting these numbers in eq. (7.4) yields

$$\begin{aligned} T_{e_t} &= 7 \times 10^2 + \frac{7 \times 10^2}{10^5} + \frac{32 \times 10^3}{10^5(0.3)} + \frac{16.2 \times 10^4}{10^5(0.3)(0.5)} \\ &\quad + \frac{2.9 \times 10^3}{10^5(0.3)(0.5)(2 \times 10^{-3})} \\ &= 7 \times 10^2 + \text{Neg.} + 1.1 + 10.8 + 96.7 \end{aligned}$$

or

$$T_{e_t} = 8.1 \times 10^2 \text{ }^\circ\text{K}$$

The controlling influence of the input amplifier is apparent from an examination of the above calculation. Its low noise figure (5 dB) contributes the majority of noise and its relatively high gain (50 dB) effectively renders all subsequent noise sources to have little influence on the overall noise performance. Even the mixer stage, which has been allotted a noise figure of 20 dB is seen to contribute negligible noise. Clearly, the mixer stage could tolerate a noise figure of up to about 40 dB without significantly affecting the overall noise performance.

The overall transmitter gain G_t is then

$$G_t = 50 - 5 - 3 - 3 - 24 + 50 = 65 \text{ dB}$$

Receiver

The receiver is shown in block diagram in Fig. 7.13. The effective noise temperature T_{e_r} can be determined from

$$T_{e_r} = T_{e_6} + \frac{T_{e_7}}{G_6} + \frac{T_{e_8}}{G_6 G_7} + \frac{T_{e_9}}{G_6 G_7 G_8} \quad (7.5)$$

where T_{e_6} , T_{e_7} , T_{e_8} and T_{e_9} are the effective noise temperatures of the r.f. amplifier, band-splitting filter/signal distribution stage, mixer and baseband filter, respectively; G_6 , G_7 and G_8 are the respective gains of the r.f. amplifier, band-splitting filter/signal distribution stage and the mixer. The band-splitting filter and signal distribution stage are assumed to be pure loss devices and are "lumped" together to simplify calculations. While the receiver

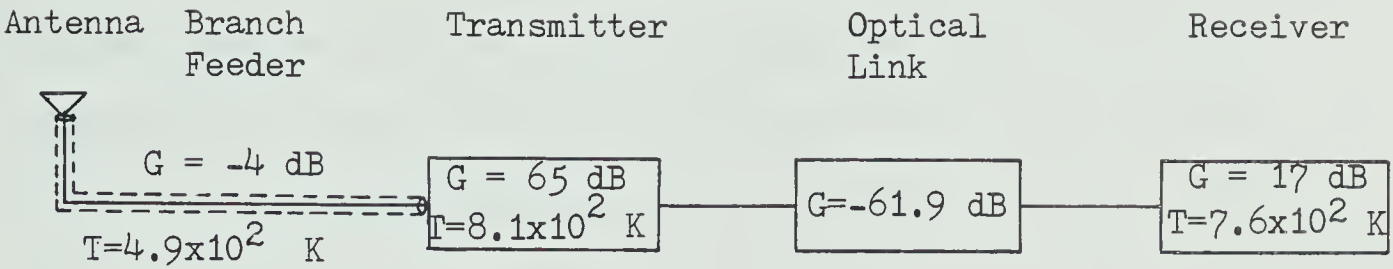


Fig. 7.11 Transmission system model for noise temperature calculations

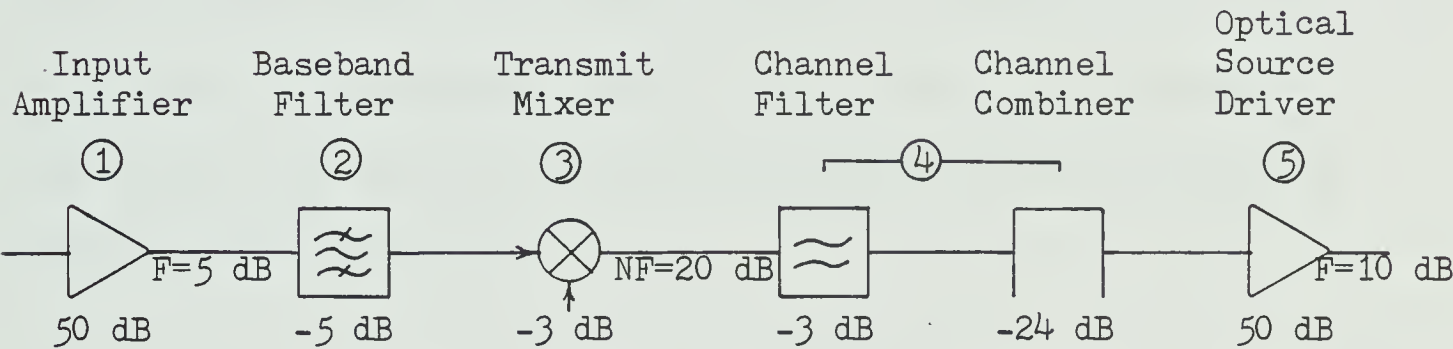


Fig. 7.12 Transmitter model for noise temperature calculations

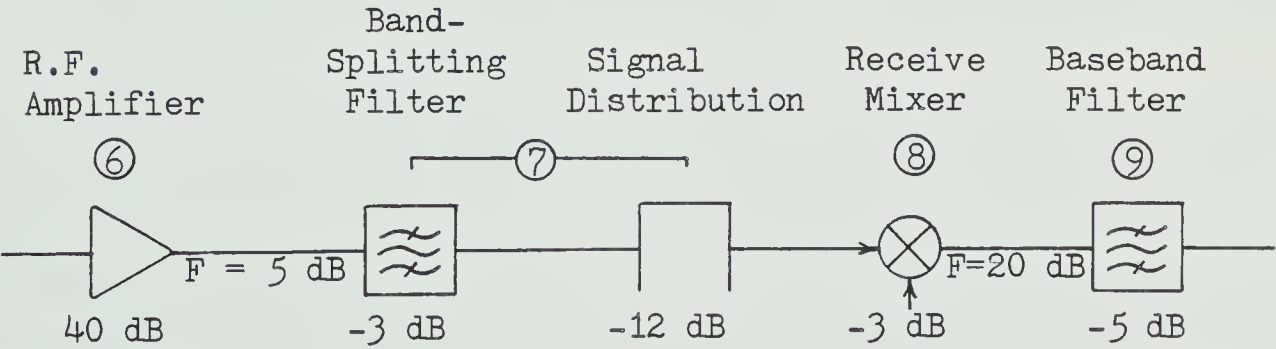


Fig. 7.13 Receiver model for noise temperature calculations

circuitry is the furthest from the antenna, it is preceded by the optical link which is a large source of loss (negative gain). This dictates that the receiver section should have very good noise performance in order that its contribution not be prohibitively large. With this in mind, the r.f. amplifier is assumed to have a noise figure of 5 dB. A gain of 40 dB will be shown to be adequate so this value will be used. The band-splitting filter and the baseband filter insertion losses will be assumed to be 3 dB and 5 dB, respectively. The signal distribution stage will be assumed to have a 12 dB loss (0.5 dB for each of 24 channels). Consistent with the transmitter, the mixer will be assumed to introduce 3 dB loss and to have a noise figure of 20 dB at the signal levels required. Using these numbers and substituting into eq. (7.3), the following parameters are determined:

$$T_{e_6} = 303(3.16 - 1) = 6.6 \times 10^2 \text{ }^\circ\text{K} \quad (10 \log 3.16 = 5 \text{ dB})$$

$$T_{e_7} = 303(31.6 - 1) = 9.3 \times 10^3 \text{ }^\circ\text{K} \quad (10 \log 31.6 = 15 \text{ dB})$$

$$T_{e_8} = 303(100 - 1) = 3 \times 10^4 \text{ }^\circ\text{K} \quad (10 \log 100 = 20 \text{ dB})$$

$$T_{e_9} = 303(3.16 - 1) = 6.6 \times 10^2 \text{ }^\circ\text{K} \quad (10 \log 3.16 = 5 \text{ dB})$$

$$G_6 = 10^4 \quad (10 \log 10^4 = 40 \text{ dB})$$

$$G_7 = 3 \times 10^{-2} \quad (10 \log [3 \times 10^{-2}] = -15 \text{ dB})$$

$$G_8 = 0.32$$

$$(10 \log 0.32 = -5 \text{ dB})$$

Substituting these numbers into eq. (7.5) yields

$$\begin{aligned} T_{e_r} &= 6.6 \times 10^2 + \frac{9.3 \times 10^3}{10^4} + \frac{3 \times 10^4}{10^4 (3 \times 10^{-2})} + \frac{6.6 \times 10^2}{10^4 (3 \times 10^{-2}) (0.32)} \\ &= 6.6 \times 10^2 + 0.9 + 100 + 6.8 \\ &= 7.6 \times 10^2 \text{ } ^\circ \text{K} \end{aligned}$$

Just as in the case of the transmitter, the amplifier is the controlling stage in the receiver. In this case, the noisy mixer is seen to contribute more noise, since the total gain preceding the mixer is less than that for the transmitter. Even so, the contribution from the mixer is less than 10% of the total noise temperature.

The overall receiver gain G_r is determined to be

$$G_r = 40 - 3 - 12 - 3 - 5 = 17 \text{ dB}$$

Optical Link

The noise performance of the optical link has already been examined from the signal-to-noise ratio viewpoint. Since we are attempting now to appraise the noise performance of the transmission system from a noise temperature viewpoint, it would appear necessary to determine the noise temperature of the optical link. However, an explicit value of noise temperature can not be readily determined

here for a number of reasons. Firstly, noise figures of optical sources and photodetectors are not specified by the manufacturers. This would require physical measurements. Secondly, the optical fiber and the associated optical couplers are not thermal noise sources. The author is not aware of any work characterizing and quantifying noise in optical fibers.

In spite of this apparent obstacle, the system noise temperature performance will be carried through if we assume that the optical link will behave as an ideal resistance acting as a thermal noise source. This analysis should yield a worst-case condition since the optical link is not a thermal noise source. Further, it will be assumed that the optical link will be operating at the maximum outdoor temperature of $+50^{\circ}\text{C}$. The losses of the various passive elements of the optical link are listed in the power budget of Fig. 7.7 and are repeated for convenience in Fig. 7.14.

It was reported in section 3.2.2 that Burrus-type LED's have quantum efficiencies of the order of 1 - 2%. Since we are considering the use of edge-emitting LED's, which have higher efficiency than the Burrus-type, the optical source will be assumed to have a quantum efficiency of 5%. This is equivalent to a loss in power of 13 dB. The photodetectors will be assumed to have an efficiency of 65% or an effective loss of 1.9 dB. The combination of the source and source-to-fiber coupler is seen to be 28 dB or an

overall efficiency of 0.0015%. This is an extremely pessimistic efficiency as evident from the discussion in chapter 5. Nevertheless, this will be used in our worst-case analysis here. The overall optical link loss, including the 6 dB degradation losses and 2 dB splice/connection loss is then

$$l_{\text{opt}} = 13 + 15 + 1.5 + 3 + 1 + 12.5 + 4 + 2 + 1.9 + 6 + 2$$

$$= 61.9 \text{ dB}$$

or the optical link gain G_o is -61.9 dB. If this is assumed to be a purely resistive network obeying thermal noise laws, the effective noise temperature T_{e_o} at 50°C is then

$$T_{e_o} = 323(1.55 \times 10^6 - 1) \quad (10 \log[1.55 \times 10^6] = 61.9 \text{ dB})$$

$$= 500 \times 10^6 \text{ }^\circ\text{K}$$

System Noise Temperature

The noise temperature T_e of the equipment beyond the antenna is given by eq. (7.2),

$$T_e = T_{e_{bf}} + \frac{T_{e_t}}{G_{bf}} + \frac{T_{e_o}}{G_{bf}G_t} + \frac{T_{e_r}}{G_{bf}G_tG_o}$$

where the parameters have been previously defined in this section and are shown in Fig. 7.11. Substituting the calculated numerical values into this equation yields an effective noise temperature

$$\begin{aligned}
T_e &= 4.9 \times 10^2 + \frac{8.1 \times 10^2}{0.4} + \frac{500 \times 10^6}{0.4(3.2 \times 10^6)} + \frac{7.6 \times 10^2}{0.4(3.2 \times 10^6)(6.5 \times 10^{-7})} \\
&= 4.9 \times 10^2 + 2 \times 10^3 + 3.9 \times 10^2 + 9.1 \times 10^2 \\
&= 3.8 \times 10^3 \text{ } ^\circ \text{K}
\end{aligned}$$

This is a factor of almost 4 smaller than the allowable value of $1.4 \times 10^4 \text{ } ^\circ \text{K}$ as specified on page 224.

It is interesting to determine the maximum noise temperature that would be allowed for the optical link such that the overall effective noise temperature of $1.4 \times 10^4 \text{ } ^\circ \text{K}$ is not exceeded. In this case, eq. 7.2 can be written

$$\begin{aligned}
T_{e_{\max}} &= 1.4 \times 10^4 \geq T_{e_{\text{bf}}} + \frac{T_{e_t}}{G_{\text{bf}}} + \frac{T_{e_o}}{G_{\text{bf}}G_t} + \frac{T_{e_r}}{G_{\text{bf}}G_tG_r} \\
&\geq 4.9 \times 10^2 + 2 \times 10^3 + \frac{T_{e_o}}{0.4(3.2 \times 10^6)} + 9.1 \times 10^2 \\
&\geq 3.4 \times 10^3 + \frac{T_{e_o}}{1.28 \times 10^6}
\end{aligned}$$

$$\begin{aligned}
\text{or, } T_{e_o} &\leq (1.4 \times 10^4 - 3.4 \times 10^3) 1.28 \times 10^6 \\
&\leq 1.36 \times 10^{10} \text{ } ^\circ \text{K} \quad (76.2 \text{ dB at } 50^\circ \text{C})
\end{aligned}$$

This is over twice as large as the value that was used based on a thermal noise mechanism. Another way of looking at this is that the 61.9 dB loss optical link could be replaced by a thermal noise controlled resistive network with a loss of 76.2 dB at an ambient

temperature of 50°C and the system would still maintain satisfactory noise performance. There can be no doubt that an optical fiber system will perform much better than an electrical cable system.

The foregoing analysis assumed a noise figure of 20 dB for the transmitter and receiver mixer stages. Since the receiver is situated in the same location as the virtually "clean" local oscillator frequency supplies, this figure should represent a maximum value for the receiver mixer. For the remote transmitters, however, additional noise is inevitable due to the loss and dispersion in the distribution system. It is interesting to consider the maximum allowable noise contribution that could be allocated to the mixer stage in the transmitter in order to consider noise effects from the local oscillator system. Writing eq. (7.2) once again, we have

$$T_e = T_{e_{bf}} + \frac{T_{e_t}}{G_{bf}} + \frac{T_{e_o}}{G_{bf}G_t} + \frac{T_{e_r}}{G_{bf}G_tG_o}$$

If we substitute the previously calculated values for all parameters except T_{e_t} and allow T_e to be the maximum allowable value of 1.4×10^4 K, we have

$$T_{e_{\max}} = 1.4 \times 10^4 \geq 4.9 \times 10^2 + \frac{T_{e_t}}{0.4} + 3.9 \times 10^2 + 9.1 \times 10^2$$

or

$$T_{e_t} \leq 4.9 \times 10^3 \text{ }^{\circ}\text{K}$$

Substituting the value into eq. (7.4) for the effective noise

temperature of the transmitter and using the previously calculated values for the other parameters, the maximum allowable noise T_{e3} of the mixer stage is calculated to be

$$\begin{aligned} T_{e3} &\leq (4.9 \times 10^3 - 7 \times 10^2 - 10.8 - 96.7) 0.3 \times 10^5 \\ &\leq 1.23 \times 10^8 \text{ } ^\circ \text{K} \end{aligned}$$

This is equivalent to a maximum allowable noise figure of

$$\log \left[\frac{1.23 \times 10^8}{323} + 1 \right] = \log(3.81 \times 10^5) = 55.8 \text{ dB}$$

This indicates that there is a considerable margin allowed in the noise performance of the mixer stage. However, this noise performance includes all the noise contributed by the mixer stage, including that of the local oscillator signal. The noise temperature of the local oscillator system will now be examined.

7.3.2 Local Oscillator Link

Fig. 7.15 shows a block diagram of the local oscillator distribution system. The local oscillator frequency supplies can be considered to be comprised of a signal generator and transmit amplifier. The noise temperature will be determined from the input of the transmit amplifier. This amplifier will be assumed to have a gain of 40 dB and a noise figure of 10 dB. The local oscillator combiner will be allowed a maximum loss of 24 dB (1 dB for each of the 24 local oscillator signals). The optical source driver will be

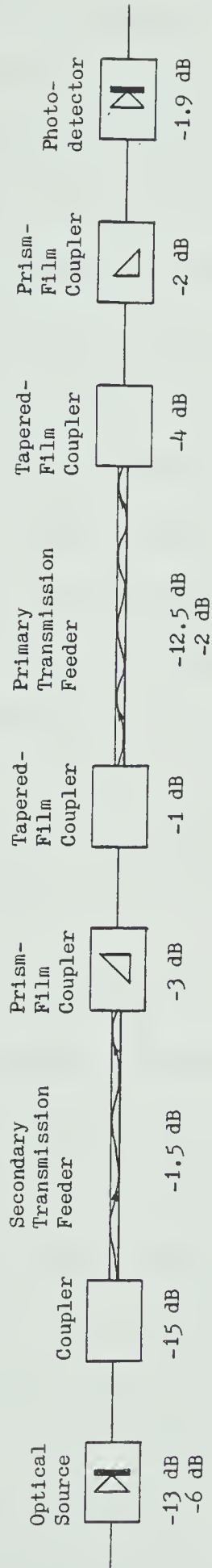


Fig. 7.14 Optical antenna signal link model for noise temperature calculations

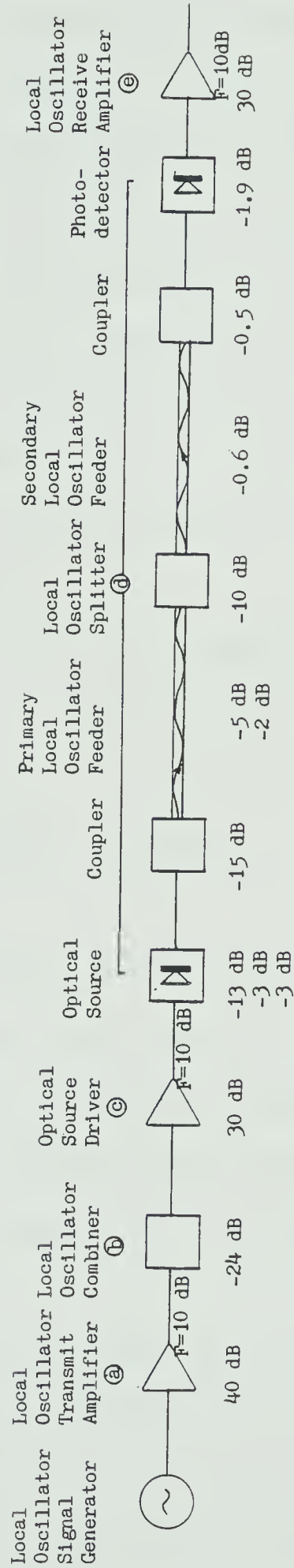


Fig. 7.15 Local oscillator link model for noise temperature calculations

allowed a noise figure of 10 dB as in the transmitter section and will be allocated a gain of 30 dB. The losses of the various elements of the optical local oscillator link total 31.1 dB as given in Fig. 7.10. The optical source and photodetector are assumed to exhibit losses of 13 and 1.9 dB, respectively, to be consistent with the antenna signal transmission system. A degradation margin of 3 dB will be allowed for the optical source, 3 dB for temperature effects and 2 dB will be allowed to account for connections and splices. The overall loss allocated to the optical section will then be 54 dB. The local oscillator receive amplifier will be assumed to have a noise figure of 10 dB and a gain of 30 dB.

The noise temperature T_{e_l} of the local oscillator system can be expressed as

$$T_{e_l} = T_{e_a} + \frac{T_{e_b}}{G_a} + \frac{T_{e_c}}{G_a G_b} + \frac{T_{e_d}}{G_a G_b G_c} + \frac{T_{e_e}}{G_a G_b G_c G_d} \quad (7.6)$$

where T_{e_a} , T_{e_b} , T_{e_c} , T_{e_d} and T_{e_e} are the effective noise temperatures of the transmit amplifier, local oscillator combiner, optical source driver, optical local oscillator link and receive amplifier, respectively. Similarly, G_a , G_b , G_c and G_d are the gains of the transmit amplifier, local oscillator combiner, optical source driver and optical local oscillator link, respectively.

Just as was done for the antenna signal transmission system, the system noise temperature will be calculated with the assumption that the optical local oscillator link acts as a thermal noise source. This will serve to make the analysis a "worst-case" situation as before.

Using eq. (7.3), the effective noise temperatures can be determined as follows:

$$T_{e_a} = 303(10 - 1) = 2.7 \times 10^3 \text{ }^\circ\text{K} \quad (10 \log 10 = 10 \text{ dB})$$

$$T_{e_b} = 303(251 - 1) = 7.6 \times 10^4 \text{ }^\circ\text{K} \quad (10 \log 251 = 24 \text{ dB})$$

$$T_{e_c} = 303(10 - 1) = 2.7 \times 10^3 \text{ }^\circ\text{K}$$

$$T_{e_d} = 323(2.5 \times 10^5 - 1) = 81 \times 10^7 \text{ }^\circ\text{K} \quad (10 \log [2.5 \times 10^5] = 54 \text{ dB})$$

$$T_{e_e} = 323(10 - 1) = 2.9 \times 10^3 \text{ }^\circ\text{K}$$

The gains are determined to be

$$G_a = 10^4 \quad (10 \log 10^4 = 40 \text{ dB})$$

$$G_b = 4 \times 10^{-3} \quad (10 \log [4 \times 10^{-3}] = -24 \text{ dB})$$

$$G_c = 10^3 \quad (10 \log 10^3 = 30 \text{ dB})$$

$$G_d = 4 \times 10^{-6} \quad (10 \log [4 \times 10^{-6}] = -54 \text{ dB})$$

Substituting these values into eq. (7.6), the effective noise temperature of the local oscillator system becomes

$$T_{e_1} = 2.7 \times 10^3 + \frac{7.6 \times 10^4}{10^4} + \frac{2.7 \times 10^3}{10^4(4 \times 10^{-3})} + \frac{8.1 \times 10^7}{10^4(4 \times 10^{-3})10^3} \\ + \frac{2.9 \times 10^3}{10^4(4 \times 10^{-3})10^3(4 \times 10^{-6})}$$

$$= 2.7 \times 10^3 + 7.6 + 67.5 + 2 \times 10^3 + 1.8 \times 10^4$$

$$= 2.3 \times 10^4 \text{ } ^\circ \text{K}$$

If the ambient temperature of the local oscillator system is considered to be at 303°K for convenience, the noise figure would be equivalent to

$$10 \log \left[\frac{2.3 \times 10^4}{303} + 1 \right] \approx 19 \text{ dB}$$

This means that the SNR of the local oscillator signal at the input to the filter stage would be 19 dB lower than at the output of the signal generator. The SNR at the output of the signal generator will be very high, being virtually pure signal with very little noise. Depending on the actual SNR at this point, the SNR of the local oscillator signal at the input to the remote mixers may be made sufficient for phase and frequency stability requirements by using relatively simple passive slot filters. If the filters are assumed to be phase-locked loops, the SNR of the local oscillator signals presented to the mixers can be higher since the PLL has its own generator (a voltage-controlled oscillator, or VCO). This depends on PLL design factors such as loop bandwidth, time constant(s), order of loop. This thesis will not attempt to present the PLL design criteria. It will be assumed that the necessary local oscillator SNR and phase and frequency stability required at the mixers will be attained using the arrangement described.

Since the noise figure of the transmitter mixers was shown to be able to be as high as 55.8 dB and still meet requirements, it

appears that there is considerable margin allowed for in the system. In view of this and the previous development, the transmission feeder system as described in this chapter is expected to contribute minimal degradation to the radio telescope sensitivity.

7.4 Excitation Errors

In chapter one, the maximum expected r.m.s. phase and amplitude excitation errors were specified to be 1° and 2%, respectively. To this point, only passing mention has been made of these important parameters. Now that a transmission system has been designed that is expected to provide satisfactory performance from the sensitivity viewpoint, it is necessary to assess its performance in terms of phase and amplitude error. McLarnon [3] discussed phase and amplitude errors at length in his coaxial cable feeder system design. In view of this, the subsequent discussion on excitation errors will be brief.

The various components in the transmission system will be examined from the point of view of excitation errors. The overall error estimates will then be determined and compared with the original specifications.

Branch Feeders

The branch feeders were considered to be RG-62 A/U coaxial cable. For the equal-length system being considered, the length of each branch feeder was determined to be 105.1 meters. McLarnon [3] had estimated that cable trimming, using the Swarup and Yang technique, should result in an r.m.s. phase error of 0.1° . This value will be assumed here as well. He also determined r.m.s. amplitude errors of

5.8×10^{-3} (0.05 dB). Since the branch feeders are much shorter than the cables considered by McLarnon, it will be assumed that r.m.s. amplitude errors can be constrained to 3.5×10^{-3} (0.03 dB).

The r.m.s. phase error $\epsilon_{\text{r.m.s.}}$ due to temperature variation can be determined from [3]

$$\epsilon_{\text{r.m.s.}} = \varphi_c |\delta T| (\delta K_p)_{\text{r.m.s.}} \times 10^{-6} \quad (7.7)$$

where $\varphi_c = 360 f_o \tau_c$, the absolute phase shift

and δT is the temperature range

δK_p is the phase-temperature coefficient (4×10^{-6})

f_o is the center frequency (12.36 MHz)

τ_c is the absolute delay.

Using a velocity factor of 0.84 for RG-62 A/U [3], the absolute delay in the branch feeders is

$$\tau_c = \frac{105.1}{0.84(3 \times 10^8)} = 0.42 \mu\text{sec.}$$

The r.m.s. phase error $\epsilon_{\text{r.m.s.}}$ is then determined to be

$$\epsilon_{\text{r.m.s.}} = 360(12.36 \times 10^6)(0.42 \times 10^{-6})(4 \times 10^{-6})|\delta T|$$

$$= 7.47 \times 10^{-3} |\delta T|$$

$$= 0.3^\circ \text{ over the temperature range of } \pm 40^\circ \text{C.}$$

McLarnon [3] assumed that amplitude variations among his feeders could be negligible. For the much shorter branch feeders considered here, this should also be valid.

Input Amplifier

For his preamplifier, McLarnon [3] estimated r.m.s. phase and amplitude errors to be 0.1° and 5.8×10^{-3} (0.05 dB), respectively. The input amplifier here is not fundamentally different from McLarnon's preamplifier. It will be assumed that the same errors can be used here.

Baseband Filters

McLarnon [3] considered the use of an eight pole Butterworth filter in his system and estimated r.m.s. phase and amplitude errors to be 0.5° and 0.010 (0.087 dB departure from nominal), respectively. The filters suggested here are five pole Butterworth filters. While these are less complex than the eight pole filters, the same errors will be assumed here.

Transmit Mixers

Excitation errors from the mixing process are directly dependent on the variation, among the mixers, of the quality of the local oscillator signals at the mixers. McLarnon [3] estimated that r.m.s. phase and amplitude errors could be held to 0.1° and 5.8×10^{-3} (0.05 dB), respectively, with his coaxial cable system. Since an optical fiber system is inherently much more stable than a coaxial cable system, it should be easier to restrict excitation errors to these values. Even so, these same values will be assumed in this design.

Channel Filters

The channel filters did not have the steep attenuation skirts that the baseband filters required. While these filters will also have to have their amplitude and phase responses carefully matched to minimize excitation errors, it should be an easier task. It will be estimated that r.m.s. phase and amplitude excitation errors will be half that of the baseband filters, or 0.25° and 5×10^{-3} (0.043 dB departure from nominal).

Channel Combiners

The channel combiner is assumed to be a linear network and should not be a major contributor to excitation errors. It will be estimated that r.m.s. phase and amplitude errors will be no greater than 0.15° and 2.5×10^{-3} (0.02 dB).

Optical Source Driver

The optical source driver is essentially an amplifier. In this respect, the same excitation errors will be assumed as for the baseband amplifier, or 0.1° r.m.s. phase error and 5.8×10^{-3} (0.05 dB) r.m.s. amplitude error.

Optical Source

The variation in phase errors among the optical sources is expected to be negligible since any phase error would be dependent on the response time of the source. Proper selection of devices and appropriate circuitry should keep amplitude errors low. It will be

assumed that r.m.s. amplitude errors will be no greater than about 3.5×10^{-3} (0.03 dB).

Optical Path

The optical path comprises all the components of the optical link except the optical source and photodetector. With the exception of the optical fiber feeders, the rest of the optical components should introduce virtually no phase error at the frequency band of interest (12.36 ± 0.1 MHz). This would allow all the optical fibers to be trimmed in phase before being installed and attached to the various couplers.

Trimming the optical fibers in phase is a problem that has not been discussed. McLarnon [3] has covered the problem of trimming coaxial cables in phase and has indicated that accuracy to $\pm 0.1^\circ$ is possible. In essence, this is accomplished by comparing the phase of the signal reflected from the far-end of the cable to the phase of the signal injected at the near-end. In principle, this method should work with comparable accuracy using optical fibers. McLarnon [3] has indicated that the relatively high attenuation of coaxial cables tends to compound the measurement problem. In this respect, the relatively low attenuation of optical fibers should be an advantage. Obtaining suitable optical apparatus for directional coupling at the near-end and providing reflection at the far-end should not be a major problem.

All the optical components and interconnections introduce losses and it would be a very difficult job to provide tight tolerances on these losses in practice. Once the optical fibers have been trimmed in phase, there will undoubtedly be some variation in the

attenuation, depending on the actual fiber lengths. At present, it is difficult to estimate this loss variation. It depends entirely on the manufacturing processes, which are in a state of evolution. However, it is anticipated that this loss variation will not be a significant problem since (1) the loss in optical fibers is virtually temperature independent over the ambient range of operation and (2) these loss variations can be compensated for by the use of gain adjustments in the r.f. demultiplexing stage.

For the purposes of this thesis it will be assumed that the optical fiber trimming and differential gain adjustments will result in r.m.s. phase and amplitude errors of no more than 0.1° and 5.8×10^{-3} (0.05 dB). These are the values estimated by McLarnon [3] for his coaxial cable feeders using the Swarup and Yang technique. For the optical fiber system, temperature effects are expected to be negligible.

Photodetectors

The photodetectors are expected to perform similar to the optical sources in terms of excitation errors. In this respect, the r.m.s. phase errors are assumed to be negligible and the r.m.s. amplitude errors are assumed to be no greater than 3.5×10^{-3} (0.03 dB).

R.F. Amplifier

The R.F. amplifier is considered to perform similar to the baseband amplifier. The estimated r.m.s. phase and amplitude errors are 0.1° and 5.8×10^{-3} (0.05 dB), respectively.

Band-Splitting_Filters

The band-splitting filters are of comparable complexity to the channel filters. The excitation error performance is expected to be similar, ie: 0.25° r.m.s. phase error and 5×10^{-3} (0.043 dB) r.m.s. amplitude error.

Signal_Distribution

The signal distribution circuitry merely provides a "fan-out" function, that is, to provide multiple identical outputs of a common input signal. Accordingly, it should be no great task to provide close tolerances among these outputs. It will be estimated that r.m.s. phase and amplitude errors will be no greater than 0.1° and 3.5×10^{-3} (0.03 dB), respectively.

Receive Mixers

Excitation errors from the receive mixers should be an improvement over the errors associated with the transmit mixer since the local oscillator signal generators are in the same physical location. This should provide much better quality signals at the receive mixers. Accordingly, the r.m.s. phase and amplitude errors will be estimated to be 0.05° and 1.7×10^{-3} (0.015 dB).

Baseband_Filters

The baseband filters in the receiver are considered to be identical to those in the transmitter. Therefore, the estimated r.m.s. phase and amplitude errors are assumed to be the same, ie: 0.5° and 0.010 (0.087 dB), respectively.

Summary

The summary of the foregoing excitation errors is presented in Table 7.1. This summary assumes that the individual error sources are independent, so that the total r.m.s. errors are simply the square root of the sum of the individual mean-square values. The results indicate that the r.m.s. phase errors are within the 1° specification, but the r.m.s. amplitude errors exceed the 2% specification. If this latter specification is to be met, a number of the individual error estimates would have to be improved upon. It is also possible to reduce the overall errors by employing phase and amplitude compensation systems. McLarnon [3] discussed compensation systems at length. For the purposes of this thesis, it will suffice to mention that, if compensation systems are to be seriously contemplated for an optical fiber transmission system, methods similar to those examined by McLarnon [3] could be adopted. Actual improvement in r.m.s. phase and amplitude errors would have to be determined at that time.

Table 7.1

Summary of Excitation Error Estimates

Source of Error	Estimated RMS Excitation Errors	
	Phase (Degrees)	Fractional Amplitude ($\times 10^{-3}$)
Branch Feeder (Measurement)	0.1	3.0
(Temperature)	0.3	—
Baseband Amplifier	0.1	5.8
Baseband Filter	0.5	10
Transmit Mixer	0.1	5.8
Channel Filter	0.25	5
Channel Combiner	0.15	2.5
Optical Source Driver	0.1	5.8
Optical Source	—	3.5
Optical Path	0.1	5.8
Photodetectors	—	3.5
R.F. Amplifier	0.1	5.8
Band-Splitting Filter	0.25	5
Signal Distribution	0.1	3.5
Receive Mixer	0.05	1.7
Baseband Filter	0.5	10
Estimated Overall	0.92	21.8
RMS Errors	(0.016 rad)	(2.2%)

CHAPTER 8

SUMMARY AND CONCLUSIONS

An optical fiber transmission system for a low-frequency radio telescope array has been presented in the preceding chapters. This presentation is in the form of a system design based on a number of assumptions, generalizations and extrapolations. The design should, therefore, be considered as being representative of various possible configurations. Depending on factors such as final antenna dipole configuration, evolution in optical and r.f. technology, or decisions relating to performance and economics, the final transmission system design may be substantially different. Since it is not possible to include all the details of a comprehensive design at this time, the design has concentrated on presenting a transmission system based on the general principles covered in the earlier chapters. However, based on the assumptions indicated and implied throughout this thesis, a number of conclusions can be reached regarding the general design of a transmission system for the proposed radio telescope:

1. An optical fiber system is not only viable but vastly superior to a coaxial cable system in terms of transmission performance, particularly over the temperature range expected. For this reason, it should not be necessary to use phase and amplitude compensation systems in the array.

2. At the frequency of interest (12.36 MHz), a digital or pulse modulation system would offer very little multiplexing capability.

With the relatively narrow bandwidth of interest (200 KHz), a large number of channels can be frequency-division-multiplexed using basic SSB-SC modulation techniques. An upper limit of 48 channels has been determined as being a practical maximum and is assumed here with 1 MHz channel separation.

3. The feeder configuration envisioned employs equal-length transmission lines throughout the array. The branch feeders from the antenna dipoles to the central transmitting locations (CTL's) use coaxial cables to retain the antenna signals in the electrical domain to facilitate frequency-division-multiplexing. At the CTL's the FDM waveforms are modulated onto an optical carrier and conveyed to the optical multiplexing locations (OML's) via optical fiber secondary transmission feeders (STF's). At the OML's the optical signals from four STF's are wavelength-division-multiplexed onto individual fiber primary transmission feeders (PTF's) for distribution to the observatory.

4. Wavelength-division-multiplexing appears to be feasible using the arrangement described. If its performance can be proven to be satisfactory in practice, it would be another means of providing savings of transmission line. With the antenna configuration depicted, there appears to be no advantage to multiplexing more than four optical signals from the STF's onto a single PTF.

5. The local oscillator signals should be available with sufficient signal-to-noise ratio out at the various CTL's in the array to facilitate frequency-division-multiplexing of the antenna signals with satisfactory performance. The local oscillator signals may even be sufficiently noise-free to preclude the use of phase-locked-loops, although their use has been assumed.

6. The use of LED's and p-i-n photodiodes appears to be feasible for the optical links from an SNR viewpoint. Continued reduction in fiber attenuation will tend to reinforce the feasibility of using these devices. Very low loss fibers are being developed and the attenuation could very probably be halved (~ 2.5 dB/km at $0.7\ \mu\text{m}$ and ~ 1 dB/km at $1.06\ \mu\text{m}$) in the near future. This would result in an increase in received optical power of almost 7 dB at $0.7\ \mu\text{m}$ and 3 dB at $1.06\ \mu\text{m}$. In addition, fibers with larger numerical apertures are appearing on the market. This will allow improved coupling efficiencies and, therefore, lower losses. Furthermore, the losses attributed to the various couplers have been conservative. With precision manufacture, losses could be similar to those attained in various laboratories. This could yield an additional 2-3 dB of optical power. With these various improvements, optical SNR will be increased substantially.

7. The noise performance of the system appears to be more than satisfactory to meet the sensitivity objectives. There is sufficient tolerance to accommodate additional noise that may result from underestimated device parameters or from changes in design. The noise performance has been determined on the basis of the optical link behaving as a thermal noise source. Since this is clearly a worst-case analysis, the noise performance of an actual system can be expected to be even better.

8. The r.m.s. excitation error performance of the system has been estimated to be 0.92° in phase and 2.18% in amplitude. In contrast to McLarnon's [3] coaxial system, this optical fiber system does not presume the necessity of day-to-day maintenance and calibration adjustments. Also, McLarnon's system was based on a

maximum of four FDM channels whereas this system is comprised of 48.

The transmission system described has been designed on the basis of general communication system principles and research results published by various authors. No experimental work was performed by this author. Therefore, before a practical system can be built, a great deal of work remains to be done:

1. Experimental work is necessary to verify the performance of the various r.f. and optical components and assemblies. For the transmission tolerances required, critical design and construction techniques will be called for. This will be especially true for the optical equipment, which requires the use of high magnification and micro-manipulators to position the various components accurately.

2. Maintaining the necessary accuracy among all similar units manufactured will be a major problem to overcome. Quality control will be of critical importance. The r.f. response curves of the various r.f. components must be carefully matched to ensure satisfactory signal performance end-to-end.

3. A practical means of ascertaining the noise temperature performance of optical links would be very useful. This would allow one to accurately predict the noise temperature performance in hybrid r.f./optical systems such as this one.

4. Equalization schemes should be examined and tested to compensate for the relatively large RC time constants encountered in photodetector receivers as a result of choosing as large a value of input resistance as possible to increase optical SNR. Previous work on optical receivers has been essentially restricted to digital signals. The case of analog signals should also be examined since this could be a critical factor in the specification of an analog system.

REFERENCES

- [1] D. Routledge, "Proposal for a Canadian decametric telescope", unpublished research report, Dept. of Elec. Eng., Univ. of Alberta, 1973.
- [2] F.S. Chute, C.G. Englefeld, P.J.R. Harding, C.R. James, and D. Routledge, "Site-testing for a proposed 12 MHz radio telescope in Alberta", J. Roy. Astron. Soc. Can., vol. 65, pp. 49-59, 1971.
- [3] B.D. McLarnon, "A feeder system for a large antenna array", unpublished Master's dissertation, Dept. of Elec. Eng., Univ. of Alberta, 1973.
- [4] Reference Data For Radio Engineers, 5th ed., chap. 7. New York: Howard W. Sams and Company, Inc., 1968.
- [5] D. Wynne, F.S. Chute, and C.R. James, "Sidelobe levels of a large radio telescope employing a combination of physical and resistive tapering", IEEE Trans. Antenna Propagat., vol. AP-23, pp. 278-283, Mar. 1975.
- [6] J.P. Wittke, "Optical fiber communications systems", unpublished research report, RCA Laboratories, 1974.
- [7] Antenna Systems Catalogue 30, Andrew Antenna Company, Ltd., 606 Beech Street, Whitby, Ontario, 1978.
- [8] S.E. Miller, E.A.J. Marcatili and Tingye Li, "Research toward optical fiber transmission systems", Proc. IEEE, vol. 61, pp. 1703-1751, Dec. 1973.
- [9] R.W. Dawson, "Effect of ambient temperature on infrared transmission through a glass fiber", Bell Syst. Tech. J., vol. 51, pp. 569-570, Feb. 1972.
- [10] L.G. Cohen and J.W. Fleming, "Effect of temperature on transmission in lightguides", Bell Syst. Tech. J., vol. 58, pp. 945-951, Apr. 1979.
- [11] R.L. Gallawa, "Optical waveguide technology for modern urban communications", IEEE Trans. Commun., vol. COM-23, pp. 131-142, Jan. 1975.
- [12] "CORGUIDETM optical fiber product bulletin and price list", Corning Glass Works, Corning, New York, 1977.
- [13] "Optical communications via glass fiber waveguides", short course presented by U.S. Department of Commerce, Office of Telecommunications and University of Colorado Electromagnetic Science Institute, Univ. of Colorado, Boulder, Colorado, 3-8 Aug., 1975.

- [14] W.B. Allan, Fiber Optics: Theory and Practice. New York: Plenum Press, 1973.
- [15] H. Matsumura, "The light acceptance angle of a graded index fiber", Opt. and Quant. Elect., no. 7, pp. 81-86, 1975.
- [16] D. Gloge and E.A.J. Marcatili, "Multimode theory of graded-core fibers", Bell Syst. Tech. J., vol. 52, pp. 1563-1578, Nov., 1973.
- [17] D. Gloge, "Weakly guiding fibers", Appl. Opt., vol. 10, pp. 2252-2258, Oct., 1971.
- [18] _____, "Dispersion in weakly guiding fibers", Appl. Opt., vol. 10, pp. 2442-2445, Nov. 1971.
- [19] C. Yeh, "Communication through light fibers", Advances in Communication Systems Theory and Applications, vol. 4. New York: Academic Press, 1975.
- [20] R.B. Dyott, "The optical fibre as a transmission line", Post Off. Elec. Eng. J., vol. 68, pp. 164-168, Apr. 1975.
- [21] F.P. Kapron and D.B. Keck, "Pulse transmission through a dielectric optical waveguide", Appl. Opt., vol. 10, pp. 1519-1523, July, 1971.
- [22] L. Smith and E. Snitzer, "Dispersion minimization in dielectric waveguides", Appl. Opt., vol. 12, pp. 1592-1599, July 1973.
- [23] D. Marcuse, "The impulse response of an optical fiber with parabolic index profile", Bell Syst. Tech. J., vol. 52, pp. 1169-1174, Sept. 1973.
- [24] D. Gloge, "optical waveguide transmission", Proc. IEEE, vol. 58, pp. 1513-1522, Oct. 1970.
- [25] D. Gloge, "Fiber delay equalization by carrier drift in the detector", Opto-Electron., vol. 5, p. 345, July 1973.
- [26] D. Marcuse, "Reduction of multimode pulse dispersion by intentional mode coupling", Bell Syst. Tech. J., vol. 53, pp. 1795-1815, Nov. 1974.
- [27] L. Jeunhomme and J.P. Pochelle, "Mode coupling in a multimode optical fiber with microbends", Appl. Opt., vol. 14, pp. 2400-2405, Oct. 1975.
- [28] D. Gloge, "Optical fibers for communication", Appl. Opt., vol. 13, pp. 249-254, Feb. 1974.
- [29] S.D. Personick, "Time dispersion in dielectric waveguides", Bell Syst. Tech. J., vol. 50, p. 843, Mar. 1971.

- [30] S.D. Personick, "Optimal trade-off of mode mixing optical filtering and index difference in digital fiber optic communication systems", Bell Syst. Tech. J., vol. 53, pp. 785-800, May-June 1974.
- [31] D. Gloge, "Impulse response of clad optical multimode fibers", Bell Syst. Tech. J., vol. 52, pp. 801-815, July-Aug. 1973.
- [32] R. Steinberg and P. Diamant, "Reduction of pulse dispersion in imperfect multimode fibers", Appl. Opt., vol. 15, pp. 869-870, April 1976.
- [33] D.B. Keck, "Spatial and temporal power transfer measurements on a low-loss optical waveguide", Appl. Opt., vol. 13, pp. 1882-1888, Aug. 1974.
- [34] D. Marcuse and H.M. Presby, "Mode coupling in an optical fiber with core distortions", Bell Syst. Tech. J., vol. 54, pp. 3-15, Jan. 1975.
- [35] A.H. Cherin, L.G. Cohen, W.S. Holden, C.A. Burrus, and P. Kaiser, "Transmission characteristics of three Corning multimode optical fibers", Appl. Opt., vol. 13, pp. 2359-2364, Oct. 1974.
- [36] R.W. Dawson, "Pulse widening in a multimode optical fiber excited by a pulsed GaAs LED", Appl. Opt., vol. 13, pp. 264-265, Feb. 1974.
- [37] D. Gloge, E.L. Chinnock, and T.P. Lee, "GaAs twin-laser setup to measure mode and material dispersion in optical fibers", Appl. Opt., vol. 13, pp. 261-263, Feb. 1974.
- [38] W.B. Bielowski, "Low-loss optical waveguides", Electron. Eng., pp. 59-66, May 1974.
- [39] C.P. Sandbank, "Fiber optic communications: a survey", Elect. Commun., vol. 50, pp. 20-27, 1975.
- [40] D.B. Keck, R.D. Maurer, and P.C. Schultz, "On the ultimate lower limit of attenuation in glass optical waveguides", Appl. Phys. Lett., vol. 22, pp. 307-309, 1 Apr. 1973.
- [41] K.J. Beales, J.E. Midwinter, G.R. Newns, C.R. Day, "Materials and fibre for optical transmission systems", Post Off. Elect. Eng. J., vol. 67, pp. 80-86, July 1974.
- [42] M.M. Ramsay, G.A. Hockham, and K.C. Kao, "Propagation in optical fiber waveguide", Elect. Commun., vol. 50, pp. 162-169, 1975.
- [43] D. Marcuse, "Rayleigh scattering and the impulse response of optical fibers", Bell Syst. Tech. J., vol. 53, pp. 705-715, Apr. 1974.

- [44] J.R. Meyer-Arendt, Introduction to Classical and Modern Optics. Englewood Cliffs, N.J., Prentice-Hall 1972.
- [45] A.H. Cherin and E.J. Murphy, "An analysis of the effect of lossy coatings on the transmission energy in a multimode optical fiber", Bell Syst. Tech. J., vol. 54, pp. 1531-1546, Nov. 1975.
- [46] _____, "Quasi-ray analysis of crosstalk between multimode optical fibers", Bell Syst. Tech. J., vol. 54, pp. 17-45, Jan. 1975.
- [47] M. Horiguchi and H. Osanai, "Spectral losses of low-OH-content optical fibers", Electron. Lett., vol. 12, p. 310, 1976.
- [48] W.G. French, J.B. MacChesney, P.B. O'Connor and G.W. Tasker, "Optical waveguides with very low losses", Bell Syst. Tech. J., vol. 53, pp. 951-954, May-June, 1974.
- [49] Bell Telephone Laboratories, Inc., Transmission Systems for Communications, revised 4th ed. Western Electric Co., Winston-Salem, N.C., 1971.
- [50] B.A. Lengyel, Introduction to Laser Physics. New York: Wiley, 1966.
- [51] C.H. Gooch, Injection Electroluminescent Devices. New York: Wiley 1973.
- [52] L.G. Cohen, "Measured attenuation and depolarization of light transmitted along glass fibers", Bell Syst. Tech. J., vol. 50, pp. 23-42, Jan. 1971.
- [53] A. Papp and H. Harms, "Polarization optics of index-gradient optical waveguide fibers", Appl. Opt., vol. 14, pp. 2406-2411, Oct. 1975.
- [54] E.U. Condon and H. Odishaw (eds.), Handbook of Physics. New York: McGraw-Hill, 1967.
- [55] F.W. Dabby, "Permanent multiple splices of fused-silica fibers", Bell Syst. Tech. J., vol. 54, pp. 451-455, Feb. 1975.
- [56] F.L. Thiel, "Utilizing optical fibers in communications systems", IEEE Int. Conf. Comm., pp. 32.1-32.4, 1975.
- [57] T.G. Giallorenzi, "Optical communication research and technology: fiber optics", Proc. IEEE, vol. 66, pp. 744-780, July 1978.
- [58] M.B. Panish, "Heterostructure injection lasers", IEEE Trans. Microwave Theory Tech., vol. MTT-23, pp. 20-30, Jan. 1975.
- [59] F.M. Mims, Light-Beam Communications. New York: Howard W. Sams and Company, Inc., 1975.

- [60] H. Kressel, H.F. Lockwood, I. Ladany, and M. Ettenberg, "Hetero-junction laser diodes for room temperature operation", Opt. Engin., vol. 13, pp. 416-422, Sept./Oct. 1974.
- [61] H. Kressel, I. Ladany, M. Ettenberg and H. Lockwood, "Light sources", Phys. Today, pp. 38-47, May 1976.
- [62] T. Tsukada, "GaAs-Ga_{1-x}Al_xAs buried-heterostructure injection lasers", J. Appl. Phys., vol. 45, pp. 4899-4905, Nov. 1974.
- [63] J.T. O'Brien, "Laser diodes provide high power for high-speed communications systems", Electronics, vol. 49, pp. 94-96, 5 Aug. 1976.
- [64] M. Maeda, K. Nagano, M. Tanaka, and K. Chiba, "Buried-hetero-structure laser packaging for wideband optical transmission systems", IEEE Trans. Commun., vol. COM-26, pp. 1076-1081, July 1978.
- [65] T.L. Paoli and J.E. Ripper, "Direct modulation of semiconductor lasers", Proc. IEEE, vol. 58, pp. 1457-1465, Oct. 1970.
- [66] K. Nawata and K. Takano, "800 Mb/s optical-repeater experiment", Electron. Lett., vol. 12, pp. 178-179, 1 Apr. 1976.
- [67] A. van der Ziel, "Noise in solid-state devices and lasers", Proc. IEEE, vol. 58, pp. 1178-1206, Aug. 1970.
- [68] "Chip lasers ready for optical systems", Electronics, vol. 48, pp. 44-45, 6 Feb. 1975.
- [69] V.J. Mazurczyk, "Description and performance of the Chicago lightwave communications project", IEEE Int. Conf. Comm., pp. 6.3.1-6.3.5, 1978.
- [70] "Diodes challenge light-link lasers", Electronics, vol. 46, p. 27, Sept. 1973.
- [71] C.A. Burrus and E.A. Ulmer, Jr., "Efficient small-area GaAs-Ga_{1-x}Al_xAs heterostructure electroluminescent diodes coupled to optical fibers", Proc. IEEE, vol. 59, pp. 1263-1264, Aug. 1971.
- [72] H. Kressel and M. Ettenberg, "A new edge-emitting (AlGa)As heterojunction LED for fiber-optic communications", Proc. IEEE, vol. 63, pp. 1360-1361, Sept. 1975.
- [73] C.A. Burrus, "Radiance of small-area high-current density electroluminescent diodes", Proc. IEEE, vol. 60, pp. 231-232, Feb. 1972.
- [74] J.P. Wittke, M. Ettenberg, and H. Kressel, "High-radiance LED for single-fiber optical links", RCA Review, vol. 37, pp. 159-183, June 1976.

- [75] "How to make light of LED work", Electronics, vol. 48, p. 116, 10 July 1975.
- [76] A.W. Mabbitt and C.D. Mosby, "High-speed high-power 1.06 μ m gallium-indium-arsenide light-emitting diodes", Electron. Lett., vol. 11, pp. 157-158, 17 Apr. 1975.
- [77] M.K. Barnoski, "Data distribution using fiber optics", Appl. Opt., vol. 14, pp. 2571-2577, Mar. 1975.
- [78] T.P. Lee, "Effect of junction capacitance on the rise time of LED's and on the turn-on delay of injection lasers", Bell Syst. Tech. J., vol. 54, pp. 55-68, Jan. 1975.
- [79] W.S. Holden, W.M. Hubbard, and S.D. Personick, "Chromatic delay in light emitting diodes", Appl. Opt., vol. 13, pp. 1050-1052, May 1974.
- [80] C.A. Burrus and B.I. Miller, "Small-area double heterostructure aluminum-gallium arsenide electroluminescent diode sources for optical-fiber transmission lines", Opt. Commun., vol. 4, pp. 307-309, Dec. 1971.
- [81] R.C. Goodfellow, A.W. Mabbitt, "Wide-bandwidth high-radiance gallium arsenide light-emitting diodes for fibre-optic communication", Electron. Lett., vol. 12, pp. 50-51, 22 Jan. 1976.
- [82] C.A. Burrus, T.P. Lee, and W.S. Holden, "Direct-modulation efficiency of LED's for optical fiber transmission applications", Proc. IEEE, vol. 63, pp. 329-331, Feb. 1975.
- [83] R.W. Dawson, "Shunt diode extends linear range of LED", Electronics, vol. 50, p. 119, 10 Nov. 1977.
- [84] T.P. Lee and C.A. Burrus, "Noise in the detected output of small area light emitting diodes", IEEE J. of Quant. Elect., vol. QE-8, p. 370, 1972.
- [85] G. Gibbons, "Progress in LED's as signal sources", Optical Fiber Transmission II Technical Digest, sponsored by Laser and Electro-Optics Technical Group, Optical Society of America, Williamsburg, Va., pp. WB1-1 to WB1-6, 22-24 Feb. 1977.
- [86] "Laser prices expected to drop below \$20 in next 10 years", Telephony, p. 24, July 1978.
- [87] H. Melchior, M.B. Fisher, and F.R. Arams, "Photodetectors for optical communication systems", Proc. IEEE, vol. 58, pp. 1466-1486, Oct. 1970.
- [88] Electro-Optics Handbook. RCA Corporation, Harrison, N.J., 1974.

- [89] "Avalanche photodiode model 50 EHS application notes", Space Technology Products, General Electric Company, 1972.
- [90] W.K. Pratt, Laser Communication Systems. New York: Wiley, 1969.
- [91] M. Ross, Laser Applications, vol. 1. New York: Academic, 1971.
- [92] W.M. Hubbard, "Utilization of optical-frequency carriers for low- and moderate-bandwidth channels", Bell Syst. Tech. J., vol. 52, May-June 1973.
- [93] S.D. Personick, "Receiver design for digital fiber-optic communication systems, I & II", Bell Syst. Tech. J., vol. 52, pp. 843-886, July-Aug. 1973.
- [94] J.E. Goell, "Input amplifiers for optical PCM receivers", Bell Syst. Tech. J., vol. 53, pp. 1771-1793, Nov. 1974.
- [95] R.W. Goranson and J.D. Skipper, "Signal-to-noise ratio in optical photodiode receivers", Proc. IEEE, vol. 62, pp. 1404-1406, Oct. 1974.
- [96] O.I. Szentesi and A.J. Szanto, "Fiber optics video transmission", SPIE/SPSE Tech. Symp. East, Reston, Virginia, 22-23 Mar. 1976.
- [97] D. Marcuse, "Excitation of parabolic-index fibers with incoherent sources", Bell Syst. Tech. J., vol. 54, pp. 1507-1529, Nov. 1975.
- [98] K.H. Yang and J.D. Kingsley, "Calculation of coupling losses between light emitting diodes and low-loss optical fibers", Appl. Opt., vol. 14, pp. 288-293, Feb. 1975.
- [99] W.W. Benson, D.A. Pinnow, and T.C. Rich, "Coupling efficiency between GaAlAs laser and low-loss optical fibers", Appl. Opt., vol. 14, pp. 2815-2816, Dec. 1975.
- [100] H. Kogelnik, "An introduction to integrated optics", IEEE Trans. Microwave Theory Tech., vol. MTT-23, pp. 2-16, Jan. 1975.
- [101] P.K. Tien, "Light waves in thin films and integrated optics", Appl. Opt., vol. 10, pp. 2395-2413, Nov. 1971.
- [102] _____ and R. Ulrich, "Theory of prism-film coupler and thin-film light guides", J. Opt. Soc. Am., vol. 60, pp. 1325-1337, Oct. 1970.
- [103] R. Ulrich, "Theory of the prism-film coupler by plane-wave analysis", J. Opt. Soc. Am., vol. 60, pp. 1337-1350, Oct. 1970.
- [104] P.I. Tien, R. Ulrich, and R.J. Martin, "Modes of propagating light waves in thin deposited semiconductor films", Appl. Phys. Lett., vol. 14, pp. 291-294, 1 May, 1969.
- [105] E.M. Conwell, "Integrated optics", Physics Today, pp. 48-59, May, 1976.

- [106] N.S. Kapany and J.J. Burke, Optical Waveguides. New York and London: Academic Press, 1972.
- [107] A.W. Snyder and J.D. Love, "Goos-Hänchen shift", Appl. Opt., vol. 15, pp. 236-238, Jan. 1976.
- [108] H.K.V. Lotsch, "Reflection and refraction of a beam of light at a plane interface", J. Opt. Soc. Am., vol. 58, pp. 551-561, Apr. 1968.
- [109] P.K. Tien, private communication.
- [110] R. Ulrich, "Optimum excitation of optical surface waves", J. Opt. Soc. Am., vol. 61, pp. 1467-1477, Nov. 1971.
- [111] A.A. Zlenko and V.A. Sychugov, "Light-injection prism with a parabolic gap profile", Sov. J. Quant. Electron., vol. 3, pp. 339-340, Jan.-Feb. 1974.
- [112] G.B. Brandt, "Birefringent coupler for integrated optics", Appl. Opt., vol. 13, pp. 1359-1362, June 1974.
- [113] L.P. Boivin, "Thin-film laser-to-fiber coupler", Appl. Opt., vol. 13, pp. 391-395, Feb. 1974.
- [114] P.K. Tien and R.J. Martin, "Experiments on light waves in a thin tapered film and a new light-wave coupler", Appl. Phys. Lett., vol. 18, pp. 398-401, 1 May 1971.
- [115] P.K. Tien, G. Smolinsky and R.J. Martin, "Radiation fields of a tapered film and a novel film-to-fiber coupler", IEEE Trans. Microwave Theory Tech., vol. MTT-23, pp. 79-85, Jan. 1975.
- [116] T. Funayama, M. Fujimori, M. Nakamura, and Y. Nishimura et al, "Light-mode phenomena at glass thin-film light-guide tapered edges", Elect. Comm. Jap., vol. 56-C, pp. 90-98, 1973.
- [117] J.F. Dalgleish, "Well-designed splices, connectors must align fibers exactly", Electronics, vol. 49, pp. 96-98, 5 Aug. 1976.
- [118] T.C. Chu and A.R. McCormick, "Measurements of loss due to offset, end separation and angular misalignment in graded index fibers excited by an incoherent source", Bell Syst. Tech. J., vol. 57, pp. 595-602, Mar. 1978.
- [119] "Smooth ends on glass fibers are a snap", Electronics, vol. 47, p. 128, 3 Oct. 1974.
- [120] J.F. Dalgleish, H.H. Lukas, and J.D. Lee, "Splicing of optical fibres", Proc. of First Europ. Conf. on Opt. Fibre Comm., pp. 87-89, 1975, Electronics Division of the IEE. Printed by The Whitefriars Press, Ltd., London and Tonbridge.

- [121] H. Murata, S. Inao, Y. Matsuda, and I. Takahashi, "Splicing of optical fiber cable on site", Proc. of First Europ. Conf. on Opt. Fibre Comm., pp. 93-95, 1975, Electronics Division of the IEE. Printed by The Whitefriars Press, Ltd., London and Tonbridge.
- [122] C.M. Miller, "Loose tube splices for optical fibers", Proc. of First Europ. Conf. on Opt. Fibre Comm., pp. 90-92, 1975, Electronics Division of the IEE. Printed by The Whitefriars Press, Ltd., London and Tonbridge.
- [123] R.D. Standley, "Fiber ribbon optical transmission lines", Bell Syst. Tech. J., vol. 53, pp. 1183-1185, July-Aug. 1974.
- [124] D.L. Bisbee and P.W. Smith, "All-glass optical-fiber tapes", Bell Syst. Tech. J., vol. 54, pp. 479-484, Mar. 1975.
- [125] E.L. Chinnock, D. Gloge, P.W. Smith, and D.L. Bisbee, "Preparation of optical-fiber ends for low-loss tape splices", Bell Syst. Tech. J., vol. 54, pp. 471-477, Mar. 1975.
- [126] Y. Kohanzadeh, "Hot splices of optical waveguide fibers", Appl. Opt., vol. 15, pp. 793-795, Mar. 1976.
- [127] H. Fujita, Y. Suzaki, and A. Tachibana, "Optical fiber splicing technique with a CO₂ laser", Appl. Opt., vol. 15, pp. 320-321, Feb. 1976.
- [128] F.L. Thiel, R.E. Love, and R.L. Smith, "In-line connectors for multimode optical waveguide bundles", Appl. Opt., vol. 13, pp. 240-242, Feb. 1974.
- [129] B.L. Board, J.F. Dalgleish, and J.H. Loughheed, "Cable installation and field testing for a fiber optic exploratory trial", IEEE Int. Conf. Comm., pp. 14.3.1-14.3.6, 1978.
- [130] "Fiber-optic field attracting new cable, connectors", Electronics, vol. 48, pp. 33-34, 15 May 1975.
- [131] "Fiber-optic cable getting connector for use in field", Electronics, vol. 48, pp. 29-30, 21 Aug. 1975.
- [132] B. LeBoss, "Fiber-optic connectors match singles", Electronics, vol. 51, p. 161, 8 June 1978.
- [133] F.D. King, "Optimized components for a trial DS-2 inter-office trunk fiber optic system", IEEE Int. Conf. Comm., pp. 14.1.1-14.1.4, 1978.
- [134] H. Taub and D.L. Schilling, Principles of Communication Systems. New York: McGraw-Hill, 1971.
- [135] J.M. Wozencraft and I.M. Jacobs, Principles of Communication Engineering. New York: Wiley, 1965.

- [136] E.L. Gruenberg, ed., Handbook of Telemetry and Remote Control. New York: McGraw-Hill, 1967.
- [137] L.E. Foster, Telemetry Systems. New York: Wiley, 1965.
- [138] S.C. Plotkin, "FM bandwidth as a function of distortion and modulation index", IEEE Trans. Commun. Tech., vol. COM-16, pp. 467-470, June 1967.
- [139] A.I. Zverev, Handbook of Filter Synthesis. New York: Wiley, 1967.
- [140] T. Miki and H. Ishio, "Viabilities of the wavelength-division-multiplexing transmission system over an optical fiber cable", IEEE Trans. Commun., vol. COM-26, pp. 1082-1087, July 1978.
- [141] A.F. Milton and A.B. Lee, "Optical access couplers and a comparison of multiterminal fiber optic communication systems", Appl. Opt., vol. 15, p. 244, 1976.
- [142] J. Guttman, H.J. Heyke and O. Krumpholz, "Dispersion measurements in new "Selfoc" fibres", Opt. and Quant. Elect., no. 7, pp. 305-309, 1975.
- [143] K. Koizumi, Y. Ikeda, I. Kitano, M. Furukawa, and T. Sumimoto, "New light-focusing fibers made by a continuous process", Appl. Opt., vol. 13, pp. 255-259, Feb. 1974.
- [144] C.A. Burrus, E.L. Chinnock, D. Gloge, W.S. Holden, Tingye Li, R.D. Standley and D.B. Keck, "Pulse dispersion and refractive-index profiles of some low-loss multimode optical fibers", Proc. IEEE, vol. 61, pp. 1498-1499, Oct. 1973.
- [145] E.L. Chinnock, L.G. Cohen, W.S. Holden, R.D. Standley and D.B. Keck, "The length dependence of pulse spreading in the CGW-Bell-10 optical fiber", Proc. IEEE, vol. 61, pp. 1499-1500, Oct. 1973.
- [146] L.G. Cohen, "Shuttle pulse measurements of pulse spreading in an optical fiber", Appl. Opt., vol. 14, pp. 1351-1356, June 1975.
- [147] L.G. Cohen and S.D. Personick, "Length dependence of pulse dispersion in a long multimode optical fiber", Appl. Opt., vol. 14, pp. 1357-1360, June 1975.
- [148] L.G. Cohen and H.M. Presby, "Shuttle pulse measurements of pulse spreading in a low-loss graded-index fiber", Appl. Opt., vol. 14, pp. 1361-1363, June 1975.
- [149] M. DiDomenico, Jr., "A review of fiber optical transmission systems", Opt. Engin., vol. 13, pp. 423-428, Sept/Oct. 1974.
- [150] W.B. Bielawski, private communication.
- [151] D. Carey, "The light fantastic", Electr. and Commun., pp. 23-26, Jan./Feb. 1977.

- [152] T. Ozeki and E.H. Hara, "Measurement of nonlinear distortion in light-emitting diodes", Electron. Lett., vol. 12, pp. 78-80, 5 Feb. 1976.
- [153] "Fiber-optic system carries voice, TV and data signals", Electronics, vol. 48, pp. 29-30, 16 Oct. 1975.
- [154] A. Szanto and J.C.W. Taylor, "An optical fiber system for wideband transmission", IEEE Int. Conf. Comm., ch. 17E, 1974.
- [155] J. Straus and O.I. Szentesi, "Linearity of high power, high radiance $\text{Ga}_{1-x}\text{Al}_x\text{As:Ge}$ double heterostructure LED's", IEEE Int. Electron Devices Mtg., Washington, D.C., pp. 484-486, Dec. 1975.
- [156] L.K. Anderson, M. DiDomenico, Jr., and M.B. Fisher, "High-speed photodetectors", Advances in Microwaves, vol. 5. New York: Academic, 1970.
- [157] T. Ozeki and E.H. Hara, "Measurement of nonlinear distortion in photodiodes", Electron. Lett., vol. 12, 5 Feb. 1976.
- [158] D.C. Johnson and B.S. Kawasaki, "The coupling of light from light-emitting diodes into optical fibers: the analysis of close-coupling geometry", Communications Research Centre report no. 1250, Department of Communications, Canada, Jan. 1974.
- [159] J.H. Harris, R.K. Winn, and D.G. Dalgoutte, "Theory and design of periodic couplers", Appl. Opt., vol. 11, pp. 2234-2241, Oct. 1972.
- [160] D.G. Dalgoutte and C.D. Wilkinson, "Thin grating couplers for integrated optics: an experimental and theoretical study", Appl. Opt., vol. 14, pp. 2983-2998, Dec. 1975.
- [161] M.L. Dakss, L. Kuhn, P.F. Heidrich, and B.A. Scott, "Grating coupler for efficient excitation of optical guided waves in thin films", Appl. Phys. Lett., vol. 16, pp. 523-525, 15 June 1970.
- [162] D.G. Dalgoutte, "A high-efficiency thin grating coupler for integrated optics", Opt. Commun., vol. 8, pp. 124-127, June 1973.
- [163] D.B. Ostrowsky and A. Jacques, "Formation of optical waveguides in photoresist films", Appl. Phys. Lett., vol. 18, pp. 556-557, 15 June 1971.
- [164] H. Kogelnik and T.P. Sosnowski, "Holographic thin-film couplers", Bell Syst. Tech. J., vol. 49, pp. 1602-1608, Sept. 1970.

APPENDIX A

MULTIMODE DISPERSION AS A FUNCTION OF REFRACTIVE INDEX PROFILE

Miller et al [8] considered the family of index distributions

$$n(r) = n_1 \left[1 - \Delta \left(\frac{r}{a} \right)^\alpha \right] \quad (\text{A.1})$$

with $\alpha = 2$ corresponding to the parabolic profile and $\alpha = \infty$ corresponding to a step-index profile. The r.m.s. width of the impulse response was determined for a variety of index distributions and the results are summarized below. Although equations (A.2) through (A.6) were derived for a square fiber, the results should be applicable in general to round fibers as well.

$$\text{Step-index } (\alpha = \infty) \quad \tau = 0.289 \frac{n_1 \Delta}{c} \quad (\text{A.2})$$

$$\text{Eighth-order } (\alpha = 8) \quad \tau = 0.165 \frac{n_1 \Delta}{c} \quad (\text{A.3})$$

$$\text{Fourth-order } (\alpha = 4) \quad \tau = 0.0873 \frac{n_1 \Delta}{c} \quad (\text{A.4})$$

$$\text{Parabolic } (\alpha = 2) \quad \tau = 0.15 \frac{n_1 \Delta^2}{c} \quad (\text{A.5})$$

$$\text{"Practical" parabolic (5\% error)} \quad \tau = 0.00591 \frac{n_1 \Delta}{c} \quad (\text{A.6})$$

$$\text{"Ideal" near-parabolic (round fiber)} \quad \tau = 0.037 \frac{n_1 \Delta^2}{c} \quad (\text{A.7})$$

The advantage of using a parabolic (or nearly parabolic) index over a step-index is obvious from an examination of eq. (A.2) and (A.5). Since Δ is of the order of 10^{-2} there is an improvement of some two orders of magnitude in the delay distortion with a pure parabolic index distribution over a step-index distribution. Considering a fiber with $n_1 = 1.5$ and $\Delta = 0.01$, eqs. (A.2), (A.3) and (A.4) predict a pulse spreading of 14.45 nsec/km for a step-index profile, 0.075 nsec/km for a pure parabolic profile and 0.3 nsec/km for a "practical" parabolic distribution.

Gloge and Marcatili [16] analyzed a class of profiles of the form

$$n(r) = \begin{cases} n_1 [1 - 2\Delta(r/a)^\alpha]^{1/2} & , r < a \\ n_1 [1 - 2\Delta]^{1/2} & , r > a \end{cases} \quad \begin{matrix} \text{(A.8a)} \\ \text{(A.8b)} \end{matrix}$$

The core profile has a "cone" shape for $\alpha = 1$, becomes nearly parabolic for $\alpha = 2$ and converges to a step profile for $\alpha = \infty$. The minimum output pulsewidth was obtained for a nearly parabolic distribution with $\alpha_{\text{opt}} = 2 - 2\Delta$. Specifically, the pulsewidth of the impulse response is

$$\tau = \left(\frac{L}{8c} \right) n_1 \Delta^2 \quad \text{(A.9)}$$

which is seen to be an improvement over eq. (2.29) by a factor of 4, or, using the same fiber parameters of $n_1 = 1.5$ and $\Delta = 0.01$,

$$\tau = 62.5 \text{ psec/km}$$

Since a physical fiber will present a certain error in the profile distribution, this must be accounted for. Assuming a value of

$$\alpha = \alpha_{\text{opt}} + d\alpha$$

it is found that the impulse response pulsewidth

$$\tau = \frac{\text{Ln } 1}{8c} \left(\Delta + \frac{2.718}{n_1 \Delta} |dn_{\text{max}}| \right)^2 \quad (\text{A.10})$$

where

$$dn_{\text{max}} = d\alpha \frac{n_1 \Delta}{5.436} \quad (\text{A.11})$$

If we again consider a fiber with $n_1 = 1.5$, $\Delta = 0.01$ and an index deviation, $dn_{\text{max}} = 10^{-4}$, from the optimum ($d\alpha = 3.624 \times 10^{-2}$), the pulsewidth becomes

$$\begin{aligned} \tau &= \frac{1.5}{8 \times 3 \times 10^5} \left[0.01 + \frac{2.718}{1.5 \times 0.01} (.0001) \right]^2 \\ &= 494 \text{ psec/km} \end{aligned}$$

It is apparent from eq. (A.10) that the delay distortion is sensitive to variations in the index distribution. However, the sensitivity is found to be critical only near the ideal near-parabolic profile [8].

The fourfold advantage predicted by equation (A.9) over equation (2.29) then diminishes rapidly as α deviates from α_{opt} .

Pulse spread due to other values of α ($\alpha \neq 2$) can be determined from [142]

$$\tau = \frac{\text{Ln } 1}{c} \Delta \frac{\alpha - 2}{\alpha + 2} \quad (\text{A.12})$$

APPENDIX B

EXPERIMENTAL DISPERSION RESULTS

Step-Index Fibers

Experiments on step-index, multimode optical fibers to determine dispersion effects consistently yield results which are better than those predicted by eq. (2.25) for multimode dispersion.

Keck [33] measured dispersion in a multimode fiber with N.A. = 0.15 and core diameter of $75\mu\text{m}$. Attenuation of higher order modes resulted in a dispersion of 17.3 nsec/km instead of a calculated value of 25.5 nsec/km. This was almost entirely due to multimode dispersion since he determined a material dispersion of only 0.16 nsec/km using a GaAs laser source.

Marcuse and Presby [34] measured dispersion in a 1 km step-index fiber with an elliptical core $30 \times 50\mu\text{m}$, $n_1 - n_2 = 0.0135$, $\Delta = 0.0093$ (N.A. = 0.198). According to eq. (2.25) the pulse spread assuming uncoupled modes is

$$\tau = \frac{L}{c} n_1 \Delta = 45 \text{ nsec}$$

The actual observed pulse width was 10 nsec indicating an improvement of 4 over theory.

Measurements on three multimode fibers at Bell Telephone Laboratories [35] revealed pulse dispersion due to multimode effects of 8.1 nsec/km, 16.0 nsec/km and 8.6 nsec/km. A summary of the results follows.

Fiber no.	1	2	3
Length, L	1 km	363 m	290 m
Maximum Δn^b	0.006	0.0085	0.005
Numerical aperture	0.133	0.157	0.121
Input pulse width ^c	2.4 nsec	1.5 nsec	0.8 nsec
Output pulse width ^d	8.4 nsec	6.0 nsec	2.6 nsec
Deconvolved output pulse width ^d	8.1 nsec	5.8 nsec	2.5 nsec
Maximum mode delay expected in length measured ^e	20.0 nsec	10.3 nsec	4.9 nsec

^a All dispersion data taken at $0.9 \mu\text{m}$

^b Obtained from interference microgram data

^c Measured at 10 dB power points

^d Deconvolved output = $[(\text{Output width})^2 - (\text{Input width})^2]^{1/2}$

^e Max. expected delay = $\frac{nL\Delta}{c}$ (from eq. (2.25)) assuming abrupt core-cladding interface and flat profile.

The lower-than-expected dispersion was attributed to both a partially-graded index and mode-mixing.

R. Dawson [36] measured pulse spreading in a 1 km length of step-index, multimode fiber excited by a pulsed LED. Using an input pulse width of 3.6 nsec, the output pulse width was measured to be 6.0 nsec. Using the convolution of cascade Gaussian waveforms, the total material and multimode dispersion was determined to be

$$\tau = \left[\tau_o^2 - (\tau_i^2 + \tau_r^2) \right]^{1/2} \quad (\text{B.1})$$

$$= \left[6.0^2 - (3.6^2 + 1.6^2) \right]^{1/2}$$

$$= 4.5 \text{ nsec}$$

where τ_o is measured output pulsewidth
 τ_i is input pulsewidth
 τ_r is response time of the receiver
(all measured at half-power points)

Of this 4.5 nsec, 4.2 nsec was attributed to material dispersion and 1.6 nsec to multimode dispersion. The fiber used was made from fused silica, which at $0.9 \mu\text{m}$ has a refractive index of $n \approx 1.452$ (from Fig. 2.10). With a core-cladding index difference of 0.003, eq. (2.25) predicts a multimode dispersion of

$$\tau_M = \frac{1}{3 \times 10^5} \frac{(1.452)}{(1.449)} (0.003) = 10 \text{ nsec/km}$$

Gloge et al [37] used a twin-laser apparatus to measure multimode and material dispersion separately. Being almost monochromatic, laser pulses are distorted essentially by multimode dispersion only. By selecting the wavelength difference ($0.9 \mu\text{m} - 0.86 \mu\text{m}$) to be compatible with the half-power spectral width of a typical LED (40 nm), they measured 3.6 nsec material dispersion and 1.3 nsec multimode dispersion in a 1 km length of fiber with N.A. of 0.09. The theoretical value of multimode dispersion was determined to be 7 nsec/km indicating substantial mode coupling. The predicted value of material dispersion from eq. (2.27) is

$$\begin{aligned}
 \tau_D &= \frac{\lambda_o \delta \lambda}{c} \frac{d^2 n_1}{d \lambda^2} \\
 &= \frac{(0.9 \times 10^{-6})(40 \times 10^{-9})}{2 \times 10^5} (0.0002 \times 10^{14}) \\
 &= 2.4 \text{ nsec}
 \end{aligned}$$

The total spread of the impulse response would be approximately

$$= \sqrt{1.3^2 + 3.6^2} = 3.8 \text{ nsec}$$

Graded-Index Fibers

Graded-index fibers have also been tested for dispersion effects. Direct measurements on new SELFOC fibers [142] indicated linear pulse broadening of ~ 11 nsec/km up to at least 700 meters using a 600 psec laser pulse input. Since the refractive index distribution was intermediate between a parabolic profile and a step-index profile, pulse spreading was calculated from eqs. (2.25) and (2.29) to be

$$\begin{aligned}
 \tau &= \frac{\text{Ln } \Delta}{c} && \text{(for step-index profile)} \\
 &= \frac{1.538}{3 \times 10^5} (0.0132) \\
 &= 68 \text{ nsec/km}
 \end{aligned}$$

and

$$\tau = \frac{\text{Ln } \Delta^2}{c} \quad \text{(for parabolic profile)}$$

$$= \frac{1.538}{3 \times 10^5} \frac{(0.0132)^2}{2}$$

$$= 0.45 \text{ nsec/km}$$

Actual pulse spread was measured to be 8 nsec in the 700 m length or 11.4 nsec/km which lies between the two calculated values. Using eq. (A.12), the value of the profile shape factor α was determined to be 2.81 (parabolic corresponds to $\alpha = 2$, step-index corresponds to $\alpha = \infty$).

Another recent investigation on SELFOC fibers [143] revealed that a 0.5 nsec pulse at $1.06 \mu\text{m}$ broadened to 0.65 nsec after travelling through a 500 m length of fiber. This indicates a Gaussian pulse spreading of some 0.4 nsec or 0.8 nsec/km, which is very near the theoretical limit for a parabolic profile.

Dispersion-Limiting Effects

Evidence of the \sqrt{L} dependence of delay distortion due to mode mixing has been determined experimentally by a number of researchers. Multimode dispersion in three low-loss, multimode fibers made by Corning was measured [144] to be < 1.5 nsec for each of two fibers 1 km long, and 3.5 nsec for the third fiber, 226 m in length. The first two fibers had refractive index profiles that were essentially graded while the third fiber had a predominantly step-index profile. This would explain the relatively large dispersion of about 14 nsec/km (assuming no mode-mixing). One of the 1 km fibers was subsequently tested [145] at wavelengths of $0.6328 \mu\text{m}$, $0.9 \mu\text{m}$ and $1.06 \mu\text{m}$, and a \sqrt{L} dependence of dispersion was found beyond 600 m. It was apparent that

mode-mixing effects reduced the multimode dispersion in this fiber, although the index profile may have influenced the initial reduction.

L. G. Cohen et al [146,147,148] used a "shuttle-pulse" technique of measuring pulse spreading in fibers. Using relatively short fibers, an input light pulse was made to reflect a number of times up and down the length to simulate transmission through a longer fiber. Measurements were made on a 1280 m length of multimode, low-loss, step-index fiber and used to determine pulse dispersion up to a 6400 m extrapolated length. The initial pulse spread of 20 nsec/km was less than the calculated value of 27 nsec/km found using eq. (2.25), since the refractive-index profile had a graded shoulder. At about 840 m, the slope dropped to 1/2 of the initial value, indicating a \sqrt{L} dependence beyond the coupling length of 840 m.

Further measurements were made on a 148 m length of graded-index, multimode fiber and used to determine pulse dispersion up to an extrapolated length of 2516 m. Pulse widths increased at a rate of 5 nsec/km at the -10 dB point and 2 nsec/km at the -3 dB point. Mode mixing in this very low loss fiber (2.3 dB/km at $0.9\mu\text{m}$) was small enough to make the coupling length L_c longer than 2500 m.

APPENDIX C

EXPERIMENTAL ATTENUATION RESULTS

Tests were conducted on three multimode fibers manufactured by Corning [35] and the results are presented in Table C.1. The discrepancy in results between Corning and Bell Telephone Laboratories is due to differences in measuring techniques. These results are similar to those represented by curve (B) in Fig. 2.16 which represents a typical 4 dB/km fiber.

Most low-loss fibers to date have been made of fused silica. This is presently considered one of the most promising materials available for optical fibers [149]. Another material that is attractive for fiber construction is borosilicate glass. The advantage of these two glasses is that, besides their inherent low loss, they can be doped to control the index of refraction.

Bell Telephone Laboratories [39] have developed a fiber with a $\text{GeO}_2\text{-SiO}_2$ core and an SiO_2 cladding. This fiber has a core approximately $35\text{ }\mu\text{m}$ in diameter and a numerical aperture of 0.235. The loss was found to vary by approximately λ^{-4} , the expected Rayleigh scattering, to a minimum of less than 2 dB/km at $1.06\text{ }\mu\text{m}$. Hydroxyl ion absorption at 0.72 , 0.88 and $0.95\text{ }\mu\text{m}$ was low, resulting in a loss at $0.9\text{ }\mu\text{m}$ of less than 10 dB/km.

Curve (D) in Fig. 2.16 illustrates the loss spectrum of a fiber made at Bell Telephone Laboratories with pure fused-silica core

and a borosilicate cladding [48]. This fiber has a core diameter of $18\mu\text{m}$, a cladding thickness of $15\mu\text{m}$ and a numerical aperture of 0.17. Average losses at 0.86, 0.90 and $1.02\mu\text{m}$ are seen to be 1.9, 2.4 and 1.1 dB/km respectively.

A graded-index fiber was fabricated at Bell Telephone Laboratories by varying the concentration of B_2O_3 from zero at the centre to about 20% at the edge of a GeO_2 -doped core and using a borosilicate cladding [48]. This fiber has a $22\mu\text{m}$ core diameter, a $15\mu\text{m}$ cladding thickness and a numerical aperture of 0.17. The spectral attenuation is represented by curve (E) of Fig. 2.16. Minimum loss of 2.3 and 1.7 dB/km is seen to occur at 0.90 and $1.04\mu\text{m}$, respectively.

Table C.1

Spectral Attenuation of 3 Multimode Fibers

Fiber	N.A.	(μm)	Loss (dB/km)	
			CGW	BTL
1	0.121	0.62	12.0	14.1
		0.8	7.4	9.5
		0.9	7.9	10.0
		1.06	5.1	6.8
2	0.133	0.62	10.9	12.9
		0.8	6.0	7.8
		0.9	9.5	11.6
		1.06	4.3	5.8
3	0.157	0.62	12.0	14.1
		0.8	5.2	6.6
		0.9	4.8	7.5
		1.06	3.5	4.3

APPENDIX D

OPTICAL FIBER STATE-OF-THE-ART

Most fibers considered in Chapter 2 have basically been "laboratory-grade". Commercially available fibers tend to have higher attenuation losses. Corning's CORGUIDE cable, introduced commercially in May, 1975 at \$13.50/meter is comprised of 6 individually jacketed fibers with a maximum attenuation of 20 dB/km at $0.82\mu\text{m}$. The fibers are multimode with a step index of refraction and a numerical aperture of 0.16. This cable should be useful to about 18 MHz in a length of one kilometer.

International Telephone & Telegraph Corporation at Roanoke, Va. has a commercial cable comprising 6 step-index, multimode fibers with an attenuation of 8 dB/km [13]. Sumitomo Electric Industries Ltd. in Japan are marketing a cable comprised of 8 quads of 4 single-strand fibers. The fibers are multimode, graded-index with a loss of ~ 10 dB/km. The cable has an outer diameter of 2.2 cm and sells for \$33/m (as of Aug./75) with an aluminum and polyethylene sheath [13]. An identical cable with a nonmetallic sheath is also available. There is no information on the dispersion or bandwidth capability of either of these fibers.

Corning had indicated in 1975 [150] that they could supply graded-index fibers with an attenuation of either 5 or 10 dB/km maximum at 820 nm at continuous lengths up to 10 km and with a maximum dispersion of either 5 or 10 nsec/km (bandwidths of 100 MHz and 50 MHz), respectively. They further indicated that costs were anticipated to decrease by an

order of magnitude or more from the 1975 level of \$1.50 per meter in 100 km quantities. While a time limit was not stated for this cost reduction, it was implied that this would be in the 1981 - 1982 time frame.

Corning has recently announced the commercial availability of 4 new graded-index fibers [12]. Two of these fibers have maximum attenuation of 10 dB/km at 820 nm with a minimum bandwidth of 200 MHz in 1 km and numerical apertures of 0.24 and 0.21. Current pricing for these fibers is \$2.00 and \$0.90, respectively, for quantities less than 100 km and \$1.50 and \$0.90, respectively, for larger quantities. These prices are in U.S. dollars. Corning has also indicated [12] that they have made and supplied on an experimental basis fibers with attenuation as low as 2 dB/km at $1.06\mu\text{m}$, bandwidth as high as 1 GHz at 1 km and continuous lengths up to 10 km. No prices have been quoted for these fibers.

The lowest estimate of fiber costs to date [151] suggests that fiber quantities in the order of 500,000 km could result in costs as low as 5¢ per meter. This figure is again mentioned in a recent tutorial paper by Giallorenzi [55]. He has projected fiber costs to be about 5¢ to 8¢ per meter in production quantities of about 10^4 to 2×10^4 km per year.

APPENDIX E

CROSSTALK IN MULTIMODE FIBERS

Cherin and Murphy [46] considered a system of clad fibers in direct contact with each other. They assumed that crosstalk was due to frustrated total reflection only. (This mechanism is discussed in section 5.2) A number of studies were conducted to determine how far-end crosstalk (FEXT) varied as a function of cladding thickness, numerical aperture, length, wavelength and K (kappa). Far-end crosstalk (FEXT) is crosstalk whose energy travels in the same direction as the signal in the disturbing channel [49]. Kappa (K) is a parameter that is a measure of the width of the incident optical beam and also an indication of the power distribution among the various modes of the fiber. Kappa can be considered to be a term used to quantify the optical coupling, or "launching" conditions. As kappa decreases, the energy distributed in the lower order modes of a fiber increases.

The input angular power distribution of the fiber is assumed to be a Gaussian function of the form [46]

$$H = \exp [-(\theta/K\theta_c)^2] \quad (E.1)$$

where θ_c is the critical angle of the fiber. A plot of eq. (E.1) for various values of kappa is presented in Fig. E.1..

Figs. E.2 to E.6 represent the dependence of FEXT on cladding thickness, numerical aperture, length, kappa and wavelength, respectively for fibers with center-to-center separation L_s and core diameter $2a$. A fiber attenuation of 20 dB/km was used in the analysis. These graphs

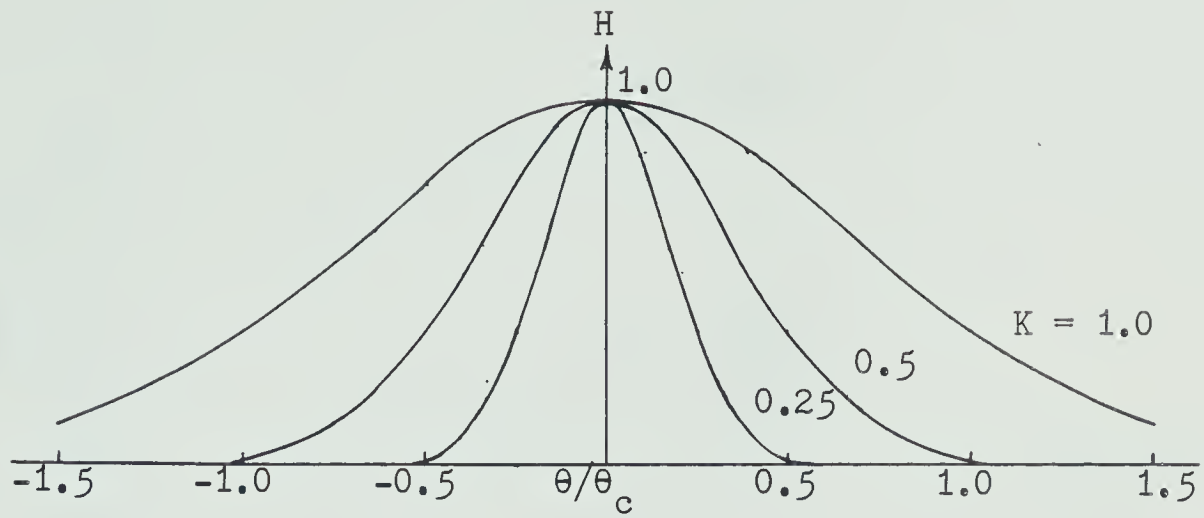


Fig. E.1 Input angular power distribution

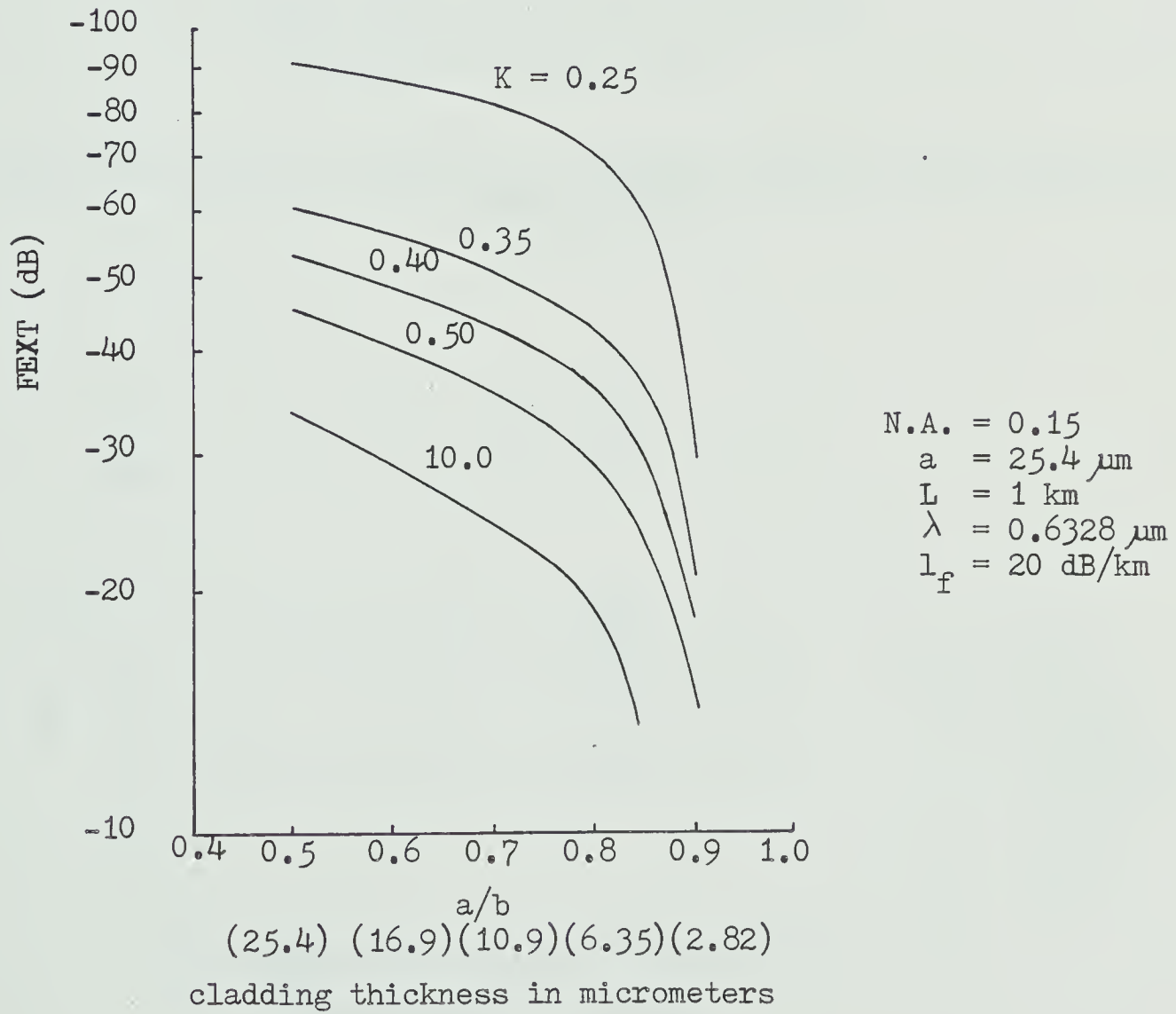


Fig. E.2 Far-end crosstalk vs. core/cladding ratio (After Cherin and Murphy [46]).

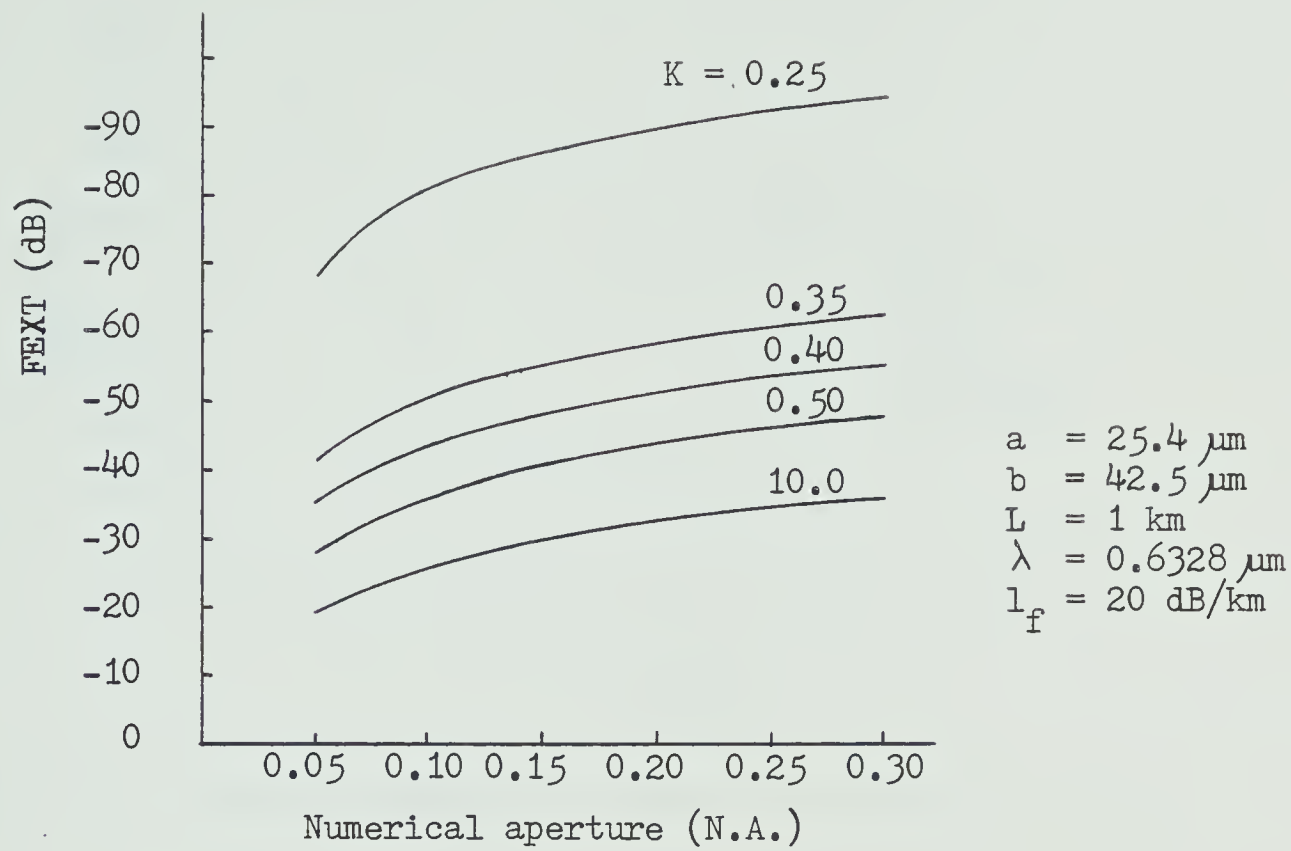


Fig. E.3 Far-end crosstalk vs. numerical aperture (After Cherin and Murphy [46]).

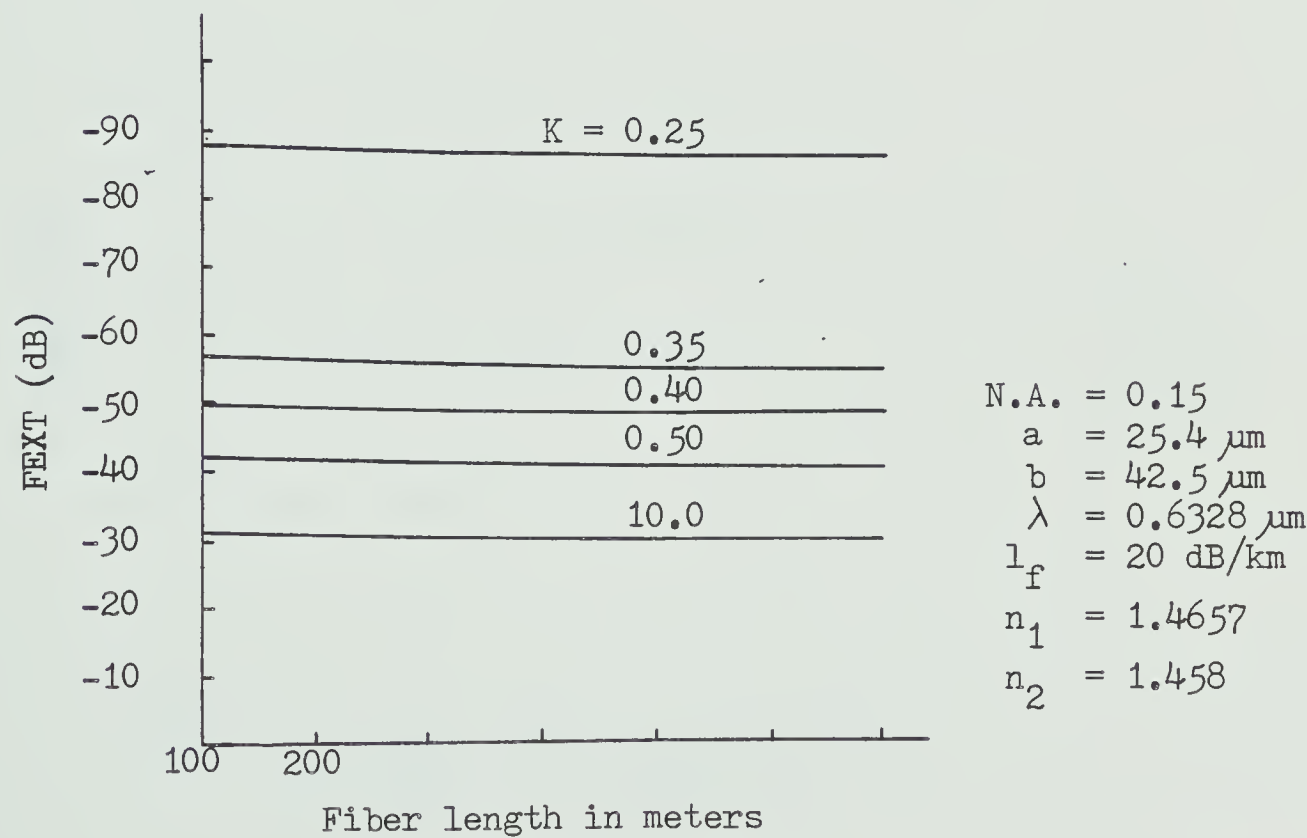


Fig. E.4 Far-end crosstalk vs. fiber length (After Cherin and Murphy [46]).

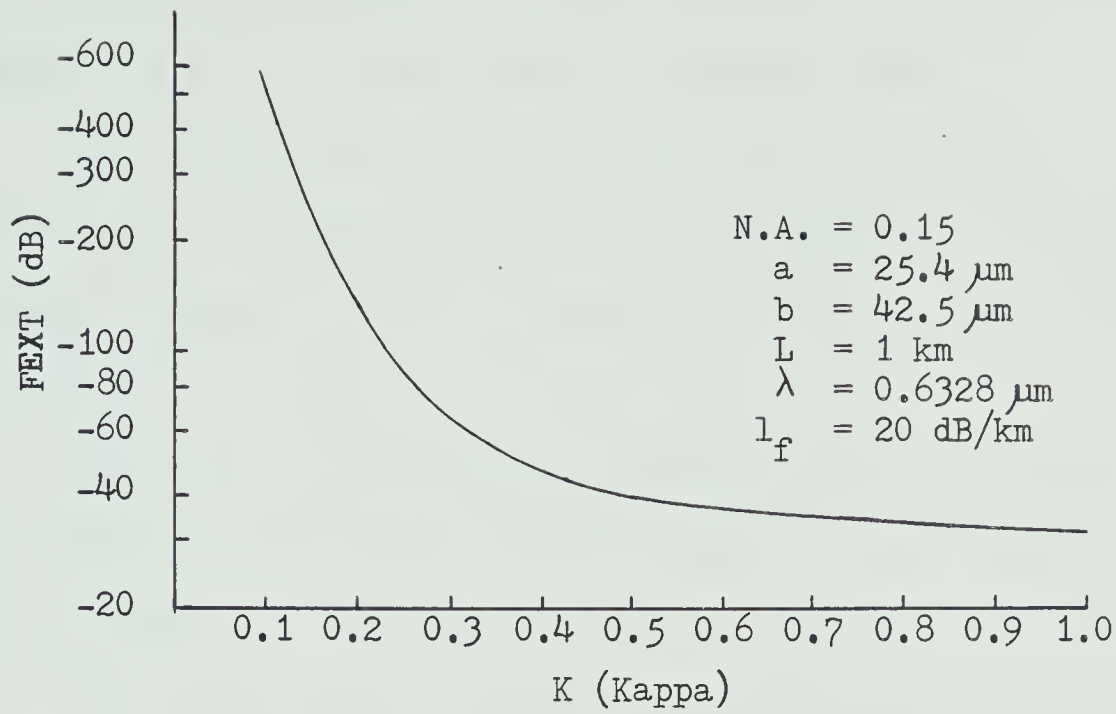


Fig. E.5 Far-end crosstalk vs. kappa (After Cherin and Murphy [46]).

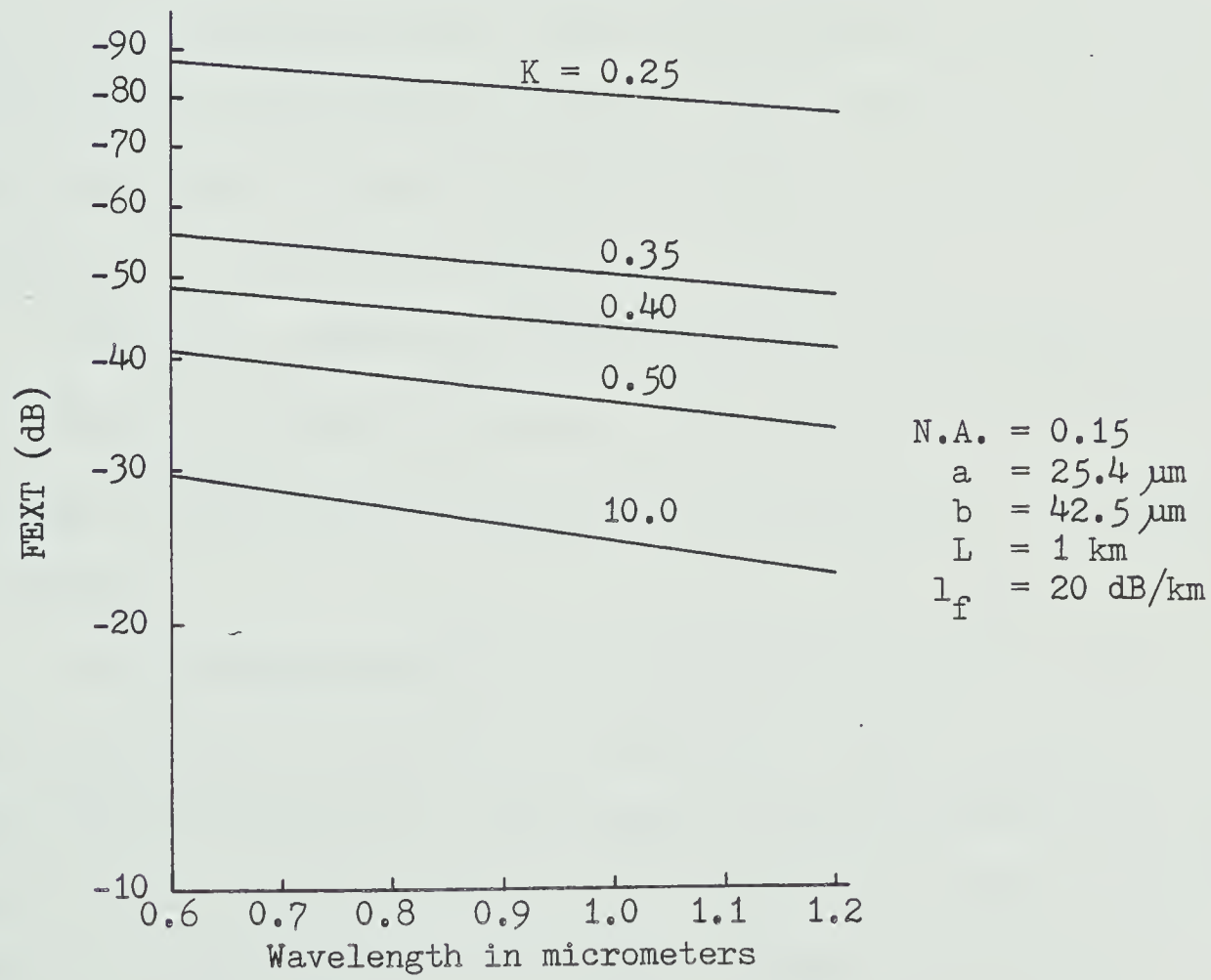


Fig. E.6 Far-end crosstalk vs. wavelength (After Cherin and Murphy [46]).

reveal a strong dependence of FEXT on κ . For FEXT isolation greater than 60 dB, κ should be less than about 0.35.

The importance of cladding thickness on crosstalk is apparent from Fig. E.2. Beyond about 12 μm in thickness, increasing the cladding thickness results in improved crosstalk isolation by approximately 0.8 dB/ μm .

Fig. E.3 indicates that crosstalk isolation is improved by about 6 dB by doubling the numerical aperture within the range from 0.10 to 0.30.

For fixed values of κ , Fig. E.4 reveals an increase in crosstalk of approximately 2 dB per decade of length.

The FEXT isolation is seen, in Fig. E.5 to increase exponentially with decreasing κ . While these results were determined for a fiber with a core diameter of 50.8 μm , they should be applicable to other fibers with the same N.A. and a/b ratio. This is because FEXT was found to be relatively independent of core size.

Fig. E.6 shows that crosstalk isolation decreases by about 7 dB when the wavelength is doubled. For systems where crosstalk is critical, it would appear advantageous to use as short a wavelength as possible.

The foregoing results are informative of crosstalk relationships but are probably of limited use in practice. Fibers enclosed in a cable will probably have a lossy jacket over the cladding which will tend to reduce crosstalk. This is the case with at least one type of commercial cable (Corning's CORGUIDE). Whether or not the sole mechanism for crosstalk is frustrated total reflection is another factor that would have to be determined by crosstalk tests.

APPENDIX F

LINEARITY MEASUREMENTS ON LED'S

Measurement of nonlinear distortion in LED's was conducted [152] using a Burrus-type surface-emitting diode. Fundamental frequencies employed were: $f_1 = 5.0013$ MHz, $f_2 = 6.0014$ MHz and $f_3 = 12.0117$ MHz and peak-to-peak modulation current was 50 mA. Second-order ($f_2 - f_1 = 1.001$ MHz) and third-order ($f_3 - (f_1 + f_2) = 1.0090$ MHz) distortion products were measured at various levels of D.C. bias as shown in Fig. F.1 (a) and at various modulation depths as shown in Fig. F.1 (b). These results indicate that second-order distortion was consistently about 40 dB down from the fundamental, while third-order distortion decreased with increasing bias current to about 75 dB below the fundamental at 95 mA. While nonlinear distortion of -40 dB is borderline for high-quality video transmission, it was determined [152] that, by excluding second-order products using an FDM scheme, the LED was suitable for high-quality, multichannel, video transmission systems.

Bell-Northern Research have developed a DH, aluminum-gallium-arsenide LED that emits 375 μ W at 150 mA drive current in the 0.8 - 0.9 μ m region [153]. Linearity is sufficiently good to meet the signal-to-noise ratios for analog transmission and can transmit studio-quality video over a link with an optical loss of up to 25 dB between transmitter and receiver.

Another analog system built at Bell-Northern Research [154] transmits multiplexed voice, video and data within a 15 MHz bandwidth.

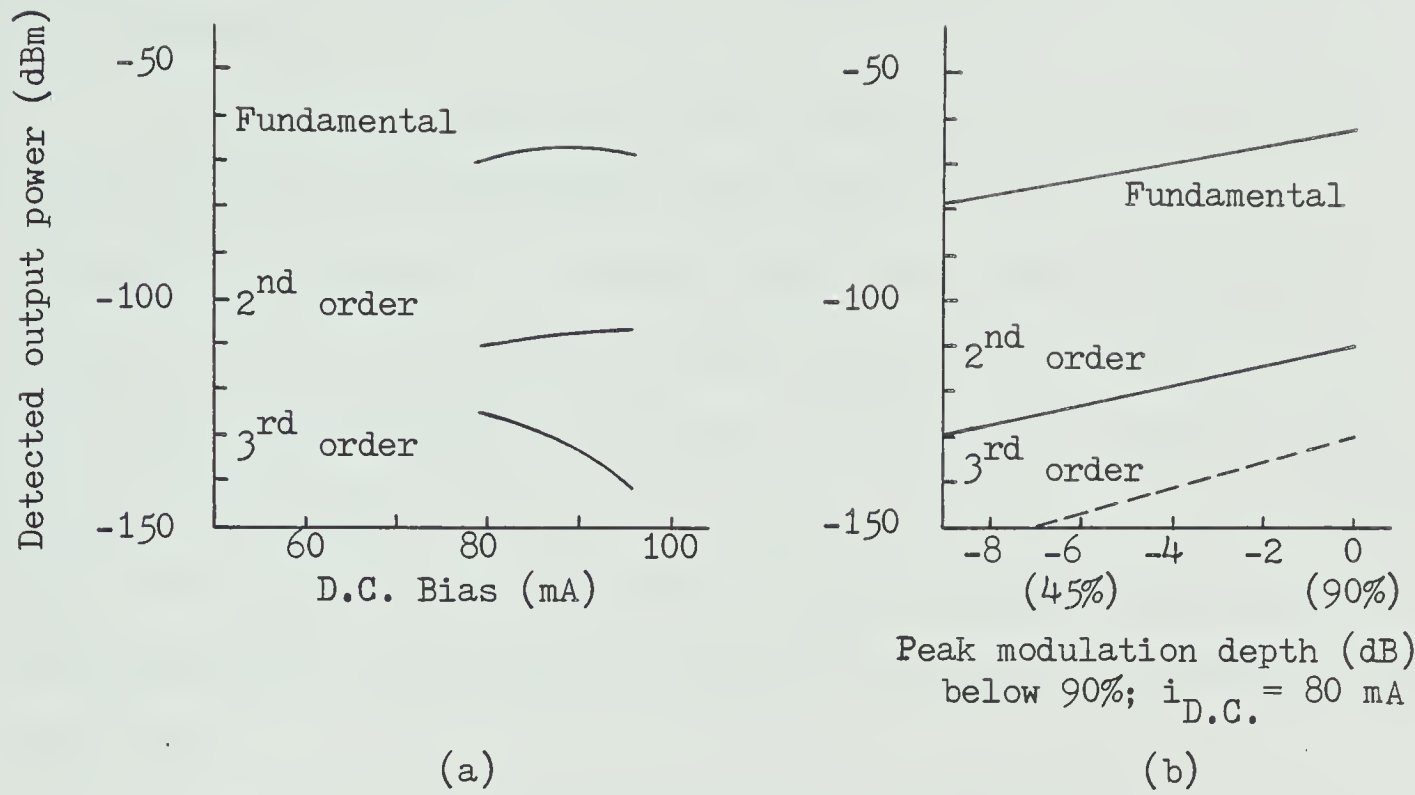


Fig. F.1 Variation of nonlinear distortion (a) with direct bias current, and (b) with modulation depth (After Ozeki and Hara [152]).

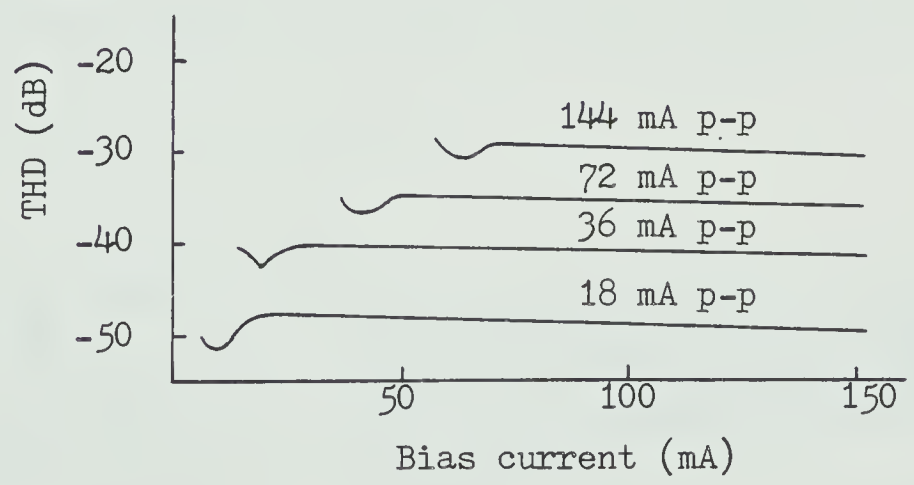


Fig. F.2 Total harmonic distortion in a typical DH high-radiance LED (After Szentesi and Szanto [96]).

The LED source was found to be the most non-linear element in the system, with second-harmonic distortion more than 50 dB down from the fundamental.

Szentesi and Szanto [96] have constructed an optical fiber system capable of transmitting studio-quality video. Harmonic distortion measurements on the LED used in the system were made at various depths of modulation and bias currents at room temperature. The results are presented in Fig. F.2. These results indicate that, for the LED biased at 100 mA with an index of modulation of 0.7 (140 mA p-p), the total harmonic distortion (largely second-order) is -30 dB. Correspondingly lower depths of modulation result in improved harmonic distortion.

Work by Straus and Szentesi [81] on the same type of LED revealed a relatively linear increase in harmonic distortion with temperature in the range from -65°C to 102°C . These results were determined with a 50 mA p-p modulating signal at 1 KHz. Fig. F.3 shows the results. At a bias of 100 mA, the harmonic distortion increases approximately $0.06 \text{ dB}/^{\circ}\text{C}$ over the temperature range indicated.

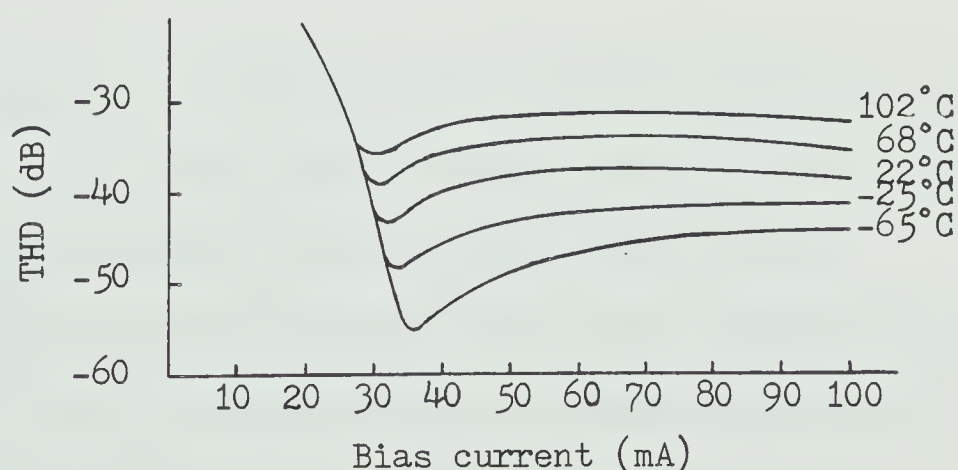


Fig. F.3 Total harmonic distortion as a function of ambient temperature in typical Ge-doped, DH LED's (After Straus and Szentesi [155]).

APPENDIX G

PHOTODETECTOR NOISE PERFORMANCE

The primary photocurrent generated by a photodetector is given by [8,91,156]

$$i_{ph} = \eta \frac{e}{hf} G P_o \quad (G.1)$$

where η is the quantum efficiency of the photodiode
 e is the electron charge
 hf is the energy per photon
 G is the avalanche gain of the photodiode
 p_o is the average received optical power.

For a sinusoidally-modulated carrier with modulation index m , the mean-square signal current in the photodetector output is given by [8,91]

$$\langle i_s^2 \rangle = 1/2 \left[\eta \frac{e}{hf} G m p_o \right] \quad (G.2)$$

There are a number of noise sources present in a photodetector circuit. These include quantum noise, thermal noise, dark current noise, leakage current noise and beat noise [8,91].

Quantum noise determines the ultimate sensitivity of the photodiode and is a function of the incident optical power. Its mean-square value is given by

$$\langle i_Q^2 \rangle = 2e \frac{e}{hf} \eta p_o G^2 F_d B \quad (G.3)$$

where F_d is an excess noise factor associated with the random nature of the avalanche process and is given approximately by $F_d \approx \sqrt{G}$ for silicon

B is the bandwidth of the information source.

Thermal noise contributes a mean-square value of

$$\langle i_T^2 \rangle = \frac{4kT}{R} B F_a \quad (G.4)$$

where k is Boltzmann's constant

T is absolute temperature

R is the equivalent load resistance

F_a is the noise figure of the baseband amplifier.

Dark current noise is caused by electrons and/or holes thermally liberated in the p-n junction which experience the avalanche gain G . The mean-square value of this source is

$$\langle i_D^2 \rangle = 2e i_d G^2 F_d B \quad (G.5)$$

where $i_d = i_{d'} + \frac{e}{hf} \eta p_b$

and $i_{d'}$ is primary photodetector dark current

p_b is the average power of incoherent background radiation incident on the photodetector.

For optical fiber systems, the background radiation p_b should be negligible.

Leakage current noise is caused by electrons and/or holes which bypass the drift region and experience no avalanche gain. The mean-square value of this component is given by

$$\langle i_L^2 \rangle = 2ei_L B \quad (G.6)$$

where i_L is the leakage current.

If an incoherent source is used, such as an LED, there will be an additional noise component present due to the beats between the various spectral components. This beat noise has a mean-square value given by

$$\langle i_B^2 \rangle = 2 \left(\frac{e}{hf} G \eta P_o \right)^2 \frac{B}{Y \delta f} \left(1 - 1/2 \frac{B}{\delta f} \right) \quad (G.7)$$

where Y is the number of spatial modes reaching the photodetector (fiber output modes)

δf is the spectral width of the source (in Hertz).

The resulting signal-to-noise ratio SNR is then given by

$$SNR = \langle i_s^2 \rangle / \langle i_n^2 \rangle \quad (G.8)$$

where

$$\langle i_n^2 \rangle = \langle i_Q^2 \rangle + \langle i_T^2 \rangle + \langle i_D^2 \rangle + \langle i_L^2 \rangle + \langle i_B^2 \rangle . \quad (G.9)$$

APPENDIX H

LINEARITY MEASUREMENTS ON PHOTODIODES

An investigation of nonlinear distortion in p-i-n and avalanche photodiodes was conducted by Ozaki and Hara [157]. The outputs of three LED's, biased at 100 mA and amplitude modulated at frequencies of 1498.2 kHz, 1503.2 kHz and 6006.5 kHz at an index of 75%, were combined and received by a photodetector. The non-linearity present resulted in harmonic mixing, with the output electrical signal being filtered to remove unwanted products, and then measured with a spectrum analyzer. The nonlinearity contribution by the associated circuitry was determined to be negligible. The distortion due to the "worst" avalanche photodiode was measured at a bias of 155 V, which corresponded to a gain of 18.8 dB at an incident optical power level of -25.2 dBm. These results are presented in Fig. H.1.

The second-harmonic distortion is seen to be approximately proportional to the square of the fundamental power level. At -20 dBm, the second-harmonic distortion is some 60 dB below the fundamental. Due to the noise in the system, third-harmonic distortion could only be measured at higher input power levels. This third-harmonic distortion is expected to be proportional to the cube of the fundamental power level [152]. Extrapolation indicates a third-harmonic distortion of 118 dB below the fundamental at an average incident optical power of -20 dBm.

Results with another avalanche photodiode yielded second-

harmonic distortion 67 dB below the fundamental at an average incident optical power of -20 dBm. Third-harmonic distortion was below the quantum noise level and was not observable below an incident power level of -10 dBm. A p-i-n photodiode biased at 5 V resulted in second-harmonic distortion of 64 dB below the fundamental power level of -10 dBm. At bias voltages higher than 10 V, the second-harmonic distortion level was below the quantum noise level and could not be measured.

Wideband analog transmission systems have been constructed to date with very low distortion. Szentesi and Szanto [96] have reported a video transmission system capable of studio quality (S/N of 56 dB and differential gain of 0.3 dB) with a total second-harmonic distortion of -40 dB. The most nonlinear element in the system was the LED, which was allowed a second-harmonic distortion of -30 dB. The p-i-n photodiode had excellent linearity, contributing distortion more than 70 dB below the fundamental. The third-harmonic component was 15 - 25 dB below the second. Another analog system with a bandwidth of 0 - 15 MHz was described by Szanto and Taylor [154]. This system also used a p-i-n photodiode with second-harmonic distortion more than 70 dB below the fundamental. In this system, the LED was again the most nonlinear element, with typical second-harmonic distortion 50 - 55 dB below the fundamental.

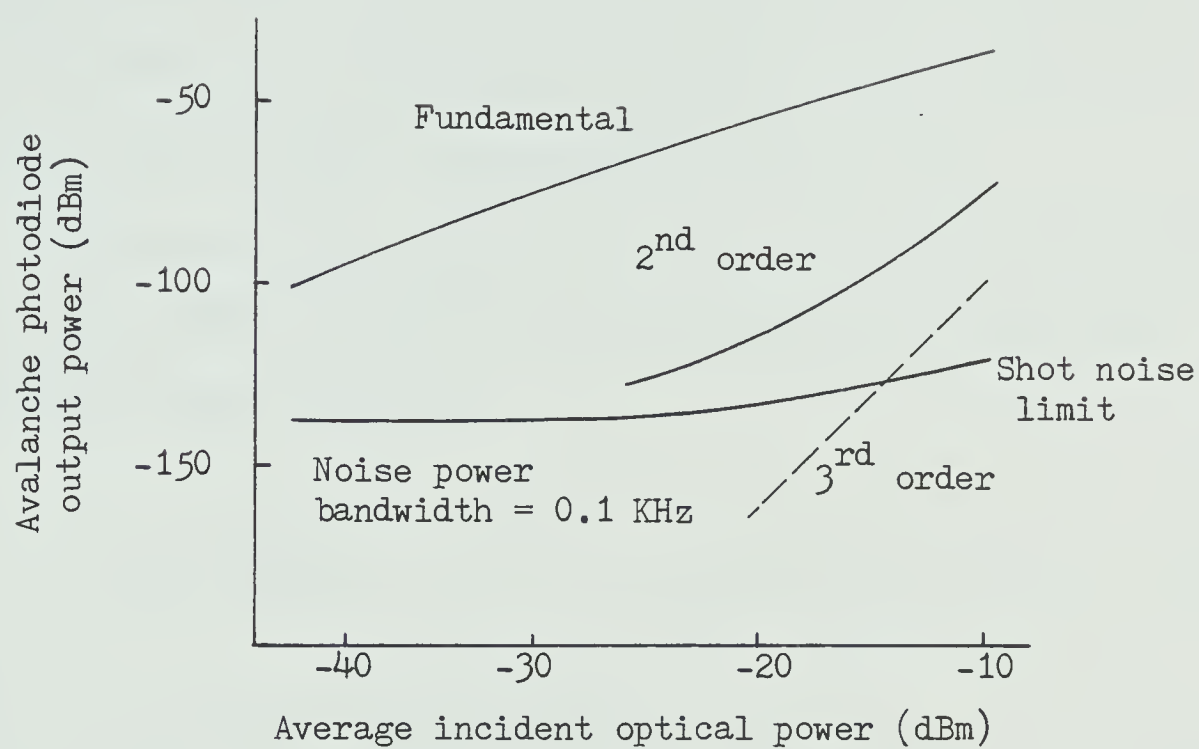


Fig. H.1 Nonlinear distortion as a function of incident power (After Ozeki and Hara [157]).

APPENDIX I

DIRECT COUPLING OF LED'S TO STEP-INDEX FIBERS

Yang and Kingsley [98] examined the case of coupling an LED to a step-index fiber. The model they used is shown in Fig. I.1. A source s of radius r_s is displaced a distance L from the end of a fiber with core of radius a and acceptance angle of θ_c .

When the distance between the source and fiber is less than $a \cot \theta_c$, the amount of radiation I_c coupled into the fiber from an elemental source area ds is

$$I_c = \Lambda \Omega_a ds \quad (I.1)$$

where Λ is the source radiance

Ω_a is the effective acceptance solid angle of any point on the end of the fiber and which is given by

$$\Omega_a = 4\pi \sin^2(\theta_c/2) \quad (I.2)$$

With the geometry of Fig. I.1, it is shown [98] that the maximum light power coupled into the fiber from a source at a distance $L \leq a \cot \theta_c$ is given approximately by

$$\begin{aligned} I_{c_{\max}} &\simeq U \Omega_a \Lambda \pi a^2 && \text{for } r_s \geq 2a \\ &= 4U \Lambda \pi^2 a^2 \sin^2(\theta_c/2) \end{aligned} \quad (I.3)$$

where U is the transmission coefficient.

Increasing the source-fiber separation greater than $L = a \cot \theta_c$, and maintaining $r_s > 2a$, will increase the effective source area, but also diminish the effective solid angle such that the coupled power does not exceed $I_{c_{\max}}$. For $r_s \geq 2a$, the coupled power is dependent on the radiance Λ which is invariant for an object and its image under any passive imaging system (e.g. a lens)[98].

The coupling efficiency is defined [98] as

$$\eta_c = \frac{I_c}{\text{total radiant power}} \quad (\text{I.4a})$$

or

$$\eta_c = \frac{I_c n_o^2}{2\pi \Lambda \pi r^2} \quad (\text{I.4b})$$

For $r_s \leq a$ and with the source-fiber separation being $L \leq (a-r_s) \cot \theta_c$, all the rays emitted by the source within the acceptance angle of the fiber strike the fiber core. In this case, the coupling efficiency has been determined [158] to be

$$\eta_c = \sin^2 \theta_c = \frac{\text{N.A.}^2}{n_o^2} \quad (\text{I.5})$$

This equation is also readily determined from eqs. (I.3) and (I.4) for small acceptance angles. A plot of coupling efficiency as a function of numerical aperture for the case of the refractive index n_o as unity is presented in Fig. I.2. This figure shows the importance of increasing numerical aperture in increasing coupling efficiency.

For source-fiber separation $L > (a-r_s) \cot \theta_c$, not all of the rays emitted by the source within the acceptance angle of the fiber

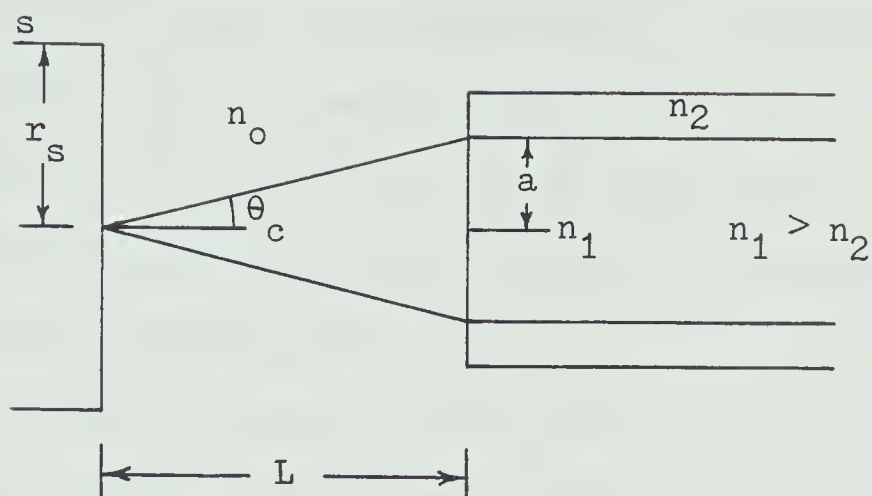


Fig. I.1 LED/fiber coupling configuration (After Yang and Kingsley [98]).

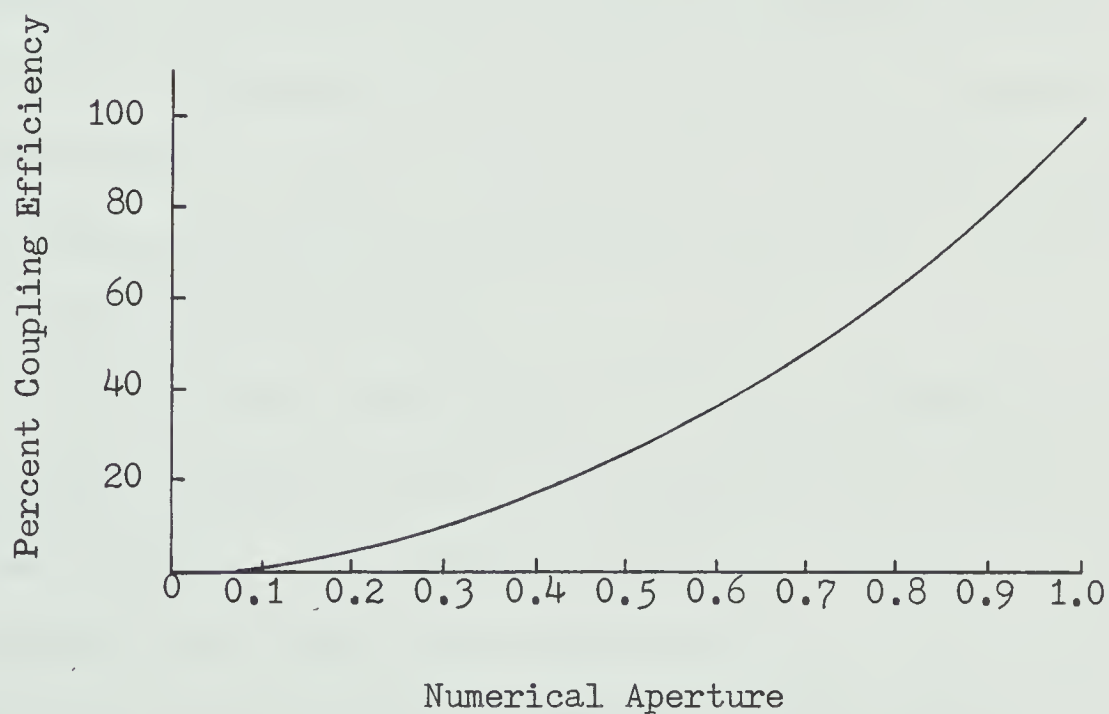


Fig. I.2 Percent coupling efficiency as a function of fiber numerical aperture (After Johnson and Kawasaki [158]).

strike the fiber core. In this case, the coupling efficiency has been determined by Kawasaki and Johnson [158] to be a complicated function of source and fiber co-ordinates and the acceptance angle. This function was evaluated numerically [158] for two situations, which are shown in Fig. I.3 and I.4. These figures tend to summarize the previous discussion and show that the best efficiency is obtained for a source-fiber separation of $L \leq (a-r_s) \cot \theta_c$ for $r_s \leq a$.

To illustrate the significance of the coupling problem, we consider a high-radiance, surface-emitting LED butted directly against a step-index fiber. The LED is assumed to have a radiance $\Lambda = 30 \text{ W/sr.cm}^2$ with emission into air ($n_o = 1.0$). However, since the LED material has a refractive index of 3.5 and is butted against the fiber, the numerical aperture of the fiber is reduced from its value in air by n_o from eq. (2.6). As the coupling efficiency is proportional to the square of the numerical aperture from eq. (1.5), the effective brightness must be increased by n_o^2 to compensate for this effect [98]. Thus, $\Lambda = 370 \text{ W/sr.cm}^2$. The fiber refractive indices are considered to be such that $n_1 + n_2 = 3.0$, $n_1 - n_2 = 0.0065$ and the core diameter is $50 \mu\text{m}$.

The acceptance half angle θ_c is readily determined from the relationships between n_1 and n_2 and by the use of eq. (2.6) for the numerical aperture. The numerical aperture is found to be 0.14 and the acceptance half angle for a direct butt ($n_o = 3.5$) is 2.29° . Substituting into eq. (1.3), the maximum coupled power is

$$I_{c \text{ max}} = U \Lambda \pi^2 4a^2 \sin^2(\theta_c/2)$$

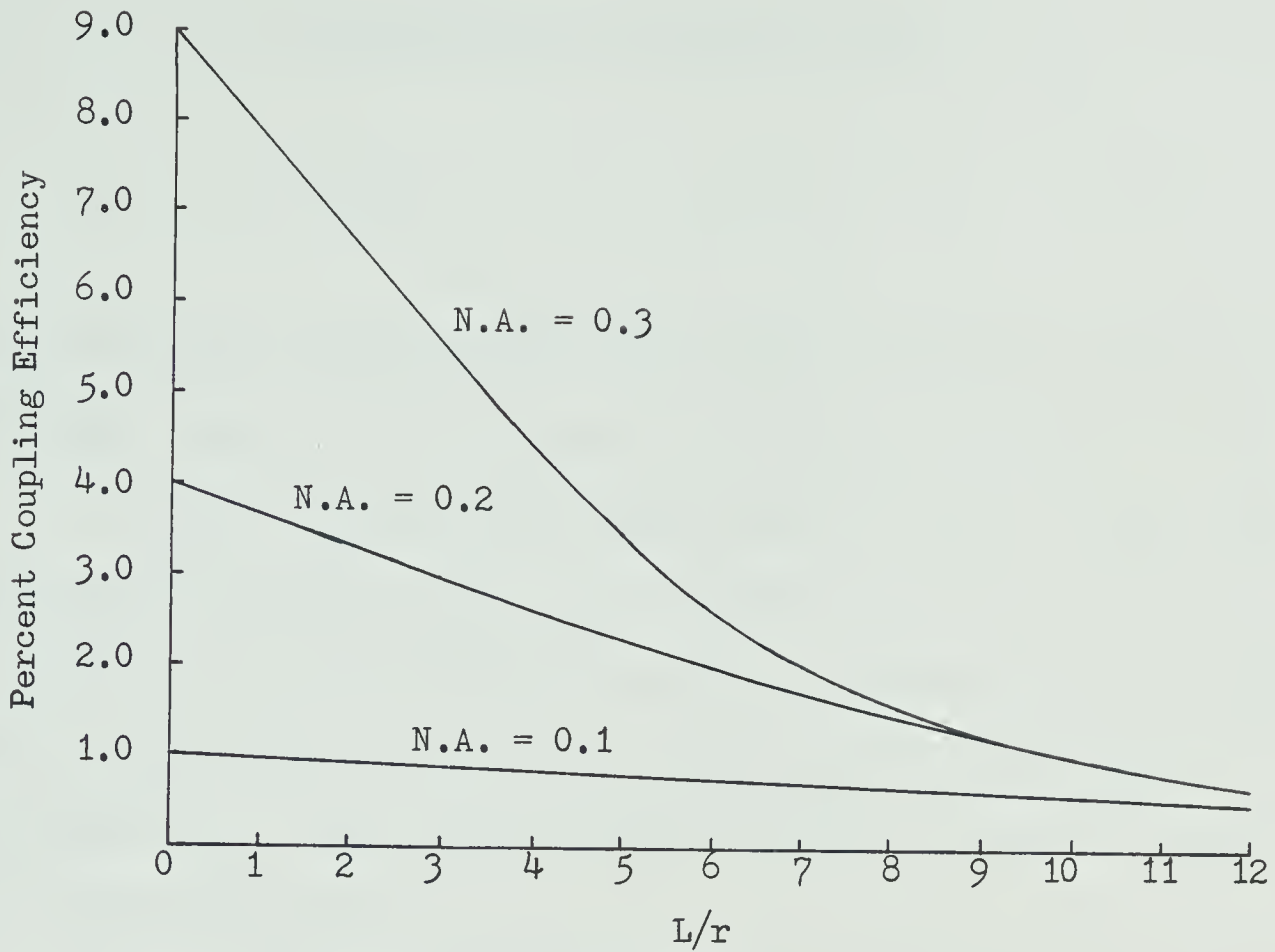


Fig. I.3 Percent coupling efficiency as a function of the ratio of the LED/fiber separation to LED radius for fibers of numerical aperture $N.A. = 0.1, 0.2$ and 0.3 . The LED and fiber core are the same size (After Johnson and Kawasaki [158]).

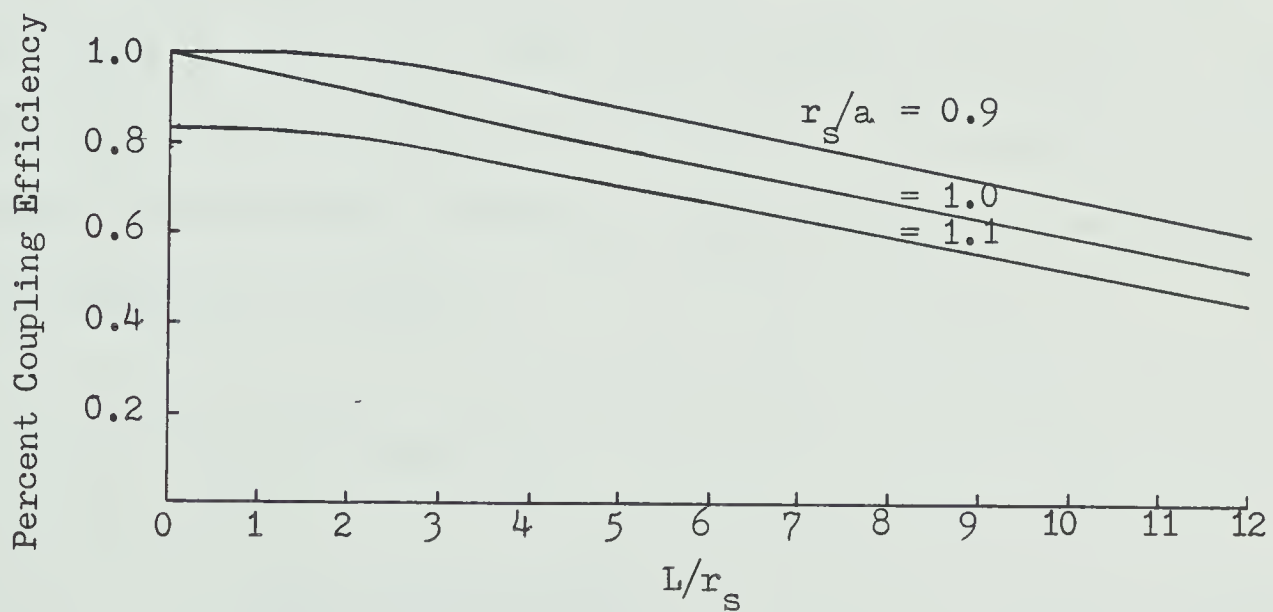


Fig. I.4 Percent coupling efficiency as a function of the ratio of the LED/fiber separation to LED radius for different ratios of LED to fiber-core radii. The fiber has a numerical aperture $N.A. = 0.1$ (After Johnson and Kawasaki [158]).

$$\begin{aligned}
&= 1(370)\pi^2(50 \times 10^{-4})^2 \sin^2(1.145) \\
&= 36 \mu\text{W}
\end{aligned}$$

For a source area equal to that of the fiber, the maximum coupling efficiency from eq. (I.4) is about 1%, or the coupling loss is 20 dB.

A lens or other optical system cannot be used to couple more energy into an optical fiber if $r_s > 2a$ since, as shown in eq. I.3, I_c depends only on the radiance Λ , which is invariant for the object and its image under the use of any passive imaging system [98]. In the region of $r_s \leq 2a$, an optical system can be utilized to increase the coupling efficiency.

Yang and Kingsley [98] considered a coupling situation represented by Fig. I.5 in which a lens of radius a is placed between the source and the fiber at a distance from the source equal to the focal length Γ . Radiation from points on the source displaced from the fiber/lens axis a distance y impinges on the end of the fiber at an angle $\theta_L = \tan^{-1} y/\Gamma$. Since this radiation propagates into the fiber only if $\theta_L \leq \theta_c$ where θ_c is given by eq. (2.6) with $n_o = 1$, the effective source radius is $\Gamma \tan \theta_c$. Since the effective solid angle is that subtended by the lens,

$$\begin{aligned}
\Omega_L &= 2\pi(1 - \cos \theta_c) \\
&= 2\pi \left[1 - \left(\frac{\Gamma^2}{\Gamma^2 + a^2} \right)^{1/2} \right] \tag{I.6}
\end{aligned}$$

the power coupled into the fiber is

$$\begin{aligned}
 I_c &= 2\pi^2 \Lambda U (\Gamma \tan \theta_c)^2 \left[1 - \left(\frac{\Gamma^2}{\Gamma^2 + a^2} \right)^{1/2} \right] \\
 &= I_{c_{\max}} \cdot \frac{2 \tan^2 \theta_c}{\sin^2 \theta_c / 2} \left(\frac{\Gamma}{2a} \right)^2 \left[1 - \left(\frac{\Gamma^2}{\Gamma^2 + a^2} \right)^{1/2} \right]
 \end{aligned} \tag{I.7}$$

The total radiated power is given by [98]

$$I_t = 2\pi^2 \Lambda (\Gamma \tan \theta_c)^2 \tag{I.8}$$

so the power coupled into the fiber is given by

$$I_c = I_t \left[1 - \left(\frac{\Gamma^2}{\Gamma^2 + a^2} \right)^{1/2} \right] \tag{I.9}$$

Using the parameters of the previous example, ie: $\theta_c = 8^\circ$, $\Lambda = 30 \text{ W/sr.cm}^2$, $U = 1$ and with $\Gamma = 2a = 50 \mu\text{m}$, the coupled power is found to be $31 \mu\text{W}$. The total radiated power, from eq. (I.8) is $292 \mu\text{W}$, resulting in a coupling loss of 9.7 dB.

The lens has thus increased the coupling efficiency 10 times, but the coupled power is about 15% less since the effective source radius is now only $\Gamma \tan \theta_c / 2$. In principle, the coupling efficiency can be increased to 100% with an ideal optical arrangement when the source is very small, but the power coupled into the fiber can never exceed $I_{c_{\max}}$ in eq. (I.3). Imaging optics permit one to reduce the junction area and increase the over-all efficiency, but the coupled power increases only if the source radiance increases as a consequence of the reduction in junction area.

It is of practical interest to determine the value of focal length required to optimize the coupling efficiency. From eq. (I.9), it is seen that the coupling efficiency is maximized when $(\Gamma^2/\Gamma^2 + a^2)^{1/2}$ is minimized. We know, from eq. (I.6) that light rays will propagate only for acceptance angles,

$$\theta_c \leq \cos^{-1} \left[\left(\frac{\Gamma^2}{\Gamma^2 + a^2} \right)^{1/2} \right]$$

Therefore,

$$\frac{\Gamma^2}{\Gamma^2 + a^2} \geq \cos^2 \theta_c$$

or
$$\Gamma^2 \geq \Gamma^2 \cos^2 \theta_c + a^2 \cdot \cos^2 \theta_c$$

$$\begin{aligned} \therefore \Gamma_{\min} &= \left(\frac{a^2 \cdot \cos^2 \theta_c}{1 - \cos^2 \theta_c} \right)^{1/2} \\ &= a \frac{\cos \theta_c}{\sin \theta_c} \end{aligned}$$

or
$$\Gamma_{\min} = a \cot \theta_c \quad (\text{I.10})$$

The coupling of light from stripe-geometry sources has also been examined by Yang and Kingsley [98]. The configuration they considered is shown in Fig. I.6. An LED whose junction plane is confined within the region between $x = z \tan \theta_c + a$ and $x = z \tan \theta_c - a$ is butted against an optical fiber of core diameter $2a$. Assuming that the junction is rectangular with length L_j , the light power coupled into the fiber, for $L_j < a \cot \theta_c$, is found to be [98]

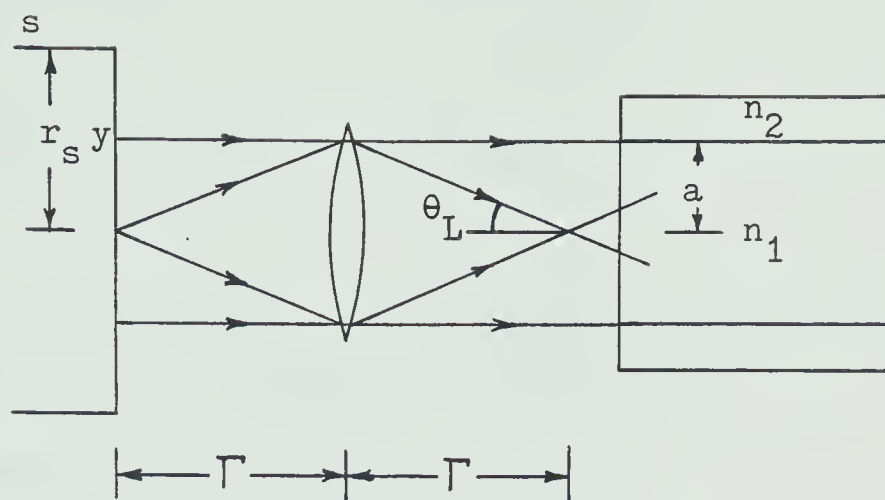


Fig. I.5 LED/fiber coupling configuration using a lens (After Yang and Kingsley [98]).

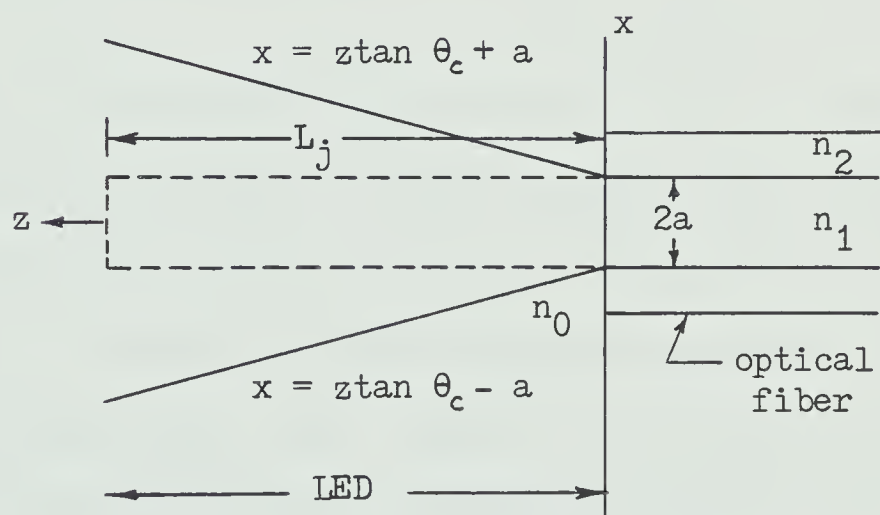


Fig. I.6 Coupling configuration using a stripe-geometry LED butted against an optical fiber (After Yang and Kingsley [98]).

$$I_c = 8.64 \Lambda L_j U a (1 - \cos \theta_c) \quad (I.11)$$

and for $L_j = a \cot \theta_c$

$$I_c = 8.64 \Lambda U a^2 \cos \theta_c \tan \theta_c / 2 \quad (I.12)$$

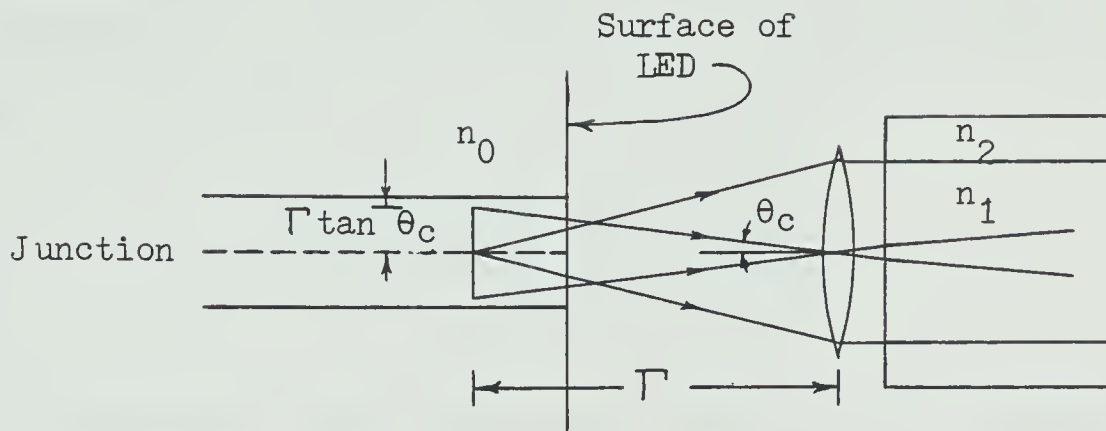
Using the parameters from the previous example, ie: $\Lambda = 370 \text{ W/sr.cm}^2$, $U = 1$, $a = 25 \mu\text{m}$, $\theta_c = 2.28^\circ$ and with $L_j = a \cot \theta_c$, the coupled power, from eq. (I.12) is 0.4 mW.

By increasing the junction length, the power coupled into the fiber can be increased. In the limit of $L_j \gg 2a$, the additional power coupled is given by [98]

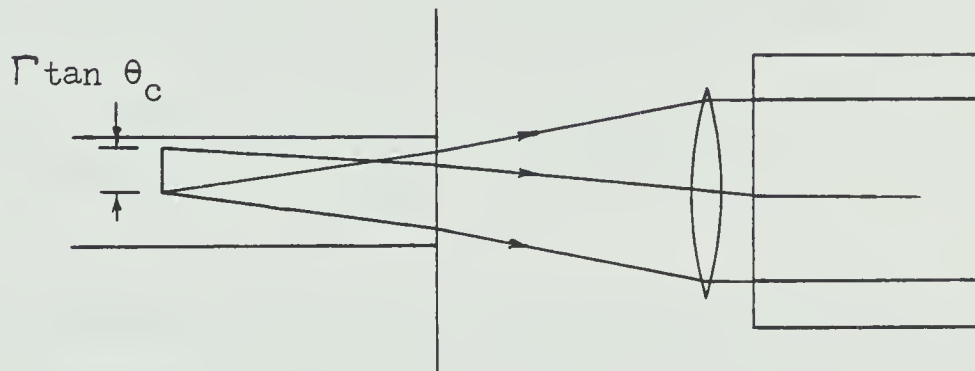
$$\delta I_c \rightarrow 4\pi \Lambda U a^2 \tan \theta_c / 2 \quad (I.13)$$

Equations (I.11) and (I.13) indicate that a very long stripe junction LED can couple up to 27 times (14 dB) the power into a fiber in a coplanar geometry (Fig. I.6) than can be coupled in the normal geometry (Fig. I.1)[98]. For the parameters previously used, the launched power approaches 1 mW. However, due to power dissipation and internal absorption effects, an LED junction much longer than $a \cot \theta_c \approx 630 \mu\text{m}$ is probably impractical [98].

As with the normal geometry, the coupling efficiency can be increased in the coplanar geometry by using a lens or mirror to couple the radiation from the LED into the fiber, but with some decrease in the maximum power that can be coupled. Yang and Kingsley [98] examined the case of the coplanar geometry using a lens as shown in Fig. I.7.



(a) $n_0 = 1$



(b) $n_0 > 1$

Fig. I.7 Coupling configuration using a stripe-geometry LED and a lens
(After Yang and Kingsley [98]).

The parameters of interest are the maximum length and width of the junction. From Fig. I.7, it can be determined that points on the LED closer to the lens than $\Gamma/\{1 + [(\Gamma \tan \theta_c)/a]\}$ cannot utilize the full aperture of the lens. This distance is then assumed to be the separation of the lens and the LED. The optimum LED junction length is then [98]

$$L_j = \frac{2n_0\Gamma^2 \tan \theta_c}{a} \left/ \left[1 - \left(\frac{\Gamma \tan \theta_c}{a} \right)^2 \right] \right. \quad (\text{I.14})$$

in the direction of the fiber axis, where n_0 is the refractive index of the LED material.

In the focal plane, points further from the axis than $\Gamma \tan \theta$ cannot be coupled into the fiber. Consequently, the junction width is assumed to be $2\Gamma \tan \theta_c$. The junction area is then

$$A = \frac{4n_0\Gamma^3}{a} \tan^2 \theta_c \left/ \left[1 - \left(\frac{\Gamma \tan \theta_c}{a} \right)^2 \right] \right. \quad (\text{I.15})$$

The effective solid angle subtended by the lens is given approximately by $\Omega_L \approx \pi(a^2/\Gamma^2)$ for points on the axis near the focal point. For points near the extremes of the junction, the effective solid angle is reduced by ~2 times so an estimate of the effective solid angle is [98]

$$I_c \approx 3\pi \frac{\Lambda U n_0 a \tan^2 \theta_c}{\{1 - [(\Gamma \tan \theta_c)/a]^2\}} \quad (\text{I.16})$$

Using the parameters from the previous examples, $\Lambda = 30 \text{ W/sr.cm}^2$, $U = 1$, $n_0 = 3.5$, $\Gamma = 2a = 50 \text{ um}$, $\theta_c = 8^\circ$, eq. (I.16) yields a coupled power of 0.26 mW. This compares with 0.4 mW coupled without focusing.

APPENDIX J

DIRECT COUPLING OF LED'S TO PARABOLIC-INDEX FIBERS

D. Marcuse [97] has examined the case of coupling light from an LED into a fiber having a parabolic index of refraction profile. He considered the coupling dependency on source-to-fiber separation, transverse displacement of the source and the use of matching lenses. The geometry of the source exciting a fiber core is illustrated in Fig. J.1.

For the case of an LED having the same diameter as the fiber core, the dependency of coupled power on source-to-fiber separation was determined [97]. A plot for various values of relative index difference Δ is presented in Fig. J.2. This plot indicates that the coupled power is relatively insensitive to source-fiber separation and particularly for smaller values of Δ .

The dependence of the coupled power on the amount of relative offset d/a for a source whose radius equals the fiber radius, and which is located at three different distances from the fiber end, is shown in Fig. J.3. This plot reveals that the relative tolerance to source offsets becomes more liberal as the distance between the source and the fiber end is increased.

Assuming the use of Burrus-type, surface-emitting LED's, whose brightness is roughly inversely proportional to their radius, Marcuse [97] determined the optimum source/fiber areas. He found that the relationship between coupled power and source/fiber area is as shown in Fig. J.4. This figure indicates that the maximum coupled

power occurs at a source-core radius ratio of $r/a = 0.8$. It also indicates that a source roughly one-half the radius of the core will couple approximately the same amount of power as will a source whose radius is equal to that of the core.

Marcuse [97] further examined the amount of coupled power as a function of electrical drive power into the LED. This relationship is shown in Fig. J.5 and is based on the use of high brightness LED's with small radii ($\lesssim 50 \mu\text{m}$), whose power consumption is virtually a linear function of the radius. The maximum of the fiber excitation efficiency is seen to occur at $r/a = 0.2$, ie: at small source radii.

A good compromise between the maximum achievable total power and the desire to obtain good excitation efficiency relative to the power input to the LED may be to operate with a diode whose radius is approximately one-half of the fiber core radius. For this case of $r/a = 0.5$, we would lose 17 percent of the optimum operating power efficiency and work 19 percent below the maximum achievable injected power.

Fig. J.5 also shows the case of coupling the power from a small source LED into a fiber via a matching lens. The matching lens transforms the small source into an image the size of the fiber core. The loss in source brightness, caused by the magnification of its image, is compensated for by the fact that many of the rays that left the diode at angles too large to be trapped when the source was in direct contact with the fiber, are now transformed to smaller angles so that a wider cone of light leaving the source is able to be accepted by the fiber. Use of a matching lens allows us to inject the same amount of power from a small LED that would be available from a large

source of equal brightness in direct contact with the fiber. However, because the achievable brightness increases with the decreasing radius of an LED, more power can be obtained from a small LED whose light is focused into the fiber with a lens. Use of a matching lens also increases the overall efficiency of operation as shown by the dotted line of Fig. J.5.

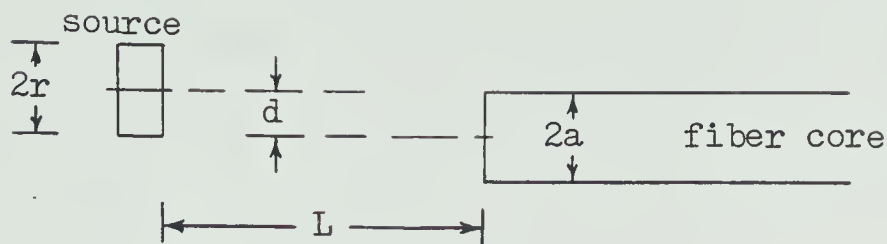


Fig. J.1 Geometry of a source exciting a fiber core (After Marcuse [97]).

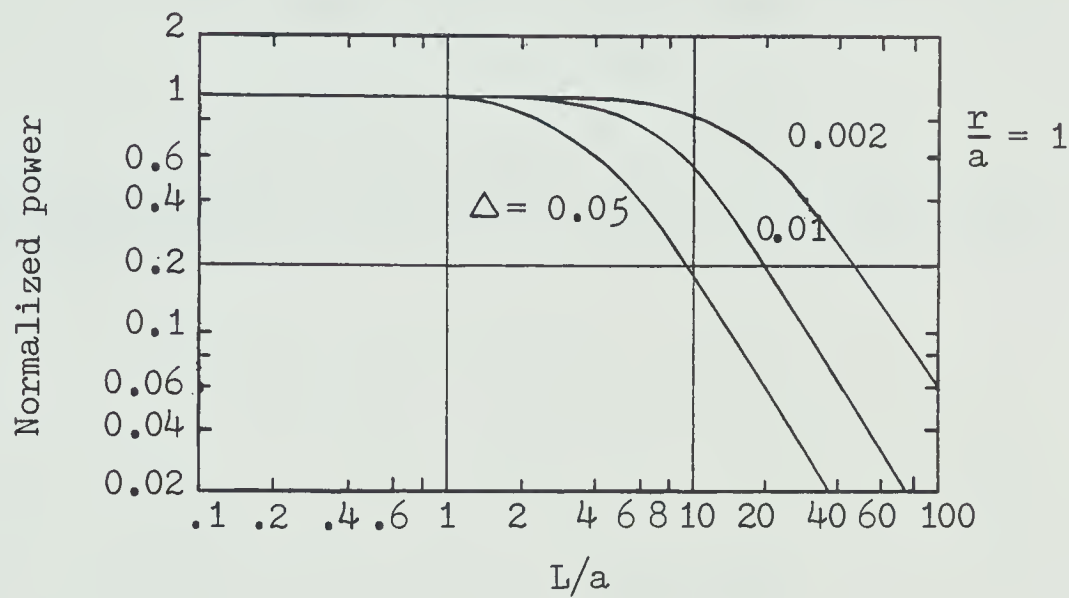


Fig. J.2 Normalized total power P_f injected into a parabolic-index fiber as a function of the distance L between source and fiber (After Marcuse [97]).

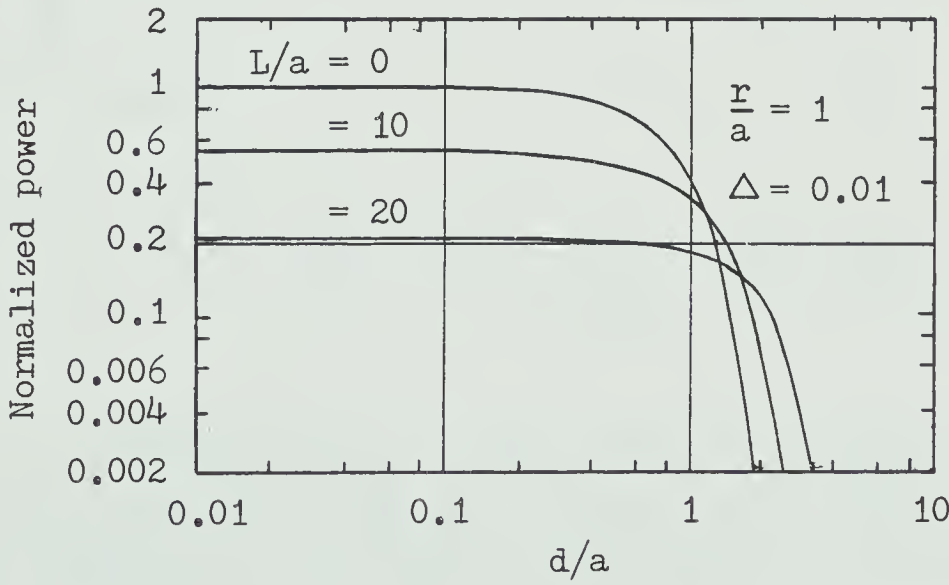


Fig. J.3 Normalized total power P_f injected into a parabolic-index fiber as a function of the transverse source displacement d for several values of the distance L of the source from the fiber and for $\Delta = 0.01$ (After Marcuse [97]).

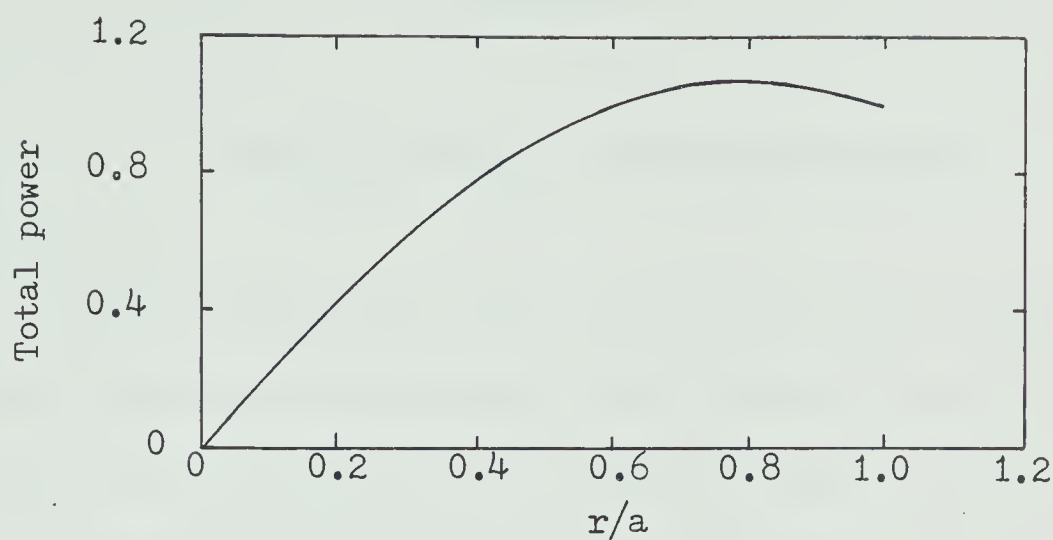


Fig. J.4 Total power injected into the fiber with a high-brightness, Burrus-type LED as a function of normalized source radius, r (After Marcuse [97]).

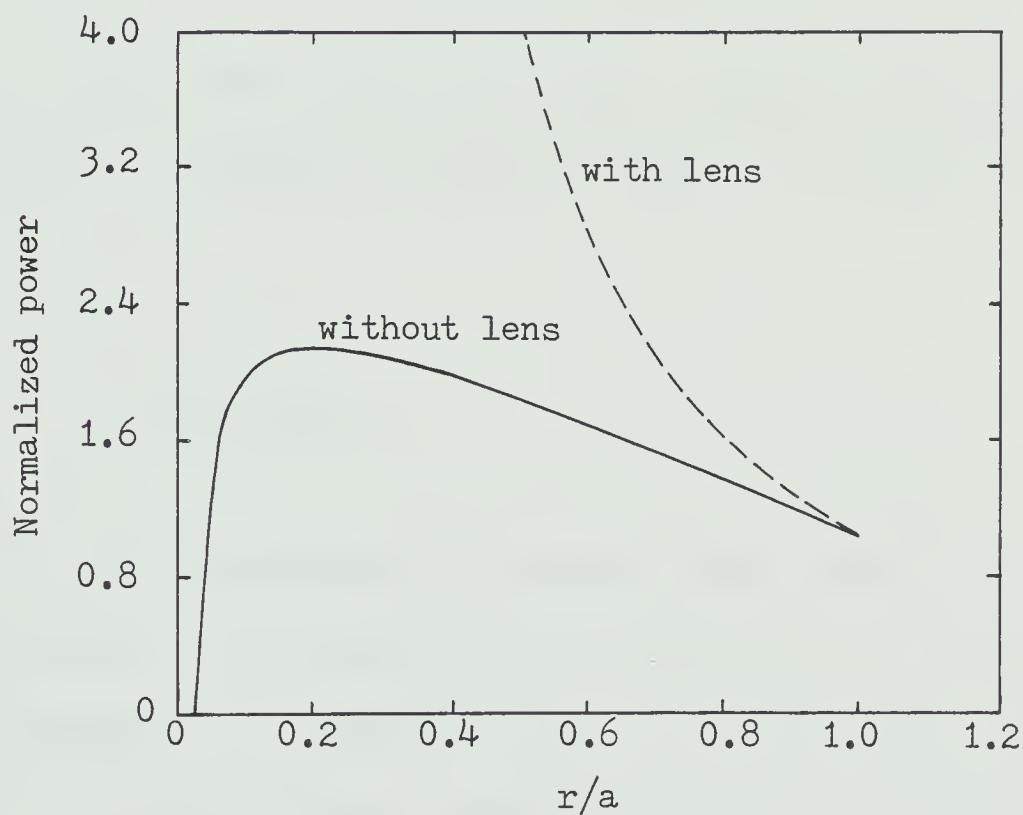


Fig. J.5 Normalized ratio of total power P_f injected into the fiber relative to the electrical drive power of the diode as a function of the normalized source radius. The solid curve applies for an LED in direct contact with the fiber; the dotted curve describes operation with a matching lens (After Marcuse [97]).

APPENDIX K

GRATING COUPLERS - THEORY AND PRACTICE

Grating couplers have been analyzed in detail by Harris et al [159] and Dalgoutte and Wilkinson [160] but the following simplified discussion will be taken from Tien [101] and Dakss et al [161].

A laser beam incident on the phase grating at an angle ϕ_i has a phase variation in the x-direction given by

$$\exp\left\{i(2\pi/\lambda_o)(\sin \phi_i)x\right\}$$

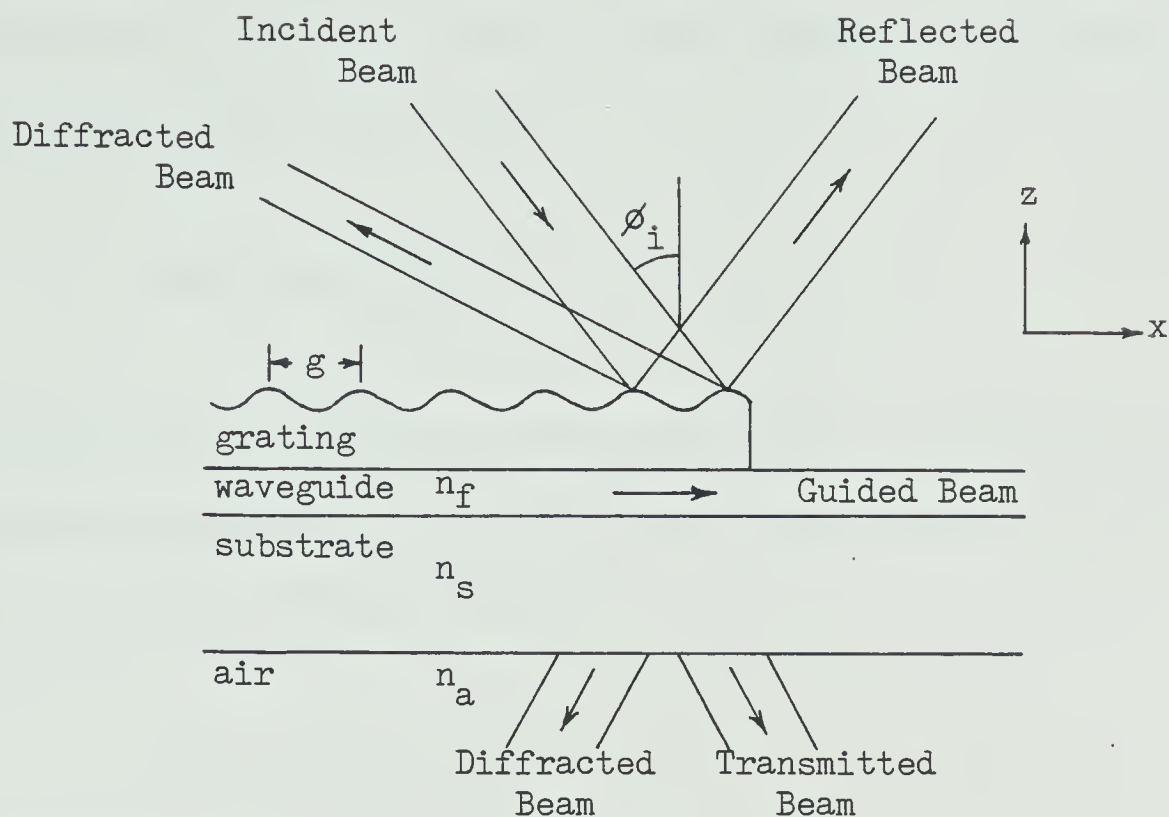
where λ_o is the vacuum laser wavelength. As the beam passes through the grating, it undergoes a phase retardation, or spatial phase modulation

$$\Xi \sin(2\pi x/g)$$

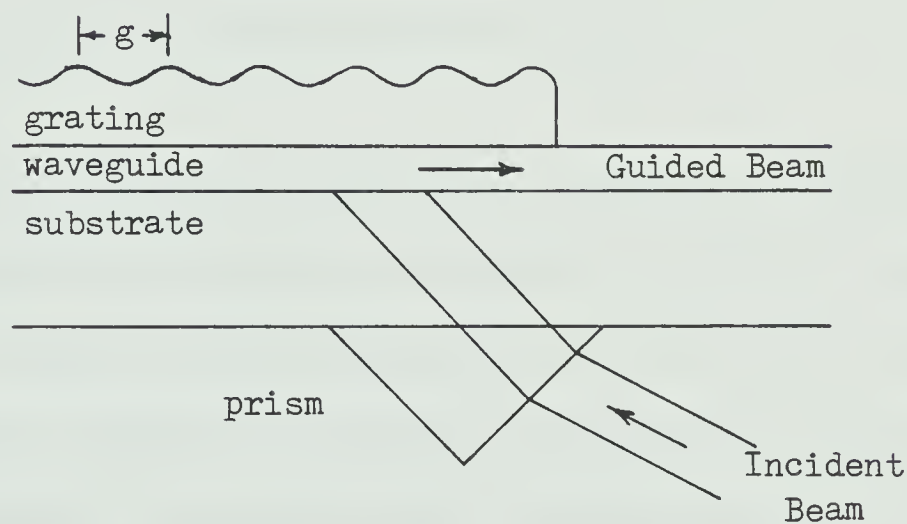
where Ξ is the amplitude of the spatial phase modulation caused by the grating and is sometimes called the phase depth of the grating (which is assumed for convenience here to be sinusoidal), and g is the periodicity of the grating. A polarization wave varying as

$$\exp\left\{i\left[\Xi \sin(2\pi x/g) + (2\pi/\lambda_o)(\sin \phi_i)x\right]\right\}$$

is thus established on the surface of the film. This polarization wave can be treated as a superposition of many Fourier components with individual phase variations



(a) Normal grating coupler



(b) Reverse coupler

Fig. K.1 Grating coupler cross-sections (a) normal grating coupler (After Dalgoutte and Wilkinson [115]) (b) reverse coupler (After Dalgoutte [162]).

$$\exp\left\{i\left[m(2\pi/g)x + (2\pi/\lambda_o)(\sin \phi_i)x\right]\right\}$$

where m is any integer. If one of these components is phase-matched to a waveguide mode of the form

$$\exp\left\{i(2\pi/\lambda_g)x\right\},$$

where λ_g is the wavelength of the guided wave, the light beam is exclusively coupled to this mode and the light energy is fed into the film. This condition implies

$$c/V_p = \sin \phi_i + \frac{m \lambda_o}{g} \quad (\text{K.1})$$

where V_p is the phase velocity of the guided wave
 c is the velocity of light in vacuum and
 λ_o is the wavelength in free space.

Harris et al [159] and Dalgoutte and Wilkinson [160] have performed comprehensive analyses on grating couplers and have determined a number of relationships which can be used to design optimal couplers. While this material is beyond the scope of this thesis, in essence it is implied that thin grating couplers can have efficiencies equalling that of prism-waveguide couplers when used in appropriate geometrical configurations. For efficiencies of up to about 50%, the normal grating coupler can be used as shown in Fig. K.1 (a). A suitable choice for grating period is between a half and one times the exciting wavelength [160]. For efficiencies greater than 40-50%, it is necessary to restrict the number of diffracted

beams to one. This can be done by using a short period grating so there is only one diffraction order [160] (ie: only one output beam from the coupler). This, however, requires coupling from the substrate in the reverse direction as shown in Fig. K.1 (b), ie: by the use of a reverse coupler.

Dalgoutte [162] has indicated that the effect of the grating of period g is to subtract an equivalent wave vector $k_e = 2\pi/g$ from the propagation constant k_w of the guided wave to give the component along the propagation direction of the wave vector of the radiated beam(s). Only one radiated beam will exist when the following condition is satisfied:

$$k_w + k_a < k_e < k_w + k_s \quad (K.2)$$

where $k_a = 2\pi/\lambda_a$, the wavenumber in the superstrate (air)
 $k_s = 2\pi/\lambda_s$, the wavenumber in the substrate

Some requirements for a good and efficient coupler are [163]

1. Use lossless and scatterfree materials.
2. Suppress unwanted grating orders.

3. Provide for sufficiently deep spatial modulation of the optical phase shift to achieve strong coupling and the associated short coupling lengths. Point 1 restricts us to phase or dielectric grating. Point 2 can be satisfied in two ways: The first is to use a thick grating and light incident near the Bragg angle. Then Bragg effects will suppress all but one diffraction order. This is a "Bragg coupler". The second possibility is to use a grating with a very large number of lines (short grating period). As mentioned above,

this will allow only one diffraction order to propagate, but will require a "reverse coupler". Point 3 is easier to satisfy with a Bragg coupler, where the phase shift accumulates throughout the thickness of the grating. A problem with using a Bragg coupler, however, is that it requires relatively soft, unstable materials [113].

Gratings are generally produced on the surface of a waveguide by applying a photoresist which is exposed to a laser interferometer pattern and then suitably developed. It has been determined [160] that the choice of photoresist is important. The refractive index should be close to that of the waveguide film and the thickness of the resist should be as small as is consistent with obtaining sufficient depth of modulation. Scattering losses at the edges of input and output gratings can be reduced by using thinner resist and also by tapering the resist. A tapered resist can increase the theoretical input coupling efficiency to nearly 100% [160]. Just as with a prism-film coupler, the leading edge of the light beam must coincide with the edge of the grating for maximum coupling efficiency [105].

Experimental Results

Dakss et al [161] coupled a $0.6328 \mu\text{m}$ laser beam (2 mm diameter) through a grating with periodicity $g = 0.665 \mu\text{m}$ into a glass film waveguide (thickness $0.76 \mu\text{m}$ and refractive index 1.73) that was r.f. sputtered onto a glass substrate (refractive index 1.515). TE and TM modes could be selectively excited by choosing the correct beam polarization. They determined a coupling efficiency of about 40%.

Ostrowsky and Jacques [163] coupled a $0.6328 \mu\text{m}$ laser beam through a grating with periodicity $0.66 \mu\text{m}$ and depth $0.06 \mu\text{m}$ into

a film of thickness $0.62\text{ }\mu\text{m}$ and refractive index 1.618 which was formed on top of a glass substrate with refractive index 1.512. According to eq. (K.1) the theoretical coupling angle was determined to be $38^{\circ}40'$. Experimentally, they found maximum coupling occurred at an angle of $37^{\circ}57'$ providing good agreement between theory and practice. The coupling efficiency was determined to be approximately 50%.

Boivin [113] utilized a grating with a periodicity of $0.57\text{ }\mu\text{m}$ to couple a $0.6328\text{ }\mu\text{m}$ laser beam with an input diameter of 0.5 mm into a thin film of thickness $2\text{ }\mu\text{m}$ and refractive index 1.62 which was deposited on a glass substrate with refractive index 1.46. Coupling efficiency for this grating was found to be about 40%.

Kogelnik and Sosnowski [164] constructed Bragg couplers using a grating of dichromated gelatin about $4\text{ }\mu\text{m}$ in thickness on sputtered glass film about $0.3\text{ }\mu\text{m}$ thick and with a refractive index of 1.62. The couplers were designed for light at wavelength $0.6328\text{ }\mu\text{m}$ and the gratings had a periodicity of about $g = 0.25\text{ }\mu\text{m}$. The best results were obtained when the light was incident from the substrate side. This configuration resulted in a coupling efficiency of 71%.

Dalgoutte [162] used a reverse coupler with a $0.68\text{ }\mu\text{m}$ thick glass film with refractive index 1.571 sputtered onto a glass substrate with refractive index 1.513. For these films, grating periods between 0.205 and $0.246\text{ }\mu\text{m}$ are required in order to satisfy eq. (K.2). The grating period used was $0.222\text{ }\mu\text{m}$ and a $0.6328\text{ }\mu\text{m}$ laser beam with input diameter of $75\text{ }\mu\text{m}$ was used. The efficiency obtained was 70.5%.

APPENDIX L

TRANSMISSION LINE LENGTHS FOR A 24 CHANNEL SYSTEM

A 24 channel, multiplexed system would probably utilize antenna groupings such as A (8 x 3) or B (4 x 6), from Fig. 6.2, for the north-south subarray and E (4 x 6) for the east-west subarray. The following calculations are made on this basis.

Primary Feeder Lengths

North-South Subarray

With grouping A, the central transmitting locations (CTL's) are located along the center of the north-south subarray as shown in Fig. 6.2. Since this grouping is 3 dipoles deep, and the total number of dipoles is 200 north-south, there will be 67 CTL's. The CTL furthest from the observatory is located one row down from the end of the subarray, or about 2415 meters distant (2427 - 12.2). The length of transmission line required to return the signals from all 67 CTL's is then

$$67 \times \frac{2415}{2} = 80.9 \text{ km}$$

With grouping B, there will be two rows of CTL's running the length of the north-south subarray, each a distance of 30.4 meters from the centerline. Since this grouping is 6 dipoles deep, there

will be 34 CTL's in each of these two rows. The length of transmission line required to bring the signals from the CTL's to the centerline will be

$$30.4 \times 2 \times 34 = 2067.2 \text{ meters}$$

The furthest CTL from the observatory is located three and one-half rows down from the end of the subarray or at a distance of about 2397 meters ($2427 - 30.5$). The total length of transmission line required to return the signals from all CTL's to the observatory then will be

$$2067.2 + (2 \times 34 \times \frac{2397}{2}) = 83.6 \text{ km}$$

East-West Subarray

The overlap region is 8 dipoles wide, so there are $320 - 8 = 312/2 = 156$ dipoles in the longitudinal direction on both sides of this region. For a 24 channel system, this corresponds to $156/6 = 26$ central transmitting locations on each side. The furthestmost CTL from the observatory will be located $2427 - 45.6 \approx 2382$ meters distant. The approximate length of transmission line required to return the signals from all CTL's in the east-west subarray is

$$26 \times \frac{2382}{2} \times 2 = 61.9 \text{ km}$$

The total length of primary feeder transmission line required for a 24 channel minimum-length system is then about:

$$80.9 + 61.9 = 142.8 \text{ km} \quad (\text{for groupings A and E})$$

$$83.6 + 61.9 = 145.5 \text{ km} \quad (\text{for groupings B and E})$$

To determine the lengths of transmission line required for an equal-length system, the distance from the observatory to the furthest CTL must be determined and multiplied by the total number of CTL's in the array. For antenna grouping A and E, this distance is 2415 meters so the total quantity will be

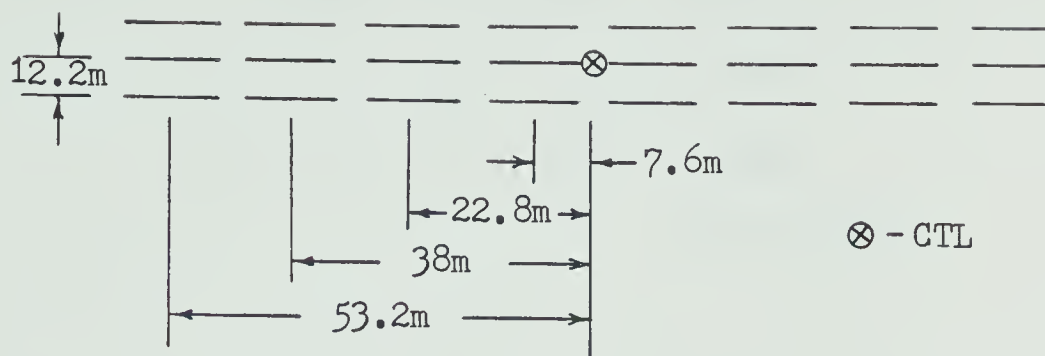
$$(2415)67 + (2415)26(2) = 287.4 \text{ km.}$$

For antenna groupings B and E, the longest distance is $2397 + 30.4 \approx 2428$ meters. In this case the total quantity required is

$$(2428)34(2) + (2428)26(2) = 291.4 \text{ km.}$$

Branch Feeders

Branch feeders are required to convey the signals from each antenna in the group to the CTL. With antenna grouping A as shown below, the length of transmission line per grouping is calculated directly.



$$4 \times (3.2 + 12.2 + 53.2) = 274.4$$

$$4 \times (3.2 + 12.2 + 38) = 213.6$$

$$4 \times (3.2 + 12.2 + 22.8) = 152.8$$

$$4 \times (3.2 + 12.2 + 7.6) = 92$$

$$2 \times (3.2 + 53.2) = 112.8$$

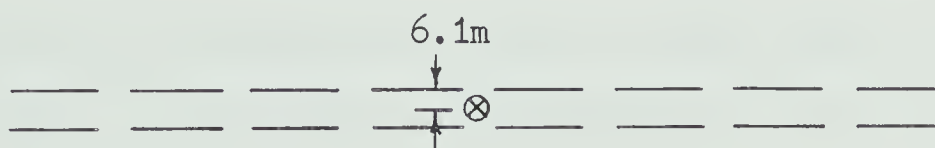
$$2 \times (3.2 + 38) = 82.4$$

$$2 \times (3.2 + 22.8) = 52$$

$$2 \times (3.2 + 7.6) = \underline{21.6}$$

1001.6 meters

Since there are 200 dipoles north-south, there will be 66 groups of 24 channels and 1 group of 16 channels. The length of transmission line for this last group is calculated below:



$$4 \times (3.2 + 6.1 + 53.2) = 250$$

$$4 \times (3.2 + 6.1 + 38) = 189.2$$

$$4 \times (3.2 + 6.1 + 22.8) = 128.4$$

$$4 \times (3.2 + 6.1 + 7.6) = \underline{67.6}$$

635.2 meters

Antenna grouping E for the east-west subarray has transmission line lengths determined as follows:



$$4 \times (3.2 + 18.3 + 38) = 238$$

$$4 \times (3.2 + 6.1 + 38) = 189.2$$

$$4 \times (3.2 + 18.3 + 22.8) = 177.2$$

$$4 \times (3.2 + 6.1 + 22.8) = 128.4$$

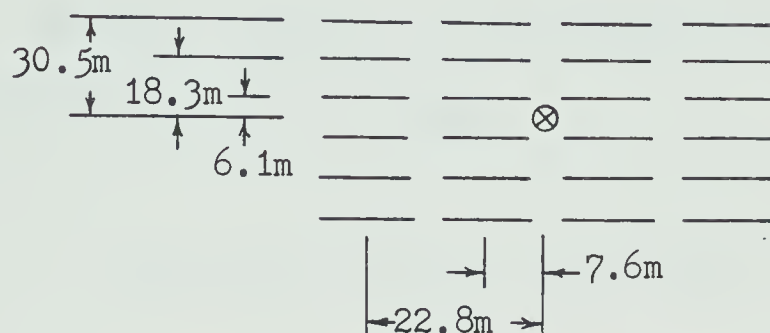
$$4 \times (3.2 + 18.3 + 7.6) = 116.4$$

$$4 \times (3.2 + 6.1 + 7.6) = \underline{67.6}$$

916.8 meters

Since there are 156 dipoles east-west on either side of the overlap region, there are an integral number (26) of antenna groupings.

If antenna grouping B is used for the north-south subarray, the length of transmission line required (per group) is as follows:



$$4 \times (3.2 + 30.5 + 22.8) = 226$$

$$4 \times (3.2 + 18.3 + 22.8) = 177.2$$

$$4 \times (3.2 + 6.1 + 22.8) = 128.4$$

$$4 \times (3.2 + 30.5 + 7.6) = 165.2$$

$$4 \times (3.2 + 18.3 + 7.6) = 116.4$$

$$4 \times (3.2 + 6.1 + 7.6) = \underline{67.6}$$

880.8 meters

With 200 dipoles north-south, there will be two columns of 33 antenna groupings, each grouping containing 24 dipoles, and two residual groupings of 8 dipoles. The length of transmission line in each of these two groupings is determined next.



$$4 \times (3.2 + 7.6 + 6.1) = 67.6$$

$$4 \times (3.2 + 22.8 + 6.1) = \underline{128.4}$$

196.0 meters

The total lengths of branch-feeder transmission line for a minimum-length system is then:

$$66(1001.6) + 635.2 + 26(916.8)2 = 114.4 \text{ km} \quad (\text{for groupings A and E})$$

$$33(880.8)2 + 2(196.0) + 26(916.8)2 = 106.2 \text{ km} \quad (\text{for groupings B and E})$$

For an equal-length transmission system, the longest branch-feeder run must be determined and multiplied by the total number of dipoles in the array. For grouping A and E, the total length of branch-feeder transmission line then, is:

$$(3.2 + 12.2 + 53.2)[(24 \times 66) + 16 + (24 \times 26 \times 2)] = 195.4 \text{ km}$$

Similarly, for grouping B and E, the total length is:

$$(3.2 + 18.3 + 38)[(24 \times 33 \times 2) + 8(2) + (24 \times 26 \times 2)] \\ = 169.5 \text{ km}$$

APPENDIX M

WAVELENGTH-DIVISION MULTIPLEXER DESIGN

In section 6.4 it was established that four optical signals was a reasonable number for wavelength-division multiplexing. Assuming the use of a prism-film coupler to accomplish the multiplexing and demultiplexing, we must now examine the feasibility of a practical design.

To be consistent with the development of section 5.2, a film waveguide thickness of $0.1\text{ }\mu\text{m}$ will be assumed. The index of refraction used will be 2.35 which is the average of 2.3 @ $0.532\text{ }\mu\text{m}$ and 2.4 @ $1.064\text{ }\mu\text{m}$ wavelengths for ZnS. Since the air gap is typically $\lambda/8$ to $\lambda/4$ in thickness, an arbitrary value of $0.125\text{ }\mu\text{m}$ will be chosen. For ease of physical placement of the feeder/imaging optics assemblies, a maximum angular separation of the beams is desired. From Figs. 5.5 & 5.6, the prism angle θ_p and refractive index n_p can be selected for a limited range of angles for wavelengths between 0.532 and $1.064\text{ }\mu\text{m}$. Since 45° is common for a prism, this value will be used for the angle θ_p . An arbitrary value of 2.5 will be selected as the refractive index of the prism. These two values result in an angular spread of about 30° from $0.532\text{ }\mu\text{m}$ to $1.064\text{ }\mu\text{m}$. The angle in the waveguide for any specific wavelength can be determined from Fig. 5.4. The choice of wavelengths will depend on the nature of the sources (LED or laser) and their spectral width as well as the spectral attenuation characteristics of the optical fiber transmission feeders. Fig. 2.16 indicates that a fiber with 4 dB/km attenuation

at $1.06\text{ }\mu\text{m}$ may have 10 dB/km at $0.6\text{ }\mu\text{m}$, with a relatively high attenuation region near $0.95\text{ }\mu\text{m}$. If we assume that the loss at the shorter wavelength can be acceptable and if we avoid the region from 0.9 to $1.0\text{ }\mu\text{m}$, we have available a bandwidth from about 0.6 to $0.9\text{ }\mu\text{m}$ and 1.0 to $1.1\text{ }\mu\text{m}$ and higher. If we further assume that the sources will be LED's, their wide spectral widths pose a problem; if lasers are used, there is no problem. As a worst-case example, LED's will be considered here.

LED's typically have a 40 nm spectral width between half-power points, as indicated in section 3.2.4. Irrespective of current device availability, the wavelengths will be chosen to give a reasonably wide angular discrimination. The advantage of doing this will soon be made apparent. The wavelengths considered will be 0.70 , 0.78 , 0.86 and $1.06\text{ }\mu\text{m}$. From Fig. 5.4, the angles in the film are 50° , 48.1° , 46.7° and 44.2° , respectively. Using eq.(5.6), the respective angles in the prism ϕ_p are found to be

$$\phi_p = \sin^{-1} \left[\frac{n_f}{n_p} \sin \phi_f \right] = \sin^{-1} \left[\frac{2.35}{2.5} \sin \phi_f \right]$$

$$= 46.1^\circ \quad \text{for } \phi_f = 50^\circ$$

$$= 44.4^\circ \quad \text{for } \phi_f = 48.1^\circ$$

$$= 43.2^\circ \quad \text{for } \phi_f = 46.7^\circ$$

$$= 41.2^\circ \quad \text{for } \phi_f = 44.5^\circ$$

Substituting these values into eqs.(5.5) and (5.6) yields the angle of incidence ϕ_i into the prism relative to the normal.

$$\begin{aligned}\phi_i &= \sin^{-1}[n_p \sin \phi_r] = \sin^{-1}[n_p \sin(\phi_p - \theta_p)] = \\ &\sin^{-1}[2.5 \sin(\phi_p - 45)] \\ &= 2.75^\circ \quad \text{for } \phi_p = 46.1^\circ \\ &= -1.5^\circ \quad \text{for } \phi_p = 44.4^\circ \\ &= -4.5^\circ \quad \text{for } \phi_p = 43.2^\circ \\ &= -9.5^\circ \quad \text{for } \phi_p = 41.2^\circ\end{aligned}$$

An examination of these numbers reveals an incident angle separation of 4.25° , 3° and 5° between the beams at 0.70, 0.78, 0.86 and $1.06 \mu\text{m}$ wavelengths, respectively. This not much separation. It is apparent that selecting wavelengths closer together, as could be the case with lasers, would severely compound the fabrication problem. This would be a logical application for integrated optics.

The following design calculations will be based on the model shown in Fig. 7.3(b). The compound lens comprised of a primary and a secondary lens is considered to be 1 cm in diameter. This should be sufficiently large for ease of fabrication and manipulation, yet small enough to keep the physical configuration to a reasonable size. A fiber with numerical aperture 0.14 ($\theta_c \simeq 8^\circ$) will be assumed for the secondary transmission feeder. If the end of this fiber is

positioned 3.5 cm from the primary lens, trigonometry indicates that some 97% of the lens diameter will be used for light transmission since the cone of illumination will cover this much of the lens. This suggests that the primary lens should have a focal length of 3.5 cm.

If we now consider the section from the secondary lens to point 0, additional parameters can be determined. Table 5.5 indicated that a beam width of 2° should not result in a noticeable decrease in coupling efficiency. This figure will be used in the design. For a focused beam with 1° convergence from the axis and a lens diameter of 1 cm, trigonometry indicates that the separation of the secondary lens and the focal point 0 would be $0.5/\tan 1^\circ \simeq 28.6$ cm.

The narrowest separation was 3° between input beams at 0.78 and 0.86 μm wavelengths. A 1 cm diameter lens would have to be a distance of at least $1/\tan 3^\circ$ or 20 cm from point 0 to be situated in direct proximity to the adjacent lenses. Since efficient coupling requires a distance of about 30 cm, lens placement should not be a problem.

It will be assumed that the focal lengths of the secondary lens will be such that the light incoming from the fiber as shown in Fig. 7.3(b) will be focused at point 0, which will be at least 30 cm from the lens.

B30303